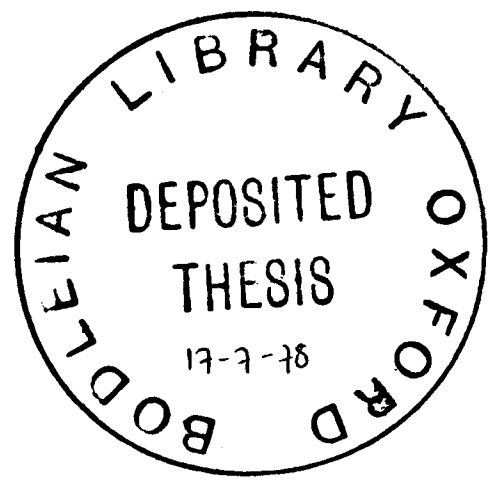

3064674995

THE APPLICATION OF ELECTRONIC TECHNIQUES TO HIGH ENERGY PARTICLE DETECTION

R.W. Pleming

St. John's College



This thesis is submitted in partial fulfilment of the requirements for the degree of Doctor of Philosophy at the University of Oxford.

August 1977

ACKNOWLEDGEMENTS

I am very grateful to:

Professor Sir Denys Wilkinson, for giving me a place in the Oxford University Nuclear Physics Laboratory;

The Science Research Council for the award of a grant enabling me to pursue this research;

The President and Fellows of St. John's College for electing me to a Senior Scholarship.

It is a rewarding experience to be part of a group whose talents and efforts are directed towards a common goal. In most large experimental projects, design decisions are made only after discussions among the members of the design group. In this way, errors are avoided and new ideas are produced. Thus I cannot claim that the work contained in this thesis, on the ISIS project, is mine exclusively.

I would like to thank in particular:-

Dr. Wade Allison, my supervisor, for his enthusiasm, encouragement and help;

Barney Brooks and Dr. John Lloyd for many useful and informative discussions;

Pete Shield, with whom I worked closely on the electronics, for all his hard work, interest and assistance;

Adib Romaya for aid with the software;

Drs. James Bunch, John Cobb, James Symons and Tony Williams, my fellow graduate students, for their friendship especially;

Roger Giles, Mike Walker and the other members of the ISIS Project group: it has been a pleasure to work with them all;

Tricia Falconer Smith for typing this thesis so patiently and so expertly.

Finally, I thank deeply my parents and my wife, Margie, for their continuing love and encouragement.

CONTENTS

		Page
ABSTRACT		(a)
CHAPTER I	INTRODUCTION	(b)
I.1	The collection of information at high rates and in noisy conditions.	1
I.2	The specific case of ISIS	9
CHAPTER II	THE GAS STATE PROCESSES IN THE ISIS CHAMBER	25
II.1	The formation of the Ionization Track	26
II.2	The effect of drift on the Ionization Track	30
II.3	Gas amplification at the wire plane	38
II.4	Factors affecting the Wire Separation	48
CHAPTER III	THE ELECTRONICS FOR ISIS	57
III.1	The organization of the electronics	58
III.2	Electronic amplification and noise sources	60
III.3	Pulse shaping	76
III.4	Ionization: Pulse integration, storage and digitization	86
III.5	Timing: Gate generation and Time-of-Arrival Memory	93
III.6	The DC baseline restorer	101
III.7	Logic control, computing and software requirements.	108

		Page
CHAPTER IV	THE PREDICTED AND MEASURED PERFORMANCE OF ISIS	112
IV.1	The use of a computer model	113
IV.2	Tests using artificial signal sources	116
IV.3	Tests with x-ray sources	121
IV.4	Tests with charged particles	136
IV.5	Derivation of optimum system design	159
IV.6	The predicted performance of ISIS	177
CHAPTER V	CONCLUSION	190
APPENDICES		
1	The form of the gas amplifier output pulse	192
2	Wire plane operating voltages and gas gain switching	199
3	Electromechanical stability of the wire plane	202
4	SIMSYS: the ISIS simulation program	207
REFERENCES		217

ABSTRACT

The technical implications are discussed, of the physical principles behind ISIS, a large volume nuclear particle detector. The particular solution adopted in ISIS is described, for the accurate acquisition of data at high rates and under poor signal-to-noise conditions.

A computer program has been written to simulate the processing of signals and noise within ISIS. To check the validity of the simulation, its predictions have been compared with the results of experiments using prototype equipment. With the aid of the simulation, the performance of ISIS has been investigated as regards the spatial resolution and the particle-identification capability of the device. An optimum design for the whole ISIS device has been attained, as a compromise between this performance and tolerable systematic effects. In addition, it has been shown that, around the operating point, there is an adequate window within which satisfactory performance is maintained.

CHAPTER I

INTRODUCTION

In I.1, some general considerations on the collection of information at high data rates and under poor signal-to-noise conditions are discussed. A specific device, ISIS, is introduced in I.2. The architecture of the system is described and compared with those of two similar devices. The rest of the thesis is devoted to a detailed examination, carried out by the author, of the implementation and characteristics of ISIS.

I.1 THE COLLECTION OF INFORMATION AT HIGH RATES AND IN NOISY CONDITIONS

A significant characteristic of contemporary high-energy physics experiments is that they involve the collection and processing of large amounts of information. This is due to the statistical nature of the subsequent data analysis. The trend is towards larger quantities of data being collected at ever-increasing rates.

Another important characteristic is the presence of the perennial signal-to-noise ratio problem. In a well-designed experiment, the ultimate accuracy is determined by the instrumental signal-to-noise ratio.

These two factors, data rate and signal-to-noise ratio, are key considerations in the design of the data acquisition systems for such experiments.

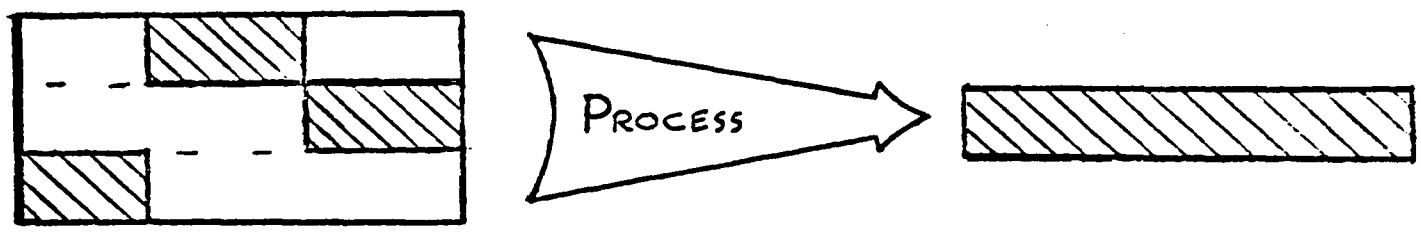
Data Rates

In practice, the maximum mean data rate within a data acquisition system is usually determined by the method of permanently recording the data. If the data is recorded onto magnetic tape, for example, the mean data rate must be less than about 10^6 bits/second, per tape recording device (9 track, 1600 bpi). If, as is often the case, the input data rate is too high, data rate reduction must be performed. Three methods of data rate reduction are outlined here:

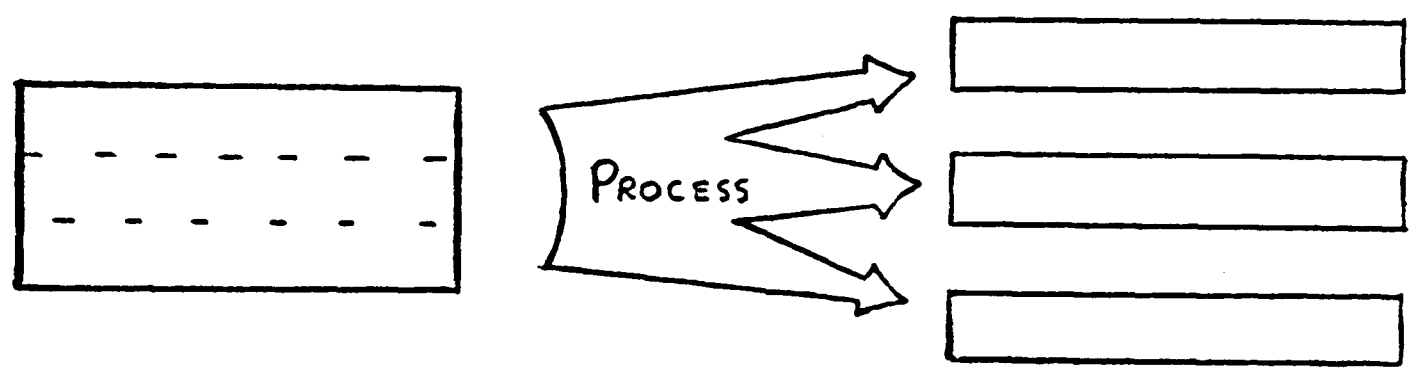
(i) Preprocessing, Fig. I.1(a)

Preprocessing of the data involves immediate extraction of the useful information, resulting directly in a data rate reduction.

(a) Preprocessing



(b) Parallel Processing



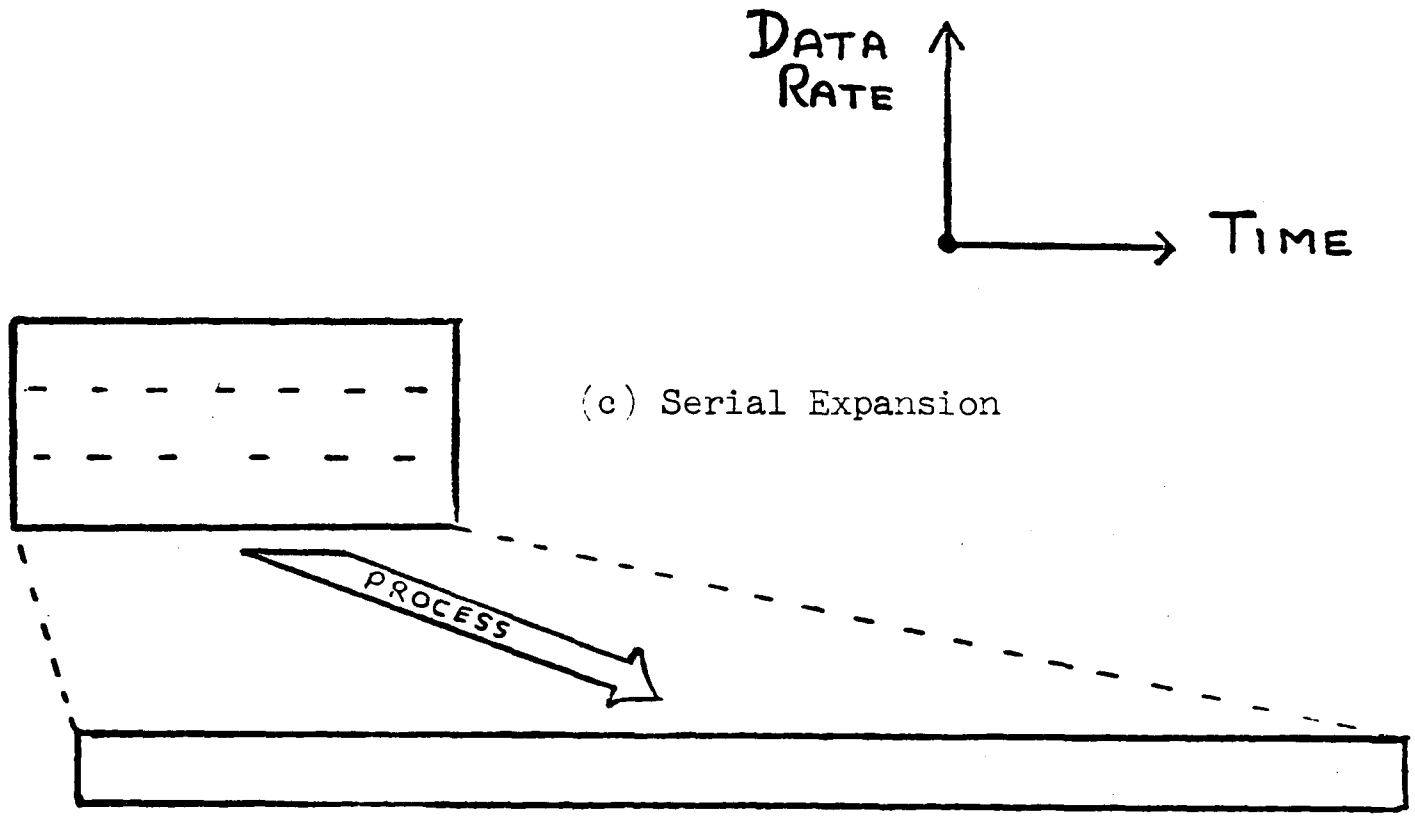


Figure 1.1 Methods of Data Rate Reduction

Redundant or useless information is discarded. Preprocessing is only efficient if a comparatively short analysis of the input data is required to effect a significant reduction in the amount of data. If the analysis is complicated, a large overhead in temporary storage may be incurred. In addition, the presence of redundant data is often useful for fault diagnosis or error recovery. Preprocessing is usually performed on data in the digital domain. An example is the fast selection of the data describing a high energy interaction, conditional on the geometry of the event [GR73]. However, preprocessing is also often implicitly performed in the analogue domain: the selection of signals as opposed to noise by discrimination is an example.

(ii) Parallel Processing, Fig. I.1(b)

The input information may be in a format that facilitates parallel processing. Parallel processing involves dividing the input data up into many logically-equivalent blocks. The blocks are then processed simultaneously by many identical channels, with each channel processing one block. The number of channels is determined by a compromise between the rate reduction required, and the complexity or cost of the channels. A typical example, in which the format of the input data demands parallel processing is the acquisition of data from an array of identical transducers, e.g. a multi-wire proportional counter [BR74]. In this particular example, preprocessing is combined with parallel processing to reduce the output data rate [BA75].

(iii) Serial Expansion, Fig. I.1 (c)

In serial expansion, the data rate is reduced by expanding the time taken to process a given amount of data: the data is mapped on to a longer time scale. Of course, this cannot be achieved with a continuous stream of input data without loss of some of the data. However, if the data occurs in bursts, the data burst may be expanded to fill the spaces between them. A burst/space ratio of α will allow a data rate reduction by a factor α. A typical example of serial expansion is parallel-to-serial format conversion e.g. [AM75].

These three methods of data rate reduction may be combined according to the nature and requirements of the device. The use of all three methods is demonstrated in I.2.

Signal and Noise Sources

The properties of signal sources are dependent on the physical processes occurring within the source itself. The characteristics of a source include:

(i) The output signal amplitude and profile.

(ii) The output impedance.

(iii) The numbers of charge carriers, and their activation energy, that are involved in the process of signal generation.

(iv) The sensitivity of the output to variations in a transduced parameter.

(v) The efficiency of detection.

(vi) Resolution, stability.

(vii) The linearity of the response.

(viii) The noise level.

In these respects, the three common types of nuclear particle detector (gas-filled, semiconductor and scintillation) have contrasting properties. For instance, the primary charge carrier activation energy in a semiconductor detector is quite small (∿4eV), compared with ∿20-30 eV for a gas-filled counter, or ∿500-1000 eV for a scintillation counter [NP74]. Thus the numbers of primary charge carriers in a semiconductor detector may be very much higher than those in the other two types. As a result, the signals from a semiconductor detector are less noisy than those from the other detectors.

The presence of noise with signal results in a degradation of the information in the signal [BL62]. Noise may be categorised into two types:-

(i) Non-deterministic

This noise has a fundamental physical origin e.g. Johnson noise (thermodynamic origin), shot noise (statistical origin) [RF62]. Non-deterministic noise gives rise to only random effects.

(ii) Deterministic

Deterministic noise is usually of man-made origin, and may, in principle, be removed completely. Examples are hum, pickup, microphony, active filter noise etc. Deterministic noise may cause systematic errors.

Noise may also be classified as to the signal-noise correlation:-

(i) Uncorrelated

Uncorrelated noise is continuously present, even in the absence of signal e.g. Johnson noise, hum.

(ii) Correlated

Correlated noise coexists with the signal and may be a feature of the signal itself, being a result of the signal generation process or the subsequent treatment of the signal. Examples are shot noise (dependent on the number of charge carriers) and active filter noise.

The Implications of a Poor Signal-to-Noise Ratio

The main results of a poor signal-to-noise ratio are impaired signal detection efficiency and inaccurate signal magnitude and timing measurement.

(i) Signal detection efficiency

The presence of noise in a system means that signals may be detected only when they are distinguishable from the noise. Signal detection is usually performed by amplitude discrimination , see Fig. I.2. The choice of discrimination level involves a compromise between the probability of signal detection, and the noise-induced false alarm rate (due to noise pulses crossing the discrimination level). There will be a bias towards the efficient detection of larger signals. However, any form of signal detection will introduce systematic distortions.

(ii) Signal magnitude and timing measurements

The noise in a system will, to a greater or lesser extent, disturb the measurement of signal magnitude or timing. If the noise is random, the measured values will be distributed about a true mean.

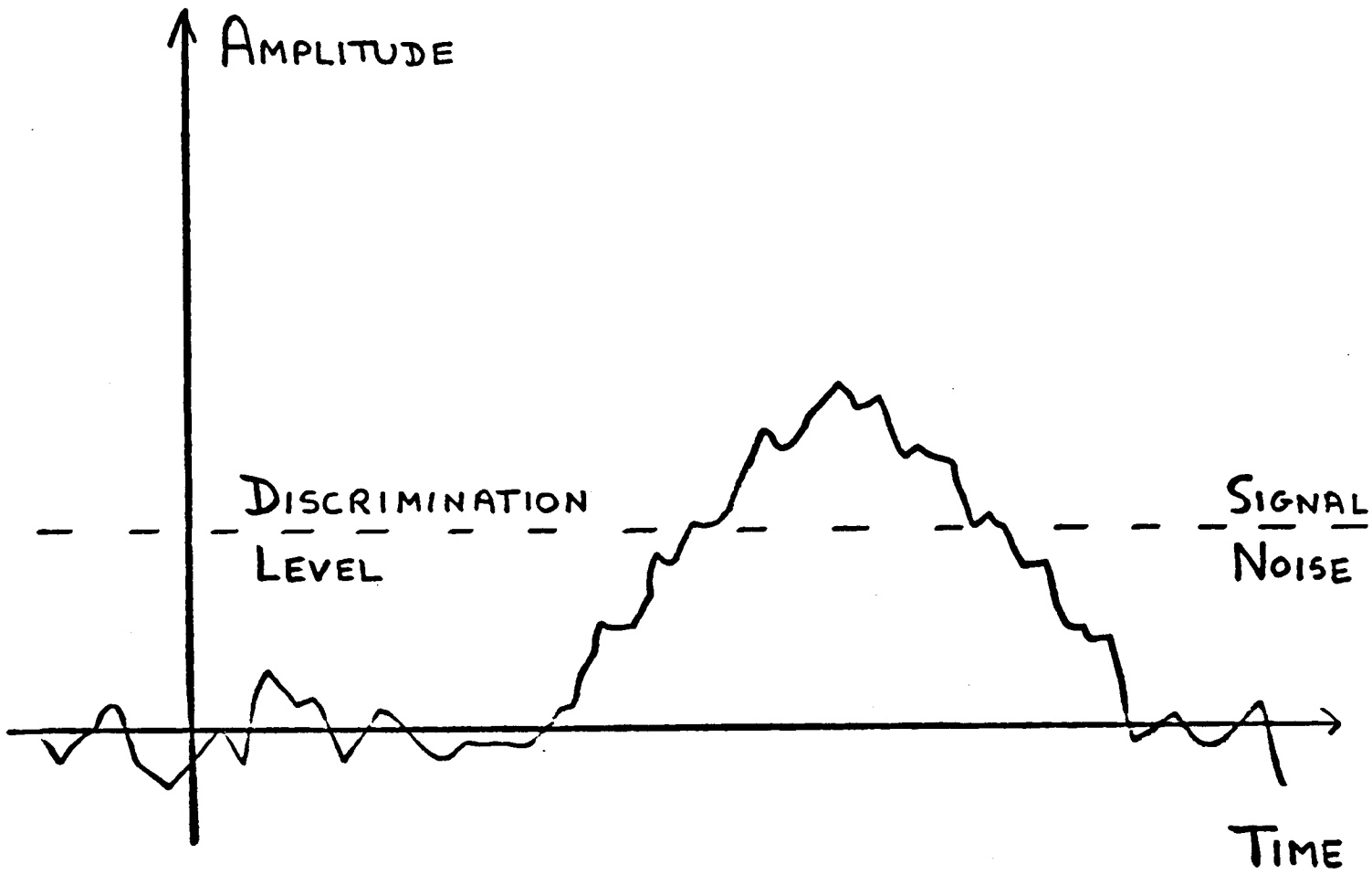


FIGURE I.2 Detection of a Signal by Amplitude Discrimination.

However, deterministic noise may cause a systematic change to the measured values. Much work has been done on the design of signal processing systems to minimise the effect of noise on the measurement of the magnitude or timing of specific signals. Mostly this involves the use of an optimized signal filter. For a review of the theoretical background, see [DW58], [RV68], [ME71]. For a review of current practice see [NP74].

Analogue-to-Digital Conversion (ADC) Techniques

In many experiments, the output from a transducer may be available in the form of an analogue signal whose amplitude or integral contains useful information. To facilitate subsequent processing of the information, possibly in conjunction with other data, the signal must be converted to the digital domain, where it will be more efficiently handled.

Two types of analogue-digital conversion are in common use: [NP74], [HL70], [HD68].

(i) Successive approximation, Fig. I.3(a)

The method involves comparison of the amplitude of the analogue signal with the output of a digital-to-analogue converter (DAC). The DAC is controlled by logic using the result of the comparison, so as to generate an analogue output which approaches that of the input signal in successively smaller (usually binary) steps. When the least significant increment has been added, the digital input to the DAC is the required digital value of the analogue input. This method is very fast, stable and accurate: digitization to 10 bits (0.1%) is possible in under 1μS with less than 0.15% differential non-linearity. However, implementation of the method is expensive because the circuitry involved can be quite complex.

(ii) Analogue-Time-Digital conversion

These are two common methods of analogue-digital conversion that involve an intermediate conversion to the time domain:

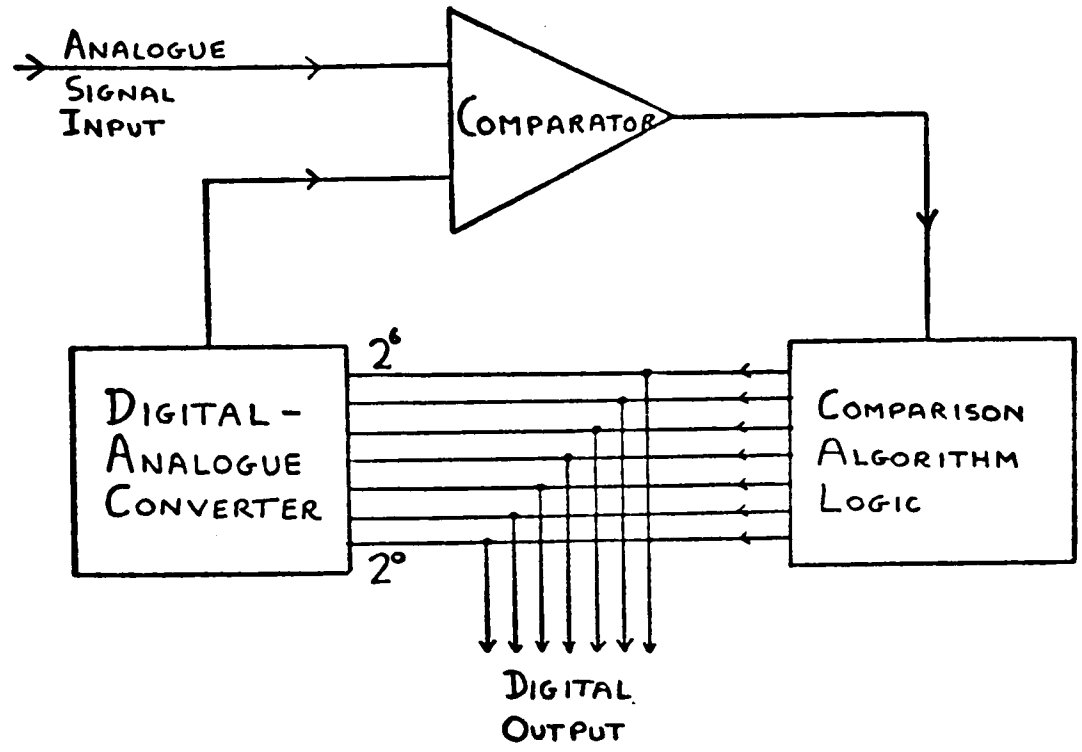
(a) Ramp comparison type, Fig. I.3(b)

The analogue input signal is sampled and an instantaneous value held using the 'sample-and-hold'. A linear ramp generator and a clocked counter are started simultaneously. A comparator stops the counter when the ramp amplitude reaches that of the held input signal.

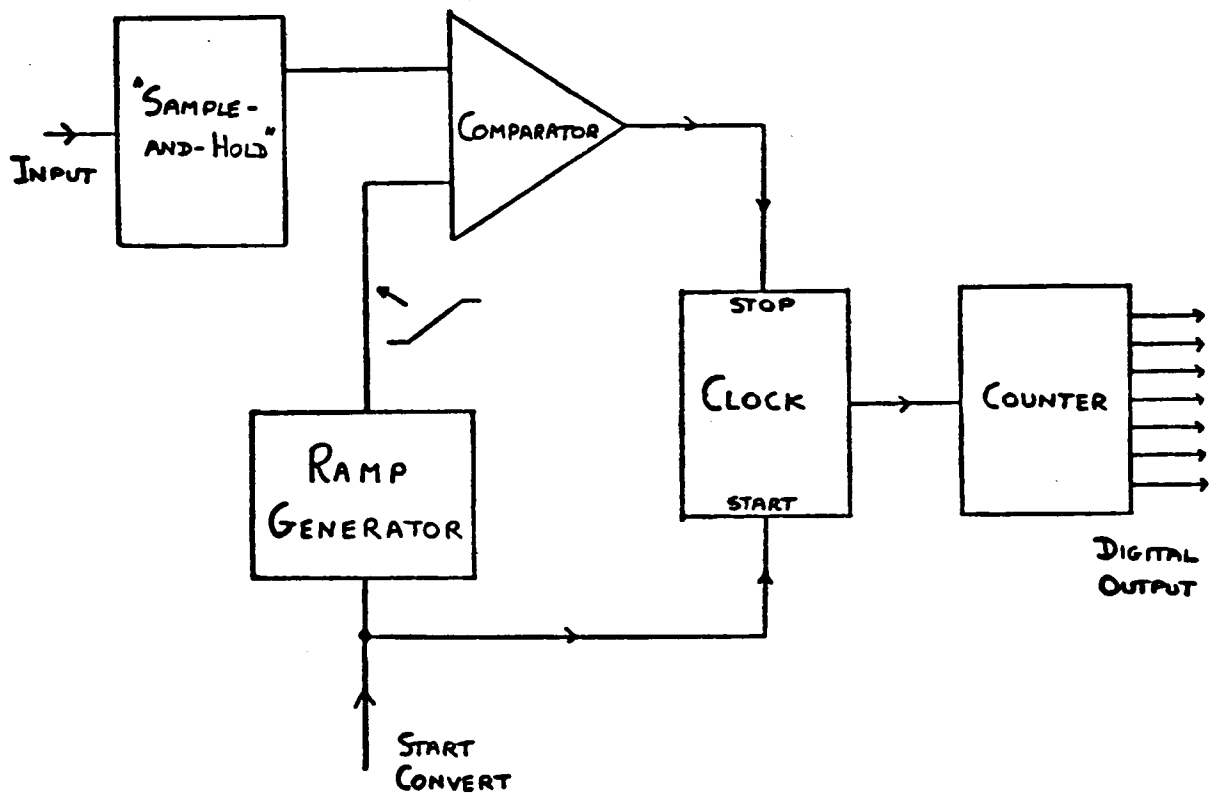
(b) Rundown (Wilkinson) type [WH50], Fig. I.3(c)

The analogue signal is stored as a proportional charge on a capacitor. (This facilitates signal integration.) The capacitor is then discharged with a constant current. The time taken to do this is measured by gating a clocked counter with the output from a comparator looking at the capacitor voltage. A pedestal level may

(a) Successive Approximation ADC



(b) Ramp Comparison ADC



(c) Wilkinson ADC

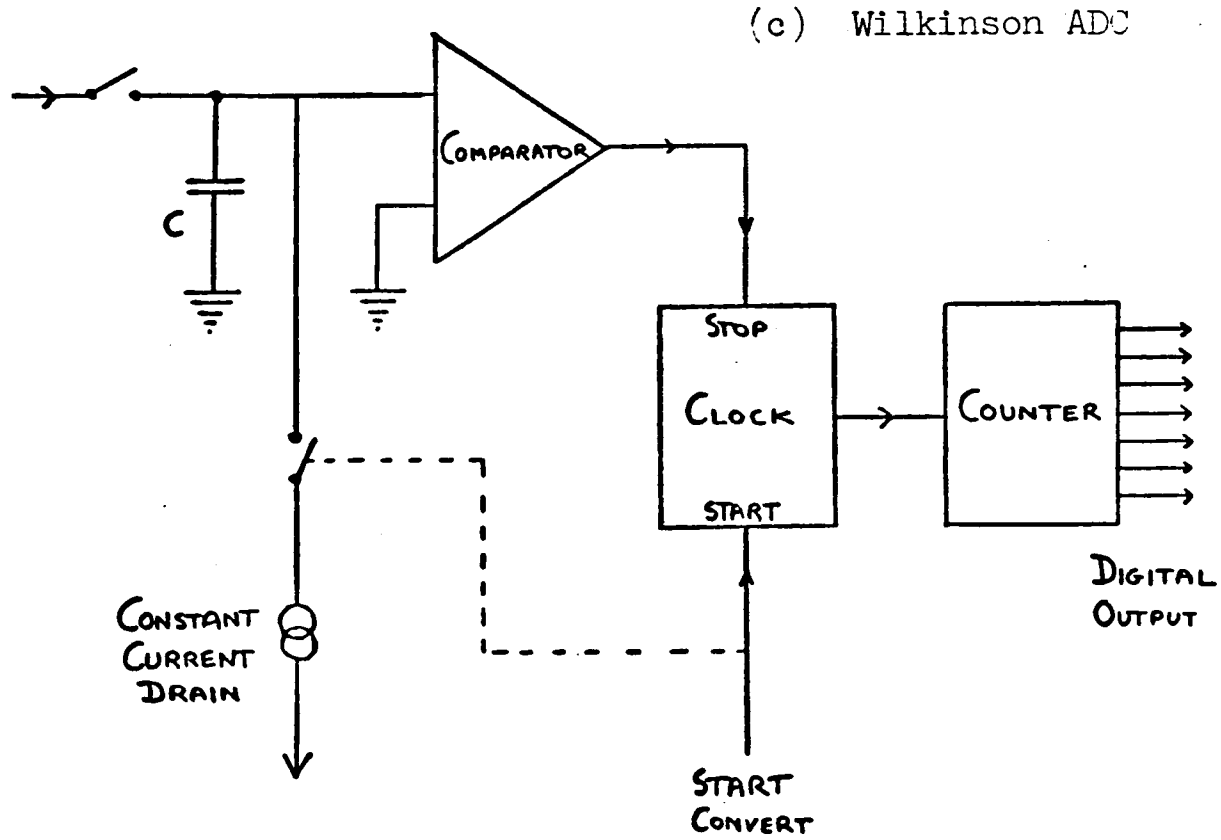


Figure 1.3 Methods of Analogue - Digital Conversion

be supplied by taking the comparator reference to a potential below that of the initial state of the capacitor.

In both cases, the digitized value of the input signal is obtained at the output of the counter. The Analogue-time-digital conversion method is cheaper and simpler than (i), but is also slower (being limited by counter speed) and slightly less accurate. Typical digitization to 8-bit accuracy (0.4%) takes up to 25 μS, with a differential non-linearity of 0.5%. Main factors affecting accuracy are the linearity of the ramp signal in (a), and the stability of the discharge current for (b).

Conclusion

The acquisition of data at high rates and under poor signal-to-noise conditions has been discussed. Next, a specific example of a device operating under these conditions is described. Later chapters contain full descriptions of the various key components of the device, and the way in which they are inter-related.

I.2 THE SPECIFIC CASE OF ISIS

Certain general considerations behind the measurement of signals at high data acquisition rates, and under poor signal-to-noise conditions, were outlined in the previous section. In this section, the architecture of a device operating under such conditions is described. The device is ISIS, a large-volume low-mass detector of relativistic charged particles. Information on both particle trajectory and particle velocity is available from the device, for up to 30 particles simultaneously. The spatial resolution of ISIS is between 1.3 cm and 2 cm depending on the trajectory of the particle. The velocity resolution is good enough to ensure separation of kaons, pions and protons of the same momentum, with an efficiency of 90%, over the momentum range of 3-100 GeV/c (although the identification efficiency at a particular momentum is dependent on the particles involved, see [EHSP]). The device is intended for use as part of a spectrometer, in the extensive investigation of high multiplicity interactions at high energies (>100 GeV) over a large solid angle [EHSP]. (This reference also discusses the justification of ISIS in terms of the physics that may be learnt with it.)

The device may be split up into two logical components: the detector itself and the associated electronics. The physical principles of the detector are discussed first. Although the basic principles have remained the same, there have been several refinements in the design since the idea was first suggested in 1972 [AW72], [AW74].

The Physical Principles of ISIS

The physical principles of operation of the ISIS device are illustrated in Fig. I.4. The particle-sensitive medium is a gas (80% argon + 20% CO_2 at atmospheric pressure). The sensitive volume is large; the gas is contained in a chamber 2.5 m wide x 4 m high x 6 m deep. This size gives the detector a large solid angle acceptance. There is very little mass in the path of particles in the chamber. (The gas and other material in the chamber represent 0.07 of a radiation length and 0.02 of an interaction length [EHSP].)

A particle crossing the chamber leaves an ionization track behind it in the gas. The quantity of ionization in the track is a function of particle velocity. Thus a measurement of the ionization will yield a value for the velocity (see II.1). In 80% argon/20% CO_2 the mean density of ionization along the track amounts to about 100 electron-ion pairs per cm of track. However, because the amount of ionization per cm fluctuates widely, the ionization distribution along at least 5 m of track mustbe measured for a satisfactory velocity resolution [CJ76].

The chamber is bisected by a wire plane of area 2.0 m x 5.1 m, consisting of alternate 12.5μ-radius anode wires, and 125μ-radius cathode wires, positioned parallel to the 2.0 m dimension, on a 4 mm pitch (see II.4). A substantial but highly uniform electric field of ∿100 kV/m is maintained between the outer (negative) electrodes and the central wire plane [IN26]. The ionization electrons from the track drift down the field lines at a constant velocity of 4 cm/μS, and are collected at the anodes (see Fig. 10(a), Fig. I.5). The maximum drift distance is 2m (from the negative electrodes) resulting in a maximum drift time of 50 μS. This is a very large drift distance compared with those used in conventional drift chambers, of a few cm (see [SB75], [RP74] for a review).

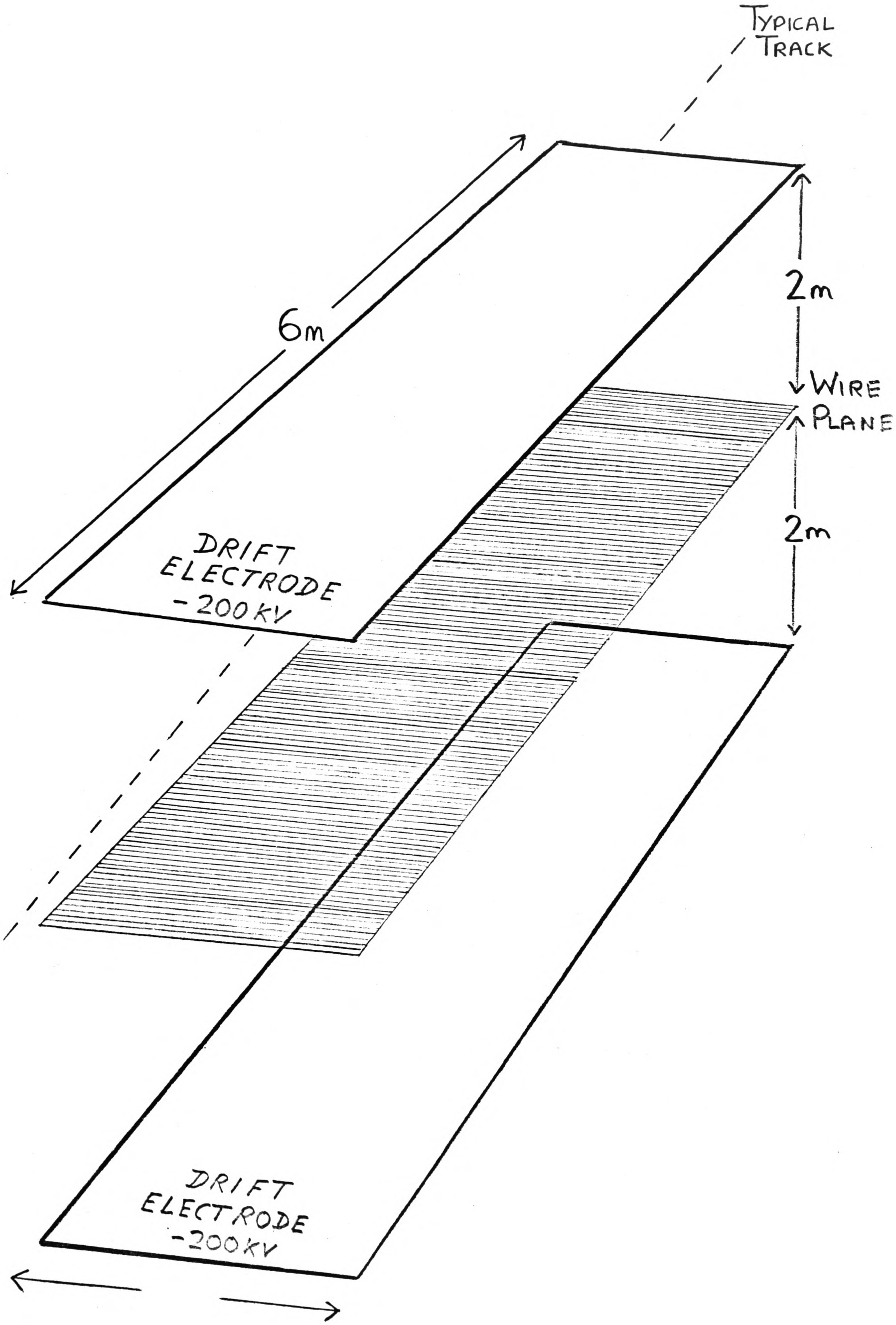


Figure 1.4 Schematic Diagram of the ISIS Chamber

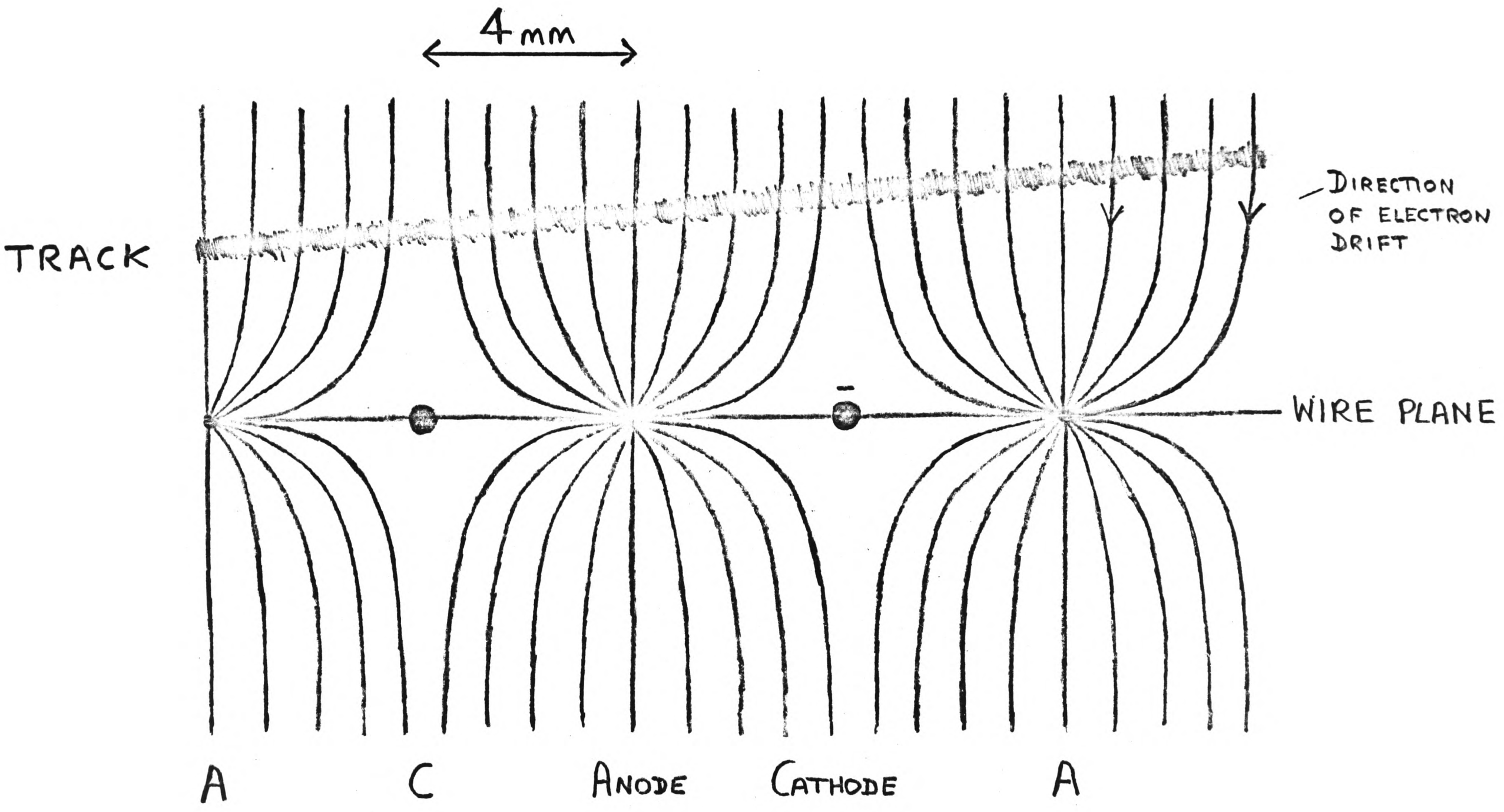


Figure 1.5 The Electric Field around the Wire Plane

In a 5.12 m length of the chamber, there are 640 anode wires. The uniformity of the field within the chamber ensures that each anode receives the ionization from the projected length of track equal to the anode-anode spacing of 8 mm. The ionization track is thus divided into 640 ionization samples. It is this feature of sampling the track ionization which gives ISIS its name: "Identification of Secondaries by Ionization Sampling", as well as its good velocity resolution.

By drifting the ionization to the central wire plane at a constant velocity, the position of the track within the chamber is mapped linearly into the time domain. The arrival time of a sample of ionization at an anode, relative to the time zero when the particle crossed the chamber, is equal to the distance drifted divided by the drift velocity. Thus measurements of the arrival times of the samples at each anode will yield two-dimensional information on the trajectories of the tracks through the chambers.

The use of a central wire plane with symmetric drift regions on either side causes an ambiguity, since, in the time domain, the tracks in the two regions will be superimposed (see Fig. I.10). The problem is resolved by measuring externally the entry and exit points of particles traversing the detector, using conventional drift chambers [EHSP]. These points are then matched with the tracks in the ISIS detector.

A potential of $\sim$2 kV is maintained between the anodes and the cathodes. Proportional gas amplification of the ionization occurs at the anodes, with an amplification factor of $\sim$10000 (see [WD50], II.3). The wire plane operates very much like that in a large multiwire proportional chamber: see [CG70], [RP74]. The cathode wires are necessary to provide fine gain control and to increase the isolation

between anodes. Although the wires are 2.0m long, only data originating from the central 1.8m is used, because of edge effects. As a result of the gas amplification, a signal current, proportional to the rate of arrival of ionization at the anode, is generated in the anode-cathode circuit.

In the time that the ionization takes to reach the anode, dispersive processes are at work (e.g. diffusion see II.2). These processes result in a spread in the arrival time of the ionization, of a few hundred nanoseconds (a few mm in terms of drift distance). The dispersion is the limiting factor on the spatial resolution of the device. A broad current pulse is produced in the anode-cathode circuit, reflecting the convolution of the dispersed arrival times of the ionization electrons with the gas amplifier response (see II.3).

The amount of ionization in the track sample is determined by integrating the signal current. The integration is performed by the electronics, which also records the time-of-arrival of the signal. To achieve the quoted velocity resolution, the signal integration must be unbiassed at the level of 1% [CJ76], [AW76]. Systematic effects and correlations at this level are important. A track ionization distribution is constructed from these measurements on the ionization samples. The shape of the distribution is shown in Fig. I.6. The velocity of the particle may be determined from this distribution by comparison with that of a particle of known velocity, e.g. a beam particle. Using a value of particle momentum obtained by magnetic analysis, the mass of the particle, and hence its identity, may be discovered.

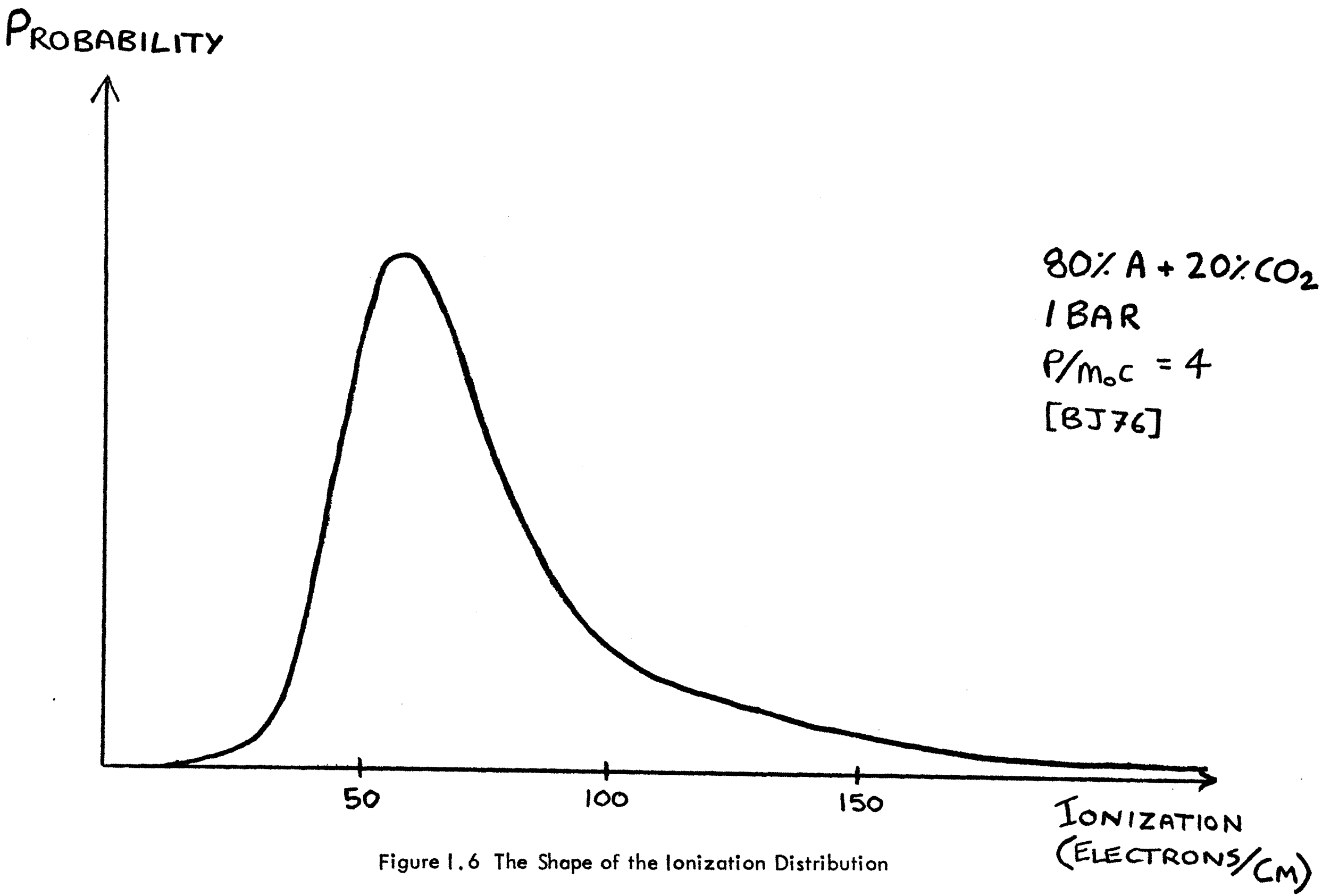


Figure 1.6 The Shape of the Ionization Distribution

Further details of the processes occurring in the gas state within the ISIS chamber itself are contained in Chapter II. In II.1, the nature of the ionization track left by a charged particle is discussed. A description of what happens to the ionization track, from the time that it is created until it reaches the wire plane, is contained in II.2. The particulars of the gas amplification process which occurs at the anodes are described in II.3. Certain considerations or the factors affecting the choice of wire separation in the wire plane are discussed II.4.

The Electronic System

The electronic processing of the signals from the ISIS chamber satisfies several requirements:

(i) The magnitude and timing of the signals from the chamber must be measured, to an accuracy of better than 1%.

(ii) The information must be converted from the analogue to the digital domain.

(iii) The data rate must be reduced to one that can be handled by conventional data processing equipment.

The electronic system in ISIS is described in detail in Chapter III. The electronic techniques used in nuclear particle detection are reviewed in [NP74] and [HL70].

As explained above, the output from the chamber consists of current signals from 640 anode circuits, each corresponding to an 8 mm sample of track ionization. The nature of the ionization and track position measurements require that these signals be processed independently, in parallel.

One electronic channel is identified with a pair of adjacent anodes (see Fig. I.7). Without harming performance, this doubles the signal available at the input of a channel, and halves the number of channels required to 320 (an important consideration because of their cost: ∿£150 each). The width of the ionization sample is effectively increased to 1.6 cm (see II.4).

A schematic diagram of one of the electronic channels is shown in Fig. I.8. In the design, advantage was taken of the environment in which ISIS is to operate. The experiments involving ISIS use a rapid cycling hydrogen bubble chamber as target and vertex detector [EHSP]. The bubble chamber is sensitive for ∿1 mS every ∿33 mS. Within the 1 mS sensitive period, an interaction can be expected, causing the simultaneous entry of several secondary particles into the ISIS chamber, (where they are to be identified). In the 33 mS insensitive period, no data need be acquired by ISIS. Thus the operation of the electronics divides naturally into two modes:

(i) Data acquisition mode, corresponding to the bubble chamber sensitive time, in which the signal magnitudes and times-of-arrival are stored temporarily, and

(ii) Data readout mode, corresponding to the insensitive period, in which the digitized values are passed to a mini-computer for recording onto magnetic tape.

There is a fundamental difference between the two modes. During data acquisition, each channel operates completely independently. In contrast, the data readout is synchronously controlled by the computer.

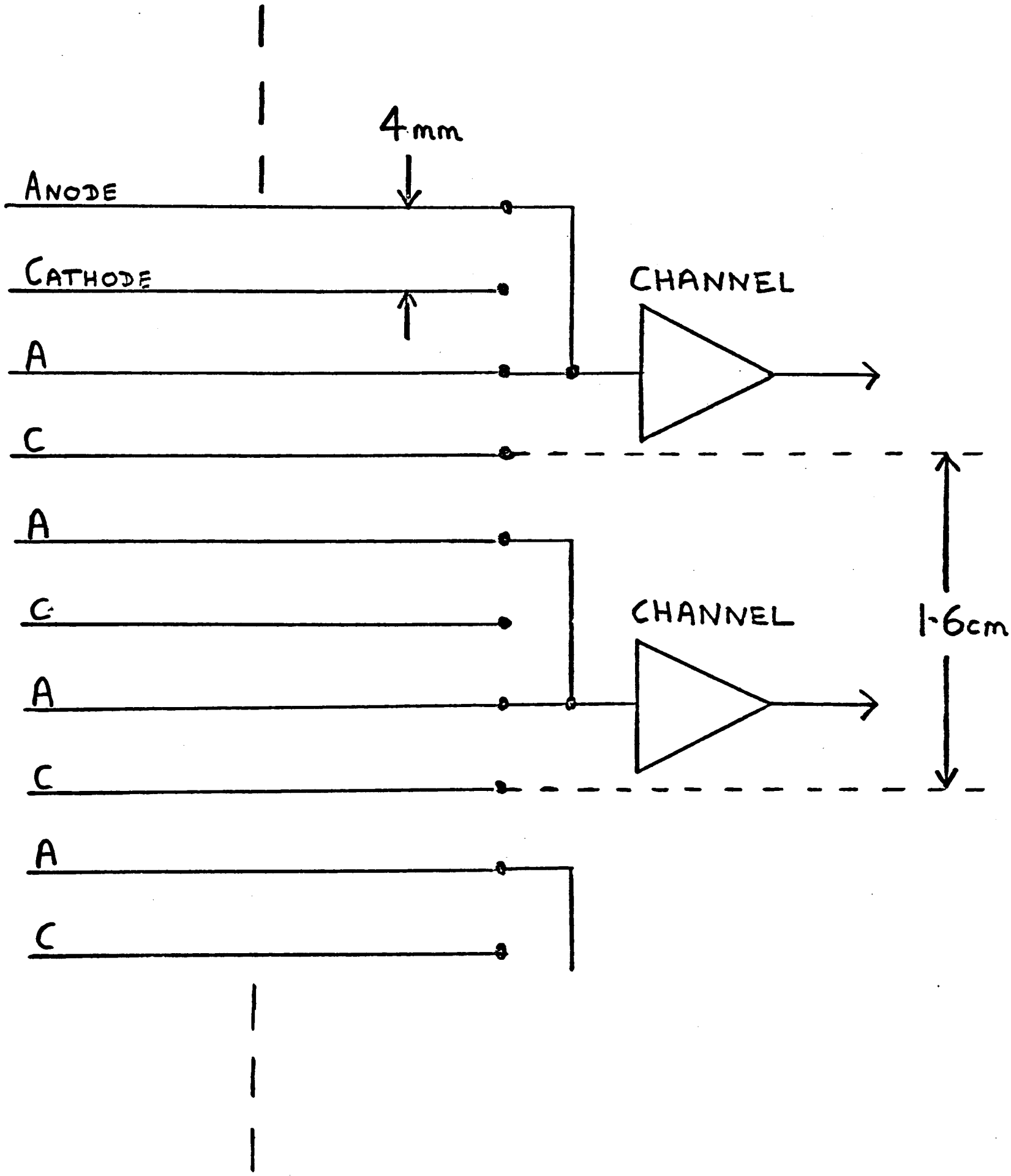


Figure 1.7 Schematic Diagram of Chamber - Channel connection

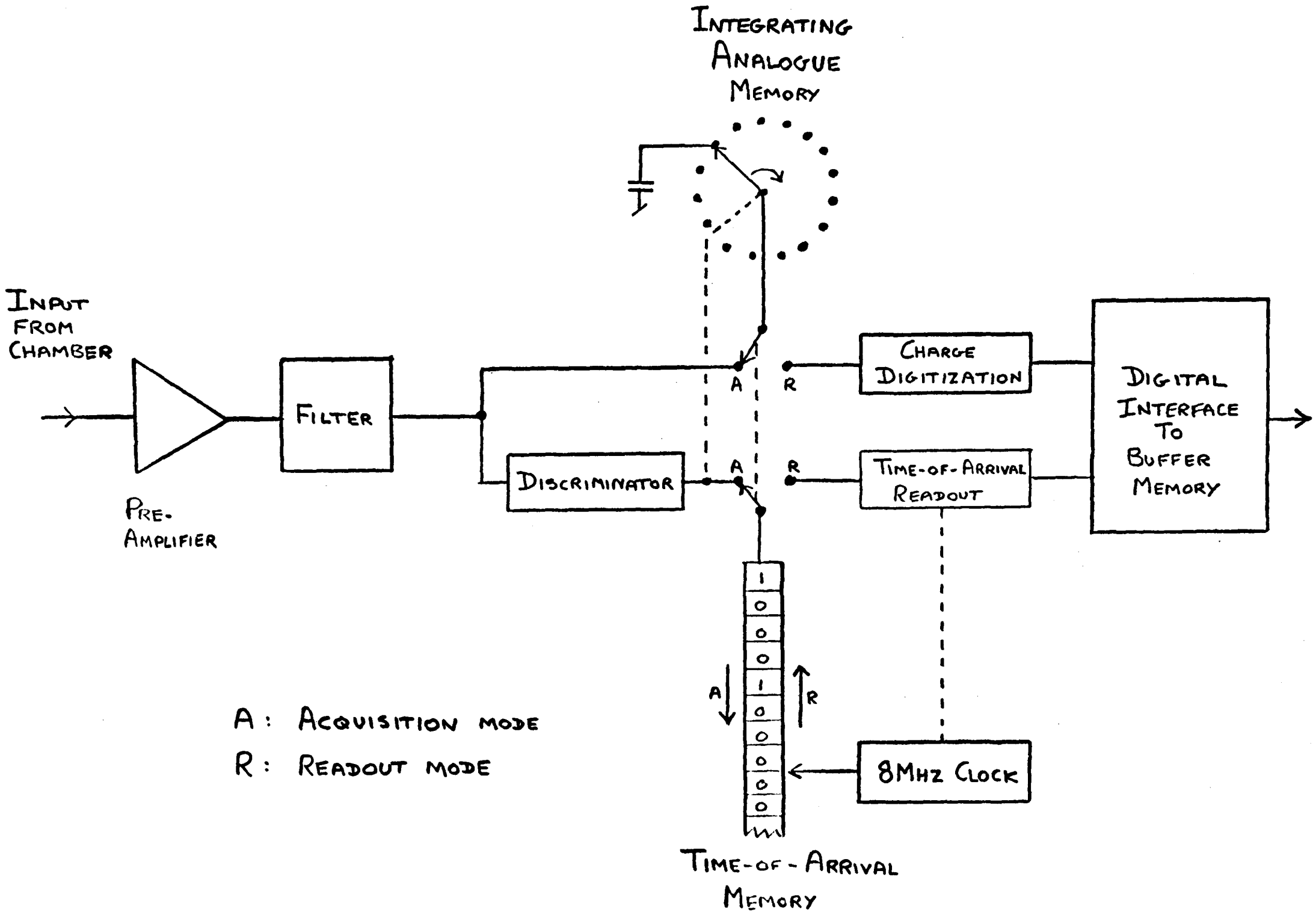


Figure 1.8 Schematic Diagram of one Electronic Channel

In the data acquisition mode, the signals from the anode wire pair are first amplified by a low noise preamplifier (see III.2). An optimum pulse shape is obtained by filtering the signals (see III.2). The presence of a signal above the noise level is detected by a discriminator (see III.5). A DC Baseline Restorer provides a stable zero signal level at the high and varying signal rates encountered (see III.6). The 3 dB bandwidth of the analogue signal path is 8 MHz, corresponding to an effective rise time of ∿40 nS.

The amount of ionization causing the signal is determined by integrating the pulse. The integration is performed by charging a capacitor with the signal current (see III.4). The duration of signal to be integrated is defined by a gate, generated by the discriminator so as to overlap the signal at the 99% level (see Fig. I.9). The capacitor is then isolated, and retains its charge to a 1% accuracy for many milliseconds. This capacitor is one of 32 in the analogue memory which are used sequentially for successive signals, in a cycle. The oldest data is overwritten by the new. The analogue memory may contain the pulse magnitudes of the previous 30 signals. (Two capacitors are always in a discharged state, ready to receive the next signals.) Thus the ionization information for up to 30 tracks may be stored temporarily.

The discriminator also provides the signal timing information. The discriminator output feeds the input of a clocked shift register. The arrival of each signal is recorded as a bit in the register (see III.5). The capacity of the register is 512 bits, and the shift rate is 8 MHz. The signal timing history is thus continuously available for the previous 64 μS, at a resolution of 125 nS (equivalent to 0.5 cm in terms of drift distance). The maximum drift time

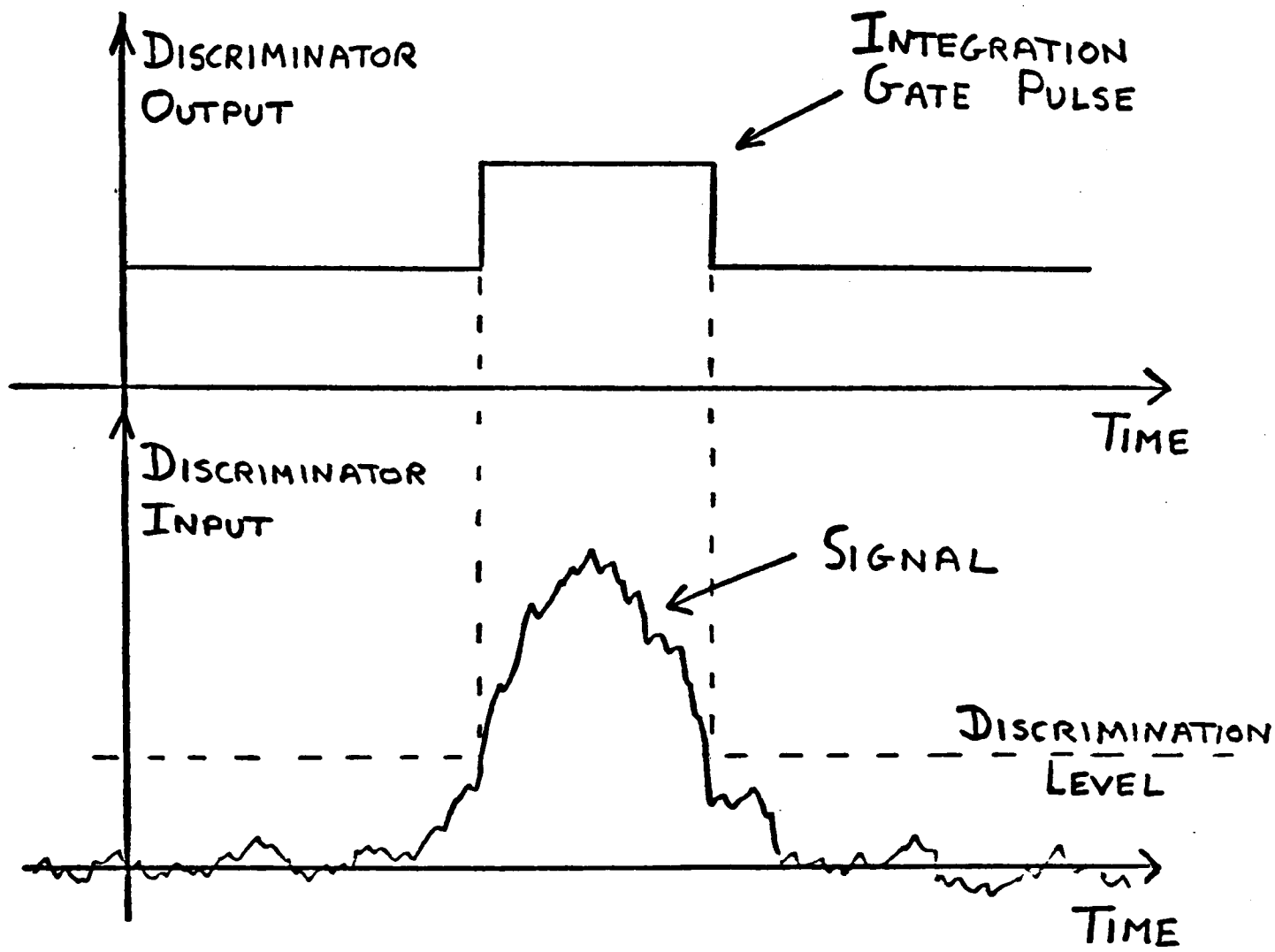


FIGURE I.9. Integration Gate Generation.

(corresponding to 2m drift) is 50 μS; this is divided into 400 drift time slices. As a result, the chamber volume is itself divided effectively into 320 x 400 = 128,000 elements, a feat which would be impossible using discrete detectors.

The channel is capable of handling signals at rates in excess of 2 MHz (1 track every 2 cm in terms of drift distance). However, the temporary data storage capacity is limited. The data pertaining to a particular interaction must be retained. So the data acquisition mode is disabled, at a fixed time of 50 μS after the interaction is detected in the apparatus. (The delay allows the collection of signals from tracks which have drifted the maximum distance of 2 m). The

signal magnitude and time-of-arrival information is 'frozen': no more charges are accepted by the analogue memory, and the shift clock of the time-of-arrival memory is stopped.

Data readout is performed under the control of a minicomputer. The charges on the capacitors of the analogue memory are digitized one-by-one, in reverse order to charging. An 8-bit Wilkinson rundown ADC is used; the maximum digitization time is 25 μS per capacitor. While a charge is being digitized, the associated time-of-arrival is retrieved from the shift register. The contents are shifted in the reverse direction until a bit is detected. The total number of shifts needed gives the time-of-arrival, relative to the moment that the shift clock was stopped. The times-of-arrival are digitized to the 9-bit accuracy required by the 512-bit capacity of the shift register.

The digital output from one channel therefore consists of a magnitude and time-of-arrival pair for each track in the chamber. These values are passed to a fast digital buffer memory in about 2 mS and thence, rather more slowly, to magnetic tape, via the computer (see III.7). The complete readout operation for 30 tracks from all 320 channels takes less than 30 mS, although the channels are ready for more signals after data transfer to the buffer memory. The total quantity of data transferred to the computer for 30 tracks amounts to $\sim 1.6 \times 10^5$ bits.

Viewing the data from all channels as a whole, a 320 line 'event-picture' may be constructed. Each line of the raster is made up from the time-of-arrival and pulse magnitude data for one channel. the event-picture shows the trajectories and ionization distributions for the tracks of the particles traversing the chamber (see Fig. I.10(a) and (b)). The tracks in the two drift regions are superimposed.

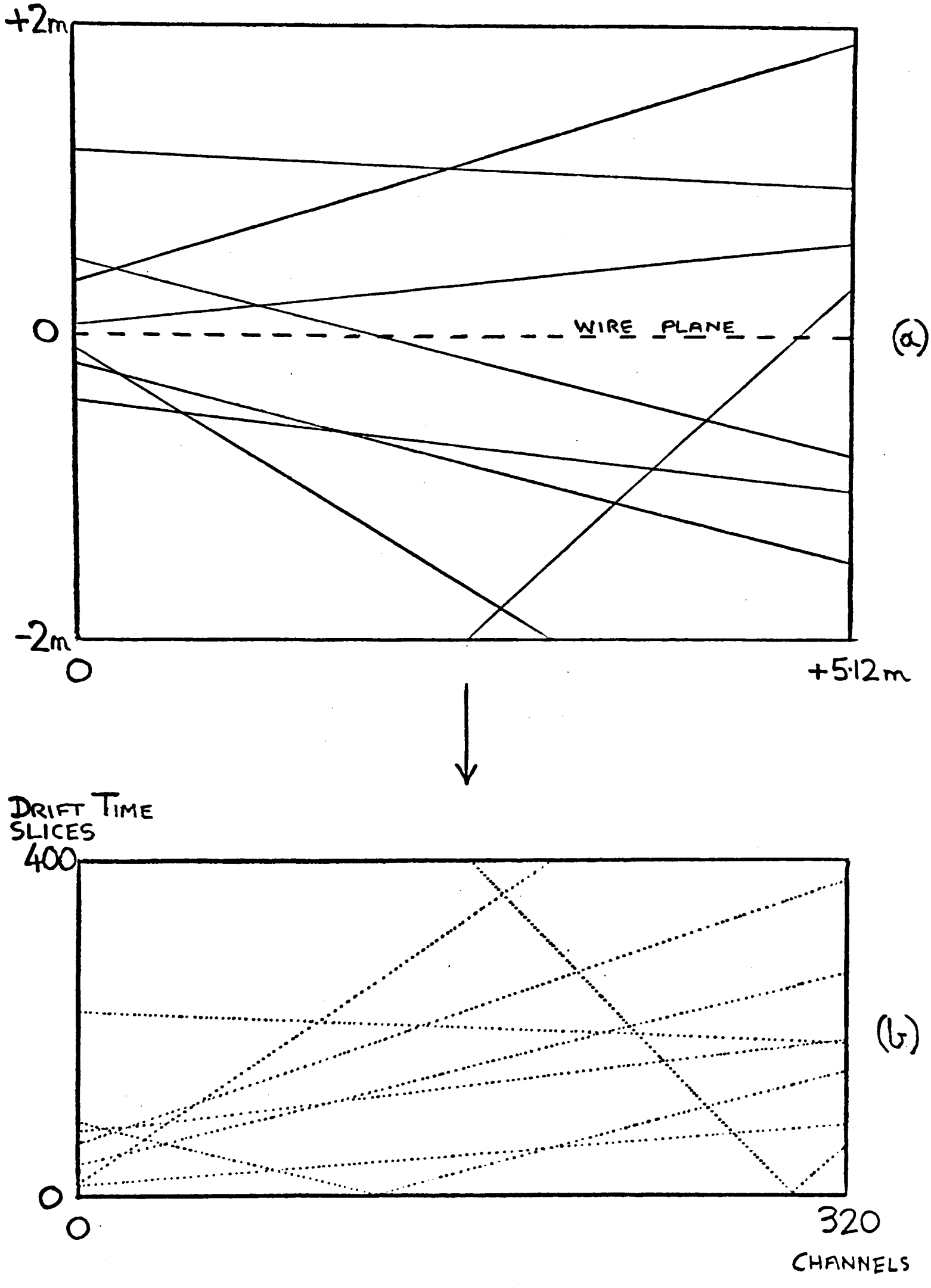


Figure 1.10 (a) Typical Tracks within the chamber

(b) The resultant 'event-picture'

A typical distribution of the 320 ionization measurements on one track is shown in the histogram of Fig. I.11 (simulated, see IV.1); from this, the particle velocity may be derived. The times of arrival are converted to distances by multiplying by the drift velocity.

Data Rate Reduction in ISIS

Five stages of data rate reduction may be identified in ISIS (see Fig. I.12):

(i) Track drift. The spatial positions of the tracks are mapped into the time domain. This represents a serial expansion of the data. The particles from an interaction take ∿16 nS to traverse the chamber. Depending on their trajectories, the signals from their tracks may be delayed by up to 50 μS. (The chamber represents a very high quality delay line, with a delay:risetime ratio of ∿250 compared with that of ∿20 for good distributed electronic delay lines.)

(ii) Multiple channels. Each of the 320 samples of ionization are processed by separate but identical channels of electronics, in parallel.

(iii) Discrimination. The signals are preprocessed by the discriminator to select out meaningful data from noise.

(iv) Analogue memory. The slow process of digitization, in taking up to 25 μS per charge, demands a serial expansion of the data within each channel: the analogue memory retains the pulse magnitude data until the digitization can be performed.

(v) Buffer memory. A serial expansion of the data occurs at the buffer memory. The digital data is transferred relatively quickly (2 mS) in parallel to the buffer memory, and thence rather more slowly (25 mS) to the computer in serial word form.

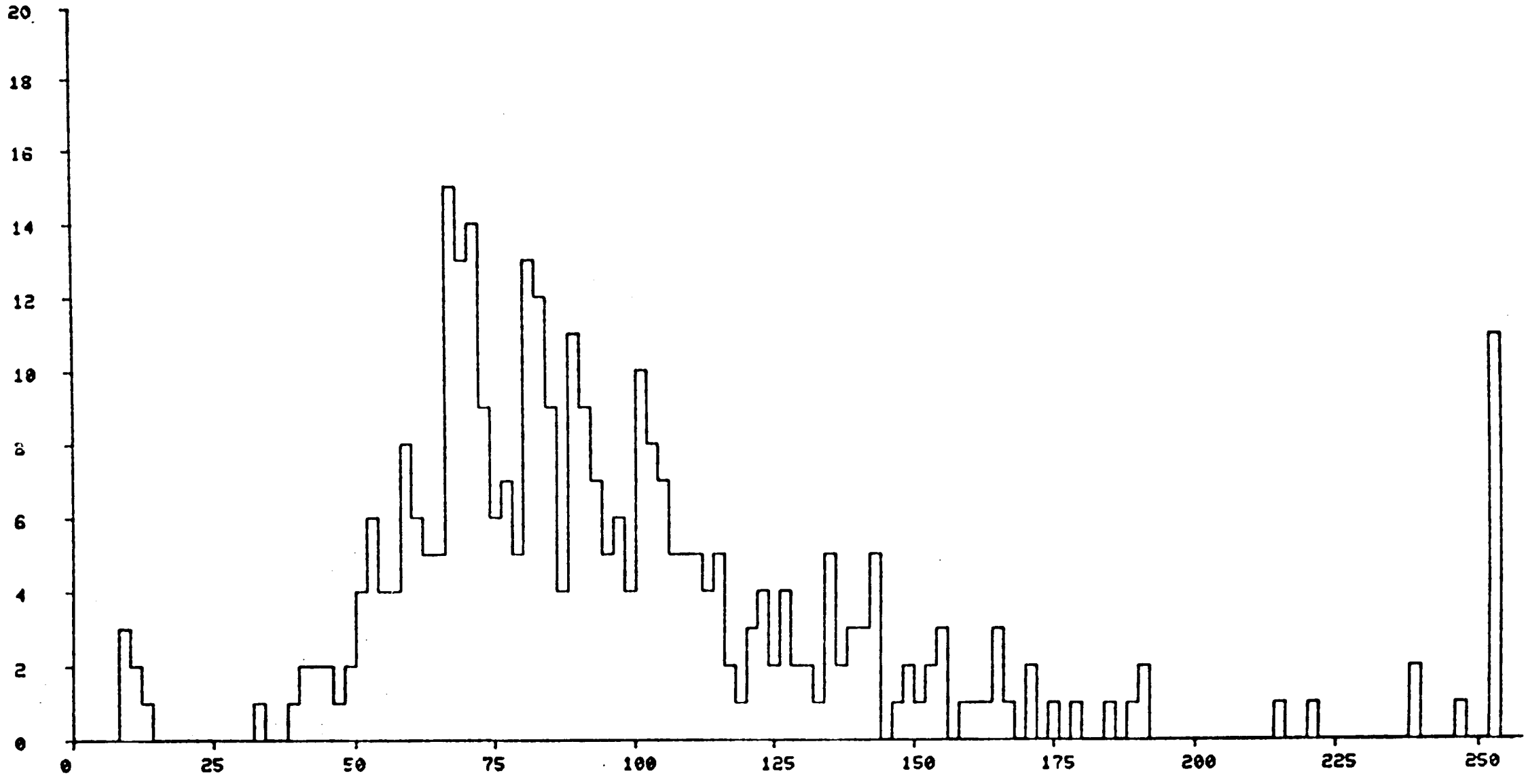


Figure I.11 The measured Ionization Distribution from one track (simulated, see IV.1)

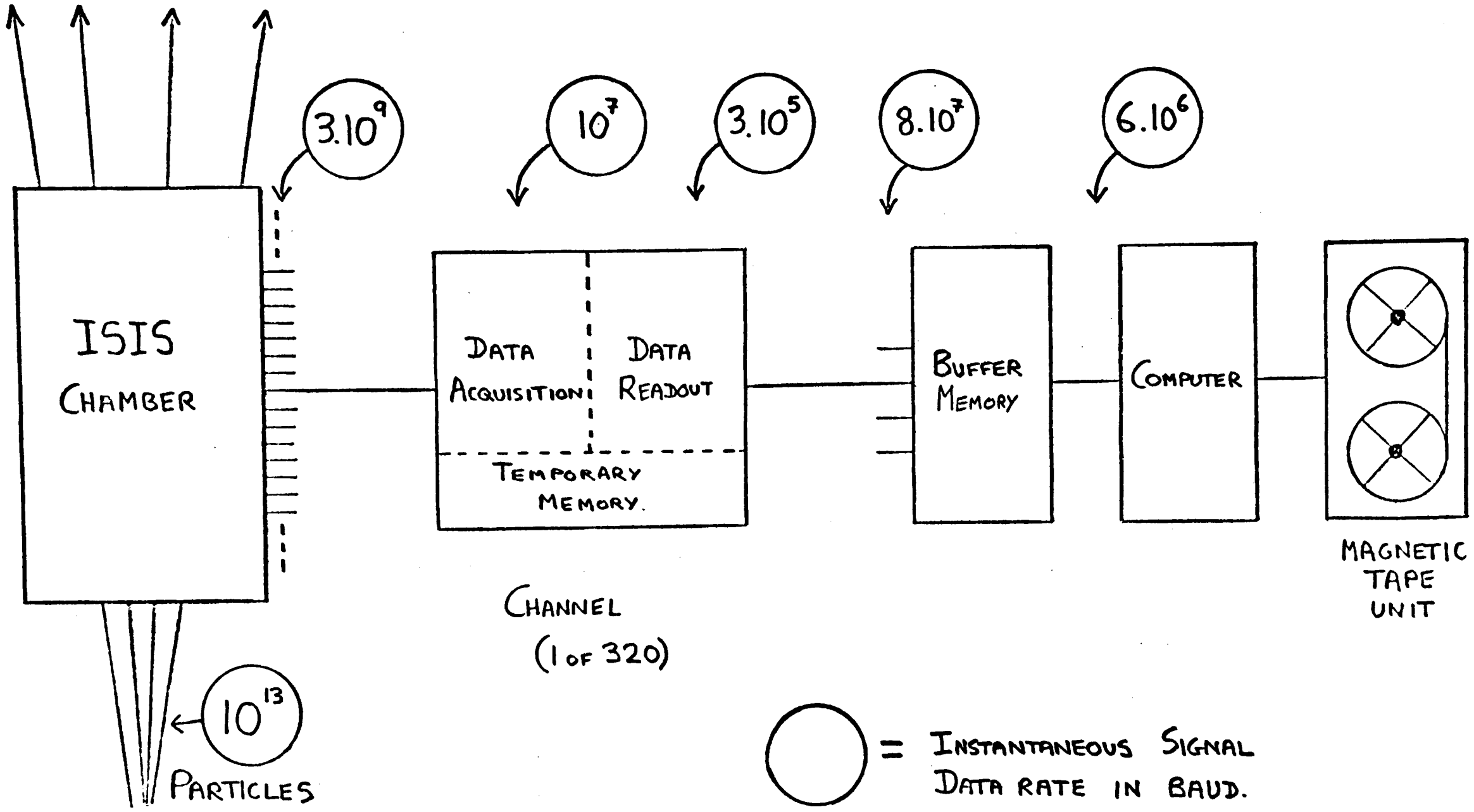


Figure 1.12 Data Rate Reduction in ISIS

The instantaneous signal data rate is reduced over these five stages from $\sim 10^{13}$ baud to $\sim 6 \times 10^{6}$ baud (for 30 tracks).

Signal-to-Noise Ratio in ISIS

There are two main sources of noise in ISIS:

(i) Shot noise. The number of ionization electrons is a sample ranges from ~40 upwards. The average number is about 100. The dispersive processes associated with ionization drift spread these electrons over a few hundred nanoseconds. Since the risetime of the analogue signal path is a few tens of nanoseconds, an appreciable shot noise component of the signal is observed.

(ii) Electronic noise. The equivalent input electronic noise level is ~15 nA r.m.s. over the 14 MHz equivalent square bandwidth. Input signal amplitudes vary from about 100 nA upwards. The signal-to-noise ratio is thus ~16 dB, minimum.

In ISIS, the most important implication of a poor signal-to-noise ratio is inaccurate signal timing measurement. To avoid random triggering, the discriminator level is well above the noise level, at ~55 nA equivalent input current. The output from the discriminator is used to generate an integration gate of duration equal to that of the signal. Thus for small signals, there is a danger that a significant proportion of the signal will be lost below the discrimination level resulting in a harmful systematic reduction in the integrated charge.

Much of the work in the following chapters is associated with analysing and optimizing the solution to this problem.

The Design Strategy

In common with other complex systems, ISIS consists of several interdependent components. The most important design consideration was to resolve the compromises arising from such dependencies. For example, the choice of gas amplification factor involved a compromise between a high signal strength and a low systematic effect due to space charge generation (see II.3).

The signal-to-noise ratio problem in particular is not capable of analytic solution in ISIS. Although optimum signal processing systems for proportional counter signals have been designed theoretically (see [GA53], [GF72], [RV68], [RV74], for example), the situation in ISIS is complicated by the fact that the resolving time of the electronics is comparable with the primary signal duration (ionization collection time).

The approach adopted is one of simulation. All the important components of ISIS (with the exception of the DC Baseline Restorer) have been modelled within a computer program. It is, as a result, possible to study the interactions between components at leisure. An optimum design has evolved, providing a satisfactory performance in all aspects.

In Chapter IV, the use of the simulation is described. Its results are compared with experiments in IV.2, IV.3 and IV.4. The optimum design is described in IV.5, and the performance of this design is described in IV.6.

Comparison of ISIS with Similar Devices

The ISIS device is compared with two other velocity and position sensitive devices having similar characteristics:

(i) The External Particle Identifier (EPI) [AM75], [JD73]

The EPI is a multilayer proportional counter system that is used to identify the secondary particles emerging from BEBC at CERN. The detector is composed of 128 layers, a layer consisting of 32 proportional countercells. Each cell is 6 cm square and 90 cm long. The size of the detector is 90 cm x 190 cm x 7.7 m (see Fig. I.13). Each of the 4096 proportional counter cells is connected to a channel of electronics which is capable of storing, digitizing and reading out one signal every 4 mS.

(ii) The Time Projection Chamber (TPC) [NDPC]

The TPC is a drift chamber of cylindrical cross-section, to be used to identify the particles emerging from an interaction at an intersection of PEP at SLAC. The direction of the drift field is along the axis of the cylinder (see Fig. I.14). The track ionization drifts to a wire plane sector at the end of the cylinder. The time profile of the signal from each wire is recorded at high rate using a charge-coupled device [SC75]. The signal profile is stored as a gated signal integral at 50 nS intervals. The charge coupled device has 455 cells; about 11.5 μS of signal may be held. The stored signal amplitudes are then read out and digitized at a much slower rate (∿10 μS intervals). Discrimination of signal from noise is performed when the signal profile is read out.

The features of ISIS, EPI and TPC are compared in Table I.1. There are two fundamental differences between ISIS and the other two devices:-

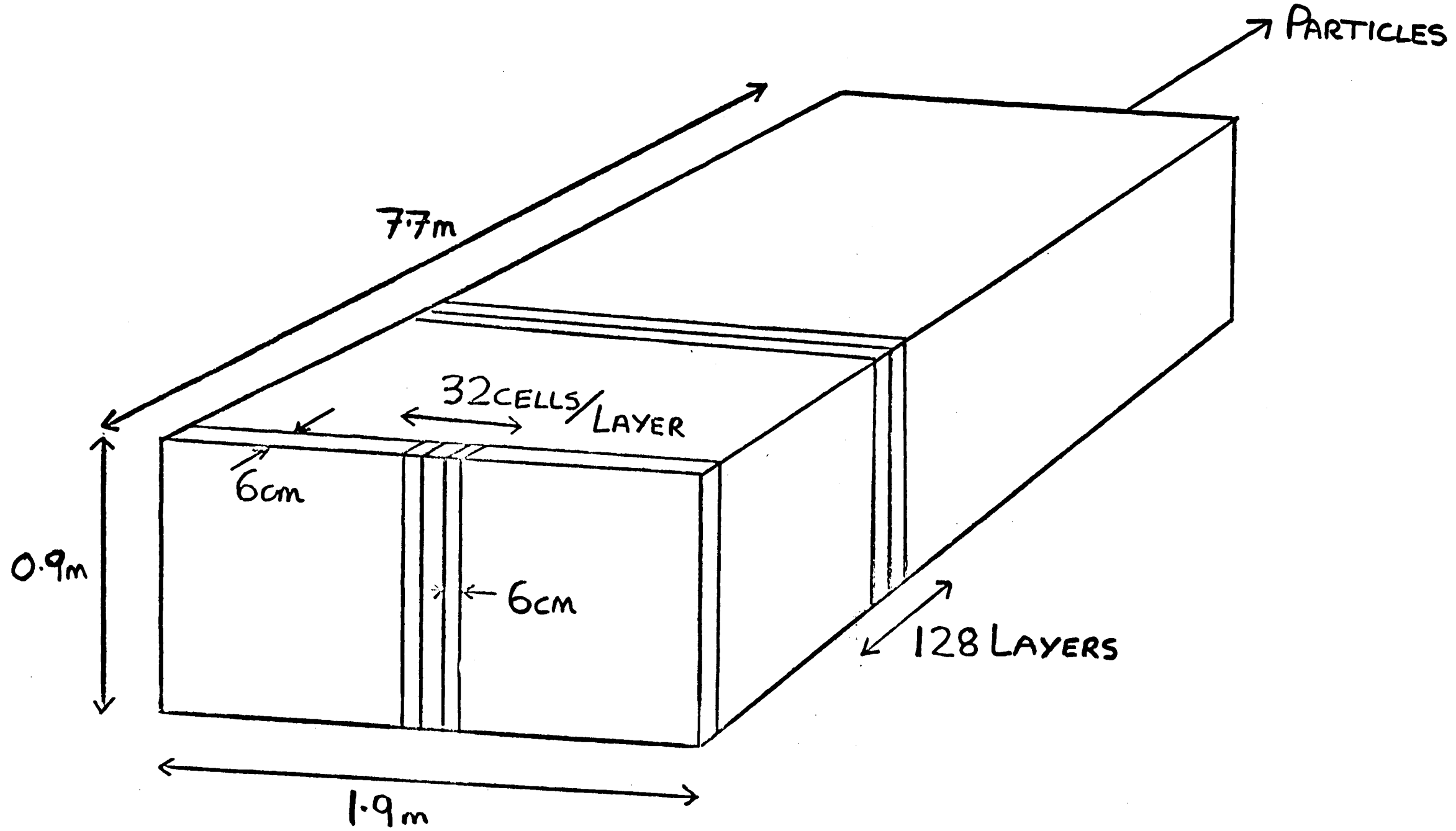


Figure 1.13 Schematic Diagram of the EPI

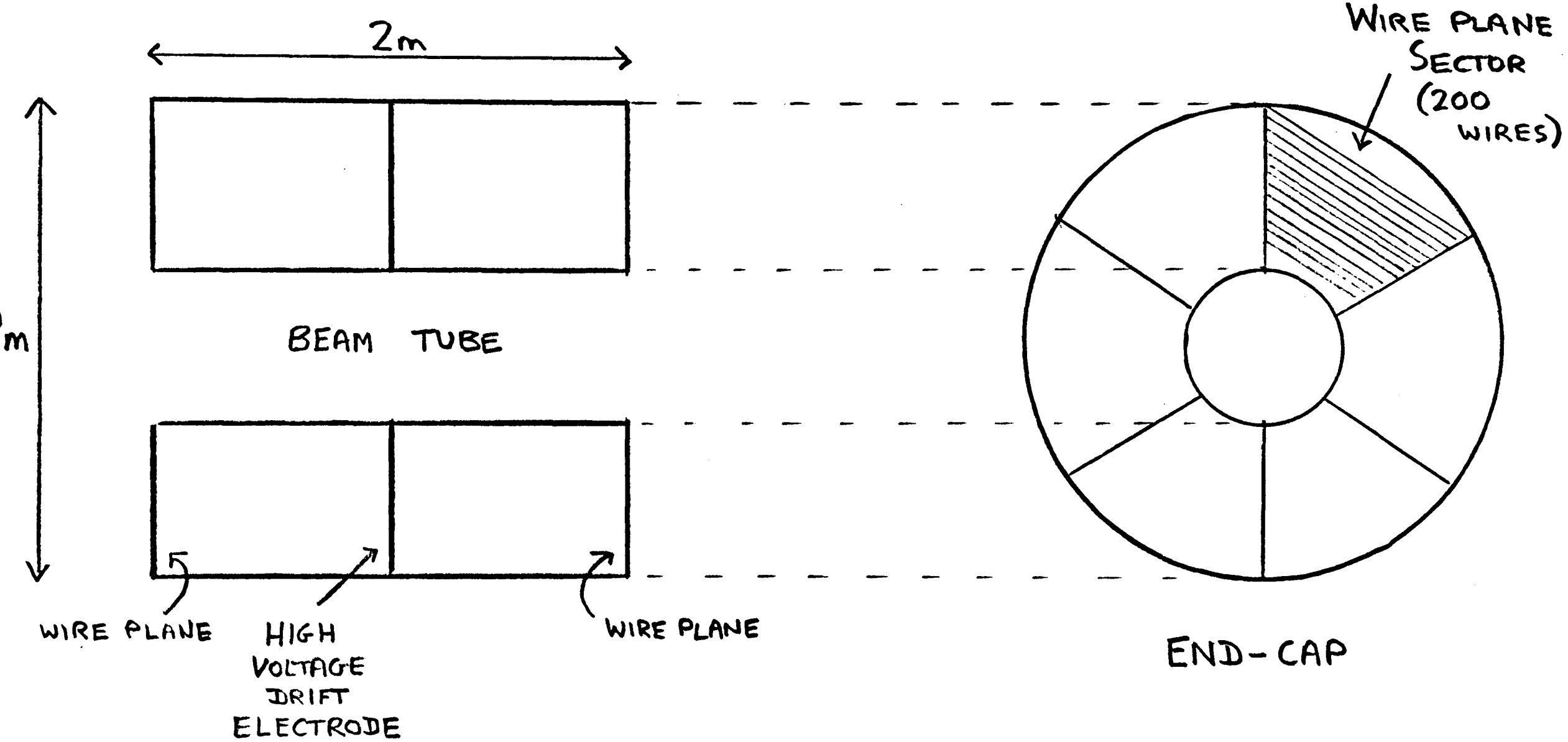


Figure I.14 Schematic Diagram of the TPC

(i) The numbers of electronic channels used in the EPI and the TPC are an order of magnitude greater than that in ISIS. In the EPI no ionization drift occurs: there is no space-time domain conversion. Only a few channels (cells) receive signals from each track. There may be null information present: this is inefficient. However, in the TPC, the fact that only a few channels receive data from each track is offset by the large solid angle acceptance of about 4π. In ISIS, all channels receive signals from each track, resulting in good data collection efficiency, over a larger solid angle that the EPI.

(ii) The triggering of each device is performed differently. In ISIS each channel is instantaneously self-triggering on the analogue signal. In the EPI, an external trigger is supplied to all channels by other particle detectors. In the TPC, the stored analogue signal profile is scanned for useful data at a relatively slow speed (after data rate reduction with the charge-coupled device): signal discrimination is delayed. This reflects in the resolving time of the electronics and in the amount of data transferred. For the TPC, the resolving time is short, and the quantity of data involved is very high. For the EPI, the resolving time is long, and the amount of data transferred is relatively low. The situation in ISIS comes between these two. However, ISIS provides better multi-track performance than the EPI because of higher spatial resolution. The cost is that a good signal-to-noise ratio is required for efficient self-triggering in ISIS.

TABLE I.1

COMPARISON OF ISIS, EPI AND TPC

		ISIS	EPI	TPC
Size	Height	4m	0.9 m	1m
	Width	2m	1.9 m	radius
	Depth (in beam direction)	5.1m	7.7 m	2m
Volume		40m^3	13m^3	6m^3
Gas		80% A/20% CO_2 at 1 bar	95% A/5% CH_4 at 1 bar	80%A/20% CH_4 at 10 bar
No of channels of electronics		320	4096	5000-10000
No. of ionization samples per track		320	128	192
Length of track sampled		5.1m	7.7m	0.77m
Resolving Time		∿125 nS	>10 μS	∿50 nS
Temporary Storage Capacity (no. per channel)		32	1	455
Readout time		25 mS	4 mS	>50 mS
ADC		Wilkinson	Ramp	-
Triggering		Internal immediate self-trigger for each channel	External immediate trigger common to all channels.	Internal delayed trigger for each channel.

Conclusion

The considerations behind the acquisition of data at high rates and under poor signal-to-noise conditions have been discussed in the context of a specific device, ISIS. The features of ISIS have been described and compared with those of similar systems. In the next two chapters, the detailed design is explained. In the fourth chapter, the measured and predicted performance of ISIS is described.

CHAPTER II

THE GAS-STATE PROCESSES IN THE ISIS CHAMBER

This chapter contains discussions of the processes which occur in the gas state within the ISIS chamber itself. The nature of the ionization track left by a charged particle traversing the chamber is discussed in II.1. The description of what happens to the track, from when it is created until it reaches the wire plane, is contained in II.2. The particulars of the gas amplification which occurs at the wire plane are discussed in II.3. The last section, II.4, contains considerations on the factors which affect the choice of inter-wire separation in the wire plane.

II.1 THE FORMATION OF THE IONIZATION TRACK

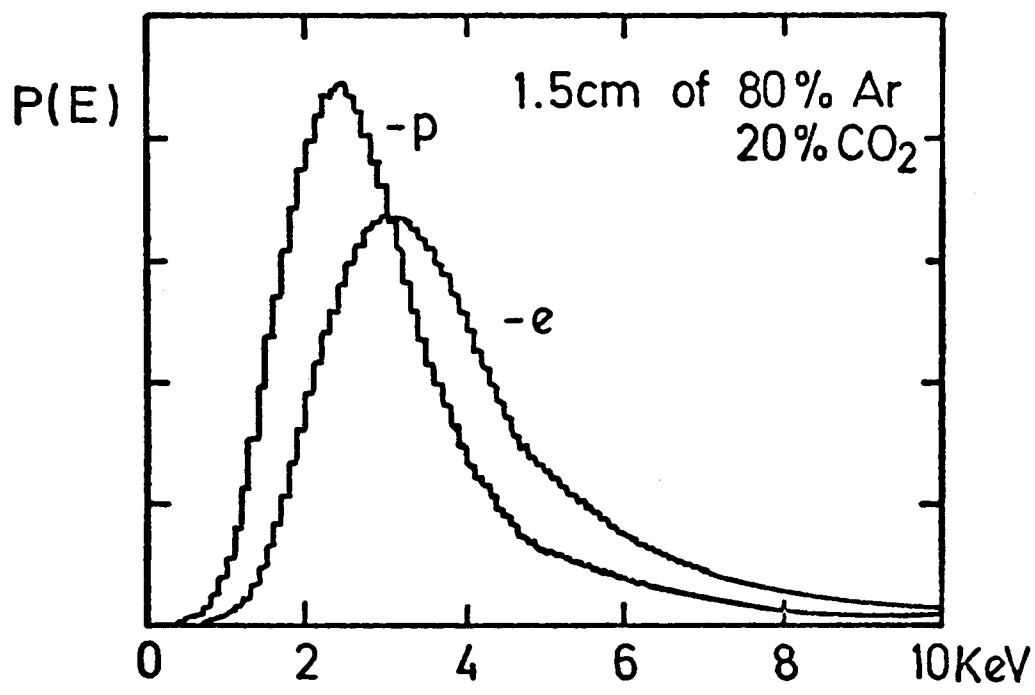
A fast moving charged particle loses energy to a surrounding medium by means of the electromagnetic interaction. The ionization so produced in a gas is the source of the signal in ISIS. This phenomenon is for the most part very well understood. A standard text will give details, see for instance [JJ75].

Consider a thin ($\sim$1.5 cm) sample of a gas such as argon. A relativistic charged particle makes about 30 collisions on traversing the sample. The number of collisions obeys a Poisson distribution.

On collisions with an atom of the gas, an ion pair may be created (A^+, e^-). The electron comes off with an energy that depends on the impact parameter, but typically of a few tens of electron volts.

The measured ionization loss in the sample has a probability distribution which is the convolution of the distribution of the numbers of collisions in the sample, with that of the energies of the electrons produced in the collisions. Ionization loss distributions are known generically as Landau distributions, after the theoretician who first discussed them [LL44]. Two Landau distributions are shown in Figure II.1, for protons and electrons of momentum 25 GeV/c, in a 1.5 cm sample of 80% argon, 20% CO_2 at 1 bar [BJ76].

Landau distributions are very wide, the width of the peak being about 100% FWHM. There is a tail going off to relatively high energies, due to the small probability of collisions at small impact parameters, which create very energetic electrons (δ-rays). These δ-rays are unimportant since they occur only a few percent of the time, and do not affect the most probable ionization loss. [LJ59]



Landau distributions for 25 GeV/c protons and electrons [B J 76]

FIGURE II.1

The energy of the most probable ionization loss depends on the velocity of the particle, which may thus be measured (at 25 GeV/c, $\gamma_{protons} = 27$, $\gamma_{electrons} = 49000$). However the broadness and long tail of the Landau distribution mean that many independent measurements of the ionization from a single particle have to be made before a reliable enough value of its velocity is known. The velocity resolution as a function of the nature and number of ionization measurements is discussed in [BJ76], [AW74], [CJ76]. To distinguish kaons, pions and protons in the range 5-50 GeV/c with a certainty of at least 90%, more than 300 independent measurements of the ionization over a track length of about 5 m are required, although the number of samples is less important than the length of track sampled.

The Dependence of Ionization Loss on Velocity

Particle velocity is conveniently parametrized as

$$\frac{P}{M_oC} = \beta\gamma = \frac{\beta}{\sqrt{1 - \beta^2}}$$

Figure II.2 shows the variation of the most probable ionization loss over a wide range of P/M_oC for 1.5 cm samples of argon [BJ76].

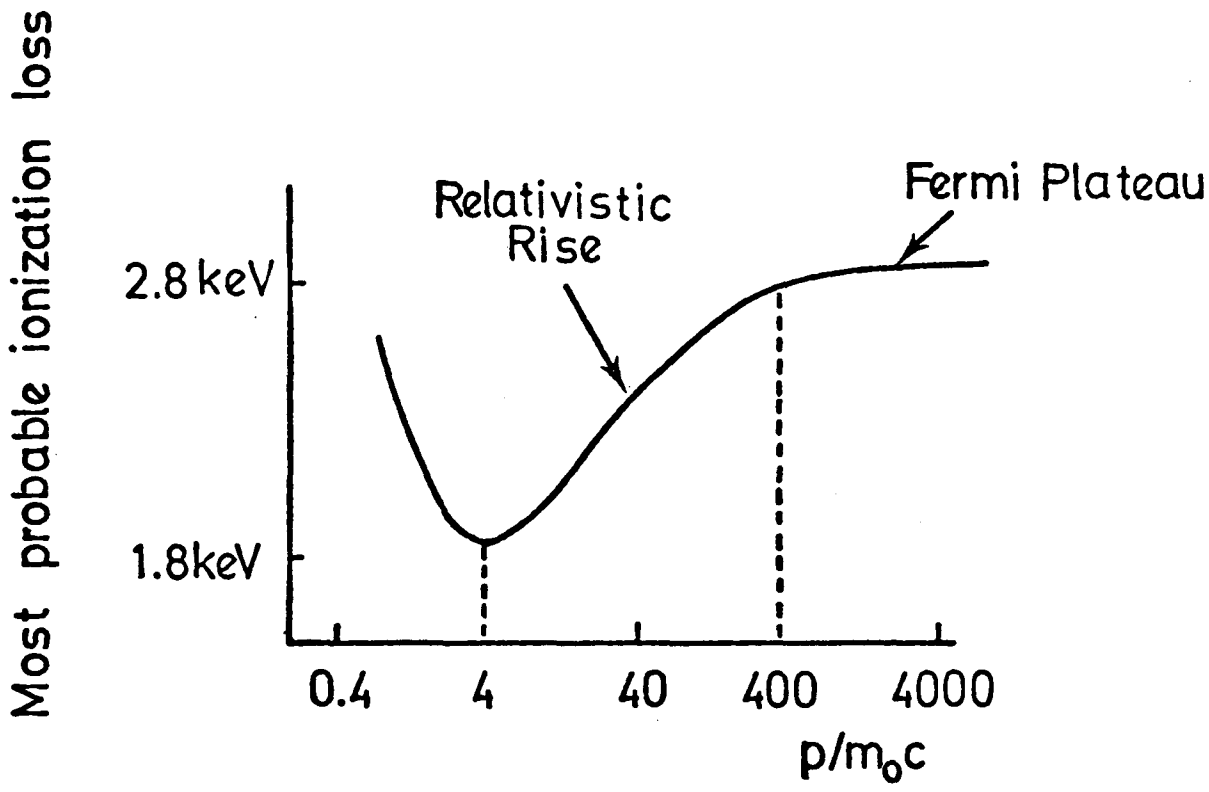


FIGURE II.2, Showing Ionization Loss Curve in the Region of Relativistic Rise

There are three distinct regions:-

(i) $P/M_oC \lesssim 4$

This is the classical region where the ionization loss varies as $1/\beta^2$ for all media.

(ii) $P/M_oC > 4$

In this region, the most probable ionization loss rises with velocity. The increase is a slow logarithmic one, and is known as the 'relativistic rise'. How far the rise goes on is dependent on the medium: for argon it is about 50% from P/M_oC = 5 to 500; for liquid neon it is about 20%, but is zero for lead.

(iii) $P/M_oC \gtrsim 100$

At large values of P/M_oC the ionization loss remains constant (apart from high energy δ-rays). This is known as the 'Fermi plateau'.

The Relativistic Rise

It is in the region of the relativistic rise that the velocity dependence of the most probable ionization loss is used by ISIS, see [CJ76], [AW76].

The relativistic rise is a consequence of the change in shape of the electric field around the moving charge as the velocity gets more relativistic. The transverse electric field becomes stronger. It is also effective on the atom for a shorter time because of the Lorentz contraction in the longitudinal direction. This makes energy transfers at large impact parameters more effective: the ionization loss increases.

The relativistic rise levels off into the Fermi plateau at large P/M_oC. At these velocities the distances over which significant energy transfers can take place have risen to a length of many hundred of times the inter-atomic spacing in the medium. Longer range energy transfers are inhibited by the shielding of the atoms undergoing collision due to the polarization of neighbouring atoms. For this reason, this is sometimes known as the 'density effect'.

The Ionization Track

The primary ionization left by the particle will contain some electrons which are energetic enough to cause secondary ionization. In the end a tenuous trail of electrons and ions is left in the gas by the particle. The cross-section of this track is 100-200μ, being the mean free path of a low energy electron. A minimum ionizing particle

($P/M_oC \gtrsim 4$) will have a most probable energy loss of ∿1.8 keV in ∿1.5 cm of argon. The mean energy loss per ion pair in argon is ∿26 eV. Therefore the above ionization loss corresponds to about 70 free electrons. The numbers of free electrons in the many samples making up the track will follow a Landau distribution characteristic of the velocity of the particle: this information is obtained in ISIS.

II.2 THE EFFECT OF DRIFT ON THE IONIZATION TRACK

The ionization track is deposited in a region of high but uniform electric field (50-100 kV/m). The electrons and ions separate. The electron track drifts at constant velocity (4 cm/μS) towards the wire plane, while the positive ion track proceeds to the negative drift electrode much more slowly (∿15m/S). The drift velocity $\underline{V}_d$ is the product of the electric field $\underline{E}$ and the appropriate (field-dependent) mobility : $\underline{V}_d = \mu\underline{E}$.

Focussing attention on the useful electron track, degradation of the information in the track can occur as it drifts, in the form of:

(i) non-simultaneous arrival of the electrons at the wire plane,

(ii) attenuation in the number of electrons [CJ75],

(iii) inter-sample correlations.

Of these, only the first is considered in detail.

The main causes of dispersion in the arrival times of the ionization electrons at the wire plane are:

(i) spatial dispersion due to diffusion,

(ii) velocity dispersion due to distortion of the electric field

(iii) spatial dispersion due to track angle.

There are two main effects of dispersion:

(i) Dispersion produces a lengthening of the current signal from the wire plane. This results in a lower amplitude, although the integral - the total charge - remains the same. The signal-to-noise is thus worsened.

(ii) More importantly, dispersion sets the limit on the spatial resolution of the chamber. In order that measurements of the amount of ionization in a track are to be accurate to ∿1%, then at least 99% of the charge in the track must be collected. The multi-track resolution for useful ionization information is determined by the duration of the signal to this level and thus by the arrival time dispersion of 99% of the electrons.

Dispersion due to Diffusion

The amount by which electrons diffuse during drift is determined by their drift time and their random kinetic energy distribution: the more energetic ('hotter') the electrons are, the further that they will diffuse. The track profile becomes a tube of Gaussian probability distribution.

After a drift distance L in a uniform field E, the r.m.s. size σ of the electron tube cross-section (assumed to be localized initially in a line) is given by [CJ75]:

$$\sigma = L\sqrt{\frac{2kT_e}{eV}} = \sqrt{\frac{2LkT_e}{eE}} \approx 3 \text{ mm for 2 m drift in typical conditions}$$

where $V = EL$

k = Boltzmann's constant

e = electronic charge

T_e = effective electron temperature.

For small diffusion, a small T_e and a large E are needed.

The electron temperature is in general a function of the reduced field E/p (p is the pressure) and of the nature of the gas. Polyatomic gases have a much smaller T_e than the diatomic or monatomic gases [EA65], [CJ75].

The choice for the chamber filling gas contains a proportion (10-20%) of carbon dioxide, which has very efficient coolant properties [CJ75]. The balance is made up of argon. This mixture is safe, cheap, convenient and easy to purify [IN23].

The proportions of CO_2 required are determined by the value of electron mobility required. This is fixed once the drift field and drift velocity are defined.

For two reasons, the chamber is operated at maximum practical drift field:

(i) diffusion is generally less,

(ii) the positive ion lifetime in the chamber is reduced (see II.3).

The possibility of breakdown fixes the maximum value of the drift electrode potential at about 200 kV. Over a drift distance of 2m, this corresponds to a maximum field of 100 kV/m.

The drift velocity is chosen to be 4 cm/μS. In the 50 μS thus required for a 2m drift, about a third of the 32 analogue memory locations (see III.4) will be filled by background tracks*. Increasing the drift velocity would necessitate the use of faster (and more expensive) electronics.

---

* (The background flux is $\lesssim 2.5 \times 10^4/m^2/s$ [EHSP] over the chamber area of 8 m^2, so in 50 μS, ∿10 particles traverse the sensitive volume, see II.3.)

The argon/CO_2 proportions for 4 cm/μS electron drift velocity over a drift field operating window of 50-100 kV/m are shown in Table II.1. This also contains figures for the electron mobility, electron temperature, r.m.s. and 99% diffusion widths after 2m drift, in terms of both distance and drift time, taken from [CJ75]. The errors shown are due to the 30% error in electron temperature.

TABLE II.1

Drift Field	Gas Proportions		Electron Mobility	Electron Temperature	Diffusion at 2m RMS		99%	
kV/m	%A	$\%CO_2$	$M^2/kV/s$	eV	mm	ns	mm	ns
50	90	10	800		4.6 ±0.7	115 ±17	18 ±3	460 ±70
				0.28 ±0.8				
100	80	20	400		3.3 ±0.5	83 ±12	13 ±2	320 ±50

Dispersion due to Non-uniform Electric Field

Any non-uniformity in electric field $\underline{E}$ will produce a variation in drift velocity $\underline{V}_d = \mu\underline{E}$ along a track, resulting in a dispersion of the electron arrival times.

The electric field distribution may be split up into two regions:

(i) the drift region, comprising most of the chamber, and

(ii) the amplification region around the wires.

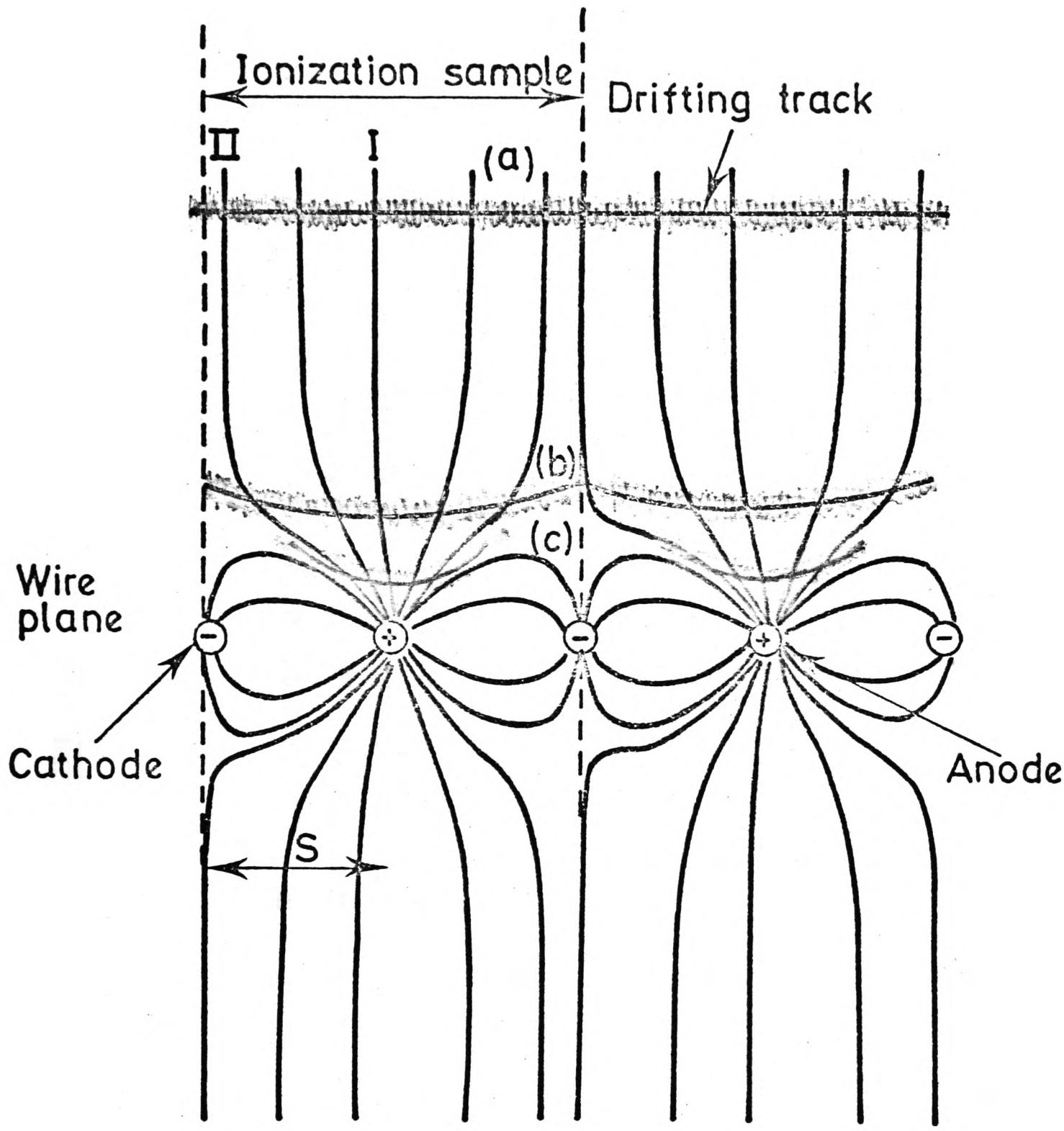
To ensure field uniformity within the drift region, a simple but effective electrostatic guard structure has been designed, that consists of a double wall of conducting tubes, held at graded potentials by a resistor chain [IN26]. For a 2m x 4m cross-section, the field will be uniform to better than 0.1% only 10 cm away from the guard structure. A field uniformity at this level corresponds to a time dispersion of better than 50 ns (≡2 mm), which may be neglected.

The field around the wire plane, shown in Fig. II.3, is definitely not uniform. As a (straight) ionization track approaches the wires, it is split into elements of length 2s, where s is the inter-wire spacing. Electrons drifting down field lines near the centre of the element (e.g. I in Fig. II.3) have to go a shorter distance to the high field region around an anode than do electrons drifting down lines towards the edge of the element (e.g. II). The resultant distortion in the track is shown at successive times (a), (b) and (c).

The drift time of an electron is given by the integral along a field line of $^{1}/V_{d}$:

$$T_d = \int \frac{1}{\underline{E}_{\mu}} \, \underline{ds}$$

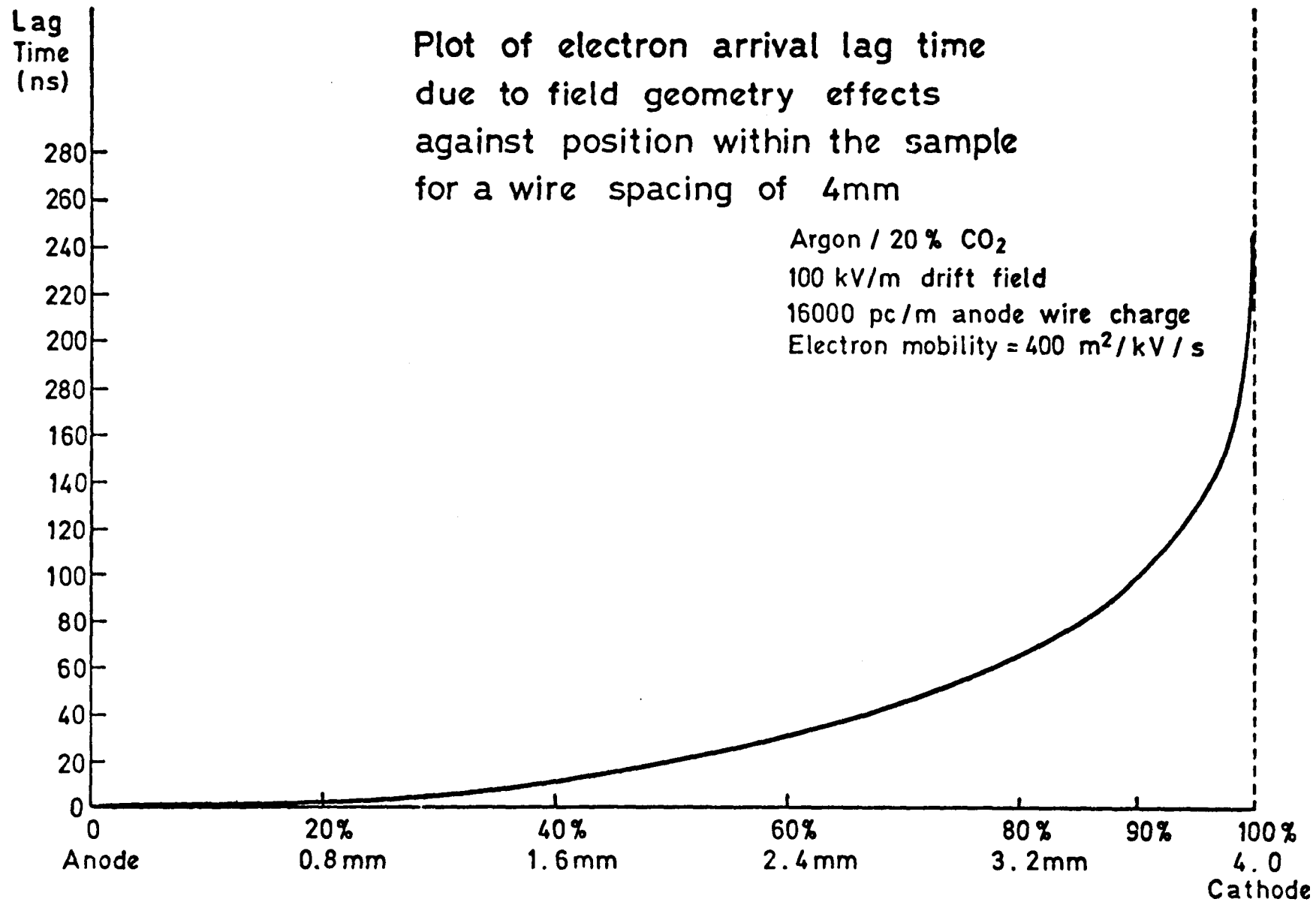
Drift times were calculated for electrons starting from various positions along the element, but far enough away from the wire plane for the field to be uniform initially. These are plotted in Fig. II.4 for a typical case, in terms of a 'lag time' for that starting position. The lag time is defined as the difference in arrival time of an electron behind one which has started at the centre of the element.



Origins of Field Geometry Time Dispersion

FIGURE II.3

FIGURE II.4


Plot of electron arrival lag time
due to field geometry effects
against position within the sample
for a wire spacing of 4mm
Argon / 20 % CO_2
100 kV/m drift field
16000 pc/m anode wire charge
Electron mobility = 400 m^2/kV/s
Lag Time (ns)
280
260
240
220
200
280
160
140
120
100
80
60
40
20
0
0
Anode
20%
0.8mm
40%
1.6mm
60%
2.4mm
80%
3.2mm
90%
100%
4.0
Cathode

(The assumption of a field-independent mobility in this calculation leads to values of the lag time which are slightly larger than in the real situation. This is because the drift velocity becomes independent of field at the high fields experienced near to the anode. The error so introduced is small, since the delays are accrued where the field is relatively low, but beneficial, since the lag time in this real situation is thus less.)

It may be seen from Fig. II.4 that the electron arrival time lag produced by the non-uniform field geometry rises steeply towards the outermost few percent of the element. This field geometry dispersion effect is thus important in determining the duration of the signal: the electron arrival time dispersion so produced is ∿180 ns (∿7 mm) at the 99% level of charge collection efficiency.

This form of dispersion applies equally to tracks from any drift distance. It is the limiting factor in the multi-track position resolution on tracks deposited close to the wire plane, but is folded with the diffusion broadening on those which have drifted a long distance. Minimization of the field geometry dispersion effect is discussed in II.4.

Dispersion Due to Track Angle

The additional dispersion introduced by a non-zero track angle to the wire plane is a simple phenomenon, illustrated in Fig. II.5. The end (a) of the sample arrives before the end (b) by a time ΔT

$$\Delta T = \frac{w \tan\theta}{Vd}$$

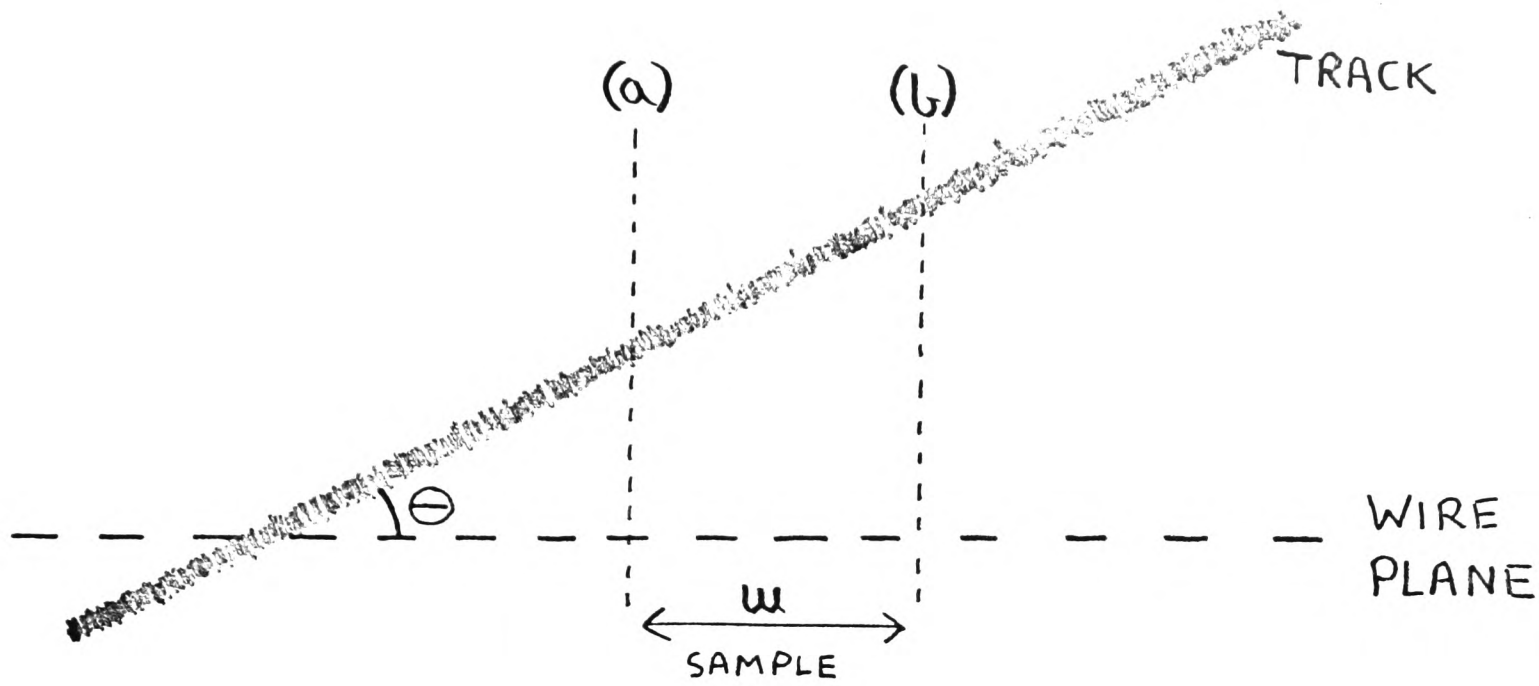


FIGURE II.5 Showing Origins of Track Angle Dispersion

The large acceptance of the chamber means that tracks may have angles of up to 18° to the wire plane [EHSP]. With $\theta = 18°$, $V_d = 4$ cm/μS, and w = 1.6 cm (see II.4)

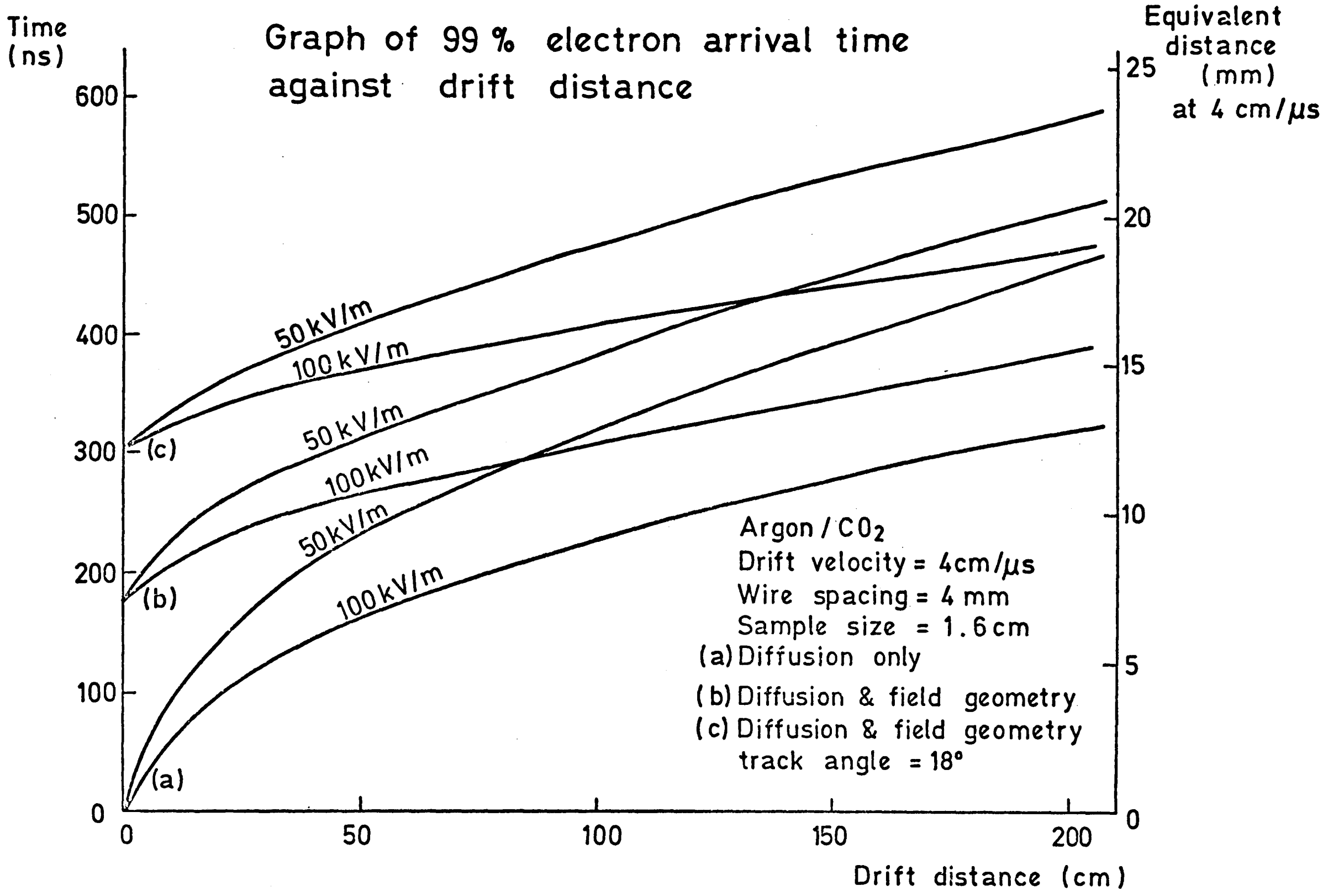
$$\Delta T \tilde{\approx} 127 \text{ nS}$$

This form of dispersion does not injure the signal-to-noise ratio because the length of track sampled, and hence the amount of charge collected, goes up as $1/\cos\theta$.

Total Dispersion for 99% Charge Collection Efficiency

When diffusion, field geometry and track angle effects are folded together, the resultant total dispersion in electron arrival times gives the theoretical minimum signal duration, and thus multi-track resolution, for a given drift distance. In Fig. II.6 in plotted the mean spread in arrival times against drift distance, for 99% of the electrons in a track, under various conditions. (These results were obtained by a Monte-Carlo simulation: see Appendix 4). The

FIGURE II.6


Graph of 99 % electron arrival time against drift distance
Time (ns)
Equivalent distance (mm) at 4 cm/μs
600
500
400
300
200
100
0
25
20
15
10
5
0
50 kV/m
100 kV/m
50 kV/m
100 kV/m
50 kV/m
100 kV/m
(c)
(b)
(a)
Argon / CO_2
Drift velocity = 4cm/μs
Wire spacing = 4 mm
Sample size = 1.6 cm
(a) Diffusion only
(b) Diffusion & field geometry
(c) Diffusion & field geometry track angle = 18°
0
50
100
150
200
Drift distance (cm)

individual effects of diffusion, field geometry dispersion and track angle dispersion may be seen to contribute roughly equally to the total, indicating that a good operating point has been chosen. With the aid of the equivalent drift distance scale, the spatial resolution for a given drift distance may be deduced: at 100 kV/m field, the effective spread of the electrons at the 99% level in ∿7 mm at zero drift distance, zero track angle, rising to ∿18 mm at 2m drift distance, 18° track angle. (The effect of the finite system bandwidth is not included but contributes only a small additional amount to the pulse width, see Chapters III and IV.)

Crosstalk Due to Diffusion

Diffusion occurs in three dimensions: the effect of diffusion transverse to the track direction has been discussed above in terms of a time dispersion of the signal, but longitudinal diffusion results in a crosstalk between adjacent samples of track. A fraction α of the signal from one sample appears in both of the neighbouring ones. Considering the spatial extent of the diffusion:

$$\alpha = \frac{1}{w\sigma\sqrt{2\pi}} \int_0^w \int_{-\infty}^0 \exp\left[-(x-w)^2/2\sigma^2\right] \, dx\,dw$$

where w is the sample width and σ is the r.m.s. diffusion.

Values of α for 20 cm and 2 m drift, at 50 and 100 kV/m fields were calculated, and are tabulated in Table II.2. The sample size was 1.6 cm and the drift velocity was 4 cm/μS.

TABLE II.2

Drift Distance	Drift Field	RMS Diffusion	Crosstalk α
cm	kV/m	mm	%
20	50	1.5 ± 0.25	3.7
20	100	1.1 ± 0.2	2.7
200	50	4.6 ± 0.7	11.4
200	100	3.3 ± 0.5	8.2

In the worst case, α = 11% (2m drift at 50 kV/m). This decreases the ionization resolution for a 5m/330 sample ISIS from $\frac{\Delta I}{I}$ = 4.7% to $\frac{\Delta I}{I}$ = 4.9%. (Values obtained from the Monte Carlo calculations of [CJ76].) This does not damage the identification ability.

II.3 GAS AMPLIFICATION AT THE WIRE PLANE

As the constituent electrons of the ionization track approach the anode wire, they experience an electric field increasing as $^1/r$. At distances r nearer than about 100μ, the electrons gain enough energy from the field between collisions with gas atoms to cause further ionization. The secondary electrons so produced are also accelerated by the field and may similarly ionize further atoms, producing third generation electrons. The process continues, forming an electron avalanche which cascades down the field into the anode. Since the electrons are quite hot, the avalanche tends to spread around the wire ([WD50] see also IV.3.)

This is the process of gas amplification, whereby a few primary electrons may cause the production of a large number of secondaries [WD50], [EA65]. A gas gain parameter may be defined as:

$$G = \frac{\text{Total number of electrons in avalanche}}{\text{Number of primary electrons}}$$

(Due to the statistical nature of the multiplication process, G is the mean of a distribution. However, the additional width so produced in the pulse height spectrum at working values of G ($\sim 10^4$) is small compared with the width of the Landau distribution [RP74].)

To be useful in a measurement of the initial amount of ionization, the gas amplifier must be linear: G must be independent of the number of primary electrons ('proportional' gas amplification).

A gas amplifier has zero inherent output noise in the absence of a signal, yet can have a high gain. These are ideal properties for the first stage of a low noise system. Full use is made of them in amplifying the weak ionization signal to one strong enough to be dealt with by conventional electronics.

There are two main factors which control the gas amplification process:

(i) The field around the anode wire

This is determined by the electrode geometry and operating voltages. The gas gain G is very dependent on the magnitude of the field around the anode: a plot of ln(G) against anode-cathode potential is a straight line, to a good approximation [BW73]. In terms of the field E_A at the surface of the anode, there is a well-defined threshold field E_{AT} ($\sim 4 \times 10^6$V/m), above which G varies approximately as:

$$G \tilde{\propto} \exp\ [k_E\ (E_A - E_{AT})] \qquad [BW73]$$

where k_E is a constant. Substituting for E_A

$$G \tilde{\propto} \exp\ [k_E \frac{Q_A - Q_{AT}}{2\pi\varepsilon_o R_A}]$$

where Q_A, Q_{AT} are the charge, and threshold charge, per unit length on the anode, and R_A is the anode radius. Rewriting this:

$$G \tilde{\propto} \exp\ [k_Q\ (Q_A - Q_{AT})]$$

An estimate can be made from this of the dependence of gas gain on anode wire charge:

$$\frac{dG}{dQ_A} \tilde{\propto} k_Q \exp\ [k_Q\ (Q_A - Q_{AT})]$$

$$\therefore \quad \frac{\Delta G}{G} \tilde{\propto} k_a\ Q_A\ \frac{\Delta Q_A}{Q_A}$$

And substituting for k_a:

$$\frac{\Delta G}{G} \tilde{\propto} \ln G.\ \frac{Q_A}{Q_A - Q_{AT}} \cdot \frac{\Delta Q_A}{Q_A}$$

For $G \tilde{\propto} 10^4$, $Q_A \tilde{\propto} 16$ nC/m, and $Q_{AT} \tilde{\propto} 3$ nC/m (see Appendix 2), so to a fair approximation:

$$\frac{\Delta G}{G} \tilde{\propto} 11\ \frac{\Delta Q_A}{Q_A}$$

This result agrees roughly with experiment. In the tests described in IV.3, it was found that, at $G \tilde{\propto} 10^4$

$$\frac{\Delta G}{G} \tilde{\propto} 13\ \frac{\Delta Q_A}{Q_A}$$

Published data is also in agreement at this gas gain:

$$\frac{\Delta G}{G} \approx 14.5 \frac{\Delta Q_A}{Q_A} \qquad \text{[PJ76]}$$

$$\frac{\Delta G}{G} \approx 16 \frac{\Delta Q_A}{Q_A} \qquad \text{[HR73]}$$

A fair estimate of the dependence of G on Q_A seems to be:

$$\frac{\Delta G}{G} \approx 14 \frac{\Delta Q_A}{Q_A}$$

It is this strong dependence which determines the precision required on many of the dimensions in the chamber design (see II.4).

(ii) The nature of the gas

The electron coolant properties of the CO_2 component of the argon/CO_2 gas mixture which result in small electron diffusion are also useful in gas amplification. The onset of Geiger-mode discharges is delayed until quite large values of the gas gain ($G > 10^5$) have been reached [BR70]. This is because the CO_2 has good absorption in the ultraviolet, and exhibits metastable state quenching properties. The presence of the CO_2 also means that G varies less strongly with the applied voltage than otherwise.

The gas gain also changes with the density ρ of the gas, but not as strongly as with the charge. Estimates show that this dependence is approximately [CJ75], [AM74]

$$\frac{\Delta G}{G} \approx -4 \frac{\Delta \rho}{\rho}$$

At constant pressure, this means that the temperature across the wire plane must be kept uniform to about 0.3K at 300K for the gain to be uniform to 0.5%.

The Output from the Gas Amplifier

The gas amplifier output signal appears as a current between anode and cathode. That the gas amplifier is an almost perfect current source is apparent when it is considered that driving potential is very high (∿2 kV, see Appendix 2).

The form of the output current for one primary electron is (see Appendix 1):

$$I_1(t) = \frac{Q_o}{t + t_o} \qquad (t > 0)$$

where $$Q_o = \frac{eG\ C_{AC}}{4\pi\varepsilon_o} \quad \text{and} \quad t_o = \frac{\pi\varepsilon_o R_A^2}{\mu_+ Q_A}$$

in which G is the gas gain, e is the electronic charge, C_{AC} is the total anode-cathode capacitance/unit length, R_A and Q_A are the anode radius and charge/unit length, and μ_+ is the positive ion mobility.

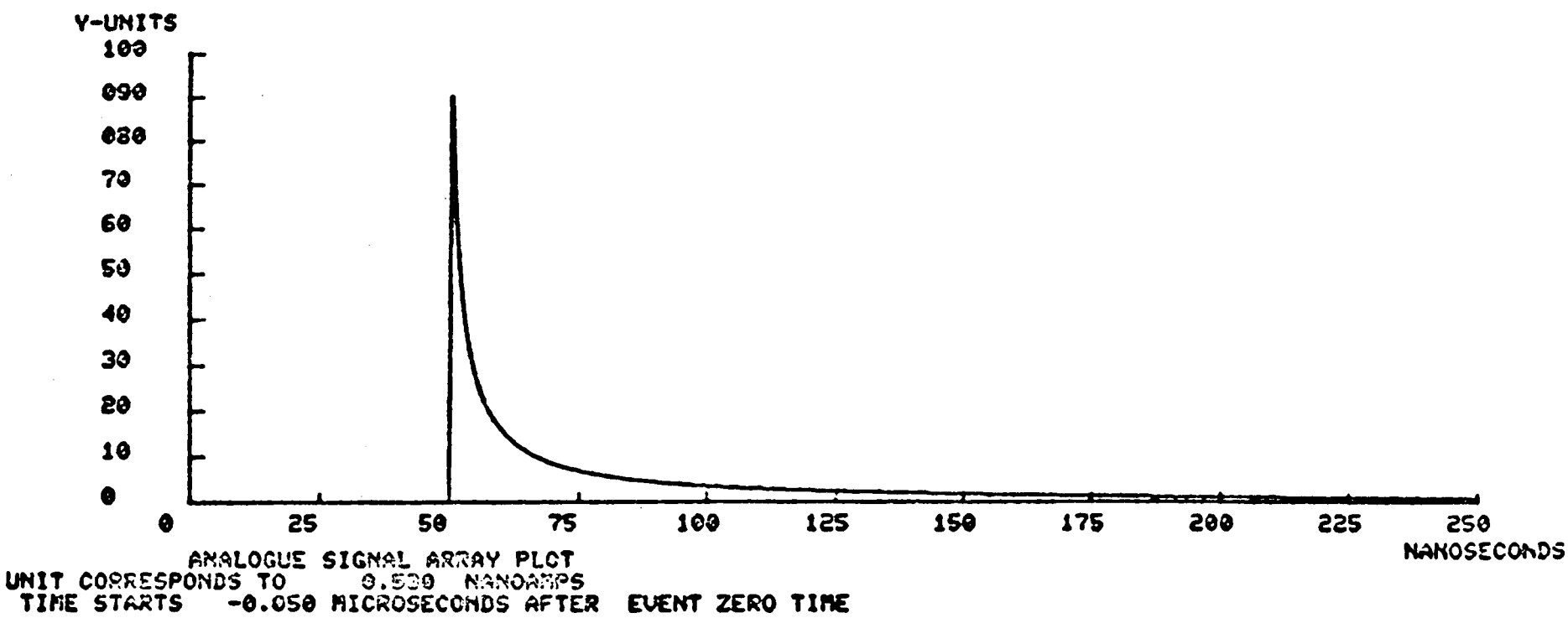


FIGURE II.7 Gas Amplifier Single Electron Response

This current pulse is shown in Fig. II.7, for

$$G = 10^4$$

$$C_{AC} = 7 \pm 1 \text{ pF/m (see Appendix 1)}$$

$$R_A = 12.5 \pm 0.7\mu \text{ (see later)}$$

$$Q_A = 16 \pm 4 \text{ nC/m (see Appendix 2)}$$

and $$\mu_+ = 1.5 \pm 0.5 \times 10^{-4} \text{ m}^2/\text{v/s} \quad [EA65].$$

With these values $Q_o = 10 \pm 2 \times 10^{-17}$ coulomb

and $t_o = 1.8^{+1.2}_{-0.8}$ ns

$$\therefore \quad I_1(0) = Q_{o/t_o} \tilde{\approx} 55 \text{ nA}$$

(Because the value of μ_+ is not well known, there is a large error on t_o.)

The rise time of the pulse is a few hundred picoseconds, being the time taken for the avalanche to form.

Linearity of the gas amplifier may be deduced from the fact that each ionization electron entering the anode region will create its own avalanche (see later). The output current due to a track containing many electrons is the single electron response $I_1(t)$ convoluted with δ-functions representing the arrival times t_i of the electrons at the anode

$$I(t) = \sum_{i=1}^{n} I_1(t + t_i) = \sum_{i=1}^{n} \frac{Q_o}{t + t_i + t_o} \qquad (t + t_i > 0)$$

This current is shown in Figure II.8 for a typical track sample of 50 electrons (ΔE = 1.3 keV) after a 2m drift. These results agree well with those of [FH75].

A noticeable feature of the output pulse is the long $^1/t$ tail, known as the 'positive ion memory', which continues for of the order of 100 μS. Methods of removing this tail are discussed in III.3.

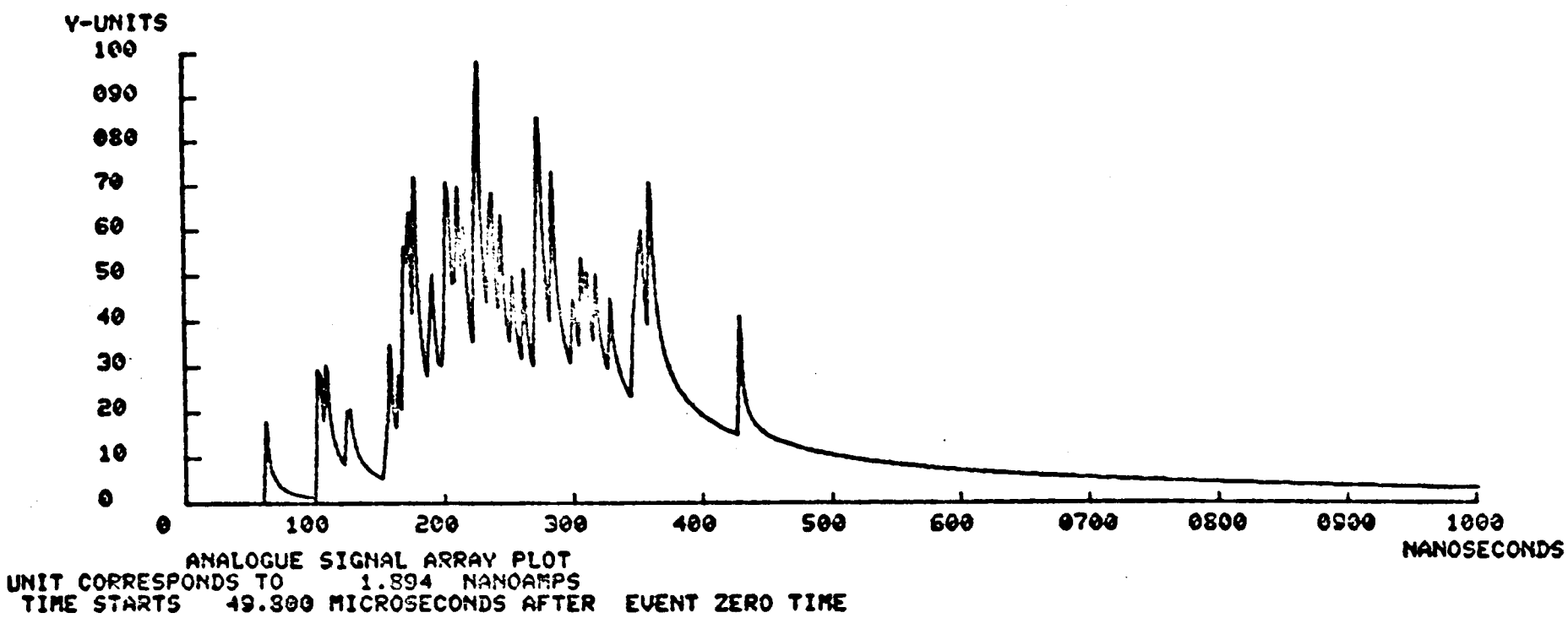


FIGURE II.8 Gas Amplifier Track Sample Response

The Choice of Wire Diameter

The characteristic time constant t_o of the gas amplifier pulse is proportional to R_A^2 (see above). The current pulse desired is one of large amplitude and short duration, obtained if R_A is very small. In addition, the voltages required to produce the high fields around the anode are less for small R_A. Consequently, the smallest wire radius practical is used. It has been found that 12.5μ radius stainless steel wires are a convenient choice.

It can be expected that G will depend on R_A at least as strongly as it does on Q_A, because of the importance of the surface field in determining the gas gain:

$$\frac{\Delta G}{G} \gtrsim -14 \frac{\Delta R}{R}$$

However, any roughness in the surface of the wire will be small compared with R_A ($\sim$12.5μ), and hence will be very small compared with the spread of the avalanches ($\sim$1 mm). The effect of wire roughness will thus average out over an avalanche.

The variation in R_A over lengths of a few cm of wire could result in a gain non-uniformity. However experience shows that the variation in G along typical lengths of wire ($\sim$10 cm) is $\sim$2%, indicating good wire diameter stability [BJ76].

The choice of cathode wire radius R_C is constrained by two considerations:

(i) Matching of the anode and cathode wire impedances for common-mode pickup rejection demands that the radii R_A and R_C should not be too different.

(ii) Secondary emission of electrons from the surface of the cathode occurs at small cathode diameters ($R_C \lesssim 30\mu$) due to positive ion bombardment. These electrons travel to the anode and cause the production of even more positive ions. Catastrophic regenerative breakdown results.

A suitable range for R_C is found to be R_C = 60-125μ.

The Effect of the Positive Ion Space Charge

For every electron arriving at the anode, there will be G ($\sim 10^4$) positive ions created in the amplification process. The large numbers of positive ions so produced represent a space charge which can alter the electric fields within the chamber. As a result, maximum values may be imposed on the gas gain G and on the product of charged particle flux ϕ and G.

There are two main considerations:

(i) Localized space charge

There will be $\sim N_e G$ positive ions generated in the series of avalanches making up the amplification of N_e primary electrons. If the charge of these ions $N_e Ge$ becomes comparable with the local charge on the anode wire, the gas amplifier will cease to be linear, since

the local electric field will be modified, and thus the gas gain will change (see [HR69]).

Because of the high dependence of G on the amplifying field, (see earlier), this effect can be expected at a distinct threshold value of $N_e G$. Typical values for this threshold in argon mixtures are $N_e G \approx 4\text{-}5 \times 10^6$ for an avalanche spread of about 1 mm [CA70], [HG49]. The threshold increases if the avalanche spread is greater (since the ratio of the positive ion charge to local anode charge is smaller), but is relatively independent of wire radius and the nature of the gas.

If the ionization from a deposited energy of 6 keV (Fe^{55} x-ray photon) is collected at an anode, the non-linearity threshold may be expected at a gain of $\sim 2 \times 10^4$. This has been observed: [BJ76].

(ii) Distributed space charge

The influence of the positive ions on the gas gain during their long lifetime ($\sim$130 mS) in the drift spaces places the tightest constraint on the maximum mean data rate per unit length of wire. Consider the magnitude of a positive ion space charge density within the chamber:

$$\rho = \frac{\phi G_e \bar{N}_e (1 - \alpha) t_r}{2} \qquad \text{[IN26]}$$

where ϕ is the mean particle flux per unit area per second

G ($\approx 10^4$) is the gas gain

e is the electronic charge

$\bar{N}_e$ ($\approx 10^4$/m) is the mean number of ionization electrons per unit length of track

τ ($\approx$130 mS) is the positive ion lifetime (= drift time for 2 m, see later)

α ($\approx$0.2) in the space charge drain parameter (see II.4)

t_r ($\approx$0.06) is the effective duty cycle due to gas gain switching (see later, and Appendix 2)

and the factor $^1/2$ accounts for the two drift regions. With these values

$$\rho = \phi G \times 5 \times 10^{-18} \text{ coulomb/m}^3$$

Using Poisson's equation, a change in field at the wire plane may be expected, of magnitude [CJ75]

$$\Delta E = \frac{\rho L}{2\varepsilon_o} \qquad \text{where L is the drift distance.}$$

The dependence of the gas gain on the drift field is

$$\frac{\Delta G}{G} \approx 14\ (1 - \alpha)\ \frac{\Delta E}{E} \quad \text{(see earlier, and II.4)}$$

Therefore $$\frac{\Delta G}{G} \approx 7\ (1 - \alpha)\ \frac{\rho L}{\varepsilon_o E}$$

With the above values, $\frac{\Delta G}{G} \approx 6.3 \times 10^{-11}\ \phi G$

The sensitivity of the associated bubble chamber puts an upper limit on background flux of $\phi = 2.5 \times 10^4/m^2/S$ [EHSP]. At a gas gain of 10^4, the gain changes by

$$\frac{\Delta G}{G} \approx 1.6\%$$

This is just tolerable. The conclusion is that the constraint on ϕ from space charge effects is within a factor of 2 of the constraint from the limited data capacity (see II.2). In terms of design consistency, this is a satisfactory situation.

The above calculations rely on the use of three methods of reducing the effect of the space charge:

(i) Minimisation of positive ion lifetime

The lifetime of the positive ions in the drift region is $\tau = \frac{L}{E\mu_+}$ where μ_+ is the positive ion mobility.

By maximizing the drift field E, the lifetime τ is reduced.

At 100 kV/m, $\tau \approx$ 130 mS for L = 2m.

(ii) Maximisation of space charge drain parameter

The amount of space charge entering the drift regions is reduced by allowing as many ions as possible to be discharged quickly (in $\sim 100\mu S$) at the cathode wires. The proportion getting in to the drift regions is $(1 - \alpha)$ where $\alpha = \frac{Q_C}{Q_A} \approx 0.2$ is the space charge drain parameter (see II.4).

(iii) Reduction of gas amplifier 'on' time

If the voltages on the wire plane are switched such that the gas gain is high only for a short time ($\sim$2mS every $\sim$33 mS), the space charge created is reduced by an effective duty cycle factor ($\sim$0.06). (See Appendix 2)

(For further details of the design and operation of multi-wire proportional chambers see [CG70] and [RP74]; a review of the factors affecting the gas gain is given in [BW73].)

II.4 FACTORS AFFECTING THE WIRE SEPARATION

The wire-to-wire separation in the wire plane is an important parameter which affects the properties of the chamber so much as to merit a separate discussion. The main parameters and properties involved are:-

(i) the drift field and the charges on the wires

(ii) the field geometry electron arrival time dispersion effect (see II.2)

(iii) the electro-mechanical stability of the wire plane

(iv) the upper limit on the space charge tolerance factor ϕG (particle flux x gas gain - see II.3)

Secondary considerations are:

(i) the constructional tolerances of the plane

(ii) the ionization sample size

(iii) the track angle time dispersion effect.

The Drift Field and the Charges on the Wires

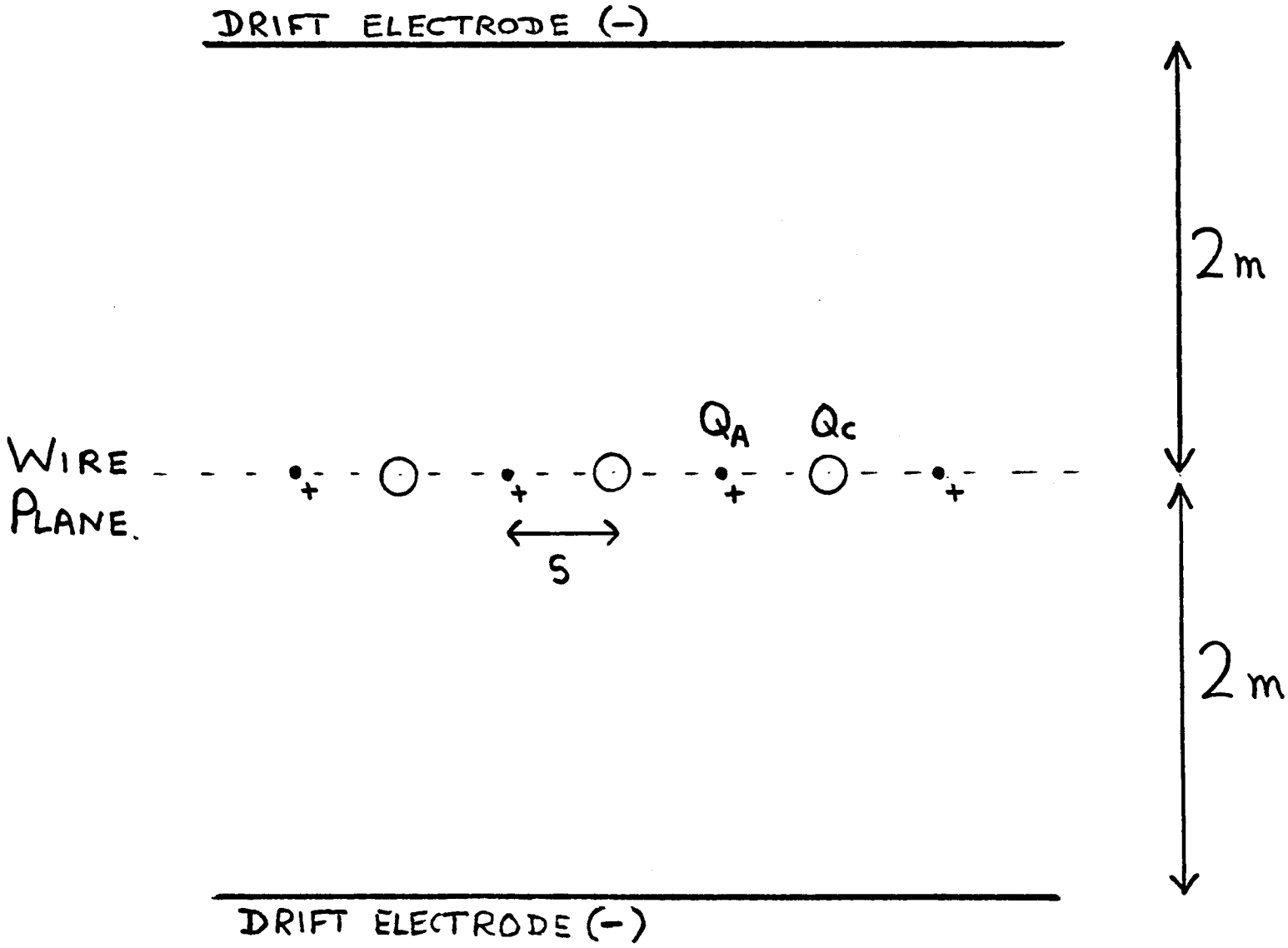


FIGURE II.9 Basic ISIS Electrostatics

The chamber electrostatic geometry is shown diagrammatically in Fig. II.9. Looking at the drift field E in terms of an average charge density, then, with two drift regions

$$Q_A + Q_C = 4s\varepsilon_o E$$

where Q_A, Q_C are the anode and cathode wire charges per unit length.

A parameter α is defined as

$$= -\frac{Q_C}{Q_A} = 1 - \frac{4s\varepsilon_o E}{Q_A}$$

All drift field lines end on anodes, if $\alpha > 0$ (as in Fig. II.3 section II.2). This is desirable as it is the condition for all the ionization in an element to end up at an anode.

In addition, for $\alpha > 0$, a fraction α of the positive ions generated at the anode in the gas amplification process go to the cathode wires. This is advantageous, because ions which go to cathode wires are discharged quickly in of the order of 100 μS. (The ions which get into the drift regions have a long lifetime (drift time) of about 130 mS.) As a result, the space charge tolerance factor ϕG (see II.3) may be increased by a factor of $(^1/1 - \alpha)$. For this reason, α is known as the space charge drain parameter, and should be as large as possible.

The anode wire charge Q_A is determined by the gas gain required. For $G \tilde{\sim} 10^4$, with 12.5μ radius wires, $Q_A = 16 \pm 4$ nC/m (see Appendix 2). The drift field operating window is (see II.2)

$$E = 75 \pm 25 \text{ kV/m}$$

Graphs of α against wire spacing s for various values of Q_A and E within these ranges are shown in Fig. II.10(i). As s increases, α decreases.

The Field Geometry Electron Arrival Time Dispersion Effect

The origin of the effect is discussed in II.2. Since the integral of the charge in a track is needed at the 99% level, this effect is parametrized as the arrival time dispersion of 99% of the electrons (the '99% lag time'). The field geometry dispersion 99% lag time is plotted against wire spacing in Fig. II.10(ii) for two values each of Q_A and E. (These results were obtained by the line integral method of II.2.)

Comparing Figs. II.10(i) and (ii), it can be seen that the 99% lag time is worst for small α. It becomes infinite at negative α, because ionization then ends up at the 'cathode' wires as well as the anodes.

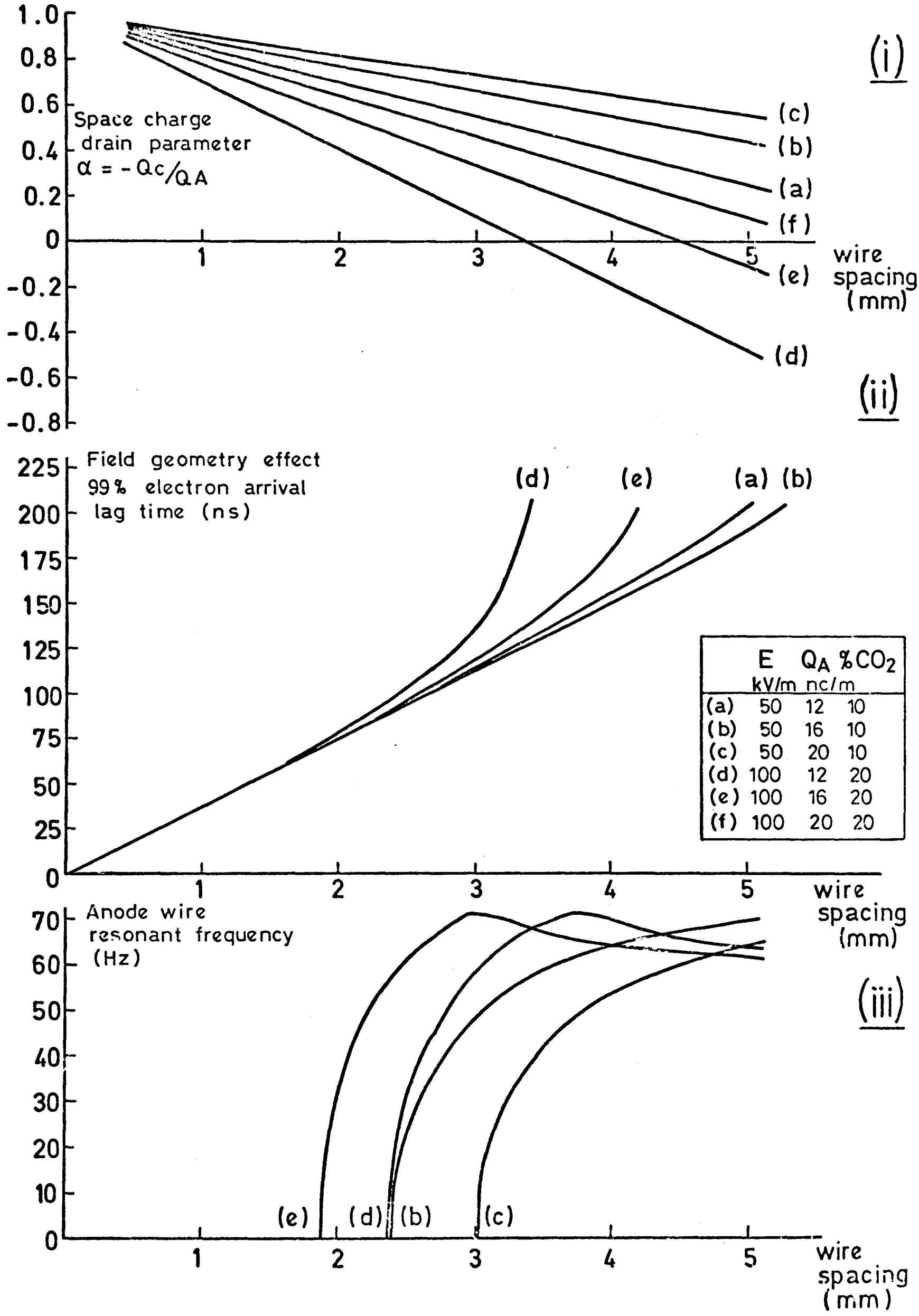

(i)
Space charge drain parameter
α = -Qc/QA
1.0
0.8
0.6
0.4
0.2
0
-0.2
-0.4
-0.6
-0.8
1
2
3
4
5
wire spacing (mm)
(c)
(b)
(a)
(f)
(e)
(d)
(ii)
Field geometry effect
99% electron arrival lag time (ns)
225
200
175
150
125
100
75
50
25
0
(d)
(e)
(a) (b)
E kV/m
Q_A nc/m
%CO2
(a) 50 12 10
(b) 50 16 10
(c) 50 20 10
(d) 100 12 20
(e) 100 16 20
(f) 100 20 20
wire spacing (mm)
Anode wire resonant frequency (Hz)
70
60
50
40
30
20
10
0
(e)
(d)
(b)
(c)
(iii)
wire spacing (mm)

FIGURE II.10

The Electro-mechanical Stability of the Wire Plane

The anode and cathode wires, being charged, experience electrostatic forces. The wires are under tension to prevent them moving under these forces. However the strength of the wires, in particular the 12.5μ-radius anodes, is finite, and therefore so is the tension in them. The tension must be sufficient by a safe margin to overcome the electrostatic forces.

It is useful to look at this problem in terms of the resonant frequency of the anode wires. (The cathode wires may be assumed to be rigid: to produce the same catenary sag due to weight in the two types of wire, the tensions are in the ratio $R_C^2/R_A^2 \approx 100{:}1$. This condition also results in them having the same resonant frequency.) The fundamental frequency is (Appendix 3)

$$f = \frac{1}{2\ell}\sqrt{\frac{T_o - T_m}{m}}$$

where $$T_m = \frac{\ell^2}{10\pi\varepsilon_o S}\left|1.23\, Q_A Q_C + 0.41\, Q_A^2\right|$$

in which ℓ is the wire length, m is the mass/unit length, and T_o is the uncharged tension in the wire.

With ℓ = 2.5 m (2m useful length plus an additional 25 cm at each end to get away from edge effects.)

T_o = 50 gms wt (70% of the breaking tension for 12.5μ radius stainless steel wires)

m = 3.8×10^{-3} gms/m again for 12.5μ radius stainless steel wires)

$Q_C = -\alpha Q_A$ (see earlier) .

the resonant frequency was calculated as a function of wire spacing s for two values each of Q_A and E. The results are plotted in Fig. II.10(iii).

Conclusions from these Considerations

From Figs. II.10(i) and (ii) it may be seen that choosing a small wire spacing has the desirable results of reducing the field geometry time lag and increasing the space charge drain parameter.

However, the anode wire resonant frequency (Fig. II.10(iii)) decreases as the wire spacing is made smaller, and falls catastrophically to zero at some wire spacing depending on the values of E and Q_A.

A further consideration is that, at low resonant frequencies, the wires are more susceptible to oscillation induced by the ambient level of vibration. As a result a minimum of 40 Hz is imposed on the operating resonant frequency. (This particular value is chosen because it is above the ∿30 Hz cycle frequency of the bubble chamber near which ISIS is to be situated [EHSP].)

Inspecting Fig. II.10 again, it may be seen that a choice of 4 mm for the wire spacing results in a minimum resonant frequency of over 50 Hz. The space charge drain parameter is positive over most of the operating window. The field geometry time lag is ∿150-180 nS (∿6-7 mm) over the useful range of positive α. These are satisfactory values.

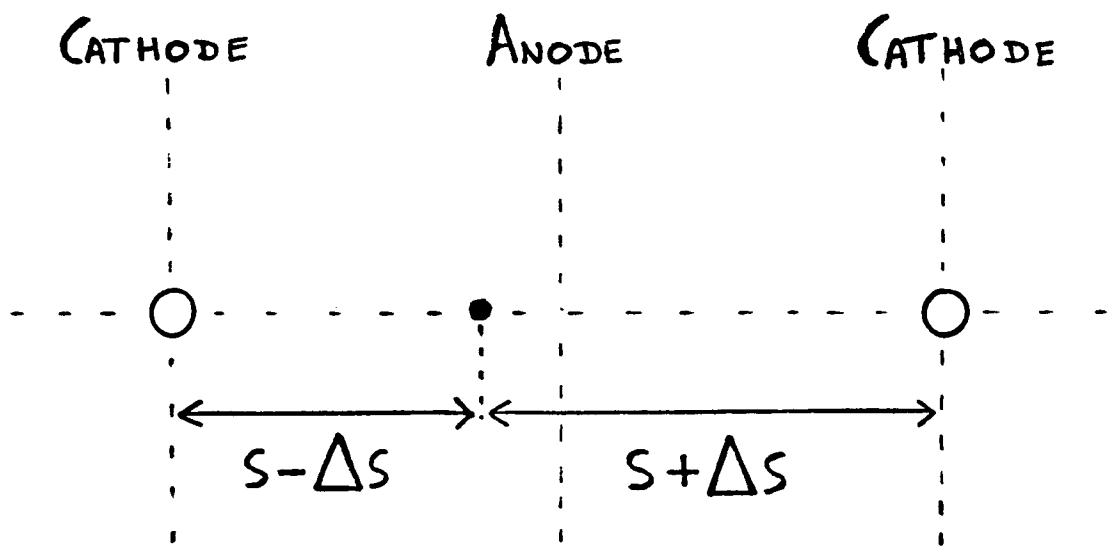
Constructional Tolerances on the Wire Plane

The constructional precision needed in the definition of the wire spacing is determined by the very sensitive dependence of the gas gain G to changes in Q_A. In the region of $G \tilde{\sim} 10^4$, $\frac{\Delta G}{G} \tilde{\sim} 14 \frac{\Delta Q_A}{Q_A}$ see (II.3). At constant voltage, this dependence applies to the wire capacitance: $\frac{\Delta G}{G} \tilde{\sim} 14 \frac{\Delta C_A}{C_A}$ where C_A is the anode capacitance/unit length.

If G is to be good to the level of 0.5%, then C_A must be constant to $\sim$0.036%, from wire to wire as well as along the length of an individual wire.

Assuming the wires remain straight and parallel, there are four cases to consider, of deviation from correct geometry:

(i) Asymmetric position of the anode wire between the cathodes



Using a standard formula for the capacitance of parallel cylinders [BB65], [SW68]

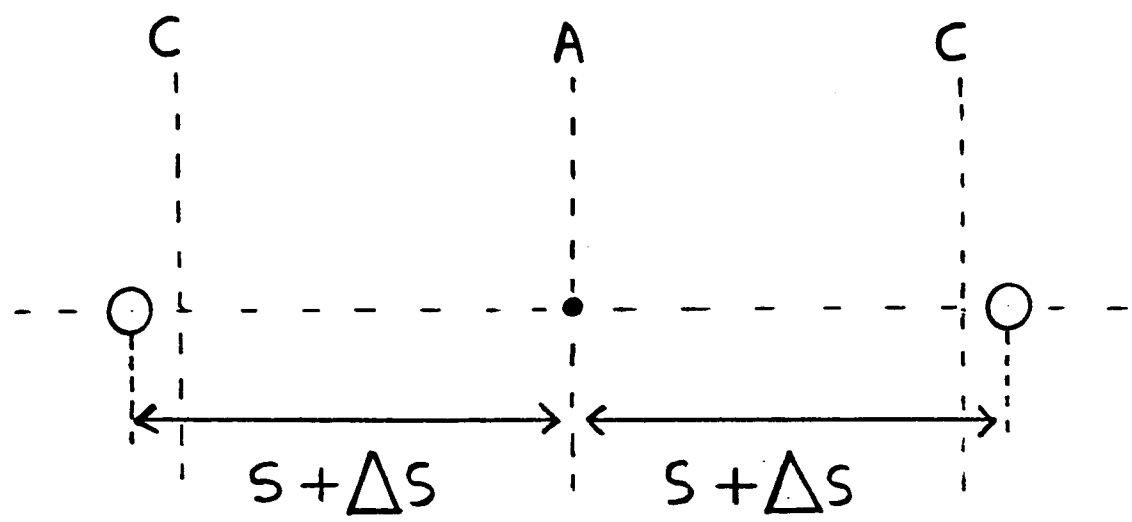
$$\frac{\Delta C_A}{C_A} = \frac{2 + \ln(s/a)}{(\ln(s/a))^2} \left(\frac{\Delta s}{s}\right)^2$$

for $\Delta s \ll s$, where $a = \sqrt{R_A R_C}$ and R_A, $R_C \ll s$. For $R_A = 12.5\mu$, $R_C = 125\mu$ (see II.3) and $s = 4$ mm, then

$$\frac{\Delta s}{s} \lesssim 4\% \text{ for } \frac{\Delta G}{G} < 0.5\%$$

The precision needed in the centralization of the anode wire between the cathodes is $\Delta s \lesssim 130\mu$. This tolerance is relatively loose, because ΔC_A is second order in Δs.

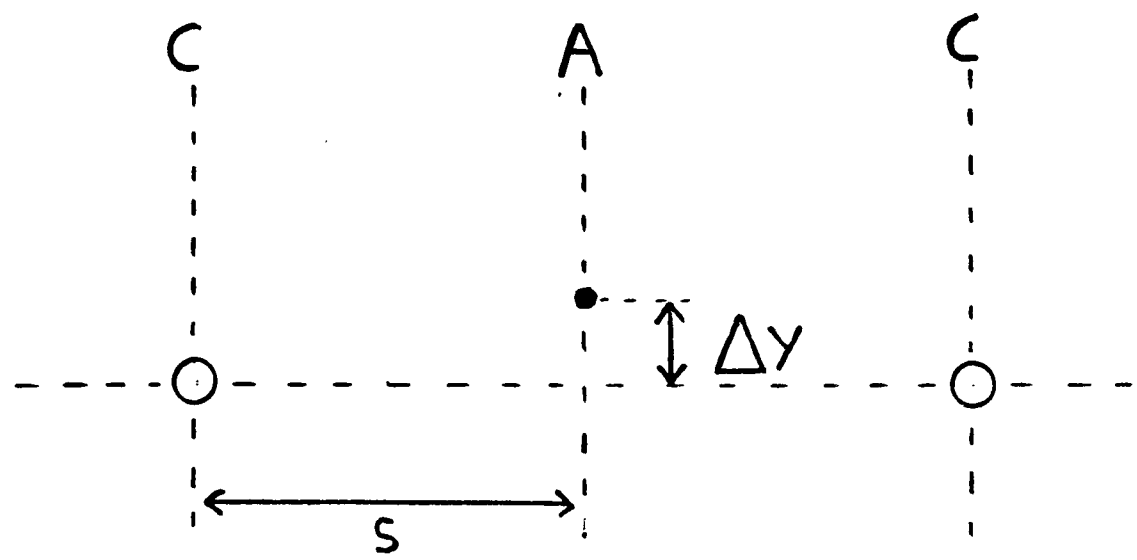
(ii) Symmetric position of the anode wire, incorrect wire spacing



In this case $\frac{\Delta C_A}{C_A} = -\frac{1}{\ln(S/a)} \quad \frac{\Delta s}{s}$

which is first order in Δs. Using the same values as (i), $\frac{\Delta s}{s} \lesssim 0.16\%$ for $\frac{\Delta G}{G} < 0.5\%$. Thus the precision needed in the definition of cathode-cathode spacing is high, being $2\Delta s \lesssim 12\mu$.

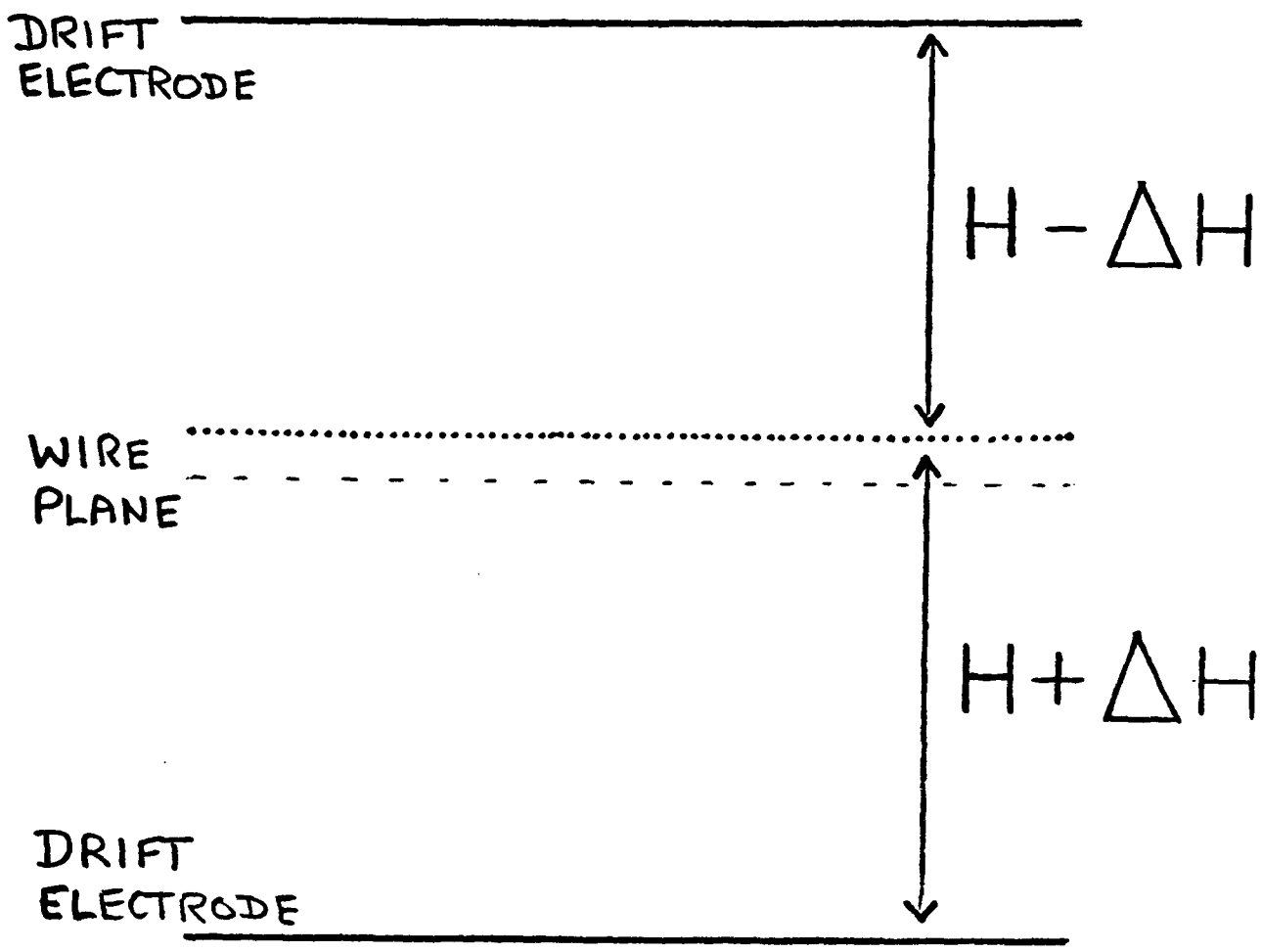
(iii) Correct wire spacing, anode wire not coplanar



For small Δy, $\frac{\Delta C_A}{C_A} = -\frac{1}{2\ln(S/a)} \left(\frac{\Delta y}{s}\right)^2$

This gives $\frac{\Delta y}{s} \lesssim 5.5\%$ for $\frac{\Delta G}{G} \lesssim 0.5\%$. The out-of-plane movement of the anode wire can be as great as $\Delta y \lesssim 200\mu$.

(iv) Asymmetric position of wire plane between drift electrodes



Ignoring the guard structure, this is simply:

$$\frac{\Delta C_A}{C_A} = 2\left(\frac{\Delta H}{H}\right)^2$$

For H = 2m, a precision $\Delta H \lesssim 26$ mm is needed for $\frac{\Delta G}{G} \lesssim 0.5\%$. There will be no trouble in achieving this precision.

The conclusions from the above calculations is that the tightest tolerance is on the cathode-cathode spacing, the precision needed here being ∿12μ (∿0.5thou') in 8 mm. The other tolerances are relatively unimportant.

These tolerances are also the upper limits on the amplitudes of any vibrations of the wires. Although acoustic coupling to the wires is small, mechanical coupling is effective in causing oscillations.

Ionization Sample Size and Track Angle Dispersion

The choice of ionization sample size is independent of the choice of wire spacing to the extent that two, three or more anodes may be connected in parallel to sum the signal from a larger sample.

The sample size is determined by the ionization resolution wanted, the total length of track to be sampled, and the expense of the electronics needed to process the signal from one sample (see II.1). About 300 samples over 5m of track are required.

The magnitude of the track angle electron arrival time dispersion effect is proportional to sample size (see II.2).

The effect of choosing different sample sizes is shown in Table II.3, for a wire spacing of 4 mm, and drift velocity of 4 cm/μS.

TABLE II.3

No. of Anodes in Parallel	Length of Sample (mm)	Length of Track for 300 Samples (m)	No. of Samples in 5m Track	Time Dispersion at θ = 18° ns	mm
1	8	2.4	625	64	2.6
2	16	4.8	313	127	5.1
3	24	7.2	208	190	7.6
4	32	9.6	156	254	10.0

A sample size of 16 mm (two anodes in parallel) is optimum, allowing 5 m of track to be sampled 313 times. The magnitude of the track angle dispersion is 127 nS (∿5mm equivalent drift distance); this is acceptable, being of roughly the same size as the other forms of dispersion (see II.2).

CHAPTER III

THE ELECTRONICS FOR ISIS

III.1. THE ORGANIZATION OF THE ELECTRONICS

In the electronic processing of the signals from the ISIS chamber, two main requirements are satisfied (see Chapter 1):

(a) Conversion of the data from the analogue domain to the digital domain with sufficient (<1%) overall accuracy.

(b) Reduction of the data rate to one that can be handled by a conventional minicomputer. This is obtained by using both temporary data storage and parallel processing.

The nature of the ionization and track position measurements necessitates the use of ∿320 identical channels of electronics, one for each sample of track ionization. This accomplishes the transformation to parallel processing. The schematic diagram of one of these channels is shown in Figure III.1. Apart from common control signals, each channel is self-triggering and operates completely independently of the other ∿319 channels. One channel contains the necessary electronics for temporary storage and digitization of the magnitude and timing of the signals from ∿30 tracks (see Chapter I). The design has been kept simple, for reliability and cheapness (the cost per channel is about £150, making the total cost of 320 channels about £48,000).

A fast low-noise preamplifier (described in III.2), located near to the chamber, boosts the signals for transmission along cables to the remote electronics. More amplification precedes linear pulse shaping, which removes some deleterious effects of the gas amplifier output signal (see III.3).

To measure the amount of ionization in the track sample, the gated integral of the chamber current signal is obtained by charging one of 32 capacitors with the signal (see III.4). This capacitor

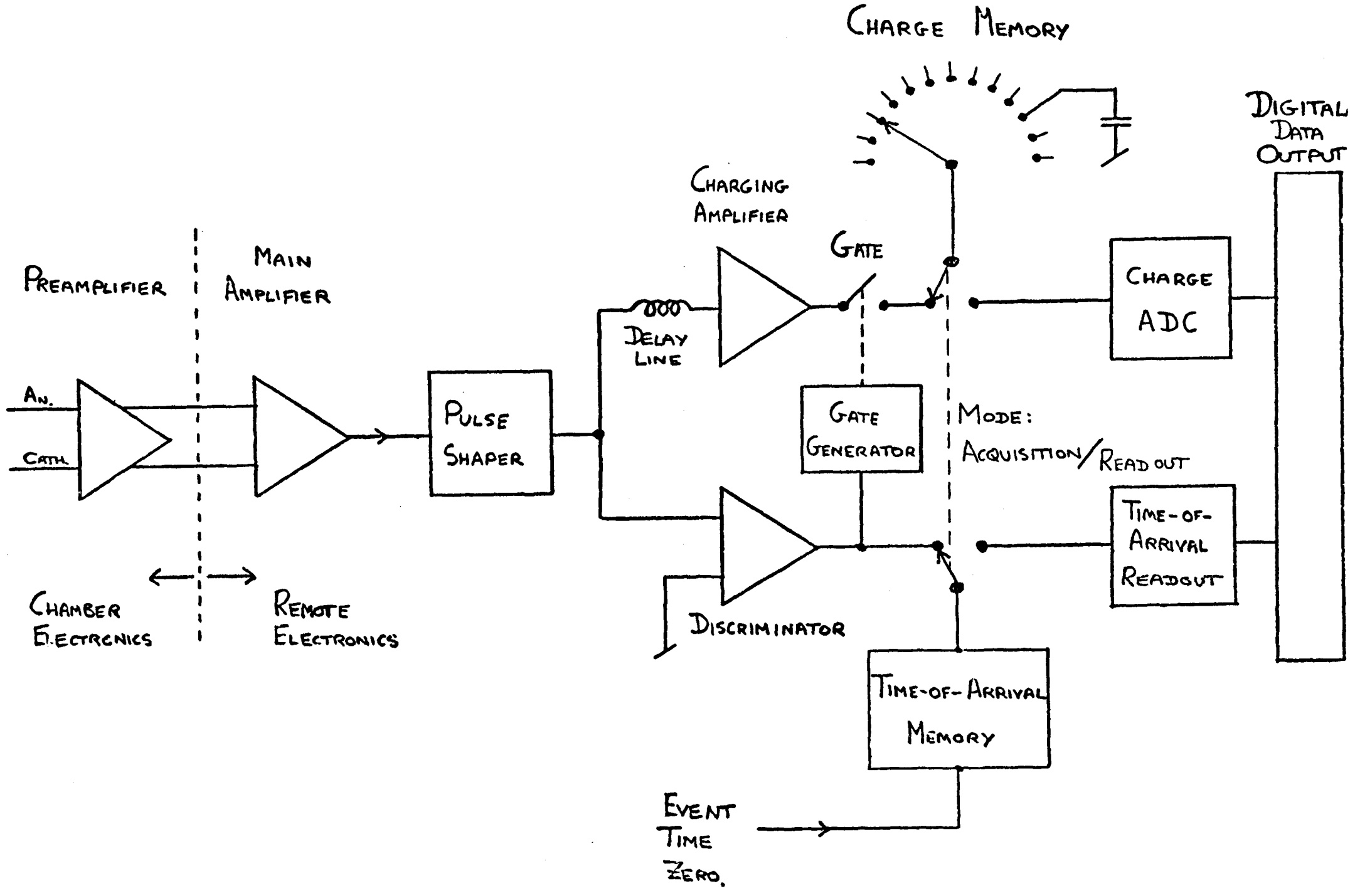


FIGURE III.1 SCHEMATIC DIAGRAM OF ONE CHANNEL OF THE ELECTRONICS

acts as an analogue memory, holding the charge for a time (∿mS) until the readout system is ready for the data. The capacitor is then discharged through an analogue-to-digital converter (ADC), and this digital data is passed to a computer. The multi-track capability is realized by multiplexing the signals around the 32 capacitors.

The track sample position is measured as a time-of-arrival relative to an event-time-zero provided by an external trigger. Multiplying this time by the drift velocity gives the drift distance. The timing information is derived from the signal by a discriminator (see III.5). The output from this is used to generate the charge integration gate, as well as in giving a time which is deposited in the 'time-of-arrival' memory. The times can subsequently be read out from the memory by the computer contemporaneously with the ionization data from the same track sample.

The ionization data has to be accurate to the 1% level. For this reason a D.C. baseline restorer is used to eliminate the systematic D.C. baseline shift problems associated with the high and varying signal rates encountered. This is not shown in Fig. III.1 but is described in III.6.

A brief discussion of the controlling logic (excluded for clarity from Fig. III.1) and computing requirements is given in III.7. This section also includes a description of the implementation of these features on the prototype channel.

The majority of the author's contributions have been to the design of the parts of the electronics described in sections III.2 and III.3

III.2 ELECTRONIC AMPLIFICATION AND NOISE SOURCES

The signal from the wireplane is small ($\sim$1 μA), although it comes from a gas amplifier of fairly high gain ($\sim 10^4$). Care has to be taken in the subsequent amplification and treatment of the signal by the electronics not to degrade the information in the signal nor the signal-to-noise ratio (SNR). In this section are discussed the various noise sources and what may be done about maximizing the SNR. The ever-important low-noise preamplifier and its connections to the wire plane are treated in some detail.

The Signal Source

The nature of the output from the gas amplifier has been discussed in Section II.3 and in Appendix 1. The signal comes from a current source. At a gas gain of $\sim 10^4$ the amplitude and duration of useful signals range from about 100 nA for 500 nS to about 3 μA for 200 nS. The first case corresponds to $\sim$40 electrons in a sample ($\Delta E \sim 1.0$ KeV) drifting 2m, the second case to $\sim$300 electrons ($\Delta E \sim 8.0$ KeV) drifting 1 cm. The rise times of the signals vary between $\sim$30 and $\sim$200 nS. The fall times can be initially as fast as the rise times, but rapidly ($\sim$tens of nanoseconds) become dominated by the $^1/t + t_o$ tail of the gas amplifier response (see II.3 and III.3).

The Noise Sources

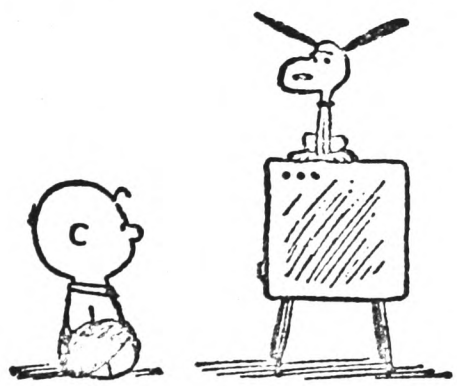
There are three main sources of the noise observed in absence of signal:

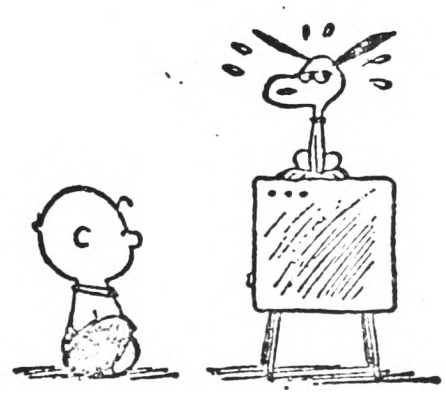
(i) Electronic Noise

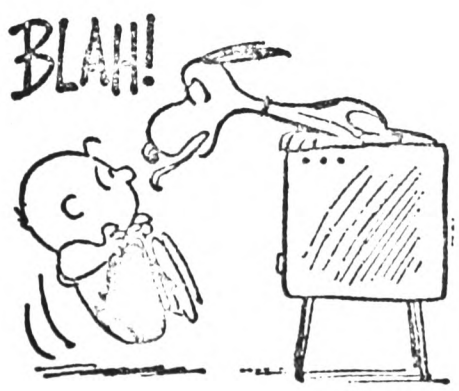
This is non-deterministic noise of fundamental origin e.g. Johnson noise from input resistors, shot noise from the base current in the first transistor etc. Electronic noise is not totally removable, but its magnitude can be minimized by careful design. This entails choosing a low noise input circuit, and optimizing the component values therein. Typical electronic noise from the prototype pre-amplifier described later is shown in Figure III.2 (a) (Time domain) and (b) (Frequency domain).

(ii) Pick-up

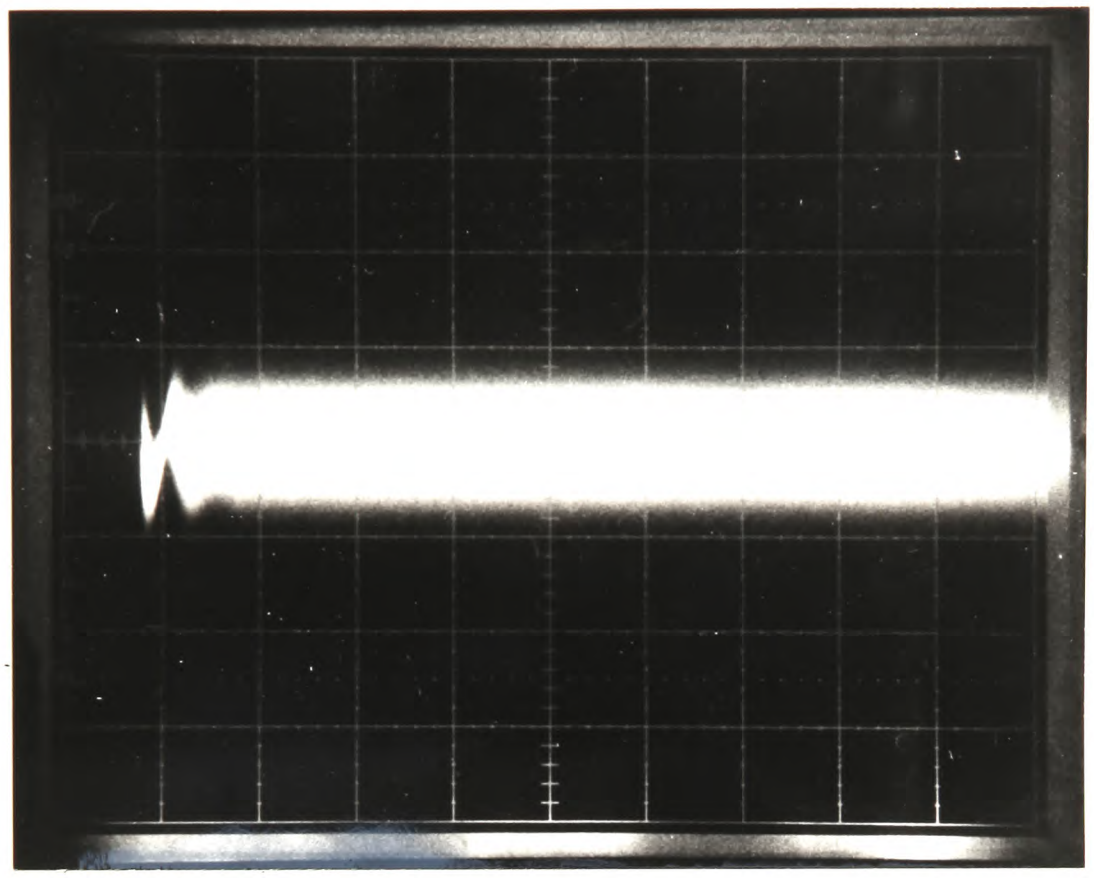
This is deterministic noise arising from the induction of currents in the signal paths by external or internal electromagnetic fields. Examples are the pick-up of external R.F. power (the 2.5m long wires are good aerials - see below), and pick-up of transients from digital waveforms within the electronics (TTL logic switches ~3v in ~10 nS). In cases like pick-up of R.F. by the wires, where there is a very strong inter-channel correlation, the effects can be serious.



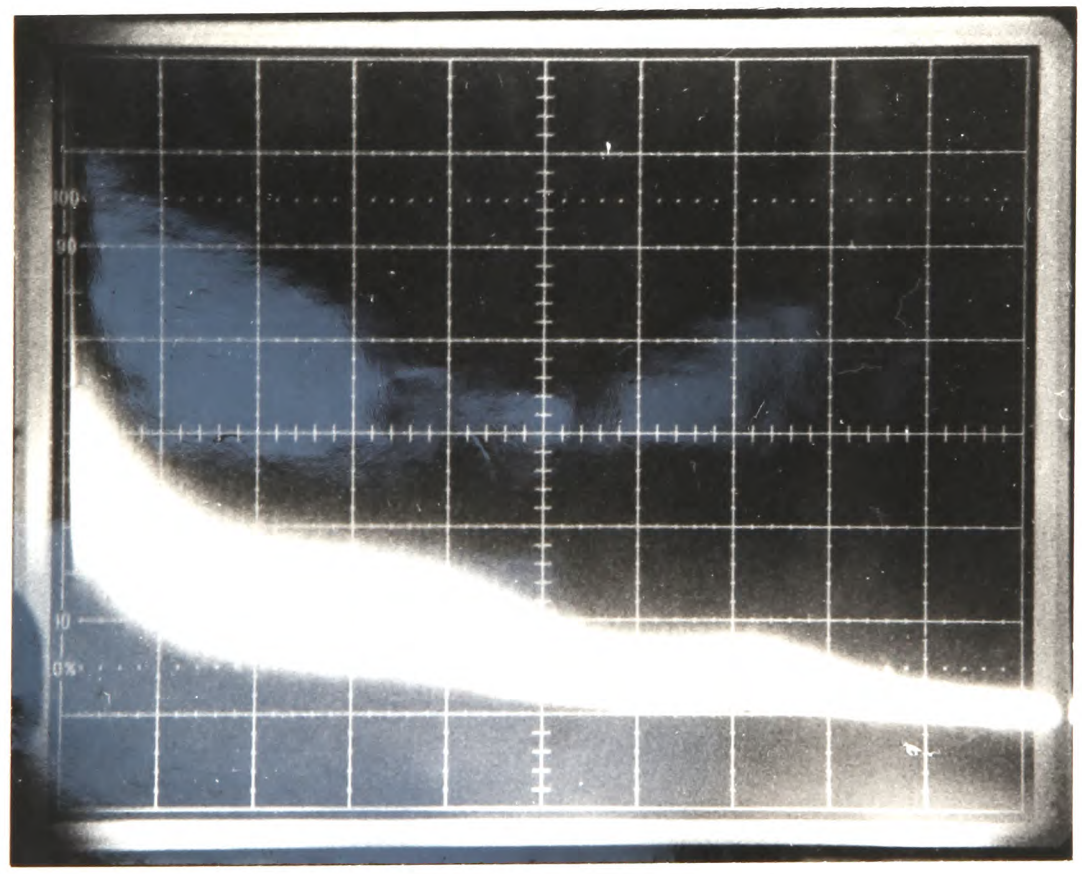






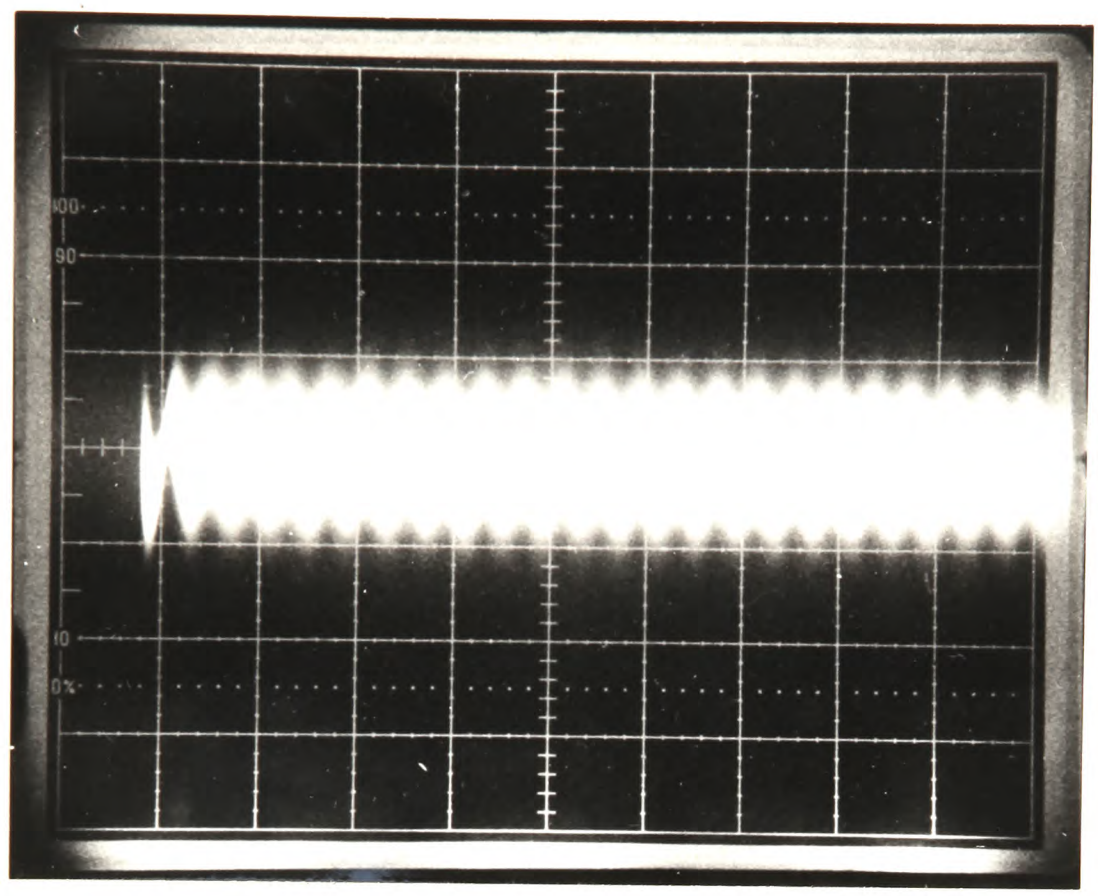


(a) Time Domain. X: 50nS/div
Y: 5mV/div

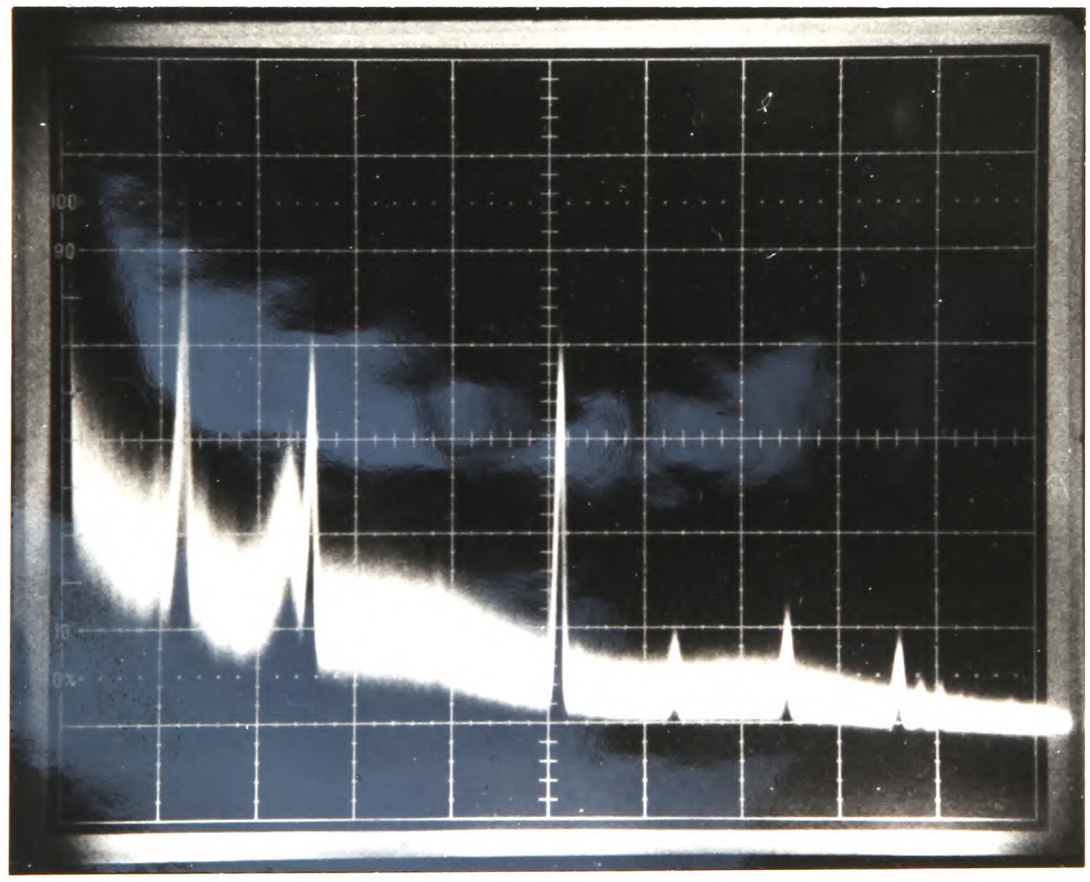


(b) Frequency Domain. X: 10MHz/div
Y: Uncalibrated

Figure III.2 Preamplifier Noise



(a) Time Domain. X: 50nS/div
Y: 5mV/div



(b) Frequency Domain. X: 10MHz/div
Y: Uncalibrated

Figure III.3 Preamplifier Noise with pick-up.

A typical case of pickup noise is shown in Figure III.3 (a) (Time domain) and (b) (Frequency domain). It can be seen that analysis of the noise frequency spectrum represents an effective method of detecting the presence of this noise.

In principle, pickup is removable. There are several methods which are employed to minimize it:

(a) a designed reduction in the sensitivity of the circuit to pickup e.g. by choosing appropriate impedance levels,

(b) screening of the sensitive areas of circuitry e.g. the earthed, metallized, gas bag around the chamber,

(c) differential operation, in which the pick-up is rejected as a common-mode signal,

(d) the use of a well defined 'earth',

(e) short wire-to-preamplifier connections,

(f) good decoupling of power supplies.

(iii) Crosstalk

This is also a deterministic noise but is highly correlated with the signal. The same methods as for pickup may be employed to minimize crosstalk. The origins of crosstalk can, however, be fundamental to the design, e.g. capacitative coupling between the wires of adjacent channels (see later).

The effects of electronic noise are random in nature. Pickup and crosstalk are worse in that they can cause systematic errors and channel-to-channel correlations. These effects must be kept down to less than $\sim$1%, for they can damage the velocity resolution if they are any greater.

The Front-end Configuration

The front end of the electronics is comprised of the first stage of the preamplifier and its connection to the chamber. The most important consideration in the design of this part of the electronics is the SNR, since the front-end performance determines the SNR in the rest of the system. The design must aim to maximize the usable signal, and to reduce the noise at its physical source. Apart from the electronic noise, which is discussed later, there are four main design considerations.

(i) Low input impedance

The chamber output pulse is a current signal (see II.3). The signal required in later stages of the electronics is one which is proportional to this current. It is therefore advantageous to go against historical precedence and measure the output current directly, instead of the voltage developed across the chamber capacitance. This entails using a current sensitive preamplifier. The SNR is not necessarily degraded by so doing (see [FE75] and also more specifically [MS69]), and in fact capacitative crosstalk between wires is reduced because the inducing voltages are smaller (see later).

To follow the current signal accurately without the detrimental effects of integration and pulse broadening, the preamplifier must be fast. This means having a low input impedance, because of the integrating effect of the input time constant $\tau_{in} = R_{in}C_{in}$, where R_{in} is the preamplifier input resistance and C_{in} is the total input capacitance.

The choice of the time constant τ_{in} involves a compromise between pulse broadening and SNR; this is discussed in IV.5. A 10-90% rise (and fall) time of 30 nS is about optimum, corresponding to $\tau_{in} = 13.5$ nS.

The total input capacitance C_{in} is made up of the chamber wire capacitance of ∿35 pF (2 x 2.5m @ 7 pF/m, see Appendix 1) and that of the preamplifier input plus strays (a few pF). This makes a total of $C_{in} \tilde{>} 40$ pF. Therefore the preamplifier input resistance R_{in} must be less than about 300Ω.

Out of the possible configurations of active devices, there are only three which satisfy the low-input impedance criterion:

(a) <u>High input impedance amplifier with shunt feedback</u>

This offers the best prospects for low noise (see [NP74]), but is rejected on the following grounds. To obtain a good SNR, a high input resistance is needed (see later). To bring this impedance down to the required value, shunt feedback through a resistive element is applied, with high open loop gain. It is difficult to maintain stability in amplifiers of very high gain-bandwidth products when feedback is applied, because of the phase shifts which occur within the amplifier (see, however [MJ74], in which a high bandwidth amplifier of this design is discussed). In addition to this, differential operation with matched input stages (see later) would be difficult to obtain. Preamplifier recovery with gas gain switching (see Appendix 2) could be a problem, because of the high impedance levels.

(b) <u>Common gate F.E.T. stage</u>

Because of the lack of a base current and its associated shot noise, the F.E.T. looks attractive as the input device. In the common gate connection, an F.E.T. has a low input impedance, and seems to offer a good solution. However, this was not employed in the prototype because of anticipated difficulties involving the matching of the differential input stages: the operating parameters (g_M, Vgs, etc.) are device-dependent.

(c) Common base bipolar transistor stage

This is the input stage chosen for the prototype. The small signal l.f. input impedance is defined by the emitter current:

$$R_{in} = r_e + \frac{r_b}{1+hf_e}$$

$$r_e \quad \text{for large } hf_e$$

where r_e and r_b are the dynamic emitter and base resistances and hf_e is the common-emitter forward current gain. For all transistors, $r_e = \frac{kT}{qI_e}$ where I_e is the standing emitter current. This gives:

$$R_{in} = \frac{1}{40I_e} \quad \text{with } kT = \frac{1}{40} \text{ eV}$$

which is independent of other components. For $R_{in} < 300\Omega$, $I_e \gtrsim 100\ \mu A$. A full analysis of the noise situation using this stage is given later.

(ii) Differential Input

Shown schematically in Fig. III.4 is the differential input connection, with the anode and cathode wires connected to the two inputs of a differential preamplifier with two matched input stages. This has two advantages over a single input preamplifier looking solely at the anodes:

(a) Any pickup on the wires or capacitative cross-talk between samples appears in common mode and is rejected to a greater or lesser extent depending on the relative gains and impedances of the anode and cathode input circuits. With 12.5μ radius anode wires and 125μ radius cathode wires of stainless steel, the common mode rejection of R.F. pickup is ∿30 dB at frequencies below about 10 MHz. Above these frequencies, the rejection is less, falling to 6 dB at 50 MHz,

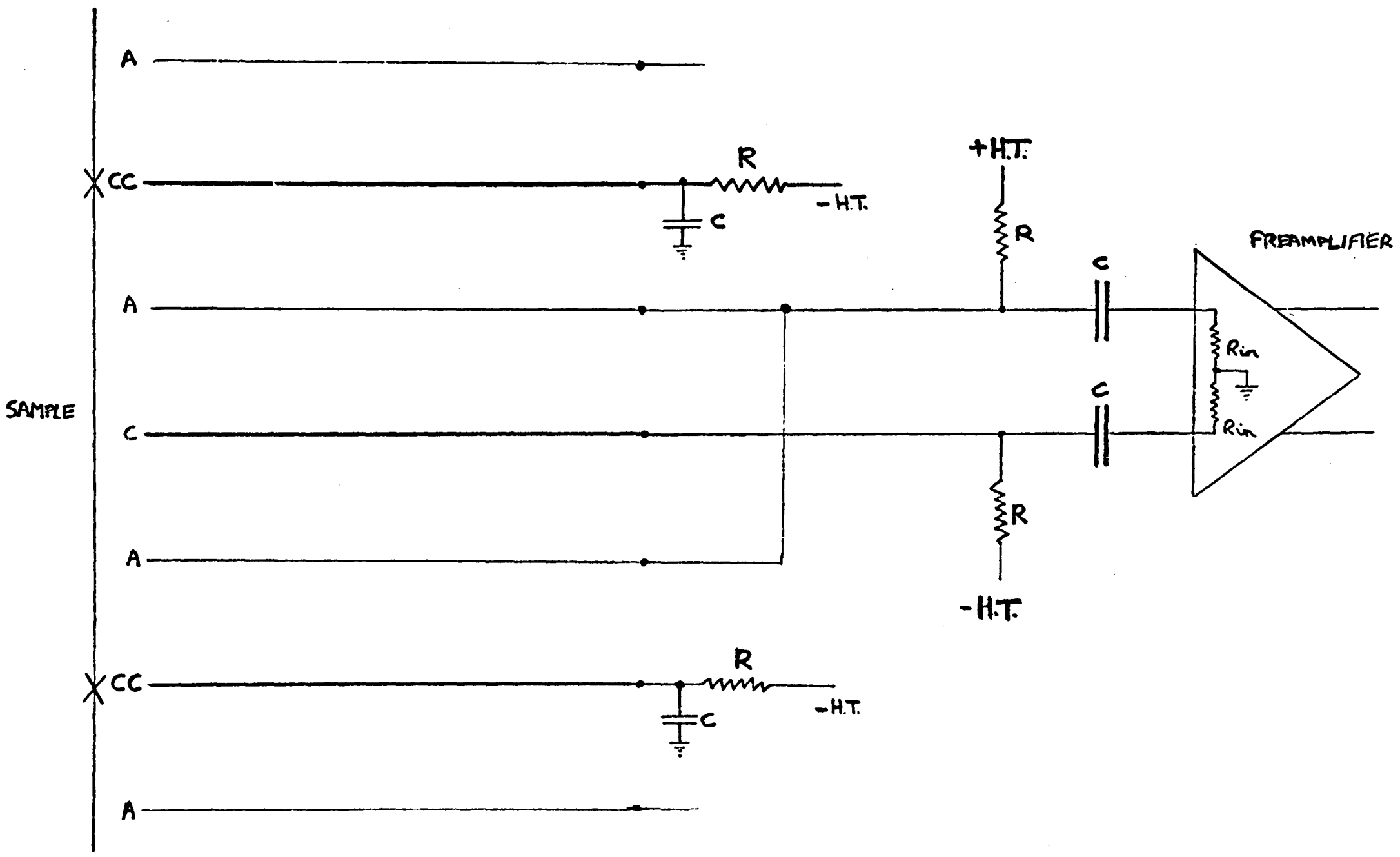


FIGURE III.4 SCHEMATIC DIAGRAM OF THE DIFFERENTIAL INPUT CONNECTION

because the wavelengths become comparable with wire lengths, and small differences in wire impedance are important.

(b) The signal observed is boosted by the current in the cathode circuit. The amount of additional signal is determined by the ratio of the number of cathodes N_c to the number of anodes N_a connected to the preamplifier. (The drift electrodes are neglected, since they have a very small capacitance to the anodes compared with the cathode wires, see Appendix 1.) To prevent inter-sample crosstalk, the common cathodes are decoupled to ground (see later). For the optimum case of two anodes coupled in parallel to form the sample (see II.4), there is only one cathode connected to the preamplifier (see Fig. III.4). Defining an effective gas amplification G_e to parametrize this signal boost: $G_e = G\left(1 + \frac{N_c}{N_a}\right)$.

It is noted that in this case $N_c/N_a = 0.5$, giving

$$G_e = 1.5G$$

There is an effective signal boost of 50%. However it must be remembered that the use of a differential preamplifier increases the noise by $\sim\sqrt{2}$ or approximately 40%, because the noise contributions from the two input stages add in quadrature (assuming them to be uncorrelated).

(iii) Wire Coupling and Decoupling

To ensure only small loss of signal due to charge sharing, the coupling (and decoupling) capacitors C in Fig. III.4 must be large ($\sim$1000 pF) compared with the inter-wire capacitance of $\sim$40 pF.

The value of the detector H.T. charging time constant $\tau = RC$ has an upper limit imposed on it by the fact that gain switching (see Appendix 2) must be completed in less than 1 mS. To stabilize the

gain at 0.5% of nominal requires the voltages to be correct to 0.036% (see II.3). In terms of an exponential of characteristic time τ, this is a limit $\sim 8\tau$. For 1 mS recovery, $\tau \lesssim 125$ μS. The maximum value of $\tau \tilde{\sim} 125$ μS is chosen: (a) to ensure the least differentiation of the signal (see III.6) and (b) to minimize the h.t. power supply current. Therefore for C = 1000 pF, the feed resistors must be $R \tilde{\sim} 125$ KΩ. The 'preferred' value consistent with this condition is 100 KΩ, (This is very large compared with the input impedance: no loss of signal occurs.)

The two outside cathodes of a sample have a signal on them which is the sum of contributions from the two adjacent samples. To prevent crosstalk they are decoupled to ground, with an identical RC to give the same H.T. charging characteristics.

(iv) H.T. Decoupling and Crosstalk

The signal on one channel can give rise to induced signals on other (not necessarily adjacent) channels by coupling through the electrode h.t. feed network, shown schematically in Fig. III.5.

A signal charge Q_s produces a signal voltage between anode and cathode of Q_s/C_c. This may be coupled to other channels through the drift electrode or the anode/cathode h.t. busses.

Coupling through C_{ad} and C_{cd} to the drift electrodes causes a proportional crosstalk

$$\frac{\Delta Q}{Q_s} \tilde{\sim} \frac{(C_{ad} - C_{cd})^2}{C_c\, C_d}$$

to appear on the other channels. This is negligible since $C_c \tilde{\sim} 1000$ pF, $C_d \tilde{\sim} 300$ pF and C_{ad}, $C_{cd} \tilde{\sim} 0.1$ pF. Coupling through the anode h.t. bus occurs with strength

$$\frac{\Delta Q}{Q_s} \tilde{\sim} \frac{Z_{ab}}{R_a + Z_{ab}} \cdot \frac{Z_{in}}{R_a + Z_{in}}$$

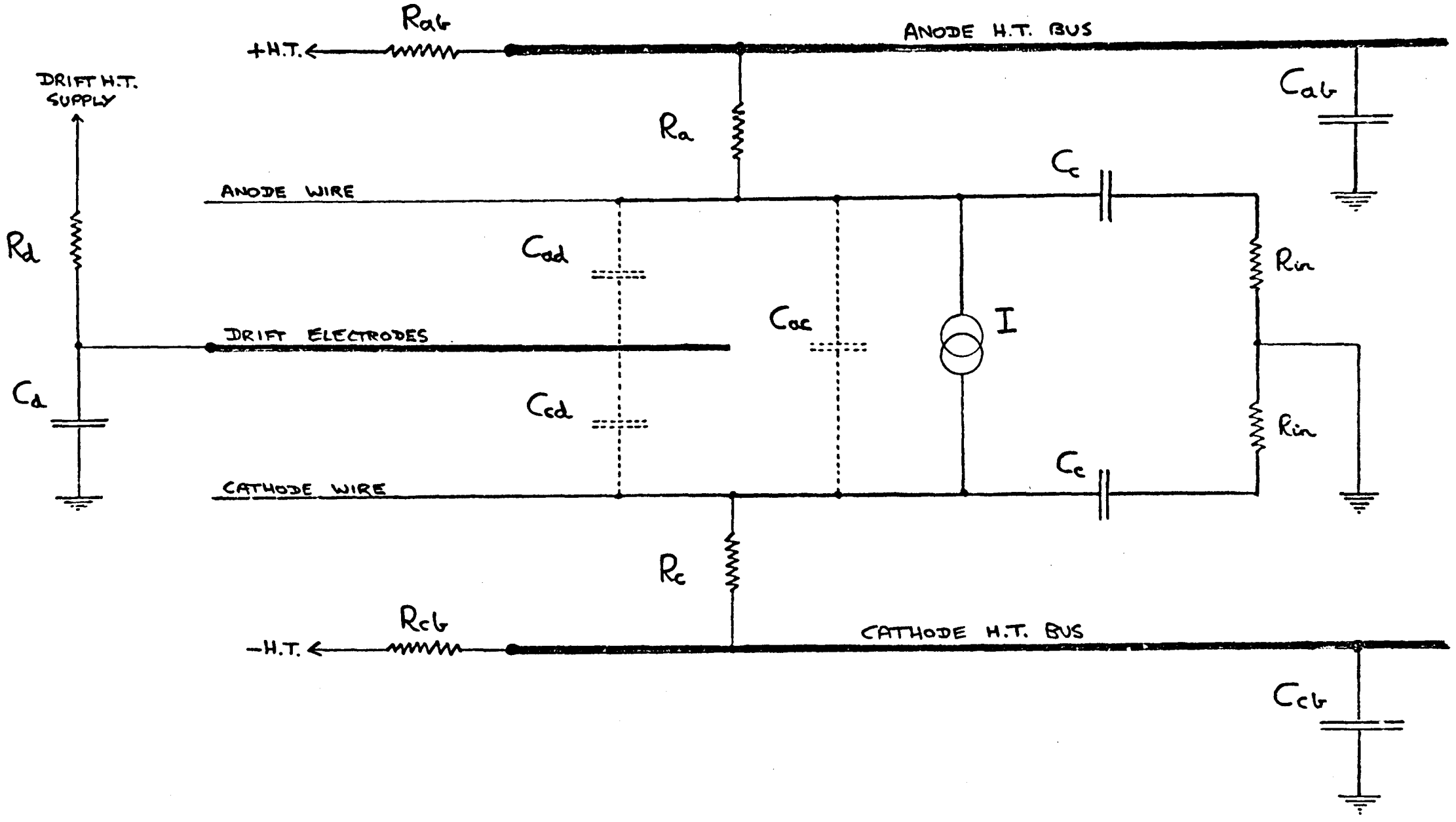


FIGURE III.5 EQUIVALENT CIRCUIT OF THE CHAMBER ELECTRODE AND H.T. FEED NETWORK.

where Z_{ab} is the parallel combination of R_{ab} and C_{ab}, and Z_{in} is the series combination of R_{in} and C_c.

With R_{ab} = 10 KΩ (typical power supply smoothing)

C_{ab} = 10 nF

R_{in} = 40 Ω (see later)

C_c = 1000 pF (see earlier)

R_a = 100 KΩ

then $\frac{\Delta Q}{Q_s} \simeq 0.2\%$ at 10 KHz, and this improves to 0.002% at 100 KHz. The same is true with the appropriate substitutions for the coupling through the cathode bus. So even with highly time-correlated signals on all (320) channels, the effective cross-talk will be below 1% at signal frequencies ($\tilde{\sim}$1 MHz).

Capacitative coupling between adjacent channels will be of strength approximately

$$\frac{\Delta Q}{Q} \approx \frac{C_{ac}}{C_c}$$

This is not greater than ∿0.7% which is tolerable (see III.2).

The Noise Equivalent Circuit of the Front End

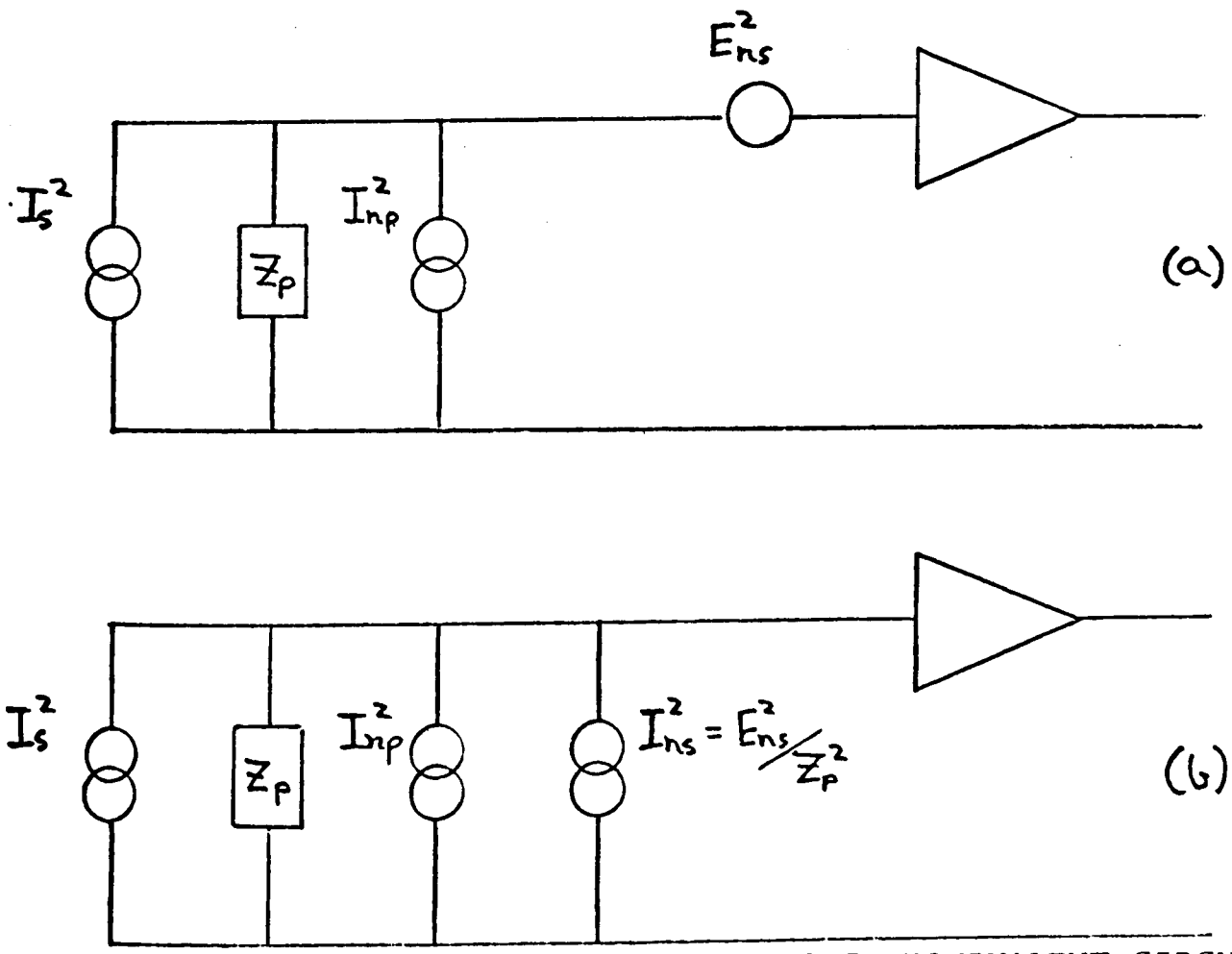


FIGURE III.6 GENERALIZED INPUT NOISE EQUIVALENT CIRCUIT.

In general, the equivalent noise in the input circuit due to an amplifier may be completely represented by the configuration shown Fig. III.6(a). Here I_{np} and E_{ns} are amplifier equivalent parallel current and series voltage noise generators, and I_s is the equivalent signal source noise current generator, all three quantities per root bandwidth. If Z_p is the parallel impedance, the E_{ns} may be replaced by an equivalent parallel current generator of strength $I_{ns} = \frac{E_{ns}}{Z_p}$ as in Fig. III.6(b) [IRE60].

The total noise is then:

$$I_n^2 = I_s^2 + I_{np}^2 + \frac{E_{ns}^2}{Z_p^2} \quad \text{per unit bandwidth.}$$

Now I_s^2 is the noise from the resistive component R_p of Z_p

$$I_s^2 = \frac{4kT}{R_p}$$

and therefore

$$I_n^2 = \frac{4kT}{R_p} + I_{np}^2 + \frac{E_{ns}^2}{Z_p^2}$$

The noise is reduced in magnitude as Z_p (and R_p) are increased. This is in conflict with the requirement for low input impedance (see earlier).

Consider now the front end stage shown in Fig. III.7. The input common-base stage is coupled through to an emitter follower stage; this configuration is employed because of the light loading of the first stage by the second. (The resistance R_p is in fact strictly an impedance consisting of the emitter load (10 KΩ) in parallel with the chamber capacitance (∿40 pF) and h.t. charging resistors (100 KΩ) see (Fig. III.4). The emitter load resistor dominates this combination.) The amplifier equivalent noise generators are [MC73]:

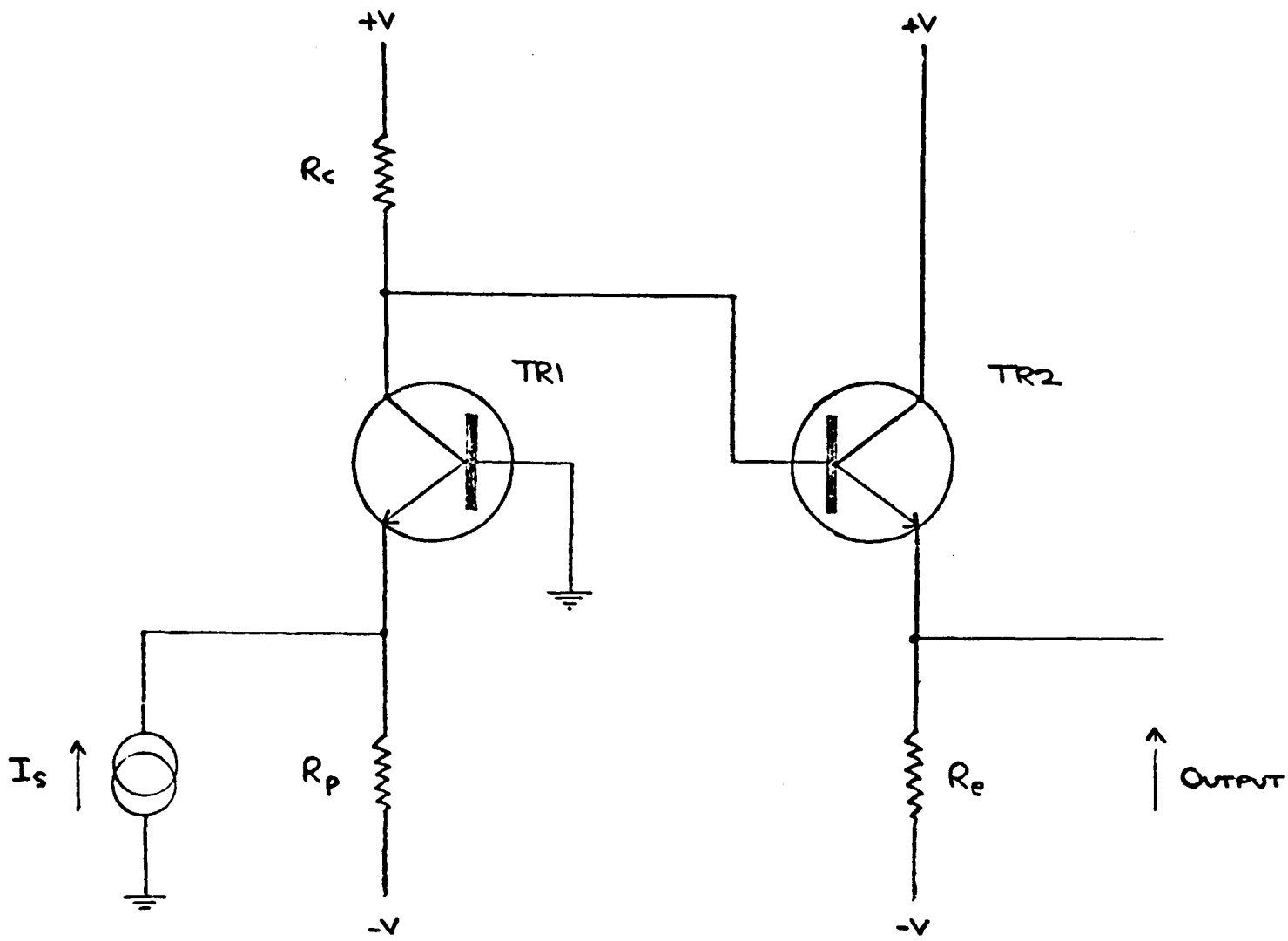


FIGURE III.7 SCHEMATIC DIAGRAM OF PREAMPLIFIER FRONT-END

$$I_{np}^2 = I_{n1}^2 + I_{n2}^2 + \frac{E_c^2 + E_{n2}^2}{R_c^2}$$

$$E_{ns}^2 = E_{n1}^2$$

in which I_{n1}, I_{n2}, E_{n1}, E_{n2} are the parallel current and series voltage noise generators for transistor TR1 and TR2 respectively. E_c is the Johnson noise from the collector load R_c. The noise from the emitter follower stage has to be included: the full equivalent current noise from the second stage transistor appears at the input. Noise from later stages is, however, ignored.

In the mid-band region, ($1KHz \lesssim f \lesssim {}^{f_T}/_{10}$), I_n is dominated by the base current shot noise:

$$I_n^2 = 2qI_B = 2q\frac{I_e}{\beta} = \frac{2kT}{\beta r_e}$$

whre r_e is the dynamic emitter resistance [ZA70], [BM74]. E_n has two components: the Johnson noise of the base resistance r_b, and the collector current shot noise, developed across the dynamic emitter resistance r_e.

$$E_n^2 = 4kTr_b + 2qI_cr_e \qquad \text{[ZA70], [BM74]}$$
$$= 4kTr_b + 2kTr_e$$

Thus for small I_n and E_n, it is best to operate with high β transistors at low collector currents.

Substituting them in the formula for the total noise equivalent (still per unit bandwidth):

$$I_n^2 = 2kT\left[\frac{1}{\beta_1 r_{e1}} + \frac{1}{\beta_2 r_{e2}} + \frac{2}{R_c}\left(1 + \frac{r_{b2}}{R_c} + \frac{r_{e2}}{R_c}\right)\right.$$
$$\left. + \frac{2}{R_p}\left(1 + \frac{r_{b1}}{R_p} + \frac{r_{e1}}{R_p}\right)\right]$$

where the subscript numerals denote the transistors.

Since $r_b \ll R_c, R_p$ this reduces to:

$$I_n^2 = 2kT\left(\frac{1}{\beta_1 r_{e1}} + \frac{1}{\beta_2 r_{e2}} + \frac{2}{R_c} + \frac{2}{R_p}\right)$$

With: $\beta = 100$ (typical values)

$r_b = 10\Omega$

$R_p = 10\ K\Omega$

$R_c = 6\ K\Omega$ (optimum values found in

$r_{e1} = 40\Omega$ practice: see later)

$r_{e2} = 30\Omega$

The equivalent input noise current per root bandwidth is

$$I_n^2 = 2kT\left(\frac{1}{4000} + \frac{1}{3000} + \frac{1}{3000} + \frac{1}{5000}\right)$$

or $$I_n = 3.0 \times 10^{-12}\ A/\sqrt{Hz}$$

It may be seen that the contributions to the total noise are roughly equal.

Assuming the noise is white (a reasonable assumption in the mid-band region) the r.m.s. input current noise of the preamplifier over an equivalent square bandwidth of 18 MHz is (multiplying by $\sqrt{2}$ to get a result for the two differential input stages),

$$I_{r.m.s.} = 18.0 \text{ nA}$$

This compares with the measured equivalent input noise of $I_{r.m.s.} = 15.5 \pm 1.6$ nA Considering the assumptions made (about the β of the transistors in particular) this agreement is good.

The SNR situation in proportional counter preamplifiers is reviewed in [RV74]. It is shown that the low noise limit is determined by the series noise of the amplifying device: the parallel noise may in principle be made negligible by the use of feedback. The minimum equivalent noise current is:

$$I_n^2 = \frac{e_n^2 C_{in}^2}{t_m^3}$$

where C_{in} is the detector capacitance

e_n is the r.m.s. equivalent series noise for the first stage amplifying device, in $V/\sqrt{Hz}$

and t_m is the half-width of the (assumed triangular) system weighting function ($\tilde{\sim}$system risetime).

For the better bipolar transistors and F.E.T.'s,

$$e_n \tilde{\sim} 10^{-9} \text{ V}/\sqrt{\text{Hz}}$$

$$C_{in} \tilde{\sim} 40 \text{ pF}$$

and $$t_m \tilde{\sim} 30 \text{ nS}$$

This gives $I_n \tilde{\sim} 6$ nA, which is about 6dB lower than the previously calculated figure. The design used in the prototype is thus not too far away from optimum.

The broadband current amplifier of [MJ74], has a r.m.s. noise of 7 nA over the same bandwidth on the prototype preamplifier, but the circuit is much more complicated.

Brief Description of the Prototype Preamplifier

The circuit diagram of the prototype preamplifier is shown in Fig. III.8, and a photograph of the unit is on the following page. Because of the large numbers (∿320) of preamplifiers required, consideration has to be made of factors such as reliability, expense, long-term stability and susceptibility to component fluctuations. The design described is simple yet efficient.

The common base input stage feeds an emitter follower as described earlier. The output from this is coupled into a low noise high gain broadband (16 MHz bandwidth) integrated amplifier (μA733). As the preamplifiers are located next to the chamber, the output from this amplifier is fed into emitter followers, which are capable of driving 50Ω cables in push-pull to the remote electronics.

The first two transistors in each input are low-noise, high β U.H.F. silicon planar transistors (Ferranti ZTX 325, Minimum f_t = 1 GHz). The current-to-voltage conversion occurs at the collector loads of the common base stages. The value of the load is ∿6KΩ, depending on the setting of the 1 KΩ differential gain balance trimming potentiometer. (This allows a ±10% control over the differential gain.) The use of a higher collector load resistance is not possible because the parallel stray capacitances (of just one or two pF) form a time constant with the load which can seriously limit the bandwidth.

The values of 10 KΩ and 8.2 KΩ for the emitter resistors of the first two transistors in each input were found by experiment.

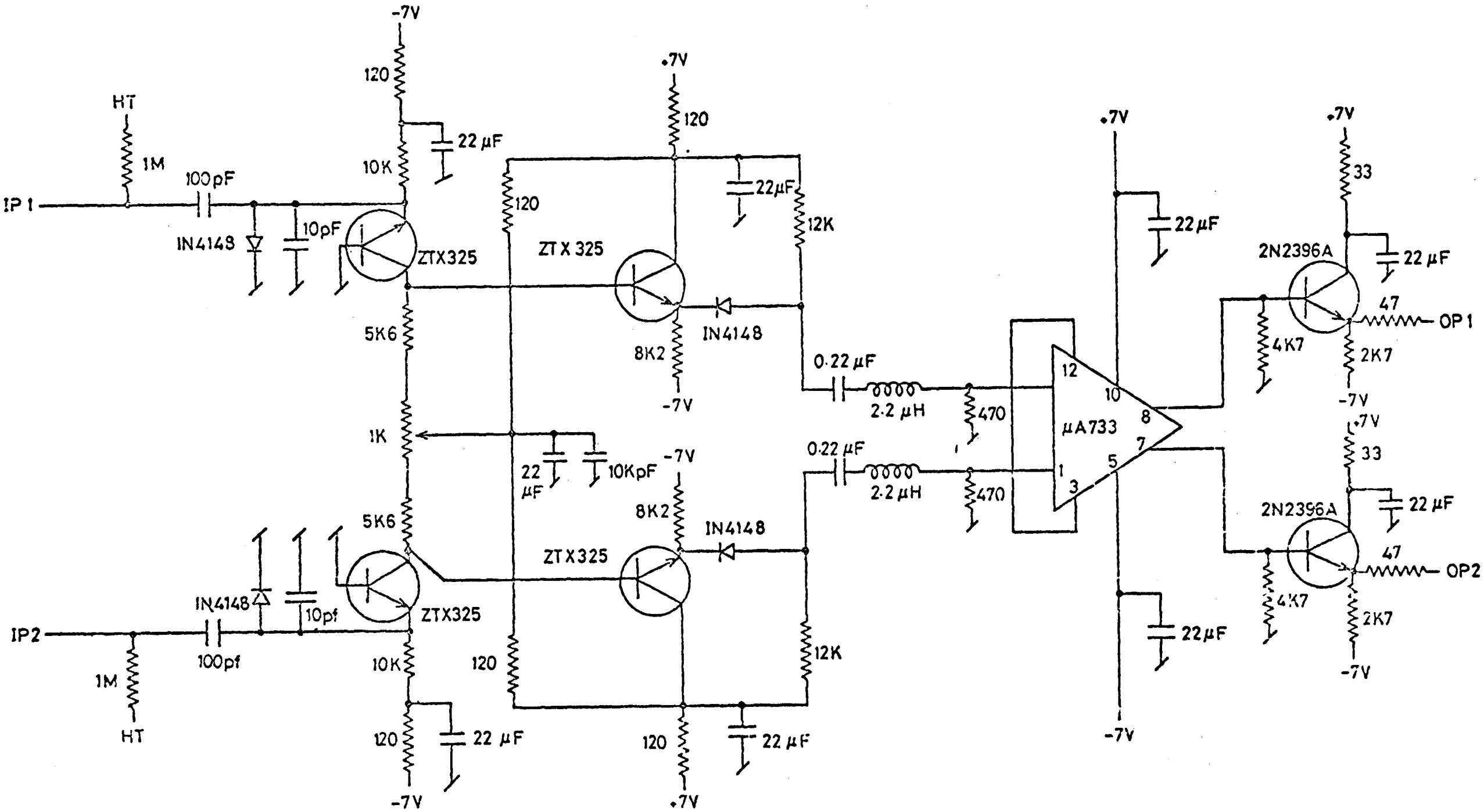
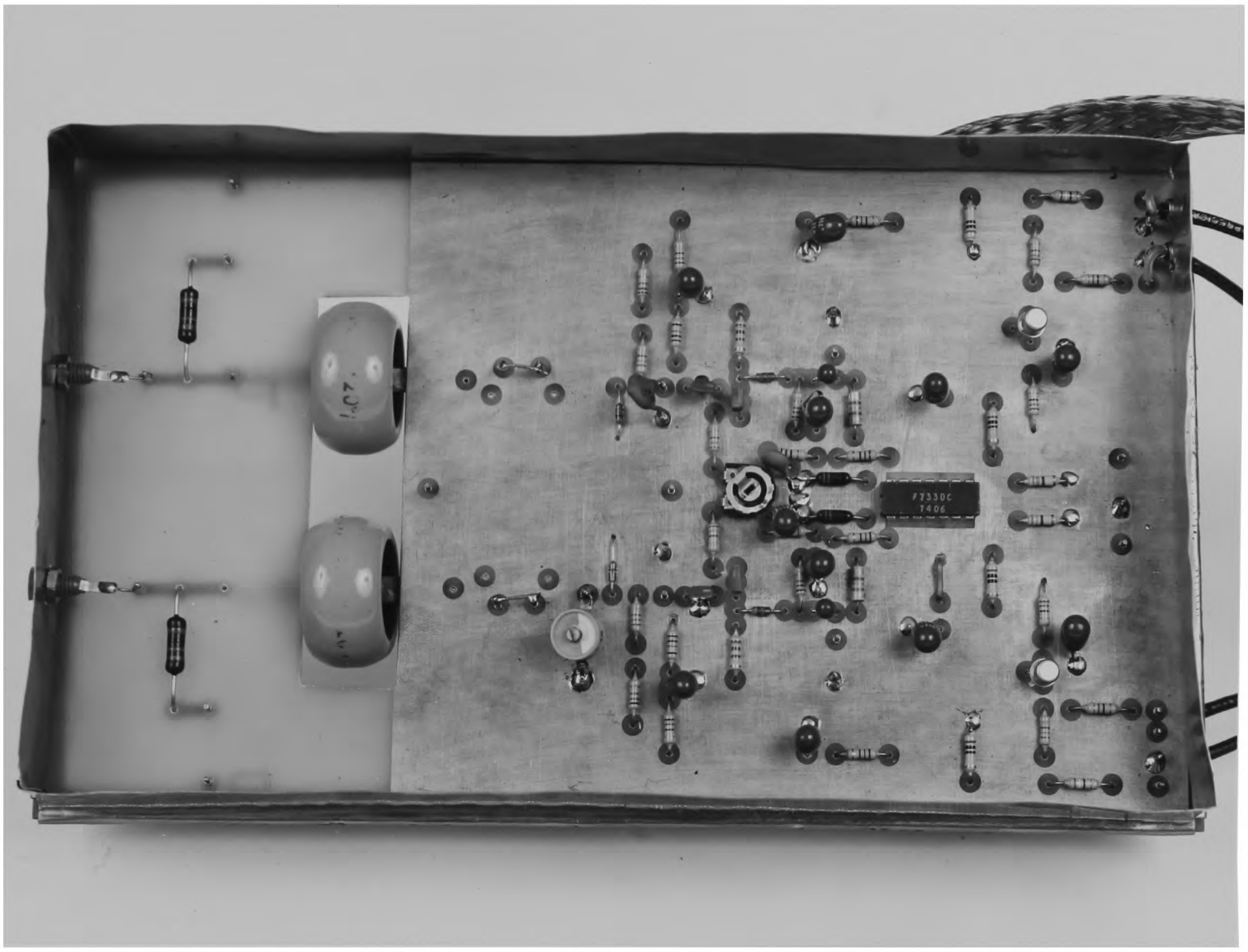
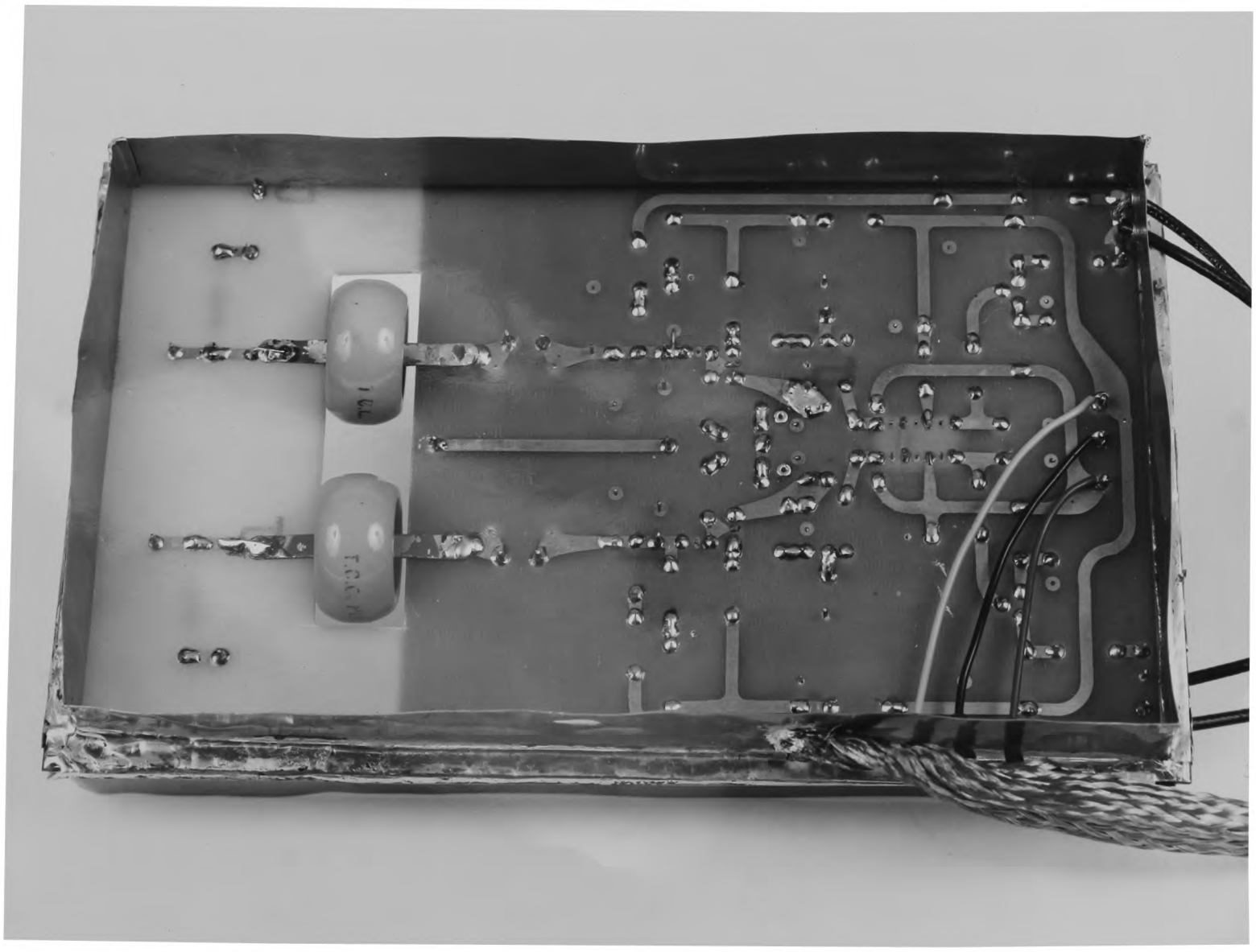


FIGURE III.8 CIRCUIT DIAGRAM OF THE PROTOTYPE PREAMPLIFIER


F7330C
T406



This choice gives a minimum in the input noise for a preamplifier rise time of 30 nS, when connected to an equivalent chamber capacitance of 40 pF.

Shown at the input are the h.t. feeder resistors (1 M) and coupling capacitors (100 pF), which were used in the tests described in Chapter IV. The inputs are protected against transients by the IN4148 diodes. Additional limiting circuitry around the output of the second transistor results in a gas-gain-switching-transient amplifier recovery time to 0.5% of about 1.2 mS.

The gain of this preamplifier is such that a 1 μA signal into one input produces a differential output of 160 ± 1 mV into 50Ω. The risetime and fall times were measured to be 33 ± 3 nS. The lower limit to the bandwidth is determined by the 100 μS coupling time constant associated with the input circuit. The equivalent input noise is 15.5 ± 1.5 nA over an equivalent square bandwidth of 18 ± 2 MHz. Linearity was better than 1% up to 30 μA input current.

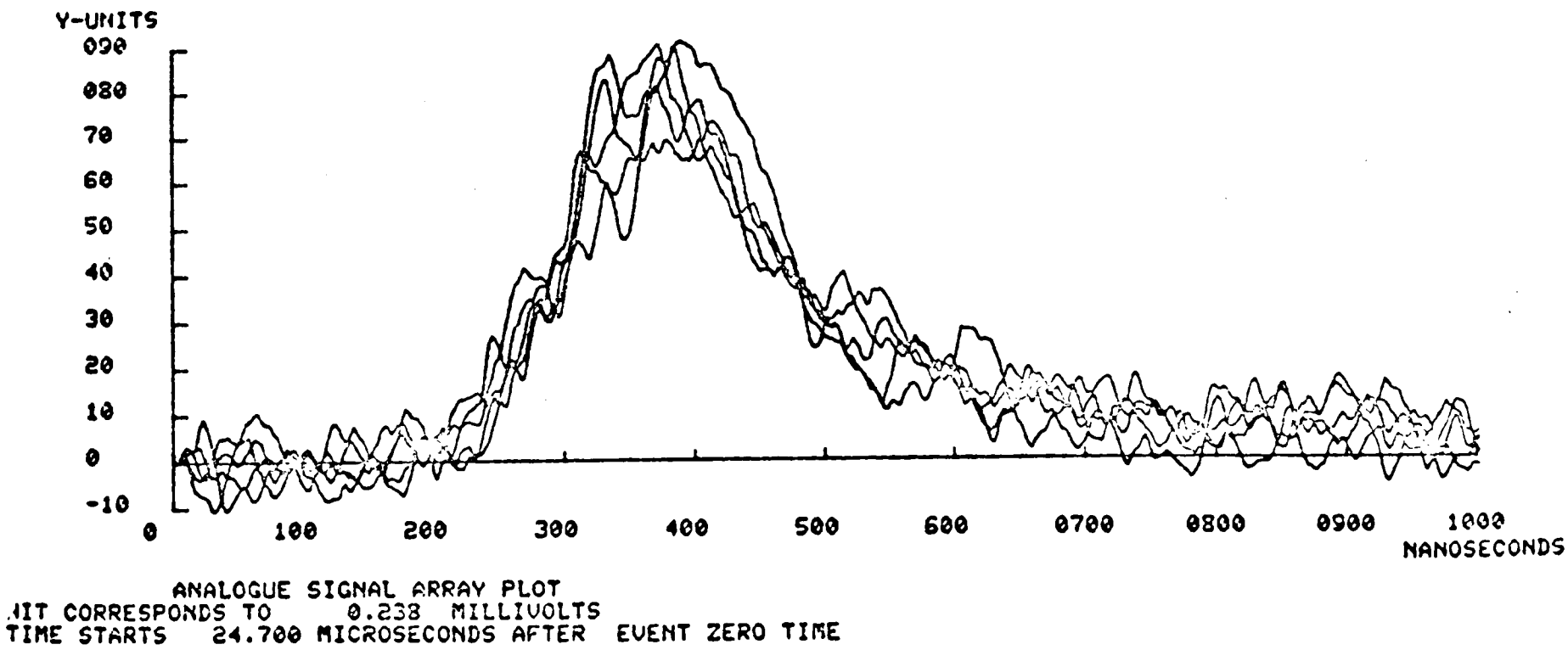


FIGURE III.9 TYPICAL PREAMPLIFIER OUTPUT SIGNALS + NOISE SIMULATED:

Typical signals will produce differential outputs of between 10 and 300 mV into 50Ω, the noise being at 2.4 mV r.m.s. The preamplifier output for a track sample of 100 electrons ($\Delta E \tilde{\sim} 2.6$ KeV) after a 1 m drift is shown in simulation in Fig. III.9 (with real noise level) and Fig. III.10 (without noise).

Some Considerations Regarding the Main Amplifier

The purpose of the main amplifier is to receive the output from the preamplifiers and to transform it without distortion to a level suitable for later stages of the system. The response of the main amplifier needs to be flat, but the bandwidth need not be higher than that of the preamplifier. The main amplifier should be d.c. coupled, and should contain a variable gain element to allow for correction of slight inter-channel variations in gain due to component tolerances for instance.

The cable connecting the preamplifiers to the main amplifiers should not be ignored. This will have a certain risetime, which must be taken into account in any description of the electronics.

A brief discussion of the prototype main amplifier is included in III.3.

III.3 PULSE SHAPING

Pulse shaping comprises an important section of the signal processing chain: the properties of the signal obtained at the preamplifier output may be enhanced by the application of suitable pulse shaping. To determine the characteristics of shaping required, the unaltered signal shape and SNR must be compared with an ideal shape and the resultant SNR.

The required pulse shape is one from which can be obtained:

(i) a presence-of-track trigger signal (see III.5) and

(ii) a pulse integral accurate to the 1% level (see III.4).

The performance in both these aspects must be pulse-shape and rate-independent to a high degree: the mean time between pulses is comparable with the primary signal duration (ionization collection time).

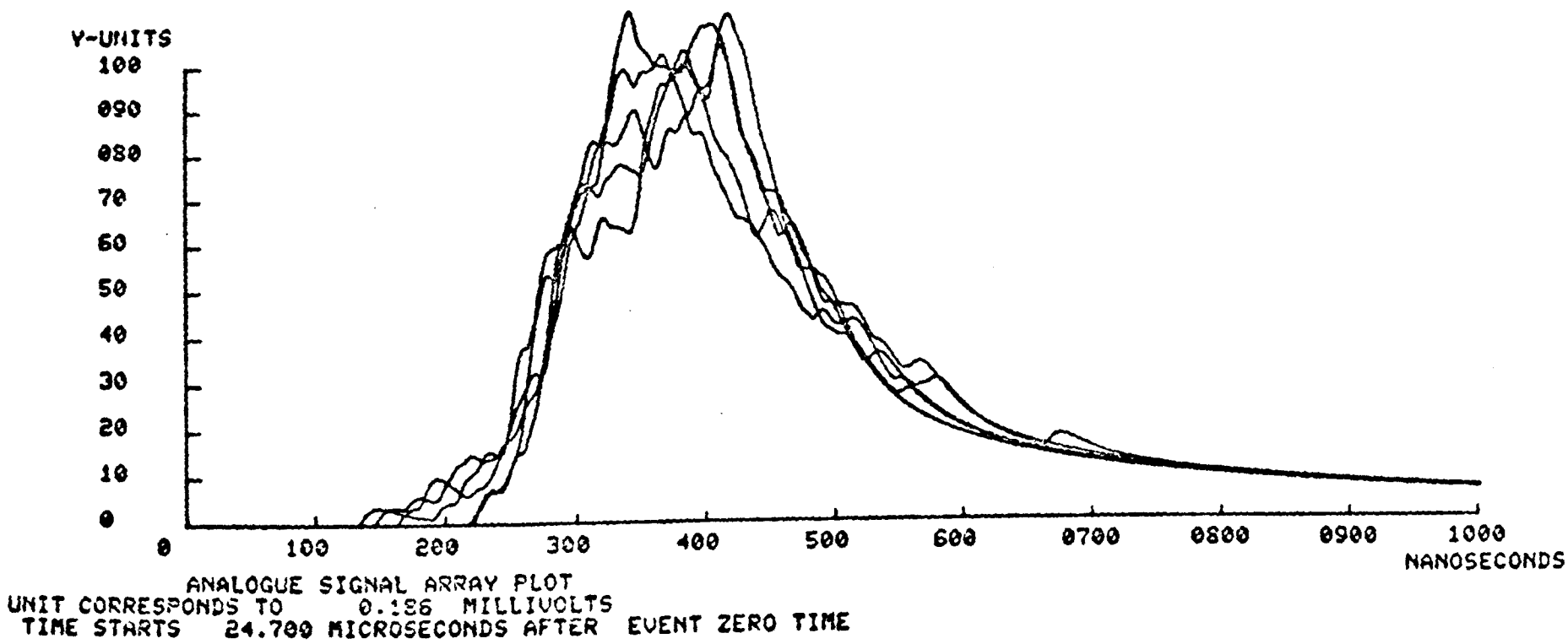


FIGURE III.10 TYPICAL PREAMPLIFIER OUTPUT SIGNALS, LESS NOISE, SIMULATED: 100 ELECTRONS, DRIFTING 1m, GAS GAIN 10^4

Preamplifier Output Signal

Typical preamplifier output pulses (simulated, without noise) are shown in Fig. III.10 for 100 electrons, (ΔE = 2.6 KeV) drifting 1m at a gas gain of 10^4. The pulses are not short: the decay of the pulses is dominated by the $^1/t + t_o$ tail of the gas amplifier response (see II.3). This leaves a memory of the pulse in the electronics lasting for several microseconds, or many centimetres, in terms of drift distance.

This pulse shape would give very poor performance in the two aspects stated above. This would be especially noticeable on signals from tracks arriving at the wire plane within a short time of each other, as shown in Fig. III.11 (simulated, without noise, for 100 electrons (2.6 KeV) each track, drifting from 1.00 m and 1.02 m at a gas gain of 10^4).

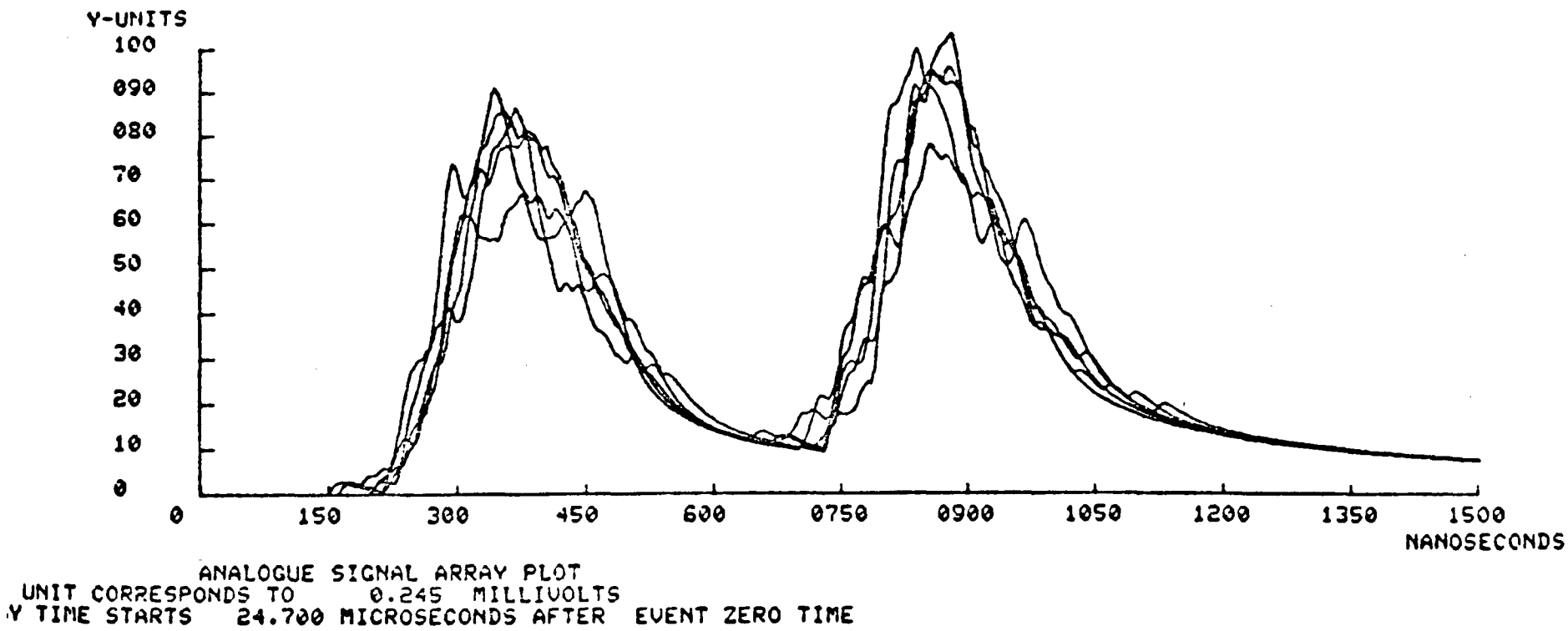


FIGURE III.11 SIMULATED TWO TRACK SIGNAL

A simple discriminator looking at this signal might not re-trigger on the second track. The gated integral of the second track would be systematically large: this is very bad. The integral of

the first would also have errors on it due to the jitter of the integration gate closing on the non-zero signal.

Clearly, the signal must be shaped so that it returns to zero as quickly as possible, for then the integration gates would shut off on zero signal with no error on the integral. The second pulse would also be well resolved as a result.

Pulse Shaping Required

There has been much published work on pulse shaping e.g. [GA53], [GF72], [RV74]. However, most of this is related to optimum SNR's in systems requiring the best signal magnitude resolution (0.05%), when the mean time between pulses and the time available for measurements are long compared with primary signal duration. In ISIS the pulse shaping must allow instead pulse magnitude measurement with reasonable (1%) errors but at the highest rates, where the mean time between pulses is comparable with the primary signal duration.

The pulse shaping required is the removal of the long tail from the gas amplifier response, by a suitable choice of high-pass filter. This would reduce specific low-frequency components associated with the tail. Since low systematic errors (<1%) are required, this process must be done accurately. The amplitude of the signal must return to the baseline as fast as possible and remain there to a high degree of precision.

Simple unipolar pulse-shaping involving differentiation and integration by a short (but equal) time constant CR-RC shaper [GA53] does not produce a good enough result. This is because of the $^{1}/t + t_{o}$ characteristic of the tail, and because of the inherent noisy variation in pulse shape. Bipolar shaping is rejected on similar grounds.

It has been found that the most efficient shaping is obtained with the use of a network which sums the original signal with appropriate amounts of several other signals, derived from the original by RC differentiation but with different time constants. The principle may be seen by inspecting Fig. III.12 (a)-(e). The original signal shape is shown in (a). In (b), (c) and (d) are shown differentiated signals with progressively shorter time constant RC networks. These four are added in the appropriate proportions to produce a signal of the required shape, shown in (e).

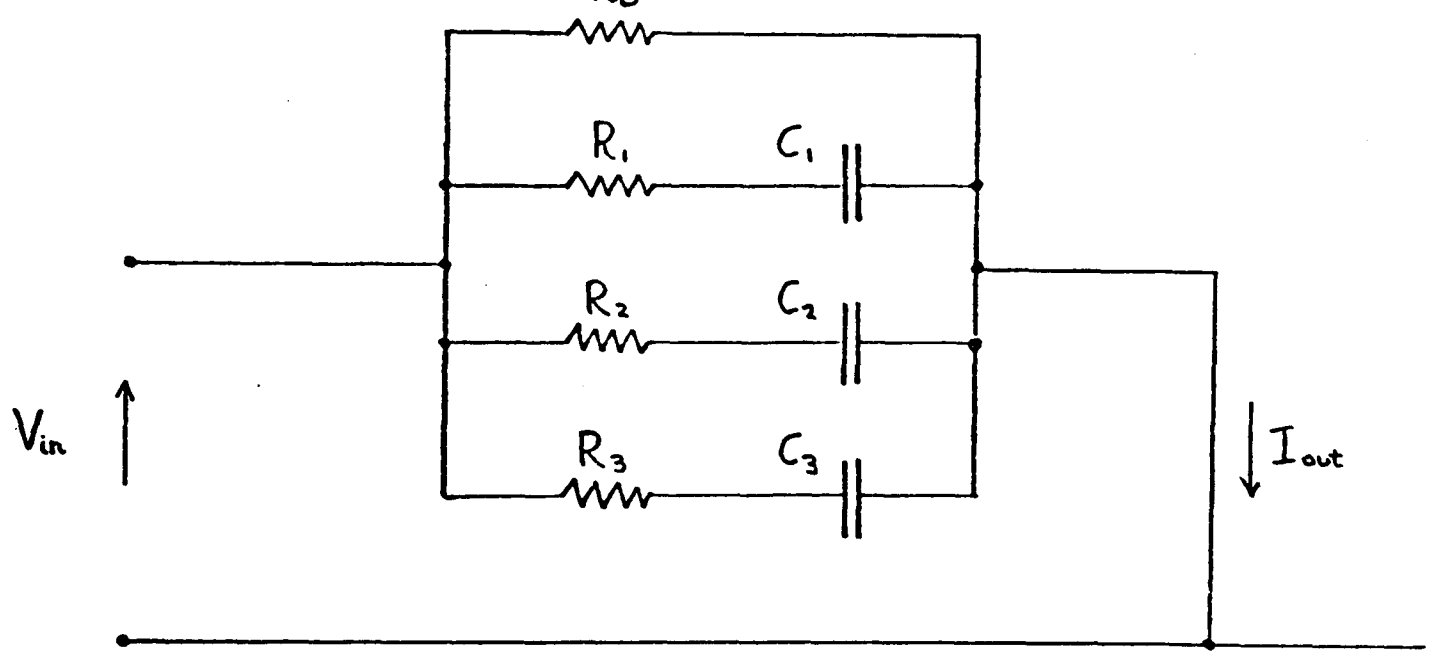
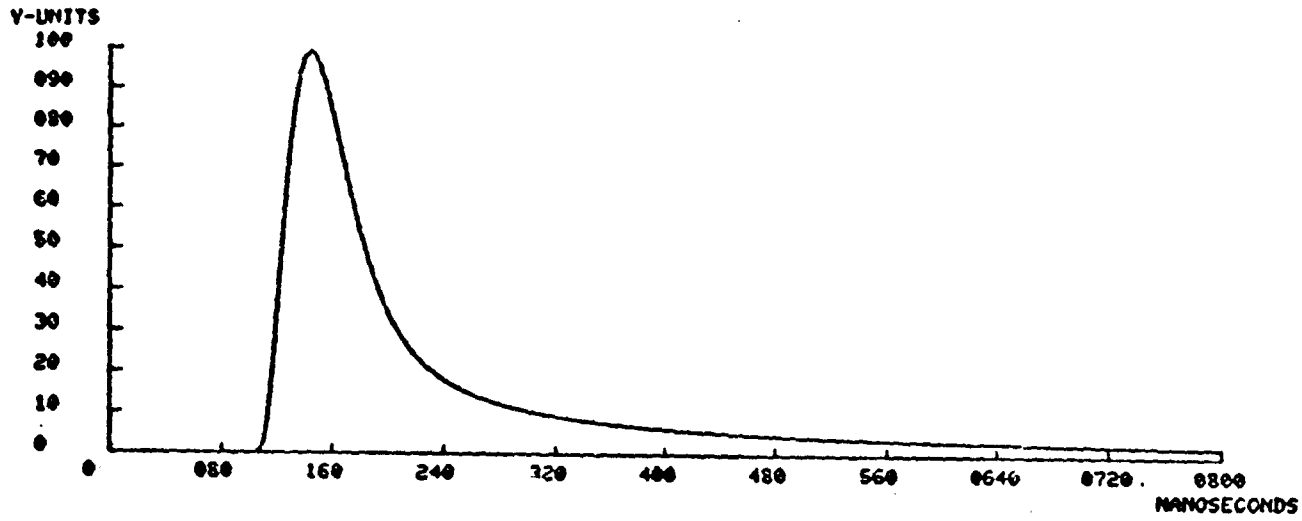


FIGURE III.13 PULSE SHAPING NETWORK

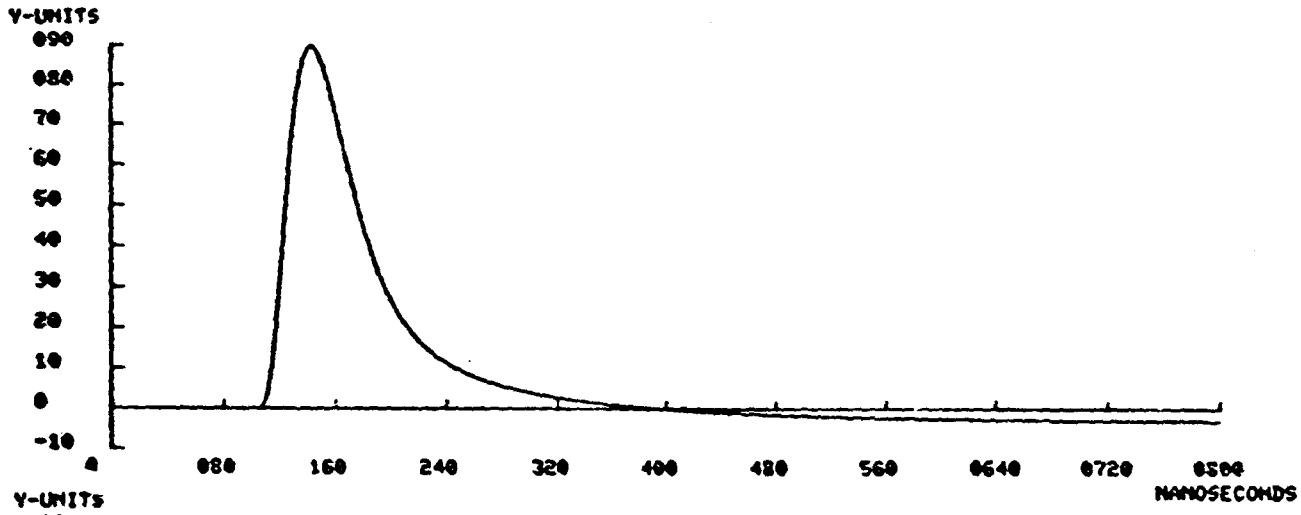
The shaping network used for this is passive, linear, simple and cheap: it is shown in Fig. III.13. The resultant signal, in terms of Fourier components, is:

$$I_{out}(\omega) = \frac{1}{R_o} + \frac{1}{R_1 - j/\omega C_1} + \frac{1}{R_2 - j/\omega C_2} + \frac{1}{R_3 - j/\omega C_3} \quad V_{in}(\omega)$$

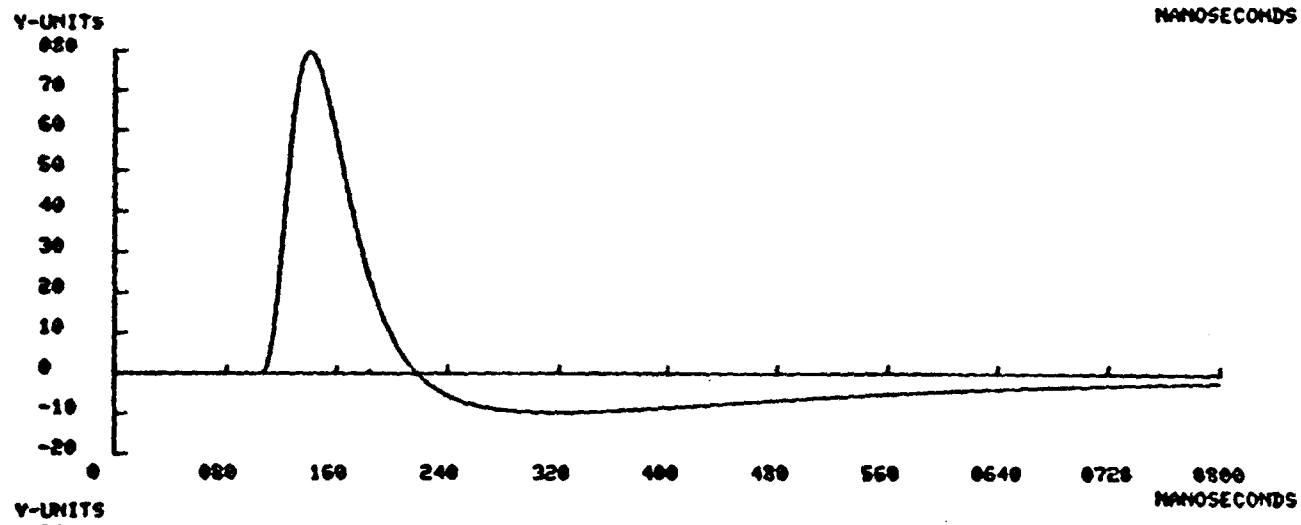
Three time constants are needed, to produce the right pulse shape over a range of 30 nS to a few microseconds, accurate to the 1% level, and R_o is needed as a form of pole-zero cancellation.



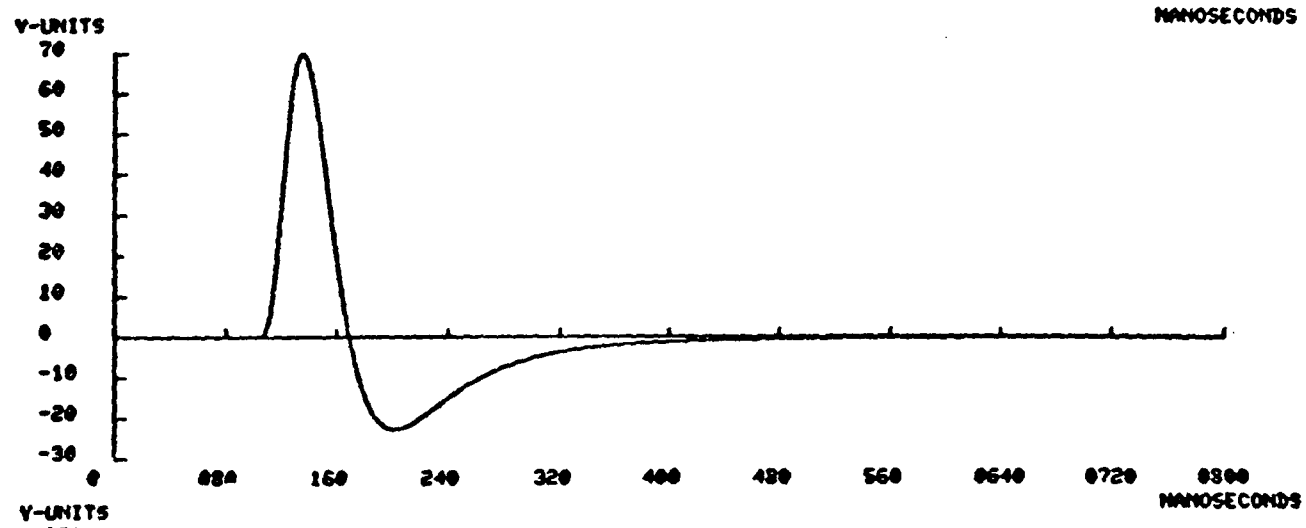
(a)
Unshaped
signal



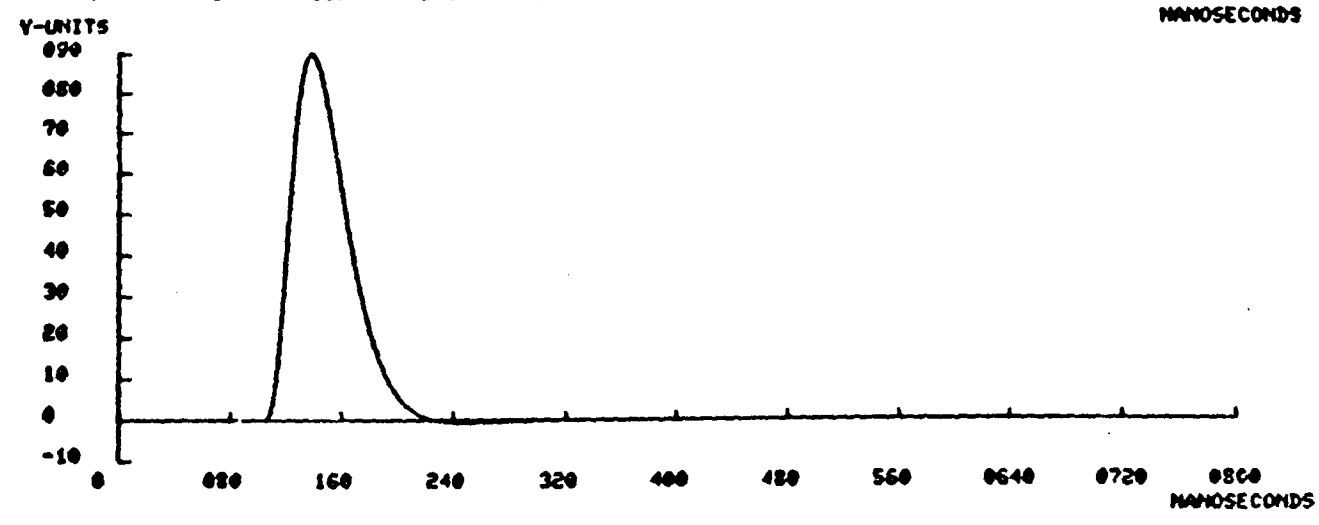
(b)
τ = 1100 nS
Diff^{n}.



(c)
τ = 190 nS
Diff^{n}.



(d)
τ = 30 nS
Diff^{n}.



(e)
Resultant
Shaped
Signal

FIGURE III.12 DIFFERENTIATED SIGNALS USED IN PULSE SHAPING.

This high-pass filter has a low-frequency-limit response ($\omega << {}^{1}/R_nC_n$) of $I_{out} = \frac{1}{R_o} V_{in}$. The high-frequency-limit response ($\omega >> {}^{1}/R_nC_n$) is $I_{out} = (\frac{1}{R_o} + \frac{1}{R_1} + \frac{1}{R_2} + \frac{1}{R_3}) V_{in}$. Response at intermediate frequency is determined by the time constants $\tau_n = R_nC_n$ and the amplitudes, proportional to ${}^{1}/R_n$.

Design of the Pulse Shaping Network

The problem of the choice of the R_n and τ_n was solved computationally. Using the simulation method described in IV.1 and Appendix 4, a model of the entire signal processing system was set up to look at the single electron ('impulse') response. All the appropriate values for the parameters of the gas amplifier response and electronic response were used, as enumerated in Appendix 4. (Since only the pulse shape is interesting, the noise and the stage gains were not included.) With the assumption that the system is linear, a result which is the best response for a single electron impulse will also be the optimum for the sum of impulses in a multi-electron signal. Consequently, the ballistic coefficient of the shaper will be the same for all pulses. The impulse response of the system without shaping looks like Fig. III.14(a).

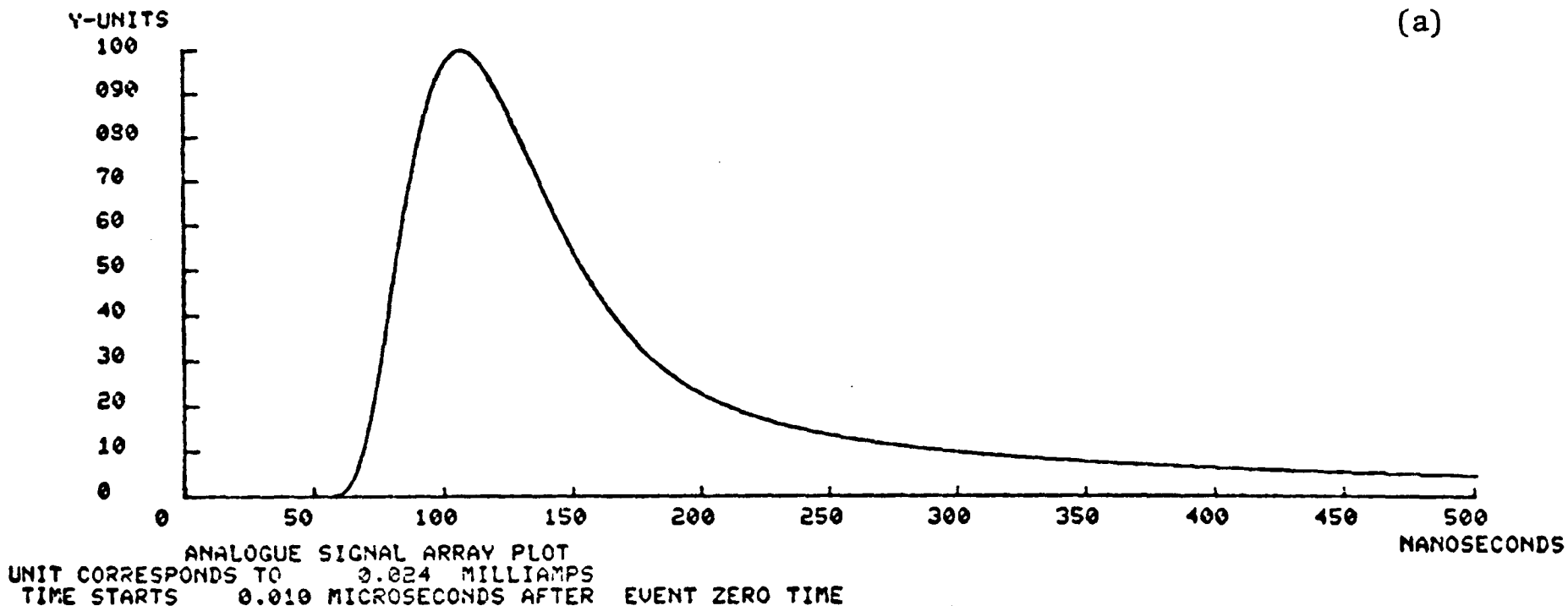
The required response is one which has:

(i) Minimum pulse integral after a certain, short, time of about 150 nS,

(ii) Slight overshoot of $\sim$0.2% to ensure that the discriminator fires off (see III.5),

(iii) Minimum loss of SNR, although this is less important.

A pulse shaping performance function was defined which evaluated the shape of the output signal using the above criteria. The parameters τ_n and $^1/R_n$ of the shaping network were made the dependent variables of a minimization routine within the program which hunted for a best performance using the defined performance function. The result of this procedure was a design of shaping network producing the almost-symmetric output signal shown in Fig. III.14(b).



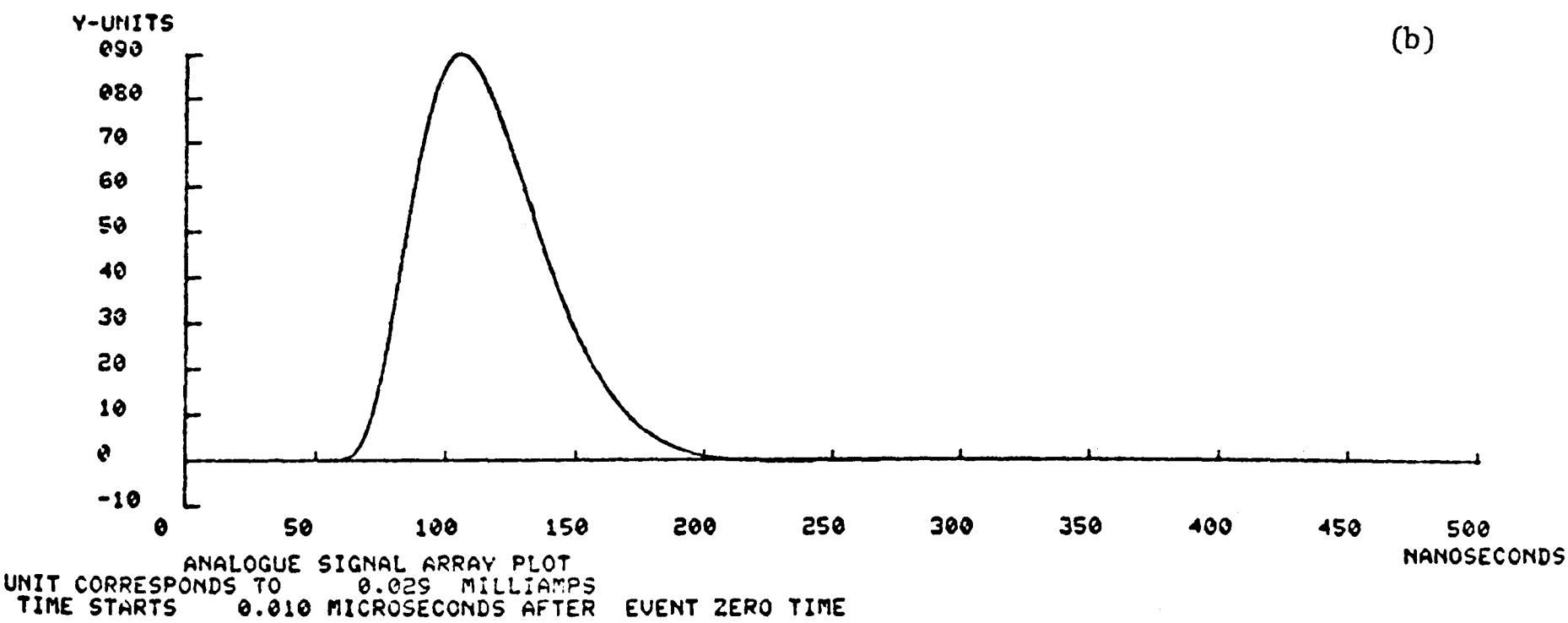


FIGURE III.14 SYSTEM IMPULSE RESPONSE

(a) Without Shaping

(b) With Shaping

The Performance of the Pulse Shaper

The parameters of the optimum pulse shaper were:-

$1/R_0 = 65\%$

$1/R_1 = 100\%$ $\tau_1 = 30$ nS

$1/R_2 = 31\%$ $\tau_2 = 190$ nS

$1/R_3 = 21\%$ $\tau_3 = 1100$ nS

The duration of the impulse response from the start to the zero crossover point was 158 nS. The amplitude of the overshoot is 0.4% of that of the main pulse. The integral of the pulse after the zero crossover (from ∿160 nS to a few μS) is 1.24% of the main pulse (from start of pulse to ∿160 nS). There is a slight reduction in SNR: for mean signals (100 electrons: 2.6 KeV, 2m drift, gas gain 10^4), the SNR drops from 29.5 dB without the shaper, to 27.5 dB with the shaper.

The effect of the pulse shaper on simulated signals can be seen qualitatively in Fig. III.15. (100 electrons each track, 1m and 1.02 m drift, gas gain 10^4.) The noise has not been included: the recovery to the baseline is good.

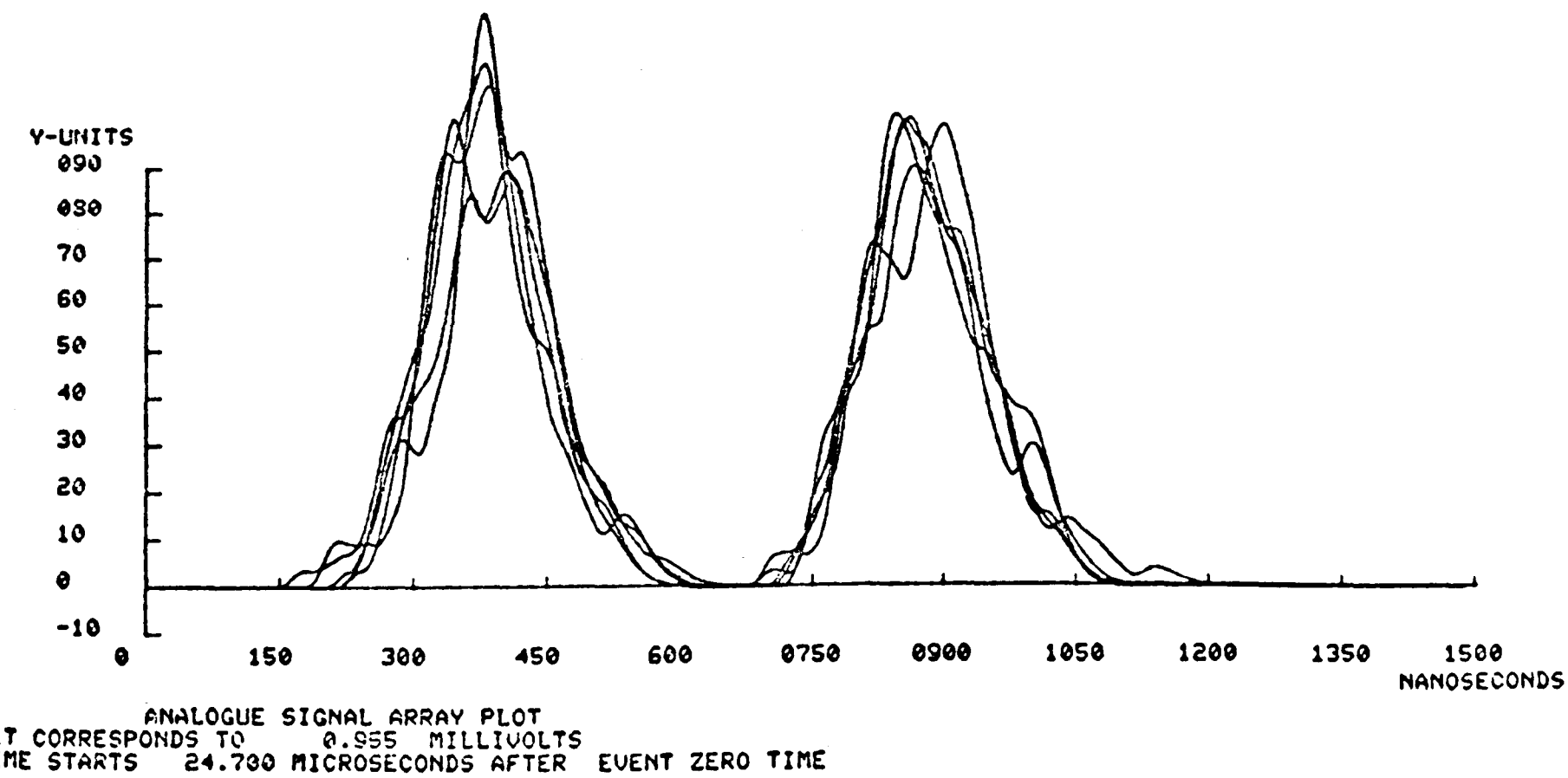


FIGURE III.15 TYPICAL PULSE SHAPER OUTPUT SIGNALS (Simulated)

Real signals using an x-ray source (see IV.3) are shown 'before' and 'after' the shaping network in Fig. III.16(a). The performance comes up to expectations, as far as can be seen on an oscilloscope.

The high-pass nature of the filter can be seen in Figs. III.16(b) and (c). In (b) is shown the frequency spectrum of unshaped gas amplifier pulses, and in (c) is shown that of the shaped pulses. The relative attenuation of frequencies below ∿1.5 MHz (∿100 nS) is quite clear. Further tests are described in Chapter IV.

The performance of the shaper to dispersed multi-electron signals was checked at the level of fractions of a percent using the simulation; it was found that the assumption of system linearity (ballistic coefficient pulse shape independence) was good for all tracks to the 0.1% level.

Tolerances on the Parameters Associated with Shaping

It is necessary to know how sensitive the quality of the operation of the shaper is to:

(a) Component variations within the shaping network

The tolerances needed on the shaper component are not tight: a ± 2% variation in any of the components does not have much effect. The most sensitive components are those associated with the shortest time constant, and the undifferentiated component through R_o. A 2% decrease in R_o increases the tail integral of the pulse by 50% from 1.24% to 1.93% of the main pulse.

(b) Gas amplifier response variation

The characteristic time constant t_o of the gas amplifier response is not known accurately. Unfortunately the shaper is not insensitive to variations of this parameter at the level of ∿20% or greater. The shaper components have been chosen

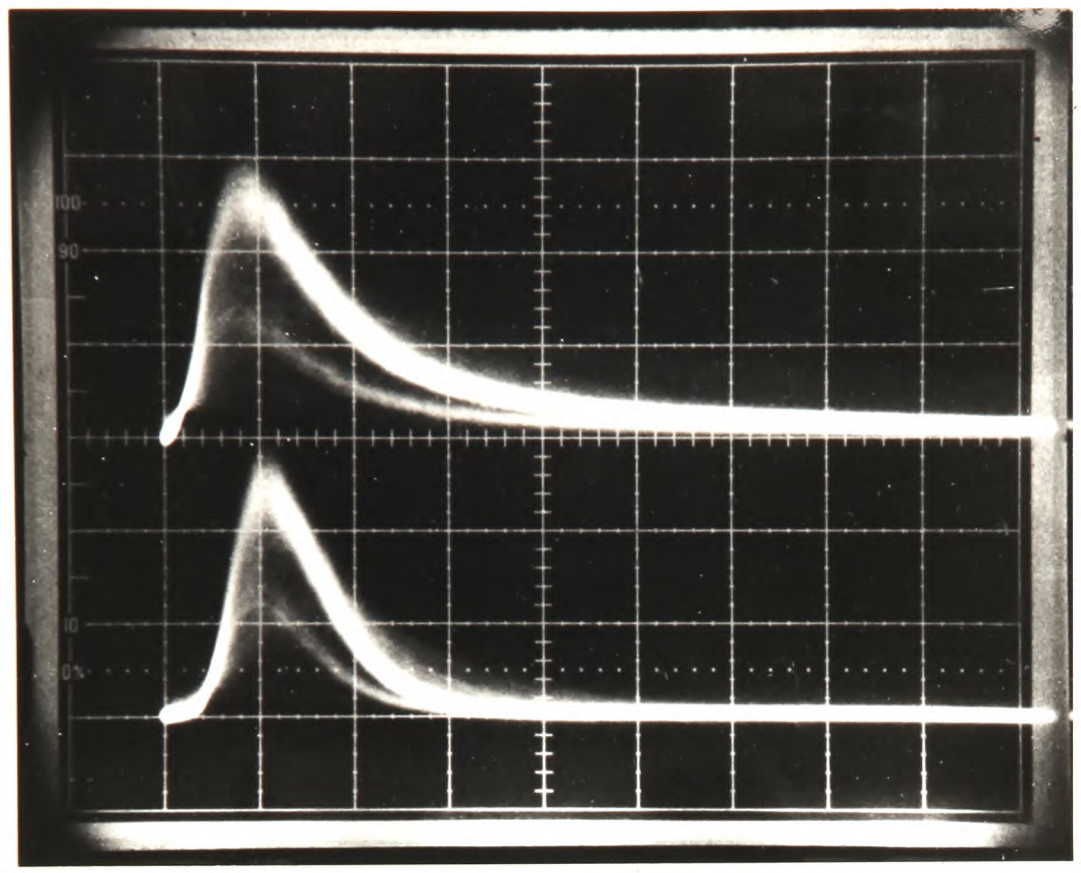


Figure III.16

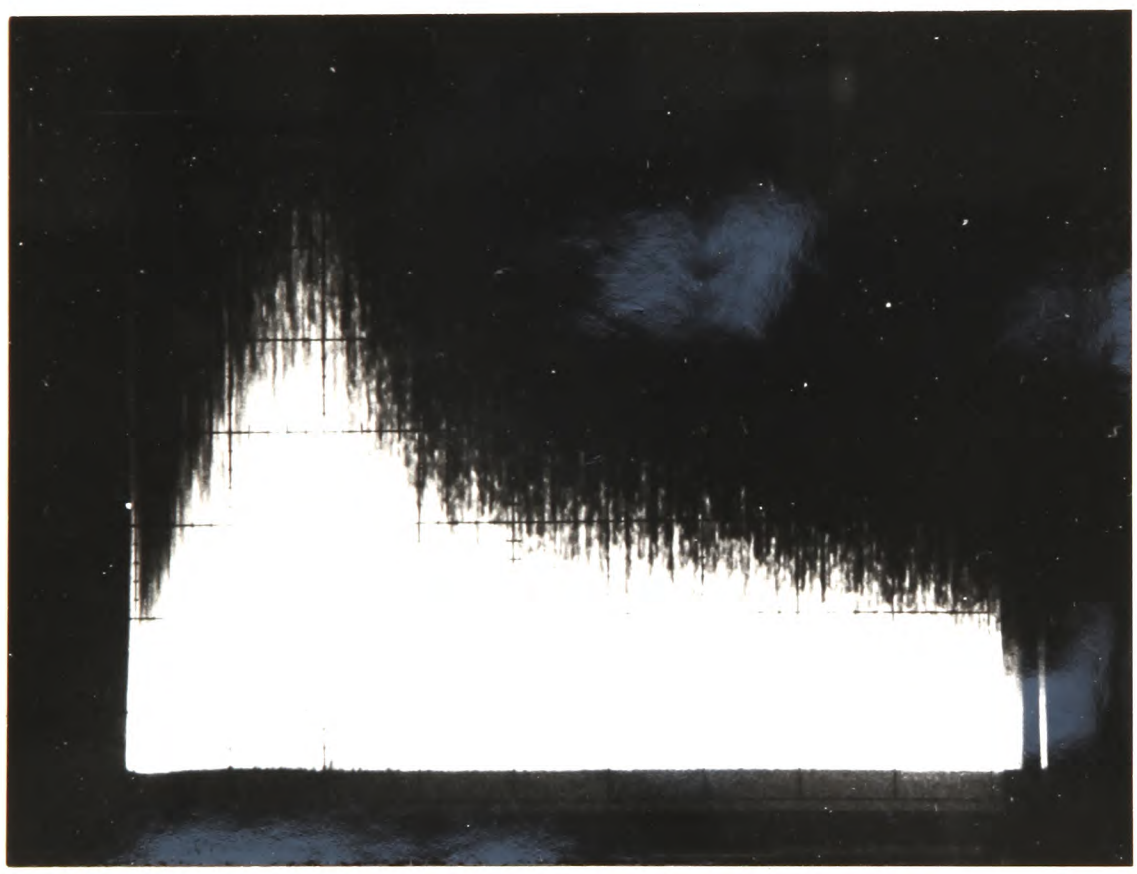
(a) Gas amplifier pulses.

Top: Unshaped

Bottom: Shaped

X: 50nS/div

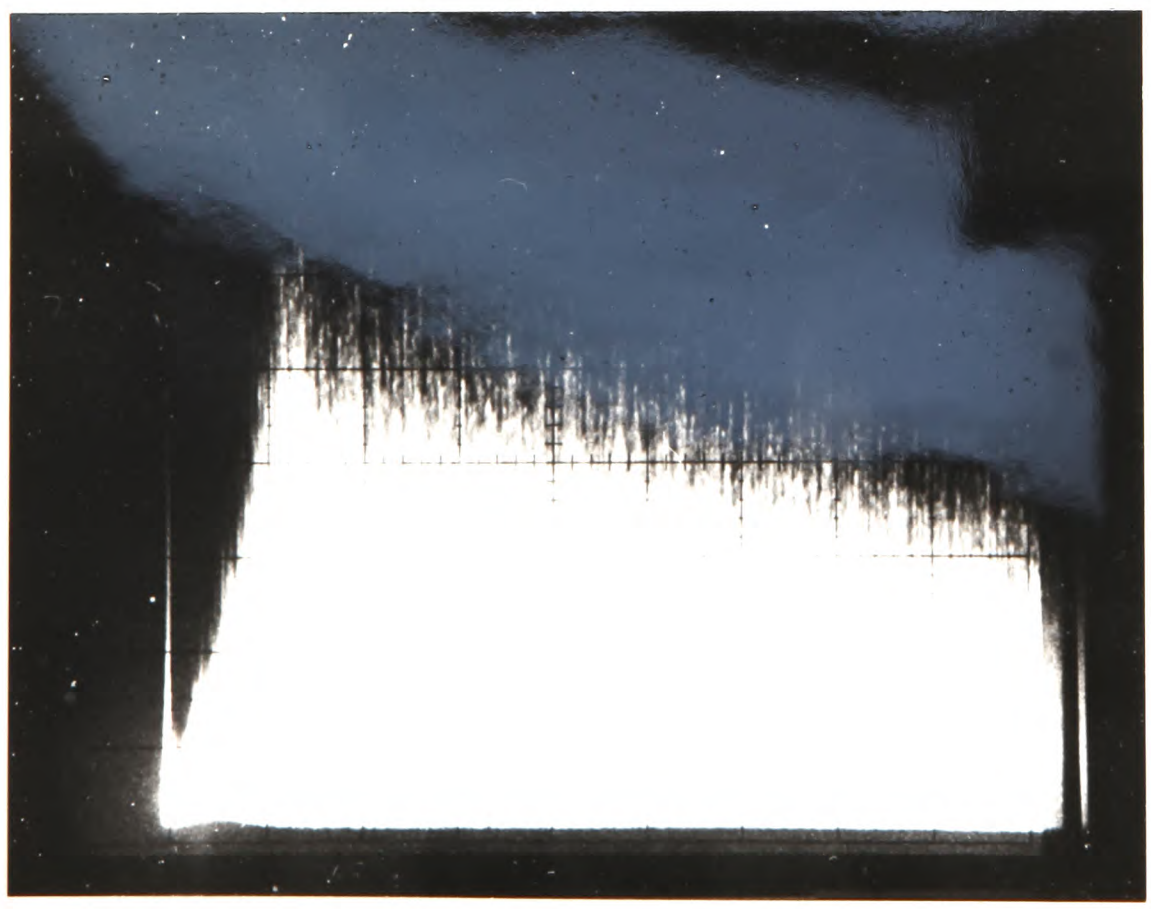
Y: Uncalibrated



(b) Frequency spectrum of unshaped gas amplifier pulses.

X: 500KHz/div

Y: Uncalibrated



(c) Frequency spectrum of shaped gas amplifier pulses.

X: 500 KHz/div

Y: Uncalibrated

for $t_o = 1.8^{+1.2}_{-0.8}$ nS, as calculated in II.3. If this is in fact 1.0 nS, the tail integral rises to 7.29% from 1.24%, and the amplitude of the overshoot becomes 1.82% instead of 0.4%. A value of t_o = 3.0 nS results in a pulse shape which does not cross zero. Further work might have to be done in this area if the value of t_o is far from that assumed.

(c) System bandwidth variation

The shaping is insensitive to a ±10% change in the main electronic risetimes which define the upper limit on system bandwidth. However, if the response of any of these elements is not an RC exponential as assumed, but is more complicated, at the 1% level, then deviations from the expected performance may occur.

If, for these reasons, the shaper performance has to be 'trimmed', (this is likely), then the most suitable single component to adjust is R_o, as this determines the compromise between time-to-crossover, and tail integral. It should be noted that the effect of D.C. baseline restoration (see III.6) is to improve the overall pulse shape characteristics.

Brief Description of Prototype Main Amplifier and Pulse Shaper

The circuit diagram of the prototype main amplifier and pulse shaper is shown in Fig. III.17. (In the final system, the pulse shaper will be in the preamplifier.)

The input to the high-bandwidth integrated main amplifier is from the differential 50Ω output of the preamplifier. The voltage gain of the main amplifier (5.63 ± 0.04) may be changed by a factor of ∿2, (from 4 → 8) using a trimming variable resistor. Coarse gain

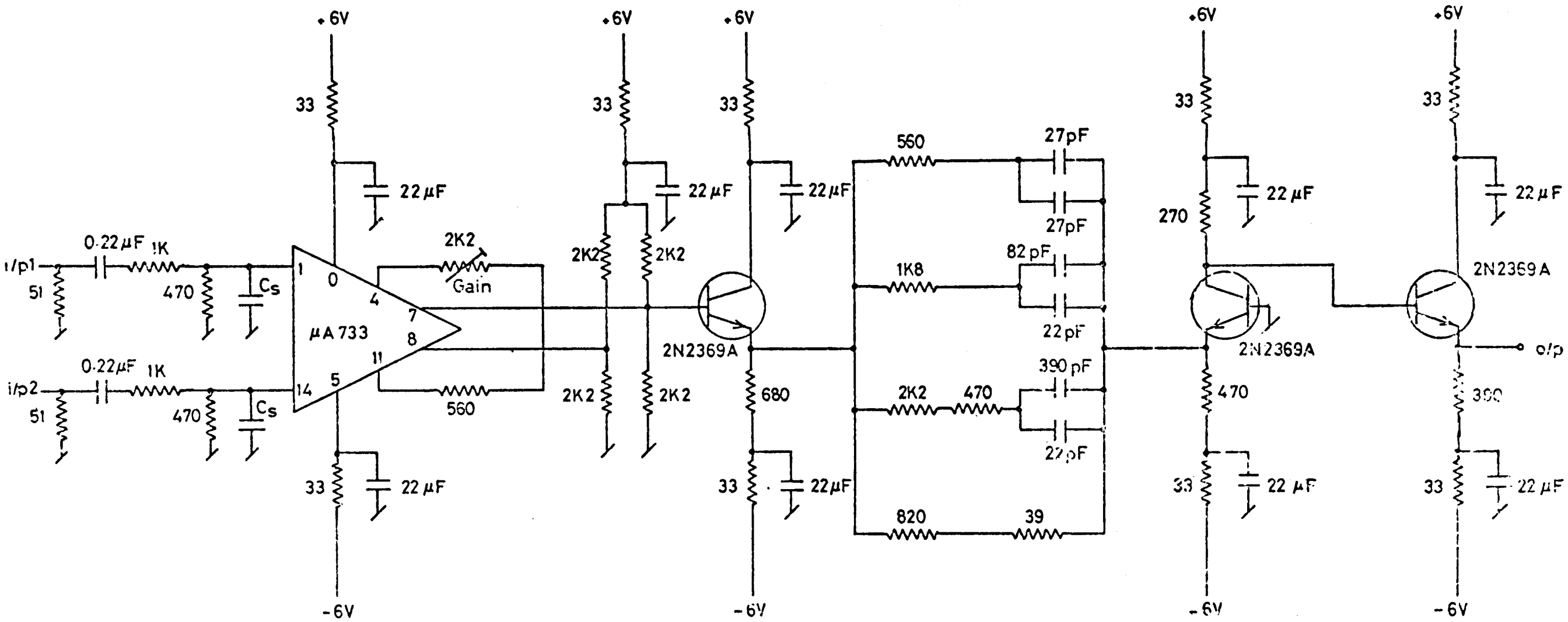


FIGURE III.17 CIRCUIT DIAGRAM OF THE PROTOTYPE MAIN AMPLIFIER AND PULSE SHAPER

control is obtained by altering the input attenuator. The capacitor C_s (45 pF) was used in the tests described in Chapter IV to provide a bandwidth limitation appropriate to the 'slow' risetime (30 nS) cables assumed in the design. The rise time of the main amplifier alone was 10 ± 2 nS.

The pulse shaping network is fed from this amplifier via an emitter follower with a low output impedance of ∿20Ω, which thus approximates a voltage source.

The output of the shaping network feeds into a common-base stage with a low input impedance of about 20Ω, which acts as a current amplifier.

The action of the pulse shaping network is therefore independent at the level of less than 1% for variation of the input and output circuit impedances.

The values of the components in the pulse shaping were chosen to be as close as possible to those required by using parallel and series combinations of preferred values. The implemented pulse shaping network has the following characteristics, compared with the design:

	Design	Prototype
$1/R_o$	65.0%	65.2%
$1/R_1$	100%	100%
$1/R_2$	31.0%	31.1%
$1/R_3$	21.0%	21.0%
τ_1	30 nS	30.2 nS
τ_2	190 nS	187.2 nS
τ_3	1100 nS	1100 nS

The output of the commonbase stage feeds the rest of the electronics via an emitter follower buffer. The voltage gain of the pulse shaper was 0.203 ± 0.001 at 1 MHz and the step function rise time was 10 ± 2 nS.

Typical Signals

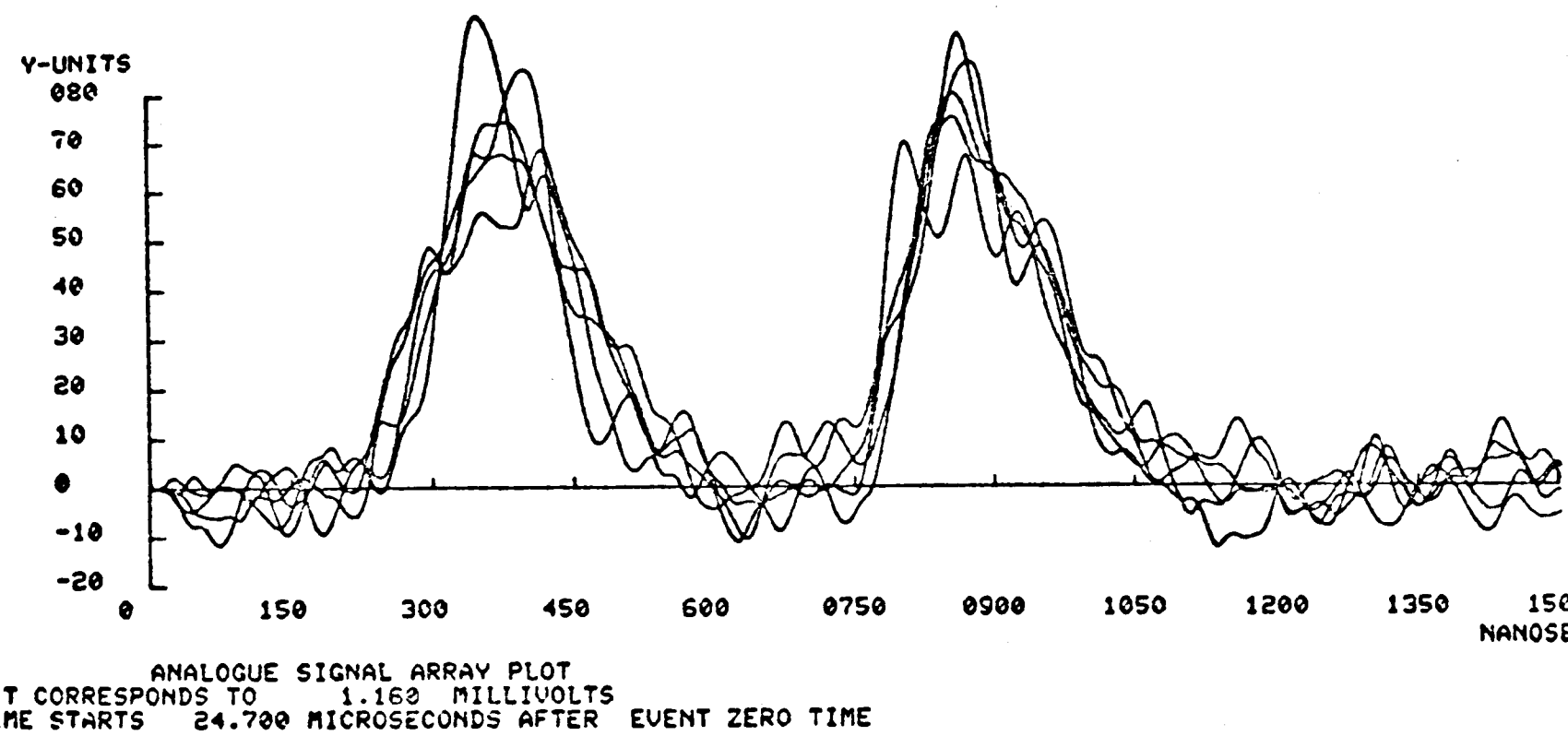


FIGURE III.18 TYPICAL SHAPER OUTPUT SIGNALS (Simulated)

Typical shaper output signals (with noise) are shown in Fig. III.18 for electron (2.6 KeV) signals, drifted 1m and 1.02 m at a gas gain of 10^4. The range of typical signal amplitude at this gas gain is from 20-300 mV, and of signal duration from 200-500 nS.

III.4 IONIZATION: PULSE INTEGRATION, STORAGE AND DIGITIZATION

The ionization information is needed in the form of a binary digital value proportional to the charge in the ionization sample of a track arriving at the wire plane.

The signal available at the output of the pulse shaping circuit is a symmetrical voltage pulse (shown in Fig. III.18) proportional to the gas amplifier output current (see II.3) and thus proportional to the rate of arrival of charge at the wire plane. The integral of this signal is required. A much simplified schematic diagram of the circuit used for this is shown in Fig. III.19.

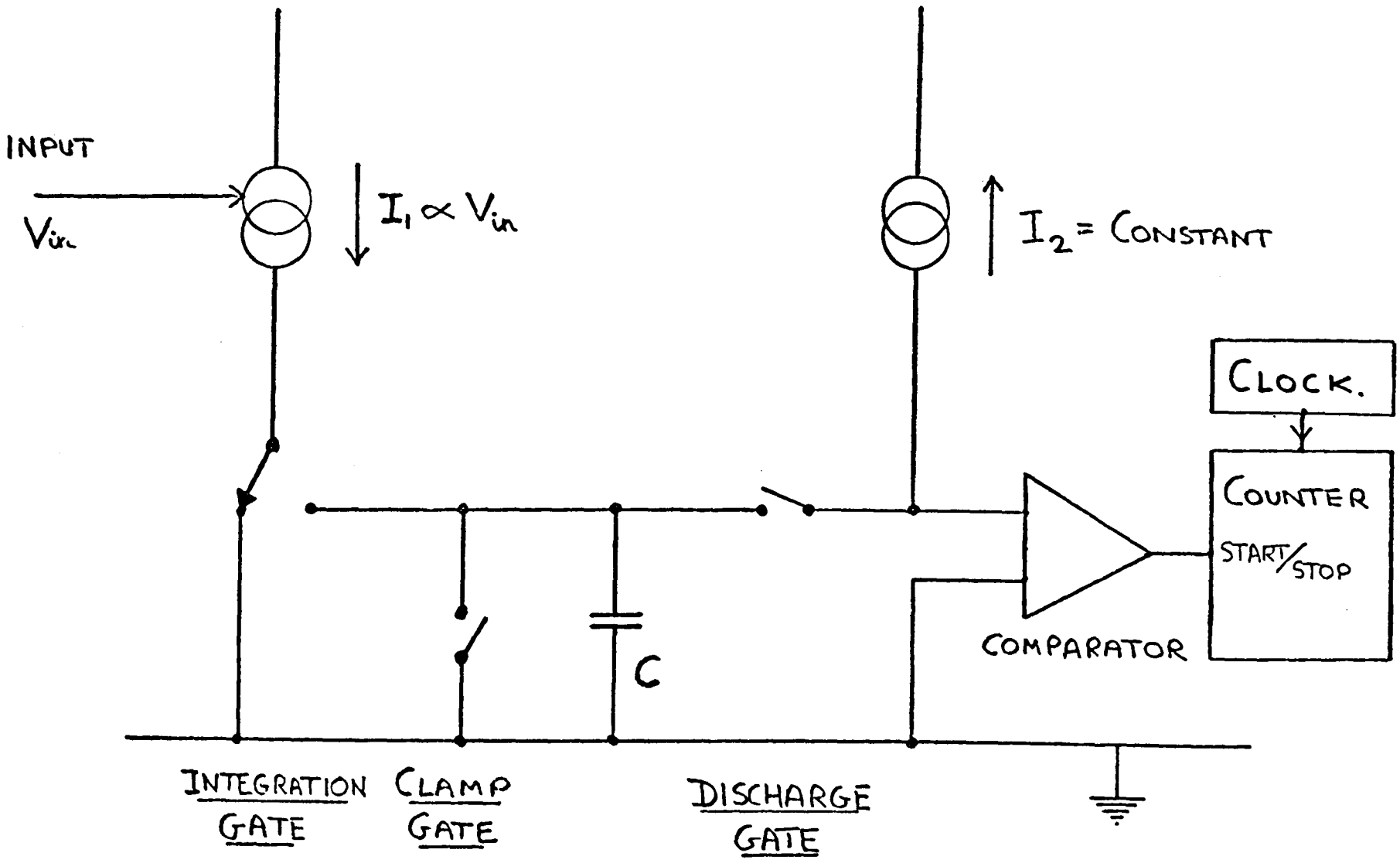


FIGURE III.19 SCHEMATIC DIAGRAM OF PULSE INTEGRATION CIRCUIT

Pulse Integration and Storage

The ionization information has to be stored temporarily until there is time to read it out (see Chapter I). It is thus found convenient to perform the signal integration by charging a capacitor with the signal and then isolating the capacitor for a period (∿a few mS) until readout. The information is stored in analogue form as the charge on the capacitor.

To produce the signal integral, the capacitor must be charged with a current proportional to the input voltage signal from the shaper. So the shaper signal (V_{in} in Fig. III.19) is passed through a charging amplifier with unity current gain but a very high output impedance. Before the arrival of the signal, the memory capacitor C is placed in an uncharged state by the clamp gate. The signal charging current I_1 (∿1 mA) is switched on to the capacitor using a fast linear integration gate. The gate opening and closing times are generated individually for each pulse so as to capture at least 99% of the current signal, (see III.5 and IV.5). Typical gate durations are 200-500 nS, and the fact that the gate opens and closes on zero signal (see III.5) means that the noise added due to jitter is small. Simulated signals and the associated gates (the vertical lines) are shown in Fig. III.20 (100 ionization electrons drifting 1m at 10^4 gas gain).

The method of gated integration has two advantages:

(i) A particular signal may be integrated correctly without including contributions from non-overlapping pulses which are slightly earlier or later.

(ii) The use of a signal-derived gate width (see III.5) for each pulse is an optimum situation for the resolution of signals of high rate and variable width (see IV.5).

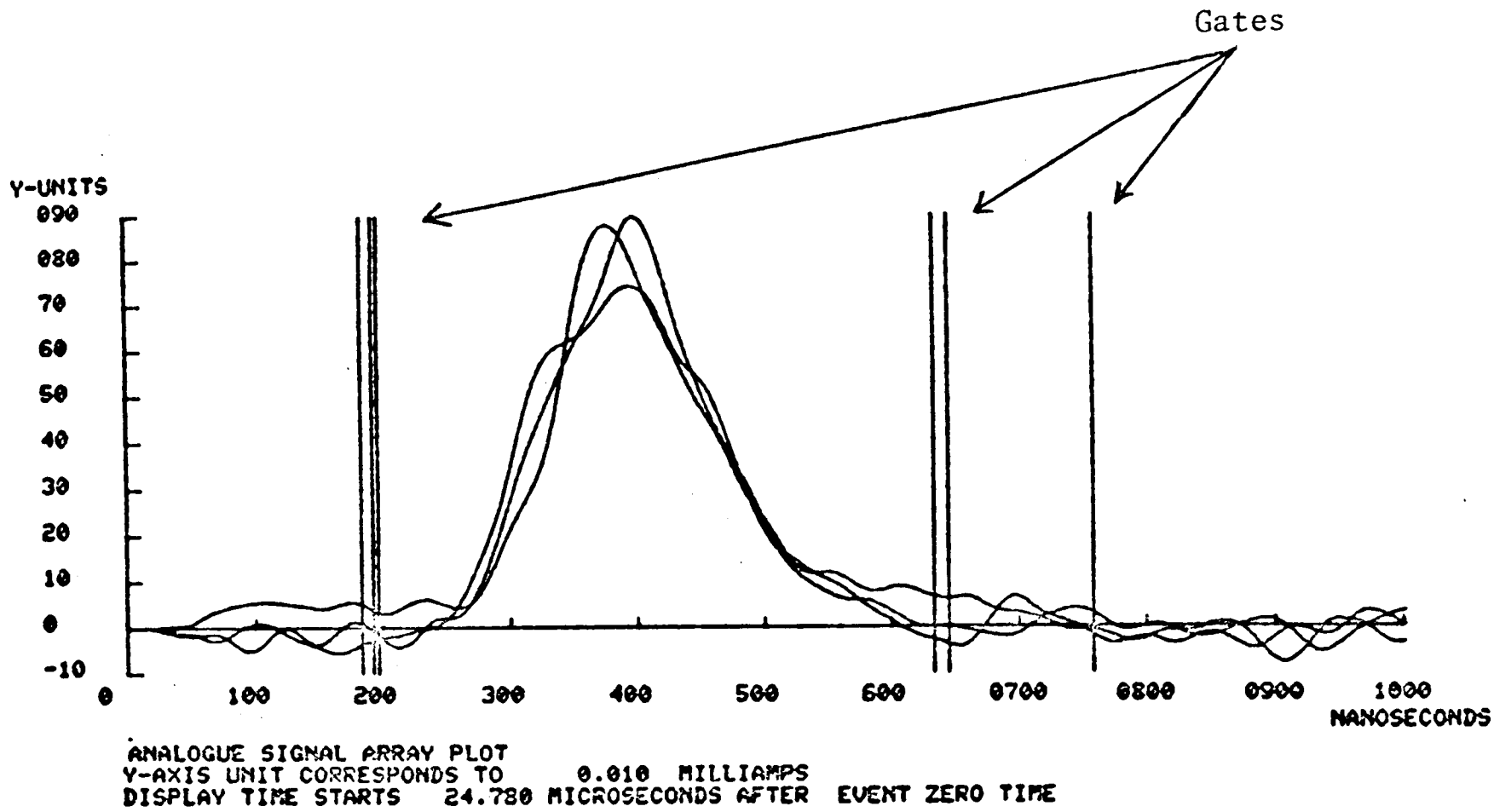


FIGURE III.20 TYPICAL ANALOGUE SIGNALS AND GATES SIMULATED: 100 ELECTRONS, DRIFTED 1m, GAS GAIN 10^4

This particular method of charge measurement is <u>in general</u> the best one in a system where there are large fluctuations in signal shape (as are experienced in ISIS). The theoretical SNR on the charge measured with this method has a limiting value of 1.28 times that of the optimum (infinite cusp shaping) [RV72], [NP74].

The important capability of this part of the electronics to measure ionization information on several tracks at high rates (∿MHz) comes from the multiplexing of the signals using many (32) memory capacitors, by the use of further (capacitor-selecting) gates, (see later). A comparable multiplexed analogue memory using 8 capacitors is described in [OA74].

<u>Charge Digitization</u>

Digitization of this ionization information and subsequent readout of the digital value occur later (∿mS) when the computer controlled readout system is ready for the data.

The Wilkinson rundown/type (see I.1) is the obvious choice of ADC for the present case because the analogue signal is already stored as a charge on a capacitor. Referring to Fig. III.19, the discharge of the capacitor C by the constant current I_2 is started by switching on the discharge gate. The comparator and counter operate as described in I.1. This type of ADC is easy and cheap to implement, an important consideration when ∿320 of them are required.

The Prototype Charge Memory and Digitizer

The circuit diagram of the prototype charging amplifier is shown in Fig. III.21. This diagram also includes some of the gating circuitry described later.

The shaping stage output feeds the 50Ω input of the charging amplifier via a delay line, (see III.5)whose risetime (∿30 nS) represents an important limitation on bandwidth. The d.c.-coupled charging amplifier uses an RCA CA3049 six-transistor integrated arrayin a simple circuit of good stability. The transconductance, determined by the input impedance, was 0.200 ± 0.001 mho. The rise/fall time was 10 ± 2 nS. The output is taken from a collector, realizing the high impedance required. Typical signal output currents are 0.1-10 mA which charge the memory capacitors (220 pF) to 0.02-4.0 volts (or 4 to 800 pC) with linearity better than 1%. The integration gates use transistors in the same array, whose bases are fed from a fast push-pull driver operated by the digital signal from the gate generator. A d.c. reference from the d.c. restorer (see III.6) is applied to the input of charging amplifier to provide a trustworthy d.c. baseline. The d.c. restorer control signal is taken from the other side of the integration gate, thus completing a gated d.c. feedback loop. The charge memory is shown schematically in Fig. III.22(a) (Data Acquisition) and (b) (Readout).

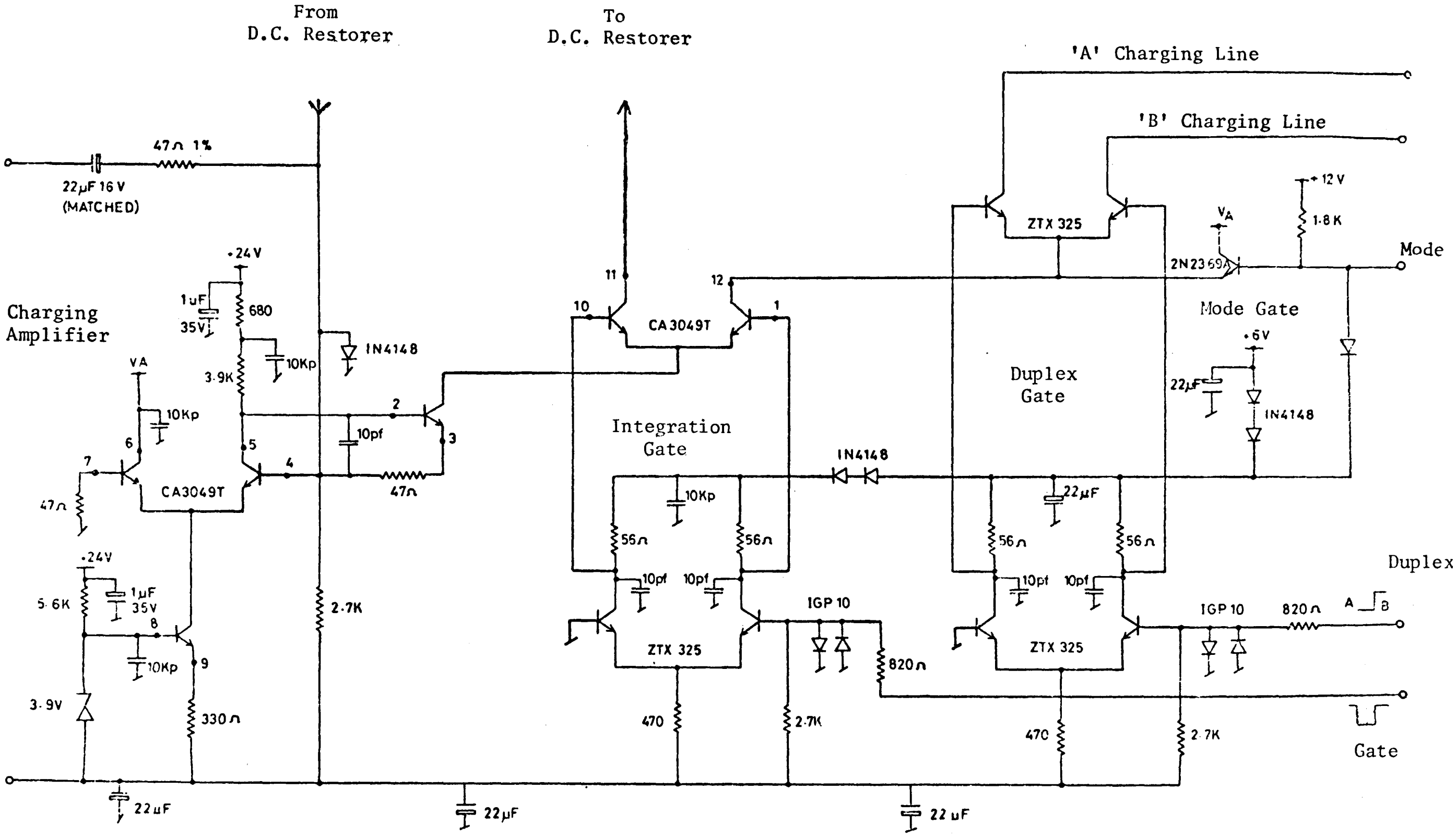


FIGURE III.21 CIRCUIT DIAGRAM OF THE PROTOTYPE CHARGING AMPLIFIER AND INTEGRATION GATE

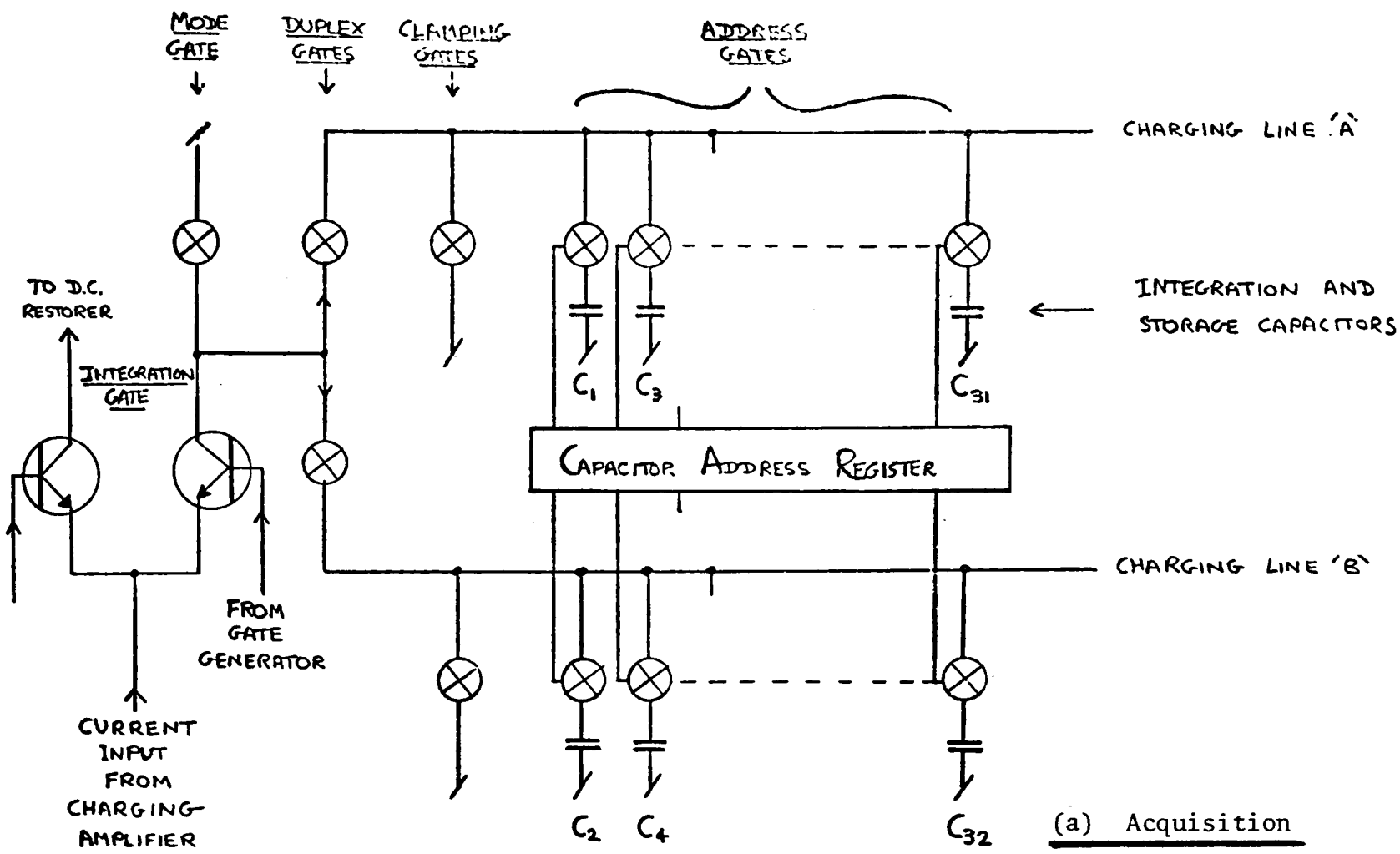


FIGURE III.22 SCHEMATIC DIAGRAM OF THE PROTOTYPE CHARGE MEMORY

The 32 memory capacitors are arranged in two banks of 16. Each capacitor is connected to one or other of two charging lines by a linear MOSFET switch (Signetics SD5000 Quad gates: 'On' resistance 30Ω, 'Off' resistance $10^{10}\Omega$, switching time: 10 nS). The isolation achieved using these is sufficient to guarantee a memory time of not less than 7 mS, for a 1 count (0.5% change in capacitor charge. Capacitor selection is done by driving these gates from a capacitor address register, which, in decoding the output of a cyclic address counter, selects successive capacitors alternately from each bank (to allow the next capacitor on the other line to be discharged: see later). The charging current is delivered to one or other charging line through the appropriate duplex gate, also driven by the capacitor address register. Each charging line has its own MOSFET clamping gate which can discharge the charging line and capacitor to 1% of reference in at most 100 nS. The mode gate operates according to (charging or digitization) mode to ensure that the charging and discharging circuits remain correctly terminated.

The memory is cyclic, and at any time can contain the charges of the last 30 signals to arrive (there are always two capacitors in the 'ready' (discharged) state). The duplexed configuration allows very fast operation with very small dead time (10 nS) and crosstalk (∿1%) at high data rates (∿2 MHz maximum). As a result the system resolution for multiple tracks is determined solely by the gate duration (and thus by the pulse duration at the 99% level, see II.2, III.5 and IV.5) and not by instrumental limitations.

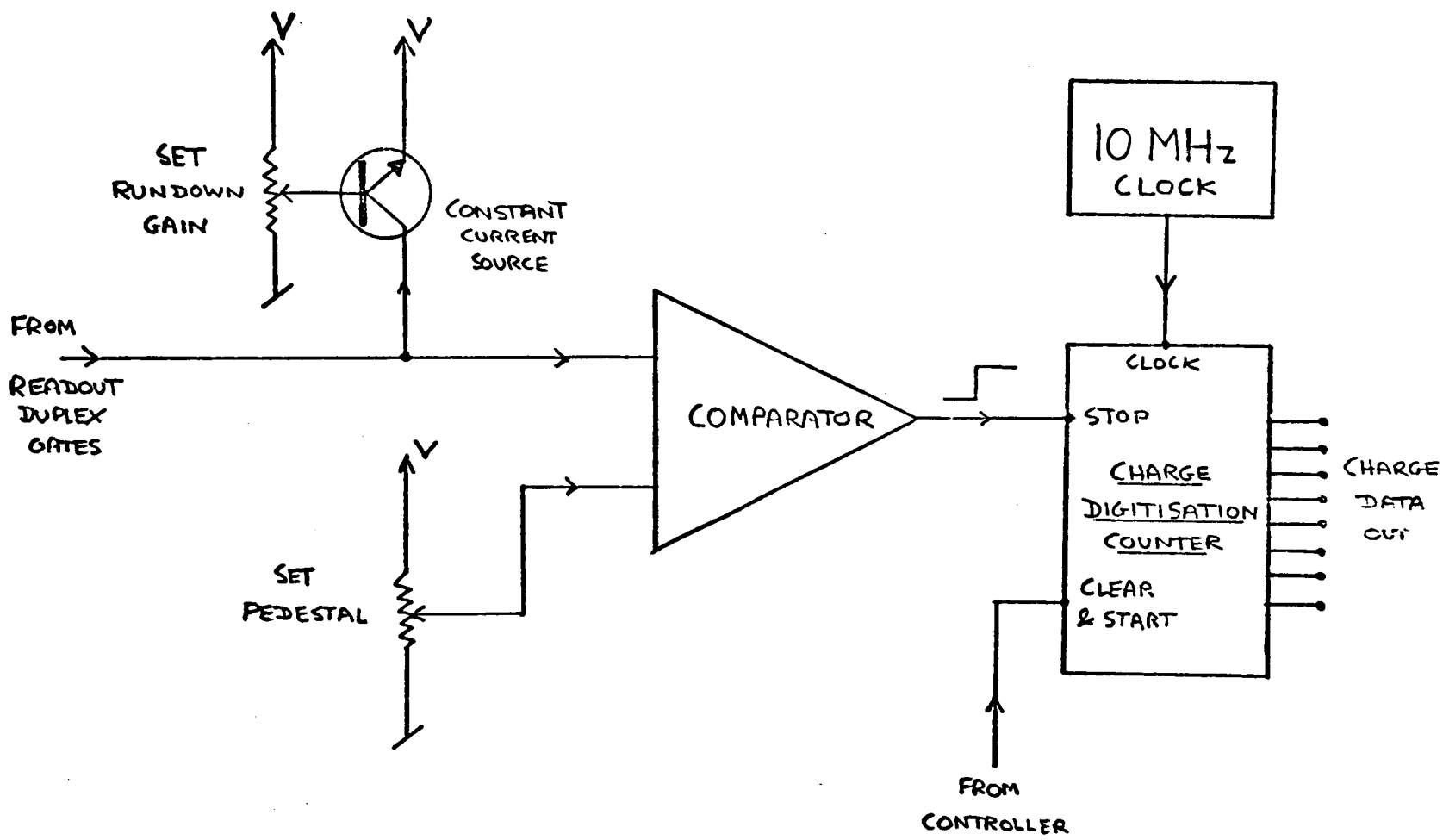


FIGURE III.23 SCHEMATIC DIAGRAM OF THE PROTOTYPE CHARGE DIGITIZATION CIRCUIT

The digitization circuit is shown schematically in Fig. III.23. The capacitors are discharged one-by-one in reverse order to charging by a current (∿25 μA) through the collector of a transistor. The magnitude of this current is variable, to alter the digitization sensitivity. A high input impedance comparator (National LM511) looks at the difference between the capacitor voltage and a reference pedestal. The TTL output from the comparator gates an 8-bit counter, clocked at 10 MHz, which thus records the rundown time (maximum: 25.6 μS or a capacitor charge of ∿640 pC). The measured digitization sensitivity was 2.97 ± 0.05 pC/bit. The accuracy is limited by the

±1 bit error in the counter, corresponding to 0.4%. The time taken for the conversion of 32 charges is ∿1 mS.

The overall linearity, short and long-term stabilities are measured to be better than 1%.

The details of the logic signals which control the operation of the integration, memory and digitization have been so far omitted for clarity. These signals are either generated by software (mode, initialization, termination etc.) or by hardware (gate sequencing etc.) (see III.7). The logic control is fairly simple, and is implemented for the most part with conventional TTL integrated circuits.

The most important part of the logic control is the operation of the gate sequence. Each capacitor is discharged to reference by the clamp gates before charging with a signal. The timing is arranged so that the current routing gates (integration gate, duplex, capacitor address) are opened before firstly the clamps go off and secondly the signals arrive. This ensures that no spurious charges exist on the capacitor or associated charging line.

At all times two capacitors (one on each charging line) are ready for signals. The charging proceeds cyclically for C_1, C_2, C_3 ... C_{32}, C_1, C_2 and so on, old data being overwritten by new. This action is continuous until the logic is stopped from accepting further charges by the event trigger (simultaneously with the inhibiting of the time-of-arrival memory clock (see III.5)). Readout of the capacitor is done in the reverse direction from the stopping point: C_3, C_2, C_1, C_{32}, C_{31} ... This is essential for the matching of capacitor with the appropriate time of arrival.

Before read out commences, a note of the contents of the capacitor address register is made to tie the charges down to being stored in known physical capacitors. This is necessary because the pedestals vary from capacitor to capacitor by a few (∿3) counts (∿2%), due to variations in component (memory capacitor, gate) characteristics. These individual values must be subtracted from the digital values read out to obtain the true signal charges. (The gain fluctuations from capacitor to capacitor are measured to be less than ∿1 count (∿0.5%) at maximum charge.)

III.5 TIMING: TRIGGERING, GATE GENERATION AND TIME-OF-ARRIVAL MEMORY

Signal-derived timing is required for:

(a) Measurement of the time-of-arrival, and hence the position of a track, and

(b) Generation of the current integration gate (see III.4).

The logic levels which define the timing are obtained from the shaped signals by the action of a discriminator. A gate generator produces gate pulses of an appropriate duration to correctly integrate the analogue signal to the 99% level. The presence of signals is recorded in a random access memory used as a shift register, whose address is incremented at a constant rate.

Triggering

The interface between analogue and digital systems is the discriminator. The form of discriminator used is shown in Fig. III.24 in schematic form. A sensitive fast comparator inspects the relative amplitudes of the shaper output signal, and a reference level determined by:

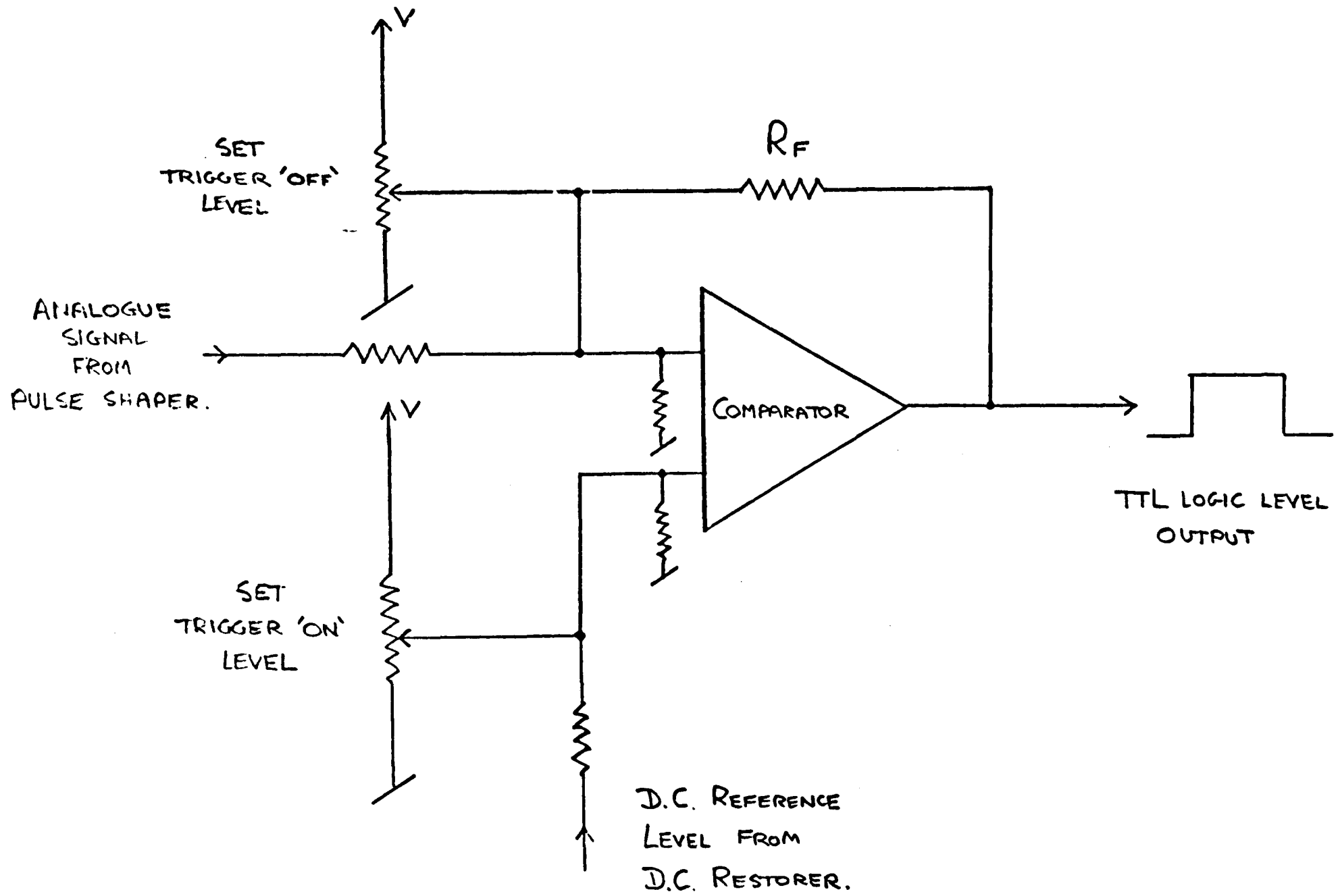


FIGURE III.24 SCHEMATIC DIAGRAM OF THE DISCRIMINATOR.

(a) The threshold level required (see later).

(b) A d.c. baseline reference signal supplied by the d.c. restorer (see III.6). This gives rate independent triggering characteristics.

(c) A hysteresis element (through R_f) which reduces noise susceptibility and multiple firing, and allows separate independently-adjustable, 'on' and 'off' triggering levels.

The circuit diagram of the prototype is shown in Fig. III.25. The comparator used is a highly sensitive (5V/mV) Signetics NE529A IC with a fast TTL logic output and short propagation delay (10 nS) and latching time (30 nS at small (1 mV) overdrive). This is driven from the shaping circuit output via an emitter follower buffer. A master 'on' threshold level, (common to all channels but decoupled at each) is applied to the other input of the comparator, together with the baseline reference and hysteresis elements. This resulting reference level is stable to better than 1% (see IV.5).

The r.m.s. noise level at the comparator input is about 2.2 mV (see IV.2). The 'on' threshold level is adjusted to the lowest level consistent with tolerable random noise triggering ('false alarms'). The maximum false alarm rate that can be tolerated is about 20 KHz; this corresponds with a threshold level set at about 4 times the r.m.s. noise level, with the present system bandwidth (see Chapter IV). In this condition, the discriminator is optimally sensitive to small signals, and operates with the highest triggering efficiency. (The discriminator will fire on the arrival of 4 electrons simultaneously at the anode, with a gas gain of 10^4, see IV.5.) This situation also gives the minimum pulse-shape-induced timing jitter.

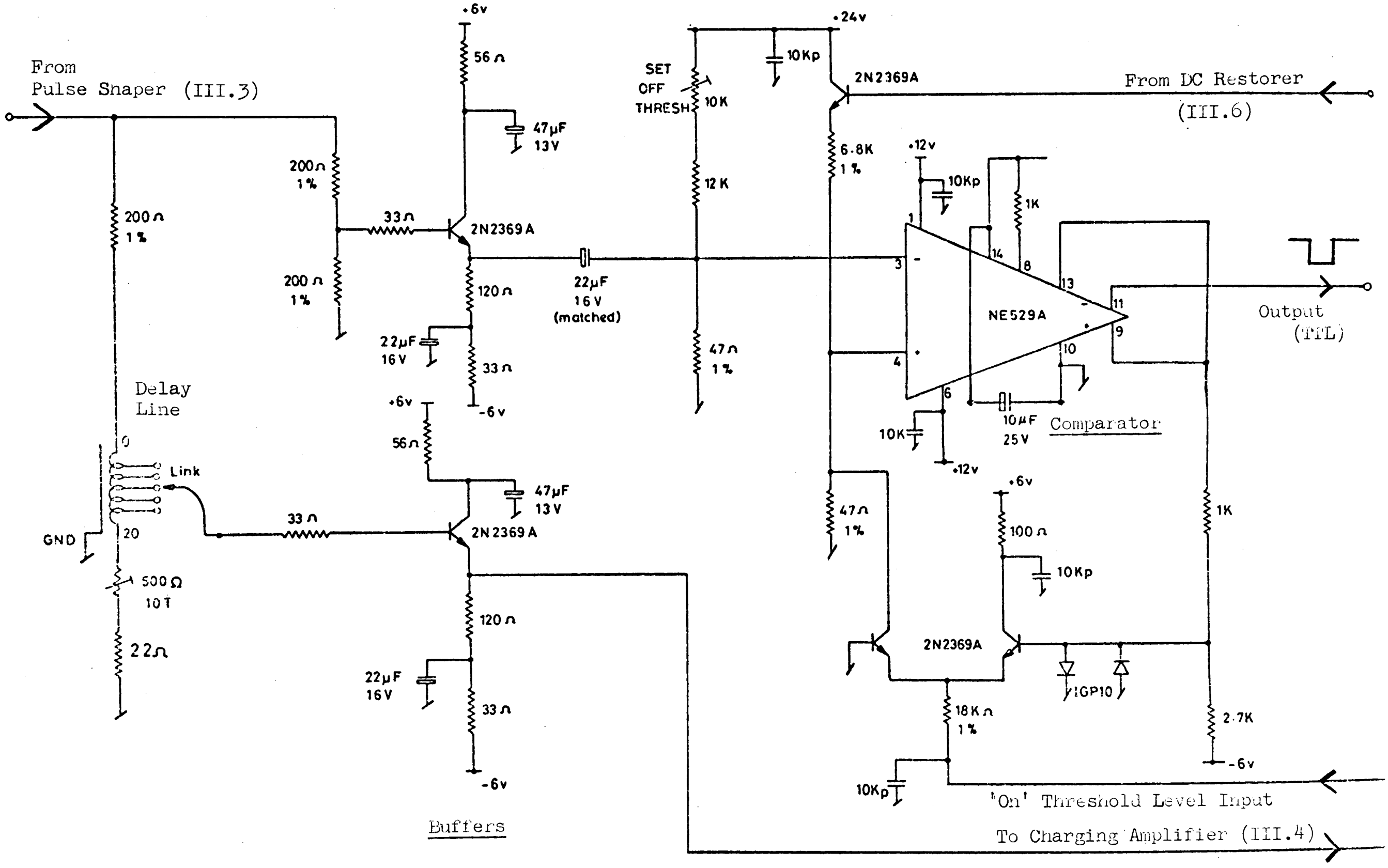


FIGURE III.25 CIRCUIT DIAGRAM OF THE PROTOTYPE DISCRIMINATOR

Since the discriminator output is to be used to give information on the pulse duration (the generation of the integration gates), the 'off' threshold level is set to zero. This hysteresis means that the discriminator will not reset until the end of the pulse, thereby producing an output of duration appropriate to that of the signal.

These aspects of triggering are shown in Fig. III.26, in which triggering occurs on simulated signals in the presence of noise; (100 electrons, 1 m drift, gas gain 10^4). The 'on' threshold level is about 8 mV (14 y-units), shown by the horizontal line. The 'off' level is at zero. The digital discriminator output is included as the vertical lines on either side of the pulses.

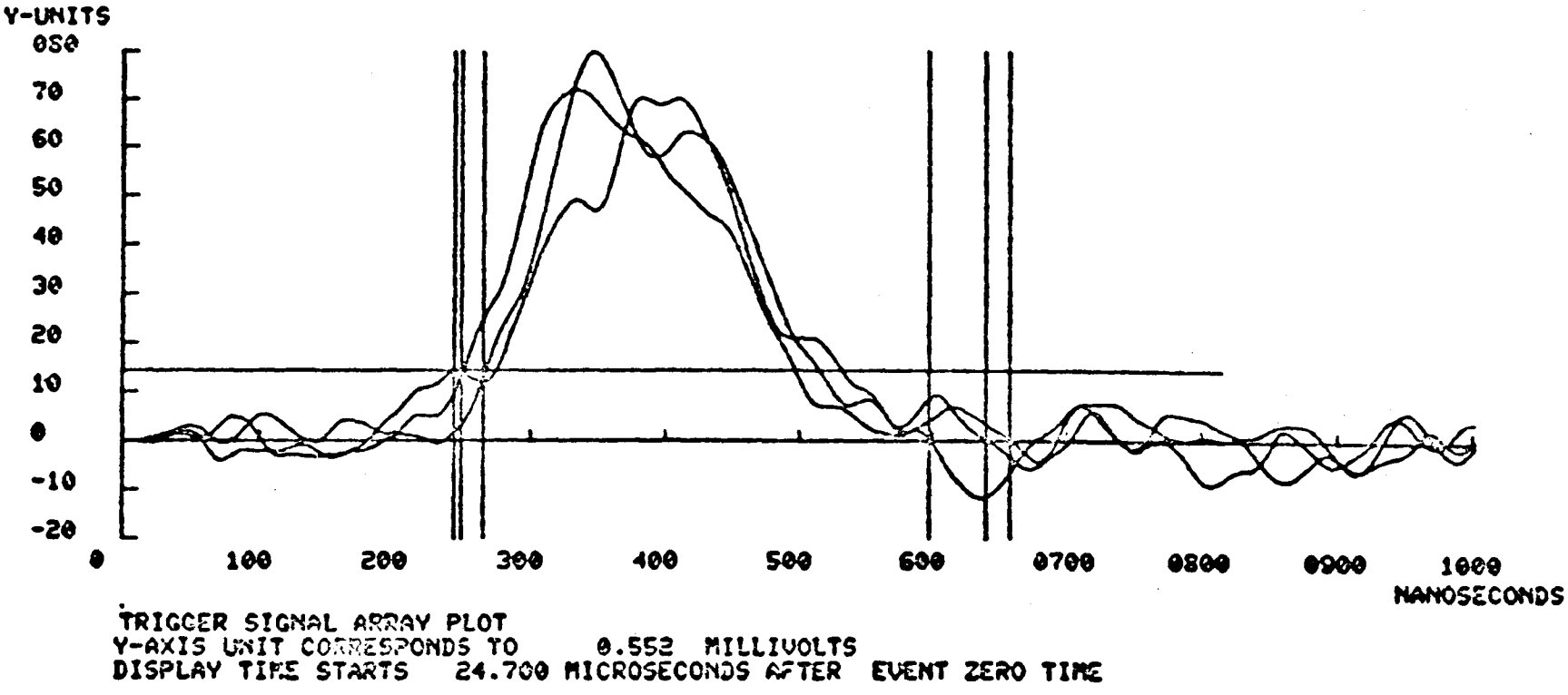


FIGURE III.26 SIMULATED DISCRIMINATOR INPUT SIGNALS WITH NOISE AND THE ASSOCIATED TRIGGER TIMES.

It is possible that a better SNR situation could be obtained at the comparator input by further signal filtering, so as to maximise performance for the expected range of signals under the Neyman-Pearson criterion (maximum probability of detection for minimum probability of false alarm, see for example, [AP72]). However, no further work has been done on this.

Gate Generation

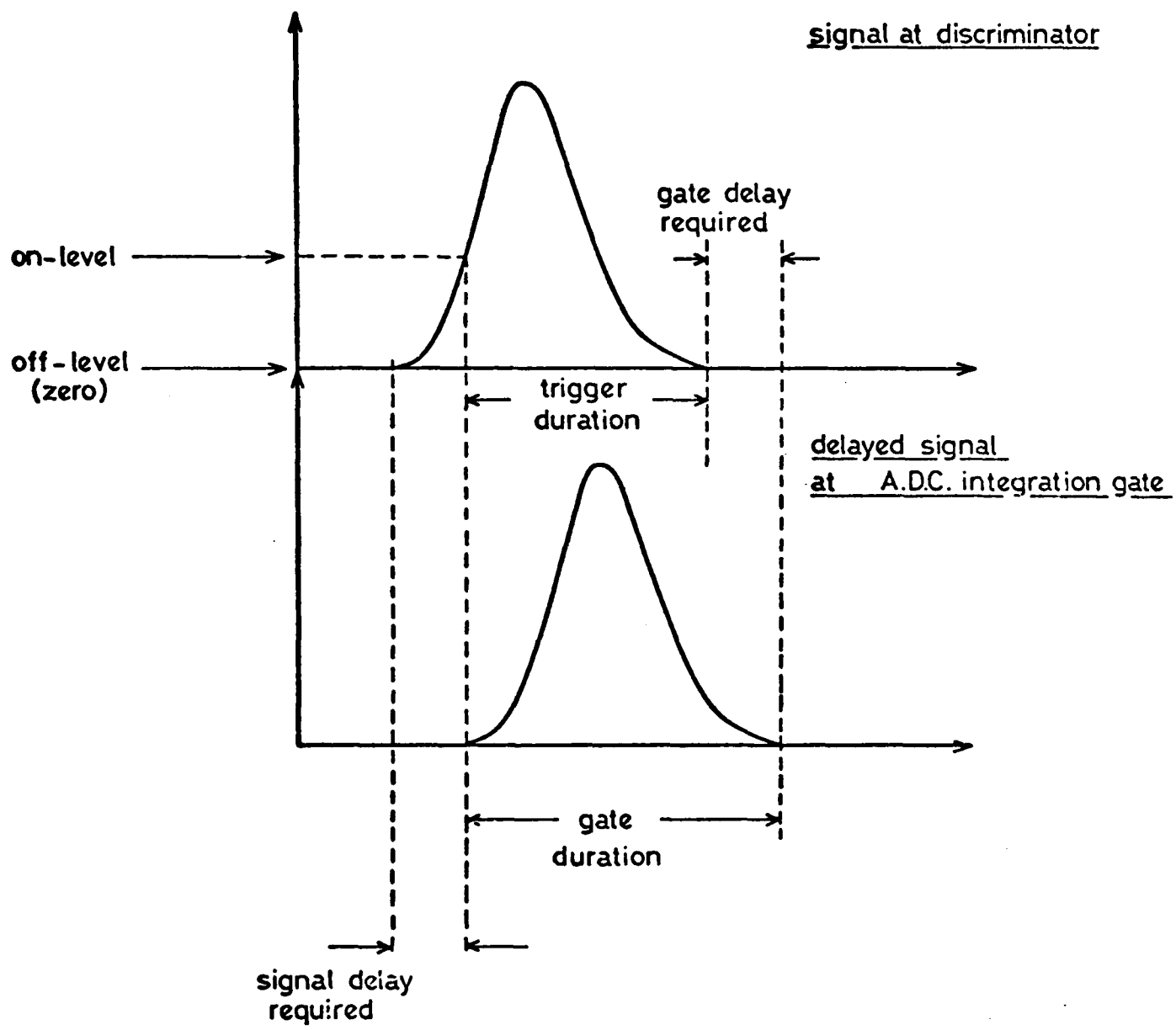


FIGURE III.27 DIAGRAM SHOWING ASPECTS OF GATE GENERATION FROM DISCRIMINATOR OUTPUT

The integrator described in III.4 requires gate pulses which overlap the signal at the 99% level or better. A fixed integrator gate duration would have to be long enough to capture 99% of the charge in the case of broadest signals. This results in lost position resolution on narrower pulses (see III.4, IV.5). A pulse-derived integration gate duration gives better position resolution on narrow signals. The price paid is that a higher SNR is required. A compromise solution is adopted (see IV.5), in which an operating point is chosen some way between the fixed and freely varying gate width configurations.

Because of finite SNR the 'on' threshold level is non-zero. Thus the discriminator fires at a certain time into the pulse, as shown in the diagram in Fig. III.27. To regain the lost (leading) part of the pulse, the signal going to the charging amplifier and integration gate must be delayed, by an amount (∿80 nS for 50 electrons, drifting 2m, gas gain 10^4, see IV.5) depending on the rise time of this signal, and the relative amplitudes of the signal and 'on' threshold level (and hence SNR, see Chapter IV). This is achieved using the delay line shown in Fig. III.25.

If this alone is done, then a similar portion of trailing edge of the pulse is lost. Therefore, to capture the whole pulse, the digital integration gate pulse must be extended by roughly the same amount as the delay used (since the 'off' transition occurs when the signal returns to zero). This is also shown in Fig. III.27.

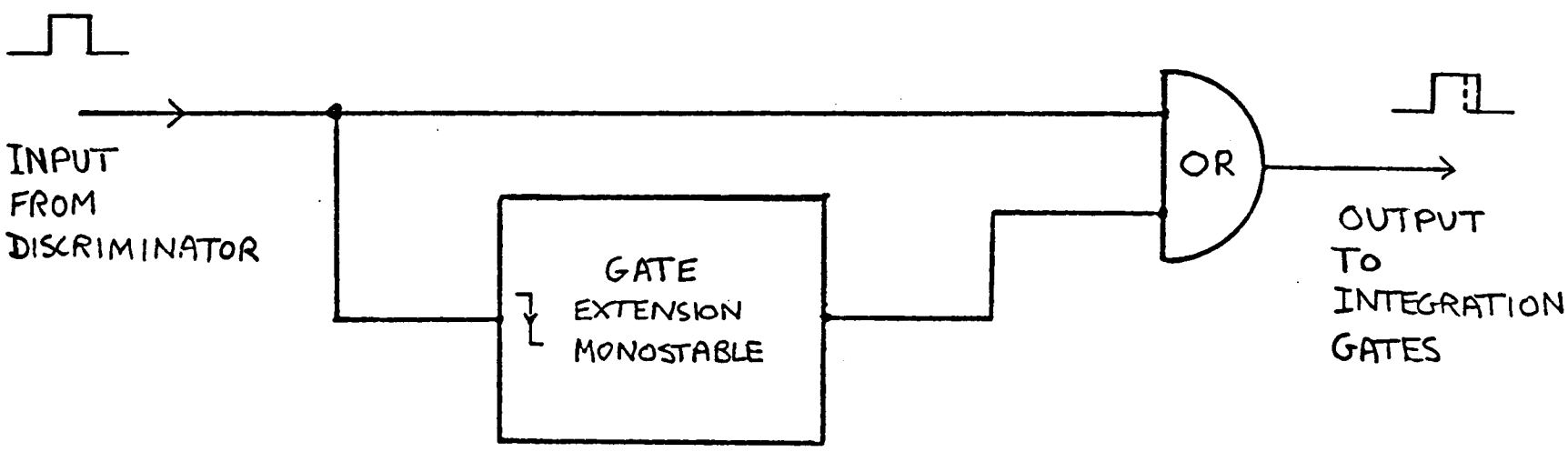


FIGURE III.28 GATE EXTENSION CIRCUITRY

The circuitry used for this is basically very simple, and is shown in schematic form in Fig. III.28. However there are some important considerations which somewhat complicate the design:

(i) To ensure that the charge on a certain capacitor (see III.4) may be associated with a particular time-of-arrival (see later), the gate generator and time-of-arrival circuitry has to be synchronized so that one cannot operate without the other. The missequencing so prevented would be disastrous.

(ii) In conditions when one pulse follows quickly (∿100's nS) on another, the operation of the gate generator must be well defined so that either

(a) the two pulses are individually treated and are both correctly integrated to the 99% level, or

(b) the two pulses are merged and treated as one.

The circuitry should prevent the half-way case of two gates being generated and two capacitors being charged, but with linear combinations of the currents in the two pulses. The requirement for reliable data means that the gate generator should, if there is any doubt, default to the treatment of two close pulses as one long pulse.

(c) A maximum gate duration (∿1 μS) is defined after which the gate goes off, independently of whether the discriminator has reset. This allows the D.C. baseline restorer to re-define the D.C. baseline in the case of anomalous (large and long) pulses in the system.

With this additional complexity, the characteristics of the gate generator are:

Minimum time between gates: 20 nS

Minimum gate width: 130 nS

Maximum gate width: 1 μS (time-out)

Propagation delay: 30 nS

(Analogue i/p to digital gate signal)

This propagation time increases the delay time needed in the analogue signal to the charging amplifier, but of course does not affect the gate extension time required.

Time-of-Arrival Memory

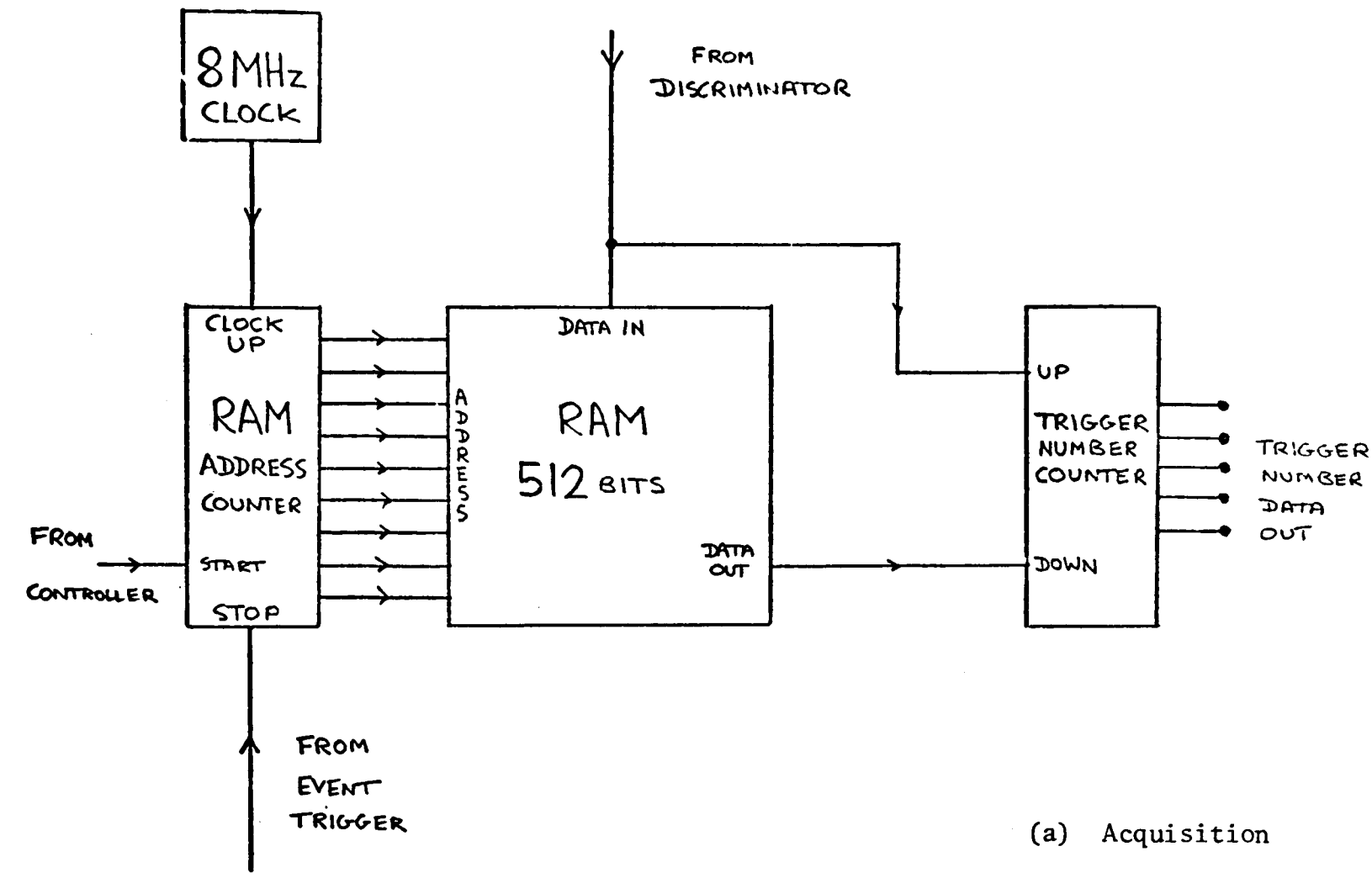
The schematic diagram of the time-of-arrival memory is shown in Fig. III.29 (a) (Data acquisition) and (b) (Readout).

The memory medium is a 512-bit random access memory operated as a shift register, where the address (Modulo 512) is incremented at a uniform rate (a maximum of ∿8 MHz). The time-of-arrival memory is thus split up into 512 x 125 nS bins (equivalent to ∿0.5 cm drift distance per bin at a drift velocity of 4cm/μS). This means that at any time during data acquisition, the memory holds the continuously-updated timing data for the last 64 μS of signal (compared with the 50 μS drift time for 2m).

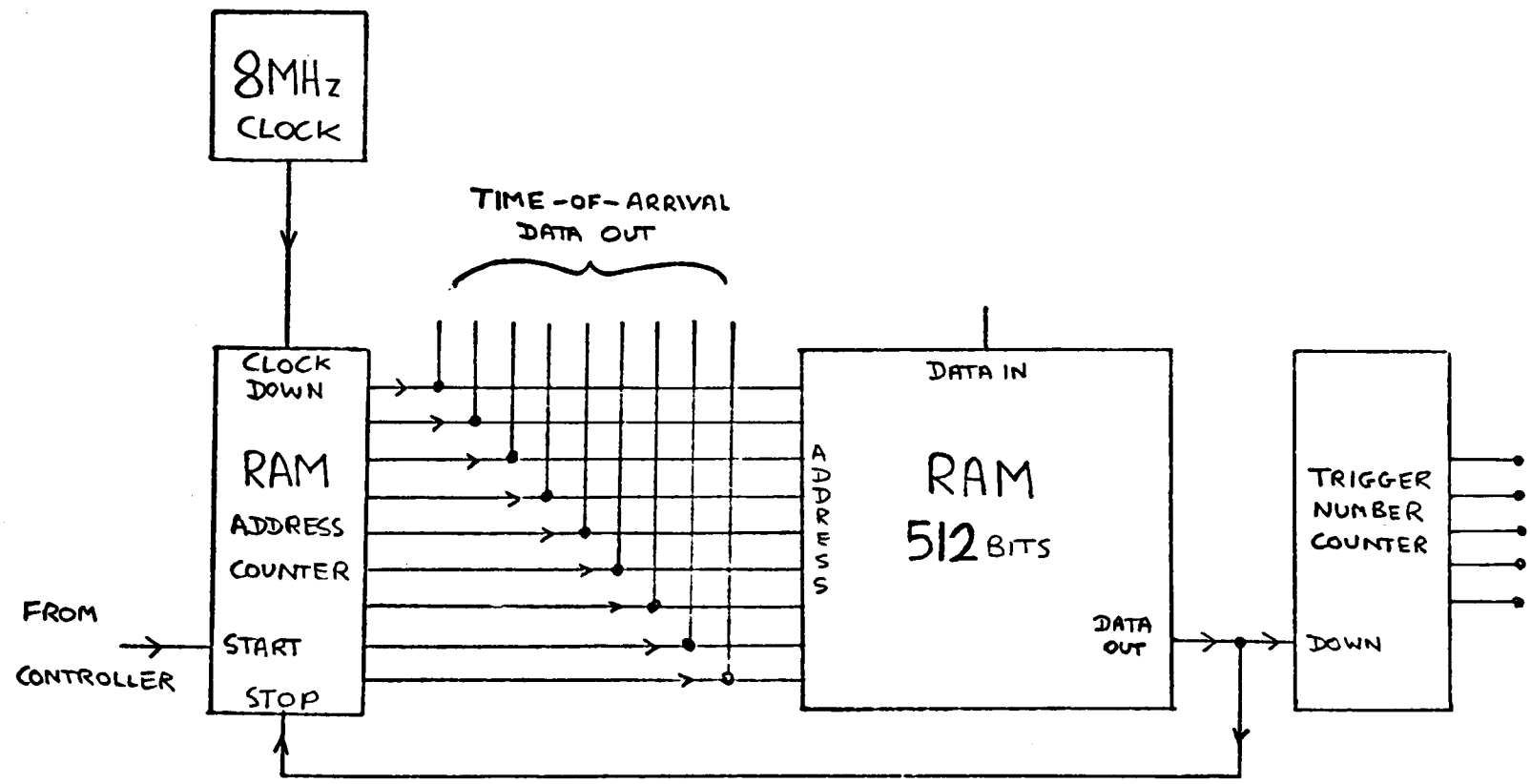
The RAM used is a Signetics 32S11 (1024-bit Schottky TTL Bipolar RAM). The random access read-write time is very fast (∿100 nS), but involves tight timing and synchronization (±5 nS) of the associated address and data inputs. For this reason the time-of-arrival logic is implemented mainly using fast Schottky TTL integrated circuits, the performance justifying the expense.

Data Acquisition (Fig. III.29(a)

The RAM is initially clear. A presence-of-track input from the discriminator causes a bit to be written at the appropriate instantaneous address (time) in the RAM, thus accomplishing the digitization to an accuracy of one clock pulse (125 nS). (There is



(a) Acquisition



(b) Readout.

FIGURE III.29 SCHEMATIC DIAGRAM OF THE TIME-OF-ARRIVAL MEMORY.

a small systematic error here (∿100 nS or 0.4 cm) due to the discriminator firing on the leading edge, not the middle, of the pulse. This is correctable.) A trigger number counter is also incremented.

After a full RAM address cycle, this bit will be detected in the first part of the read-write sequence, and causes the trigger number to be decremented. This counter therefore contains the total number of bits set in the RAM (modulo 64), and thus the total number of triggers over the previous 64 μS. The maximum number of stored arrival times is 512, but only ∿37 of these are read out (see later).

Readout (Fig. III.29(b))

To obtain positional data from these times, a further piece of information has to be added. This is the event time, accurate to a few tens of nanoseconds, from an external event trigger. When an event occurs, tracks may be deposited at all drift distances, and thus may require a full drift time of 50 μS to arrive at the wire plane. The RAM address counter is stopped at a time equal to a full drift time of 50 μS after the event occurs, the last signals to arrive being those from the furthest tracks. The RAM address at this stage is denoted by T_o. Time-of-arrival data T for the past 64 μS exists in the RAM, and may be simply converted to positional data X. For the N^{th} track

$$X(N) = |T_o - T(N) + 512|_{512} \quad \frac{V_d}{f}$$

where V_d is the drift velocity (4 cm/μS, see II.2),

f is the RAM address clock frequency (∿8 MHz).

Readout of the T(n) in terms of the RAM address is accomplished easily. After T_o and the trigger number are recorded, the address counter is decremented back down from T_o until it is stopped by the presence of a bit in the RAM. (See Fig. III.29(b)). The trigger number is also decremented. Reading the value of the RAM address gives the appropriate T. This is continued until one of two conditions obtains:

(i) The RAM address has completed one cycle (at which stage the trigger number counter should be zero: this serves as a check), or

(ii) More than a certain number (~37, limited by buffer memory size, see III.7) of times have been read out.

III.6 THE D.C. BASELINE RESTORER

The ionization information in the form of the charges on the memory capacitors is required to be accurate at the 1% level (see III.4). The charge is obtained from the integration of a current signal I(t):

$$Q = \int_o^t I(t)\,dt$$

This integral is, in practice, made up of two superimposed contributions: a signal $I_s(t)$ and a baseline current I_B which is effectively constant over the integration limit (200-500 nS). The integral becomes:

$$Q = \int_0^t I_s(t)\,dt + I_B t$$

The integral of a non-zero baseline current I_B over the gate duration t may represent a non-negligible additive systematic error if I_B is more than a fraction of a percent of the signal amplitude. If I_B were constant from pulse-to-pulse, the error could be simply removed. However, in general, I_B varies from pulse-to-pulse.

The reference levels applied to the discriminator input must also reflect an accurate signal baseline to much the same precision as that required for integration (see III.5). Any variation of more than about one percent in the relation of threshold reference level to signal baseline, can alter the triggering characteristics sufficiently to cause either excessive noise-induced random triggering, or loss of signal upon integration (see IV.5)

These problems, associated with baseline fluctuations, have an infamous reputation in high resolution, high rate electronics, (see for instance [NP74]), as they are highly signal-correlated.

The main cause of baseline errors in the ISIS electronics occurs from the use of capacitor coupling between electronic stages. By the very nature of this form of coupling, transmission of truly unipolar pulses is impossible. The main effect is a proportional amplitude error ΔP in the baseline that is almost equal to the mean duty cycle (or mark-space ratio),

$$\Delta P = ft$$

where f is the mean pulse repetition frequency and t is the mean pulse duration. The dependence of this effect on the rate f is well-known. For 50% duty cycle, i.e. 250 nS pulses at 2 MHz, the baseline shift ΔP is 50%. This is intolerable. The effect is, of course, removed in a totally d.c. coupled system, but a.c. coupling of the chamber wires to the preamplifiers is unavoidable (see III.2).

(It is assumed that the coupling time constants are long enough ($\gtrsim$100 μS) to assume that overshoot from a single pulse is small ($\lesssim$0.5% for $\sim$1 μS pulses.)

Secondary, but not unimportant causes of fluctuations in the baseline are:-

(i) Incomplete removal of the gas amplifier response 'tail' at long times ($\gtrsim$1 μS). The error can be as much as a few percent at high rates. See II.3, III.3.

(ii) The presence of low frequency noise: hum (50, 100 Hz), microphonics (A.F.) etc. Again these could be as much as a few percent of signal.

(iii) The gas amplification switching transients (see Appendix 2).

(iv) Any other long-lasting pulse property, due to, for instance, poor amplifier recovery at the 1% level.

As a result, the restoration of the signal d.c. baseline to a well-defined reference quickly ($\sim$100 nS) and accurately (<1%) comprises an important part of the signal processing system.

Choice of D.C. Baseline Restorer (DCBR)

There has been a large amount of published work on the design of DCBR's, owing to their use in high resolution nuclear spectroscopy systems. For a review, see [NP74]. In general, DCBR's are a special class of non-linear time-variant signal processing and belong to one or other of two types:

(i) Current switching

A typical example of this type is the Robinson restorer [RL61] (see also [BM72], [RV67]). It uses a double diode configuration

to remove 'negative' portions of the waveform. The disadvantage of such a system lies in the use of 'real' components which exhibit undesirable characteristics (e.g. the 'on' resistance of a diode). This result is incomplete, slow restoration.

(ii) D.C. Feedback

In this method, the d.c. level at the desired point in the system is maintained by the use of a d.c. coupled negative feedback configuration, which locks on to the background signal level between pulses. This method is fast and accurate, although it requires a gating signal to inhibit restoring action for the duration of a signal pulse (this makes the DCBR highly non-linear). An example of this type of DCBR [WG76] shows 0.1% baseline shift at 1 MHz rate. Possible imperfections of the method are (i) DCBR overshoot and undershoot, and (ii) the loss of ability to suppress 1.f. noise at the highest duty cycles (this is common to all DCBR's, see [WG76]).

Although the d.c. feedback method is more complex than the current switching method, the advantages of speed and accuracy demand the choice of the d.c. feedback method for the DCBR in ISIS.

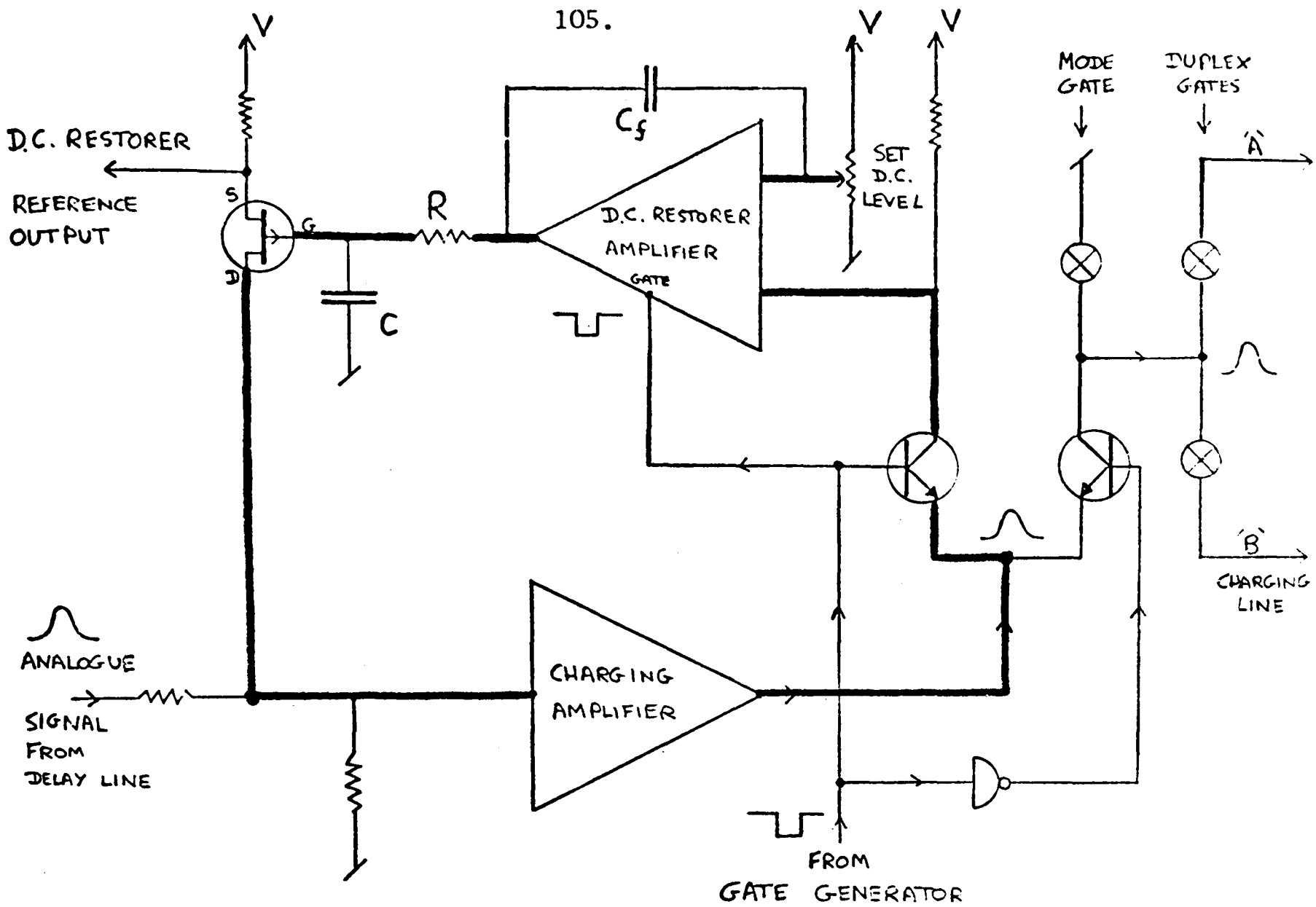


FIGURE III.30 SCHEMATIC DIAGRAM OF THE PROTOTYPE D.C. BASELINE RESTORER

The Prototype D.C. Baseline Restorer

The DCBR in ISIS must follow the d.c. background level, and compensate for the variation of this at the charging amplifier input (see III.4) and the discriminator reference (see III.5). The schematic diagram of the d.c. feedback baseline restorer is shown in Fig. III.30, and the circuit diagram in Fig. III.31. The independence of individual channels is ensured, because each channel has its own DCBR.

In the absence of any signal large enough ($\gtrsim$8 mV) and fast enough (risetime $\lesssim$100's nS), to trigger the discriminator, the DCBR consists of a stable servo loop which inspects the output of the charging amplifier, relative to a variable reference, and supplies an error signal that corrects the output back to the chosen baseline.

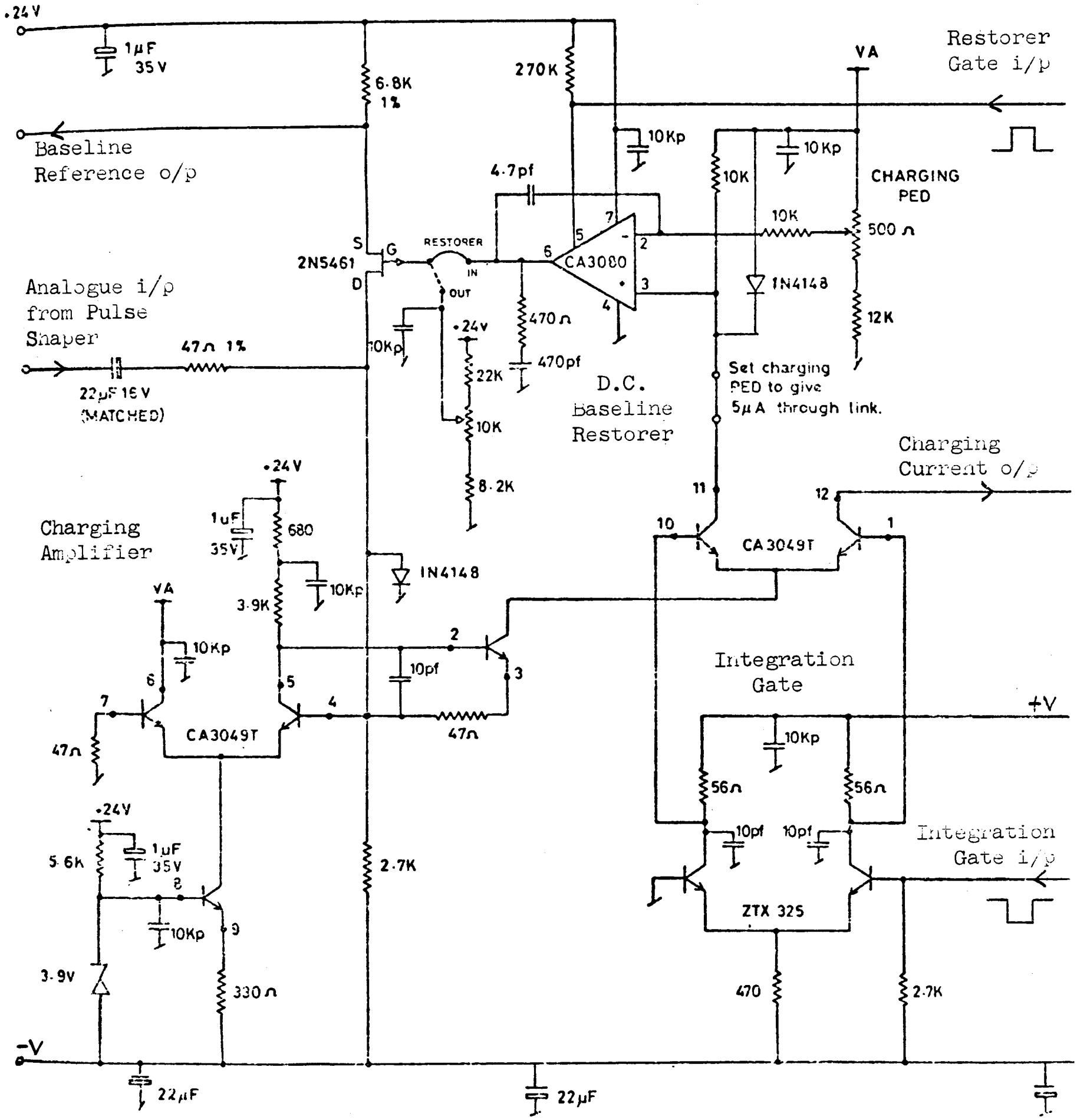


FIGURE III.31 CIRCUIT DIAGRAM OF THE PROTOTYPE D.C. BASELINE RESTORER

The error signal resides as the voltage on the DCBR memory capacitor C (470 pF), charged through R(470Ω) by the DCBR feedback amplifier. This amplifier is a high-input-impedance operational transconductance amplifier (RCA type CA3080), having a high impedance (15 MΩ) current output. Local feed back is applied through C_f(4.7 pF) to limit the DCBR bandwidth.

The voltage on the capacitor C is measured by a FET which supplies the DCBR reference output as a current to the input node of the charging amplifier, thus completing the loop. A voltage reference output is also available, at the source of the FET. This is used directly as the discriminator DCBR reference signal, since the ratio of gains to the discriminator input and to the charging amplifier input is unity.

(The presence of the delay (∿100 nS) in the reference signal to the discriminator means that the action of the DCBR cannot affect the triggering characteristics. The restoring action is not harmed because the delay is less than the typical timescales of D.C. restoration required.)

The behaviour of the DCBR on the arrival of signals which trigger the discriminator is shown in exaggerated form in Fig. III.32(a)-(d). The un-restored input signals are shown in (a). The generation of an integration gate (b) causes the DCBR input current to be switched onto the capacitor charging lines (see III.4). At the same time, the gate is also applied to the DCBR feedback amplifier, which essentially switches off the output, keeping it at very high impedance. This isolates the memory capacitance C, and locks the DCBR reference level at that registered in the time (∿100 nS) just before the signal (shown in (c)). This reference memory time is well in excess of 100 μS for 1% change.

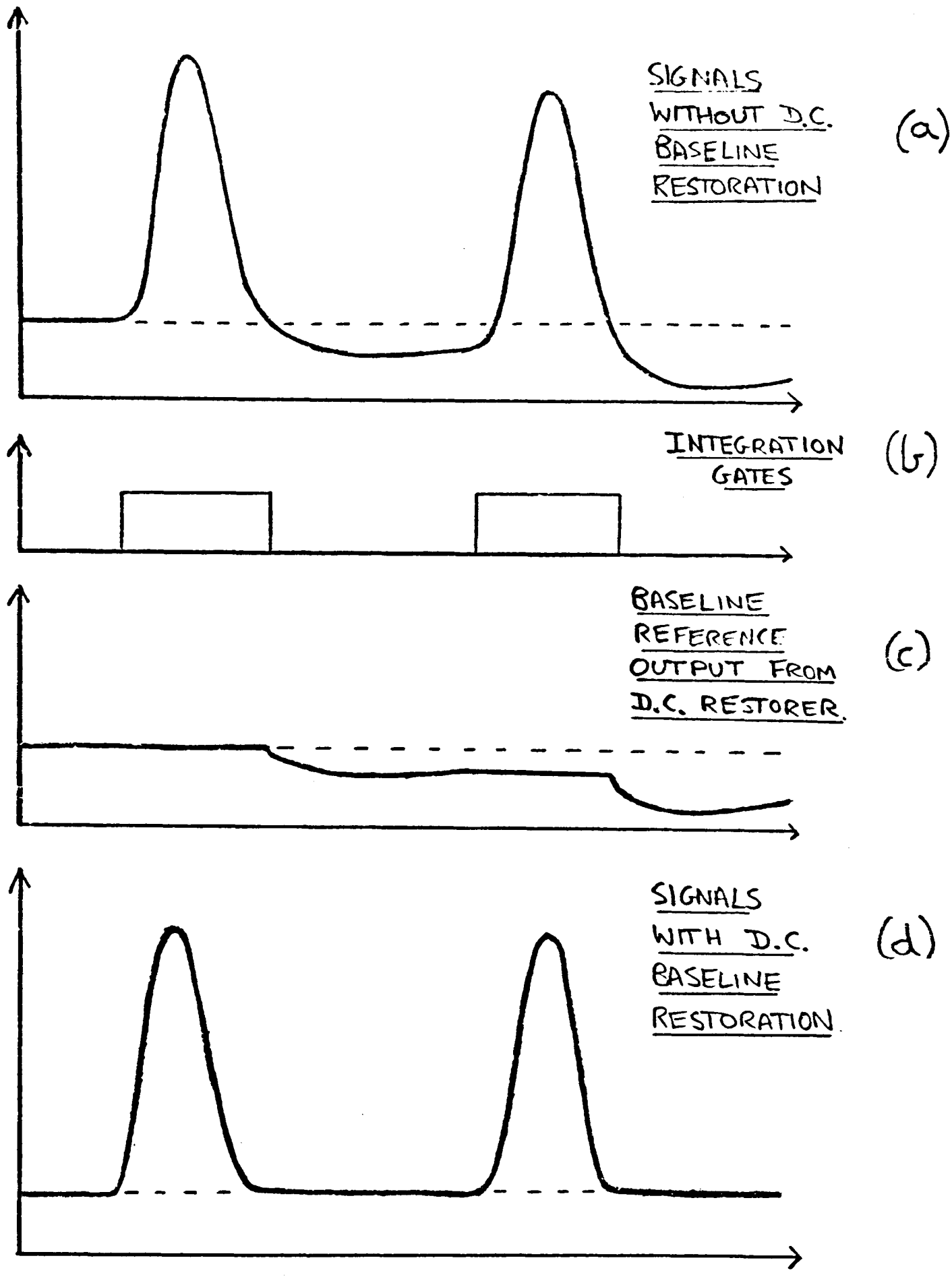


FIGURE III.32 SHOWING THE PRINCIPLES OF OPERATION OF THE PROTOTYPE DCBR

On the termination of the gated integration, the DCBR is released to follow the signal to the (new) baseline. This occurs fast, in ∿100 nS, but is limited by the maximum 'on' output current of the DCBR amplifier, of ∿200 μA. A slewing rate of ∿400 mV/μS is obtained with a 470 pF memory capacitor C (compared to noise of 3 mV, and signal of 5-500 mV). This is a further contribution to the non-linearity of the DCBR response. For small signals (and noise) of amplitude <20 mV, the DCBR time constant is just $\tau_t = C/g_m \sim 60$ nS, where g_m (∿8 mmho) is the transconductance of the DCBR feedback amplifier.

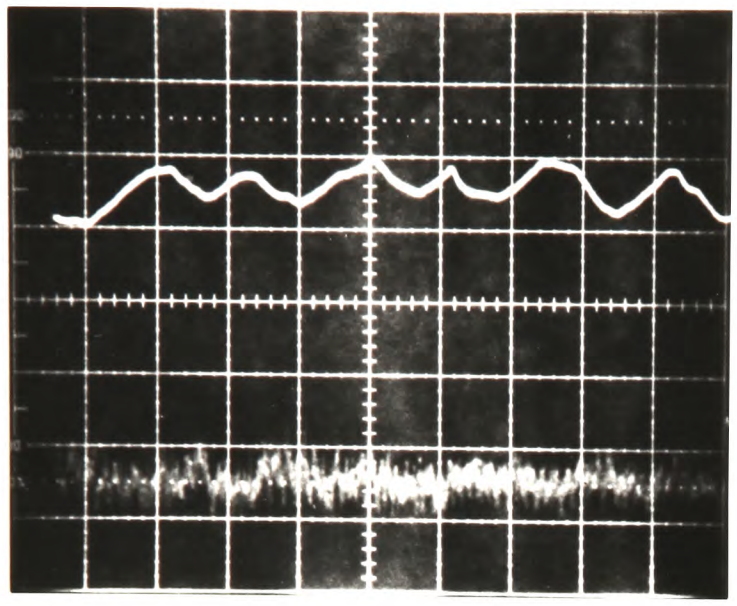
Performance of the Prototype Baseline Restorer

The performance of the prototype DCBR is shown qualitatively in the 'scope traces in Fig. III.33 (a)-(c). The first photograph (a) shows the response of the restorer in following noise. Although the vertical scales are different for the two traces, the reduction in the noise bandwidth at the d.c. restorer output will be noticed.

The second and third photographs show the effect of d.c. baseline restoration on the gas amplifier signals from a small drift chamber (see IV.4).

In (b), the restorer was not operating, and the baseline variation of the signals throughout the accelerator beam duration (∿600 mS) can be seen. The signals were negative-going, of 50-100 mV amplitude. A baseline shift of ∿30% is observed. In (c) the baseline was restored. It can be seen that restoration to the baseline is good to a few percent throughout the whole beam pulse.

Figure III.33

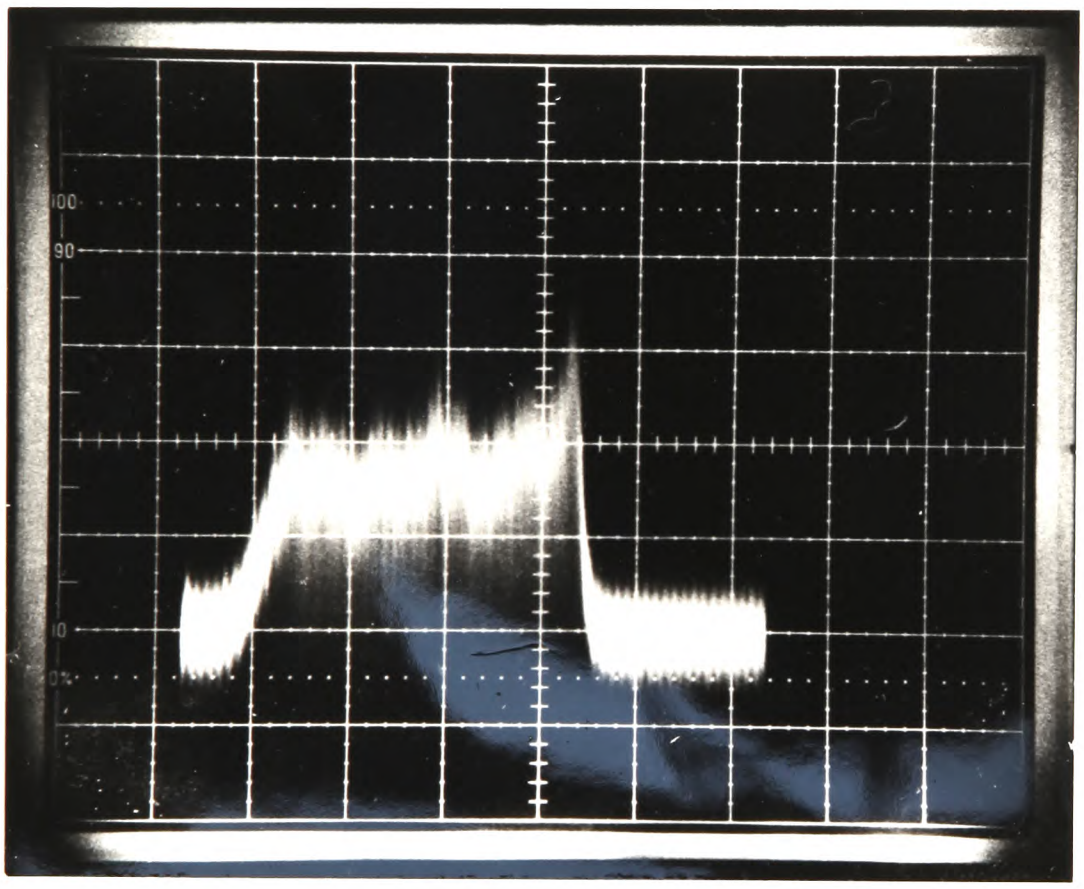


(a) D.C. Restorer Noise Response

← D.C. Reference output.

X: 1μS/div

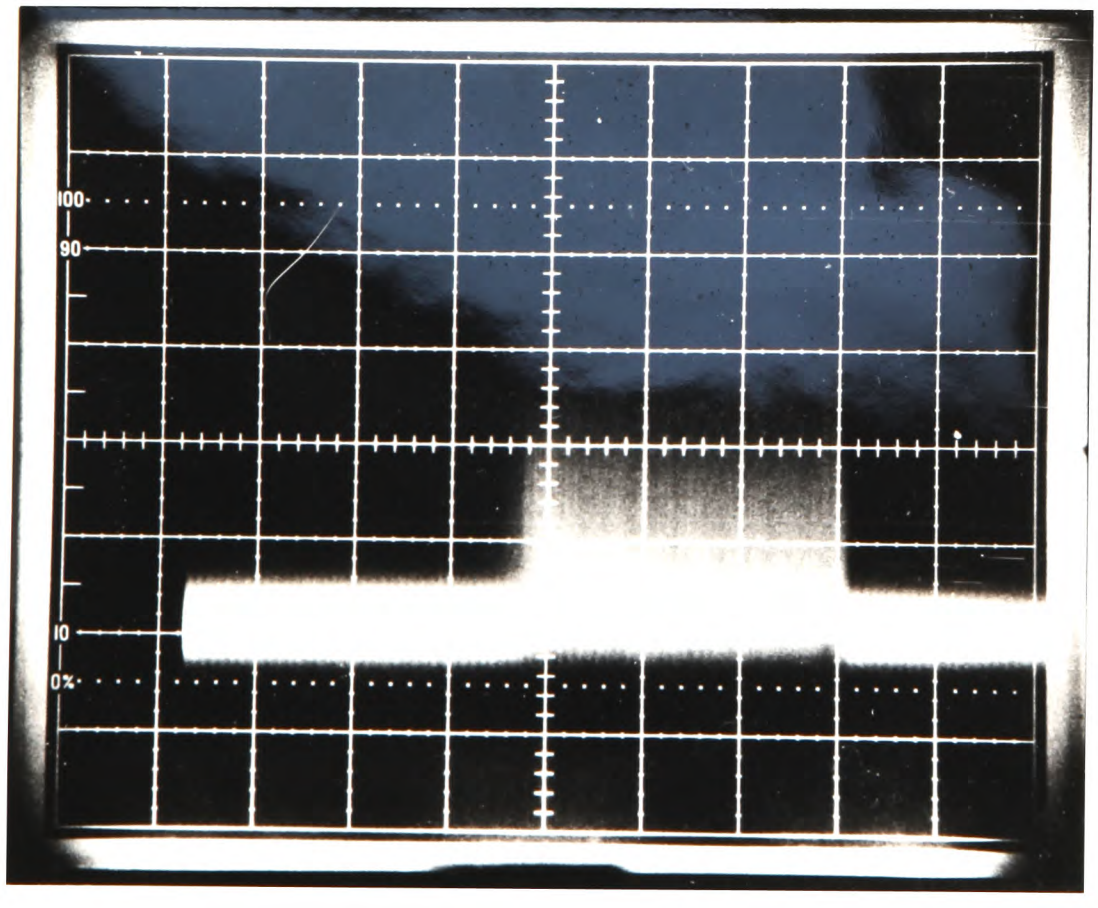
← D.C. Restorer input from charge amplifier



(b) Charge amplifier d.c. level without d.c. restorer

X: 200mS/div

Y: 10mV/div



(c) Charge amplifier d.c. level with d.c. restorer.

X: 200mS/div

Y: 10mV/div

Further quantitative tests using bursts of pulses from a signal generator showed that the performance of the prototype D.C. restorer was good enough to restore the baseline to better than 1% of reference at 2 MHz, with 50% duty cycle (250 nS wide pulses). This is sufficiently accurate and fast.

III.7 LOGIC CONTROL, COMPUTING AND SOFTWARE REQUIREMENTS

This brief discussion of logic control and the associated computing requirements is divided into two sections. The first is that associated with the testing of the prototype channel of electronics (see Chapter IV), the second with the additional problem of handling ∿300 such channels in the final device.

Prototype channel Control

The internal hardware controlling logic in the prototype was designed (a) to accept certain command pulses (software-sequenced) from a computer and (b) to write data out to the computer. These commands may be split into five groups which are largely self-explanatory. In summary:

(i)	Initialize:	clears counters, sets initial addresses etc.	
(ii)	Mode:	(a) Data Acquisition (continuous)	
		(b) Data Digitization and Readout (trigger-by-trigger)	
(iii)	Enable and Start:	in the appropriate mode	
(iv)	Stop and Disable:		
(v)	Read Data:	(a) Ionization (b) Capacitor Address	See III.4
		(c) Time-of-Arrival (d) Trigger Number	See III.5

The prototype channel of electronics was built for use in a CAMAC environment. (A photograph of the prototype channel, complete but for preamplifier, is shown on the next page.) A channel controller in a separate CAMAC unit decoded command signals from the CAMAC 'F' and 'A' lines in the crate and passed them to the channel via a front panel link. The channel controller also accepted the external event trigger, from which the 'stop acquisition' pulse was generated a certain fixed time afterwards (see III.5).

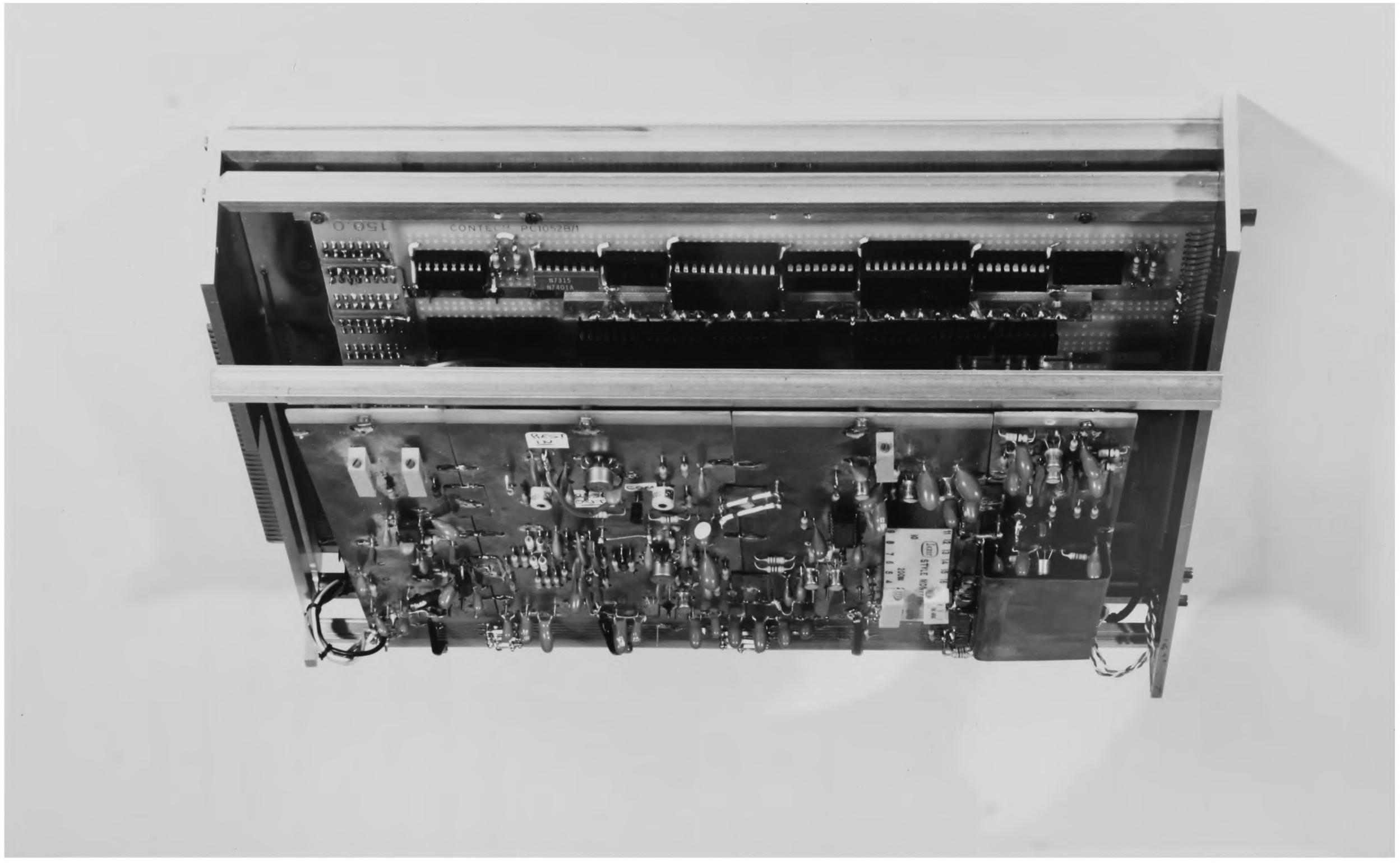
The CAMAC crate controller was interfaced to a DEC PDP8 minicomputer (8-12K word core). The flexibility of CAMAC allowed the simple addition of a display, a scaler, input and output registers to the computer-accessible hardware.

Prototype Channel Software

The PDP8 was programmed at assembler language level (PAL). Two programs were produced, one with the accent on efficient and flexible data collection, the other emphasizing the aspects required for testing the prototype hardware.

Both programs included checks on the validity of the data received. This was made possible by the presence of certain redundancies in the data. For instance, a condition was imposed to make sure that the times-of-arrival read out were in a monotonically decreasing order (see III.5) etc.

The ability to display on-line data, either on an event-by-event basis, or as a histogram of a certain portion of data over several events, proved most useful.


CONTECH PC1052B/1
N7315
N7401A

Shown in Fig. III.34(a), (b) and (c) are three examples. The photograph in (a) shows an updating event-by-event display of all the data output for one event by the prototype channel. The regularity of the features in the display occurs because the signals were produced by a pulse generator (see IV.2). It it will be noticed that four of the pulse heights are lower than the rest: one of the quad MOSFET capacitor address gates was substandard. This diagnosis is typical of the uses of such a display when 'debugging' the electronics.

In (b), the on-line ionization spectrum from an x-ray source is shown (see IV.3). In (c), the on-line time-of-arrival histogram is shown for particle data (see IV.4) (after subtraction of the event-time zero - see III.5) The peak in the histogram is due to the coincidence with the event trigger.

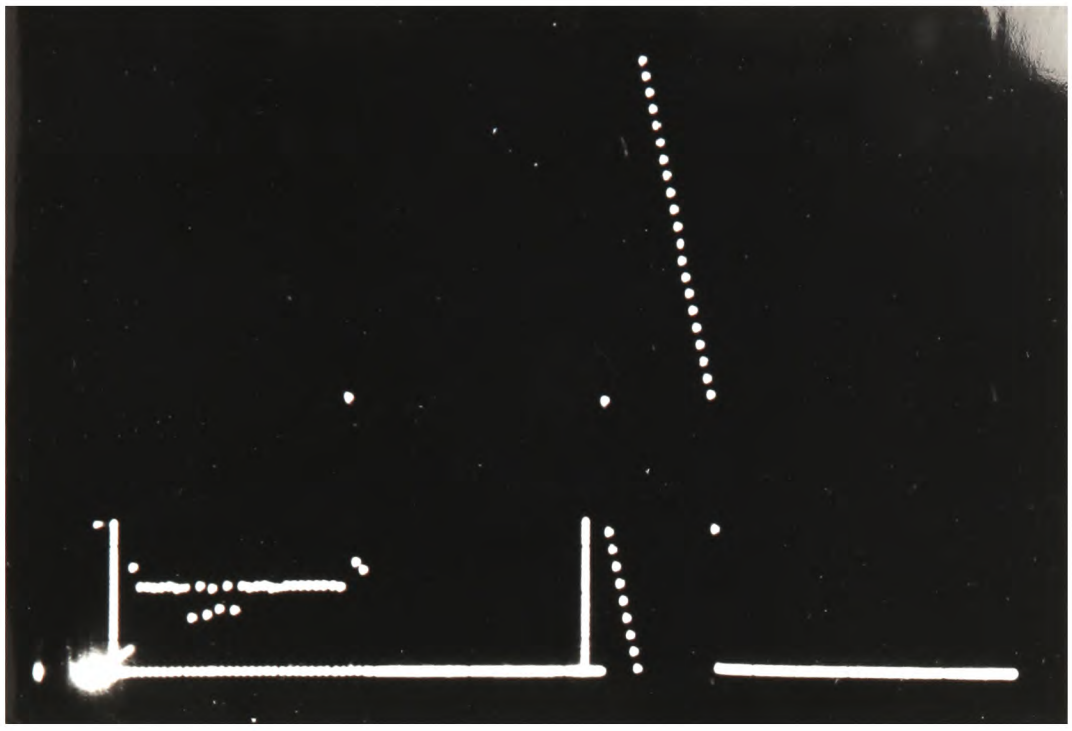
The experience of the tests was that on-line data displays are an important tool in attaining a state of correct system operation.

Final Device Control

The situation in the final device (with ∿320 channels) involves much larger quantities of data. From one event in ISIS there will be ∿320 measurements of the time-of-arrival (9 bits) and ionization (7 bits) on about 30 tracks, making a total of ∿10K 16 bit words (plus one status word per channel). Events can occur at the rate of ∿30 Hz [EHSP].

To reduce the channel output data rate to one which can be handled by a computer, a fast buffer memory is used. The ∿320 channels are split into four sector of 80 channels apiece (see [IN21]).

Figure III.34

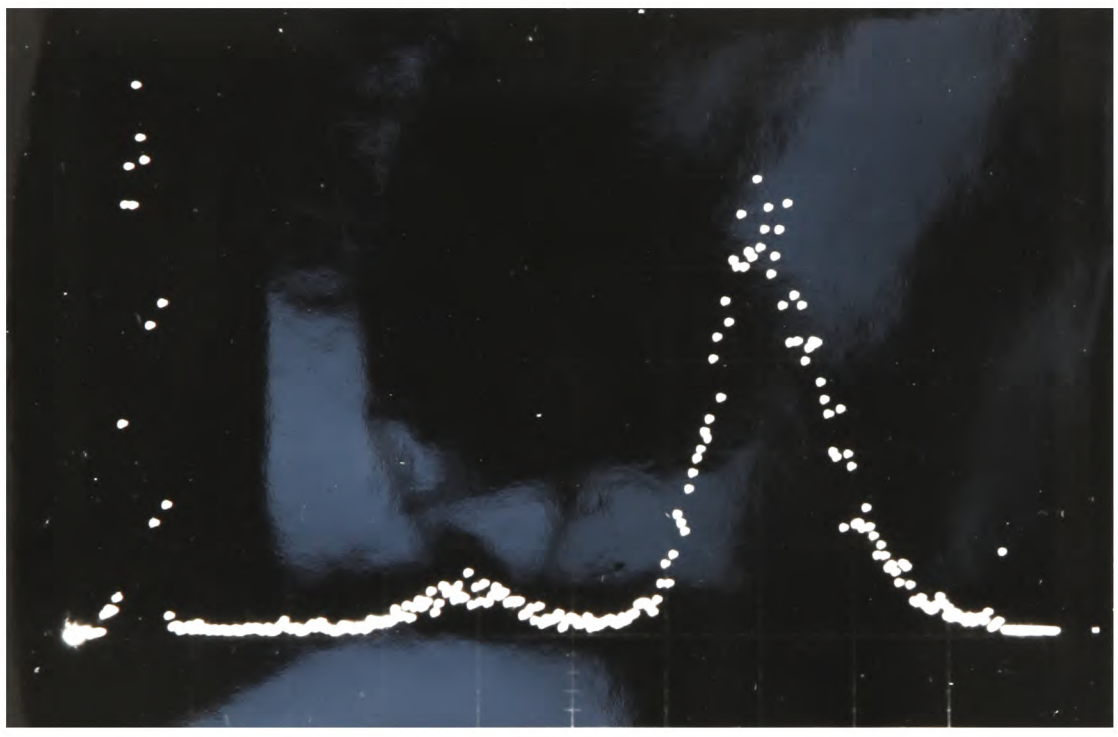


← Pulse Height →
Data

← Time →
of arrival
Data

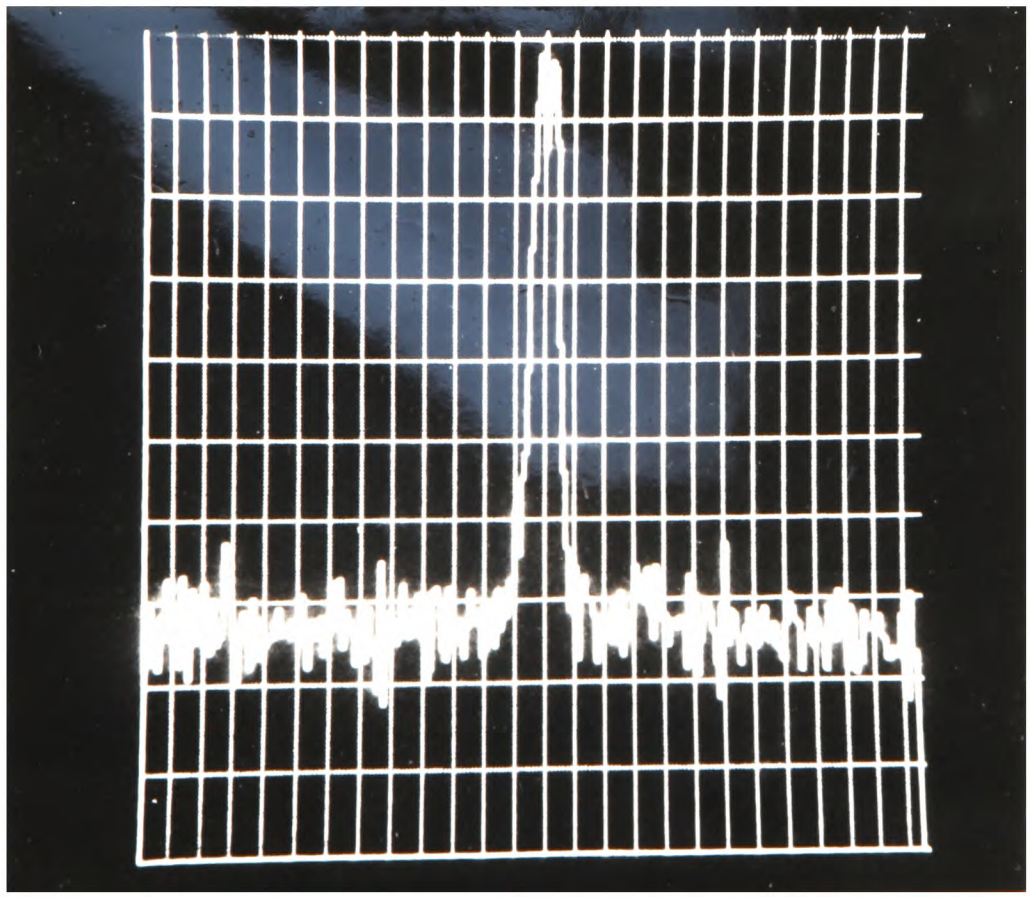
(a) On-line event-by-event data acquisition display.

Pulse generator signals:see IV.2



(b) On-line pulse height histogram.

Fe^{55} x-ray signals: see IV.3



(c) On-line time-of-arrival histogram.

Charged particle signals: see IV.4

Control of the channels is done by a sector controller which performs most of the sequencing actions undertaken by the software in the prototype (see [IN30]). The data from the 80 channels in a sector (when digitization is complete) are read into a fast CAMAC 12K buffer memory via one of four memory ports. The time taken for readout of the information on ∿30 tracks to the buffer is ∿2 mS.

The data is then transferred to the memory of the controlling computer by direct memory access through one port. At 4 M words/sec, the transfer time is 25 mS, leaving the system ready in time for another event. With a 64K main memory, about 6 events can be taken before the memory is full. The data is then read out onto magnetic tape at the end of the beam spill. Tape is used at the rate of about one reel every 30 minutes at 1600 bpi, 9 tracks.

The controlling computer will allow some on-line analysis of data, and will also monitor (and control) chamber characteristics such as oxygen concentration, temperature, drift velocity, false alarm trigger rate, etc.

The off-line computing, done with a much larger and faster computer, involves:

(a) the matching of the tracks in ISIS with those in the rest of the apparatus (bubble chambers, drift chambers etc.) (see [EHSP]),

(b) the subtraction of the pedestals from the ionization data (see III.4) for each of the 10000 memory capacitors,

(c) the application of an estimator to determine the most probable ionization loss, (after correcting for track angle) and thus particle velocity (see II.1),

(d) calibration (using beam tracks) and additional checks on the data.

CHAPTER IV

THE PREDICTED AND MEASURED PERFORMANCE OF ISIS

The use of a computer model of ISIS is discussed in IV.1. The various experimental tests made to confirm the validity of the model are described in IV.2 (with artificial signals), IV.3 (with proportional counter signals from an x-ray source) and IV.4 (with charged particle signals from a prototype ISIS chamber). The derivation of the optimum design is discussed in IV.5. The predicted performance of the whole system is described in IV.6.

IV.1 THE USE OF A COMPUTER MODEL

It would be foolish to build an expensive piece of apparatus for experimental physics without previously ascertaining that the performance of the equipment would be to a sufficient standard.

With this in mind, a computer model has been set up of the handling of ionization track signals by ISIS. The program contains routines that simulate all the important gas state, electronic and noise processes, as described in Chapters II and III. The value of the simulation lies in the ability to vary the parameters of the model and inspect the results of so doing. The simulation was used:

(a) To optimize the design with respect to the compromise between attainable SNR and tolerable systematic effects (e.g. inefficient charge collection, see later).

(b) To determine the performance characteristics of the final, optimum, design.

The Model

The computer program models the treatment of the signal from one ionization sample (one channel of the 320) during its progress through the signal processing system. Signal processing in this context includes everything that occurs from the time that the charged particle traverses the chamber, to the time that digital values are available representing the amount of ionization in a sample and the time-of-arrival of that ionization.

A schematic diagram of the simulated system is shown in Figure IV.1. The event-specific input data consists of:

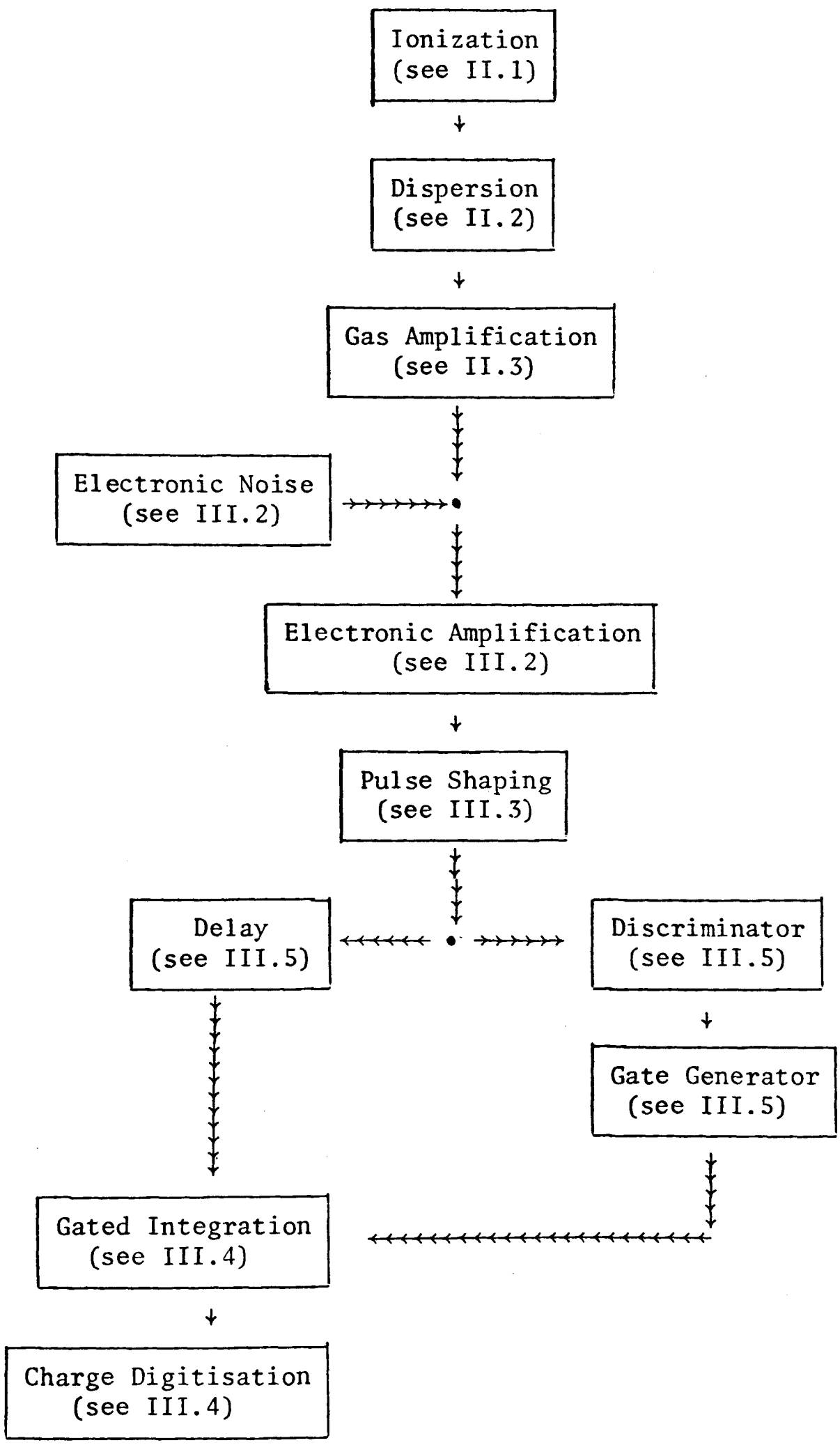
(a) The number of ionization electrons in the sample

(b) The sample drift distance

(c) The track angle.

(d) The event time - zero.

FIGURE IV.1 PROCESSES INCLUDED IN THE SIMULATION



The ionization electrons are given random, weighted, arrival times characteristic of their drift (see later). The simulated gas amplifier output pulse has an effective electronic noise current added to it, after which the signal is processed in a simulation of the electronics. This includes the effects of amplifier responses, pulse shaping, pulse discrimination, gated integration and digitization. (No attempt was made to simulate the D.C. Baseline Restorer, since this acts on a timescale long in comparison with signal durations.)

Noise processes are included using the Monte-Carlo technique as:-

(i) Dispersion of the electron arrival times. This results in a noisy signal, and is characterized by the weighting of the random electron arrival times, according to the dispersive process: (see II.2).

(a) diffusion dispersion

(b) field geometry dispersion

(c) track angle dispersion

(ii) Electronic noise. This noise is continuous. It is of fundamental electronic origin, being associated with the preamplifier input stages. In the program, Gaussian random white noise of the correct (measured) spectral density is added to the signal (see III.2).

A more detailed discussion of the program is given in Appendix 4, which also includes a description of the parametrization of the simulated processes. It is useful to regard most of the parameters as 'fixed' and a few as 'variable'. The fixed parameters are those which are known from previous work or from measurements:

e.g. (i) the characteristics of the dispersive processes

(ii) the magnitude of the electronic noise

(iii) the gain and linear response of the electronics.

The variable parameters are those which can be altered to obtain optimum performance. These are:

(i) gas gain G ($\lesssim 10^4$, see II.3)

(ii) trigger-on-firing level

(iii) trigger-off-firing level

(iv) analogue signal delay

(v) integration gate extension

} see III.5

The output of one run of the simulation program takes the form of:

(i) the value of the gated integral of the signal

(ii) the digitized value of this integral

(iii) the values of the discriminator and gate firing times

(iv) an optional display of the signal profile and gate timings.

The gated integral is compared with that expected from the original charge in the ionization sample, giving a system charge collection efficiency. To be useful, this must be better than ∿99% (see IV.5) and so represents the tightest constraint on design. The variable parameters of the model are chosen to satisfy this condition compatible with minimum gate width (see IV.5).

Because of the effect of the noise processes, no two runs of the program with identical parameters will yield the same output values. For this reason, many runs (usually ∿300) of the simulation are made, allowing statistics to be obtained on the system performance for a certain set of parameters.

Before the predictions of system performance could be trusted, checks on the validity of the simulation were made. The tests are described in the next three sections, and were chosen to approach, as near as was feasible in the time available, the testing of the full-scale device. In all cases measurements on real prototype equipment are compared with those expected using the simulation. Confidence having been gained in the simulation, this model can then be relied on to be useful in the design of an optimum system (IV.5), and in the prediction of the performance of such a system (IV.6).

IV.2 TESTS USING ARTIFICAL SIGNAL SOURCES

The initial testing of the prototype electronics during development (see Chapter III) was done with the 'artificial' signals available from pulse generators, sine wave generators etc. In this section the response of the electronics is compared with the simulated response, for three categories of measurement:

(a) verification of signal response

(b) verification of noise response

(c) verification of integration gate timing.

Inasmuch as the measured parameters of the electronics (gains, risetimes etc., see Appendix 4) are used in the simulation, the tests are tautological. However, they serve to check the consistency of the model.

Verification of Signal Response

The response of the electronics to signals was checked by two methods:

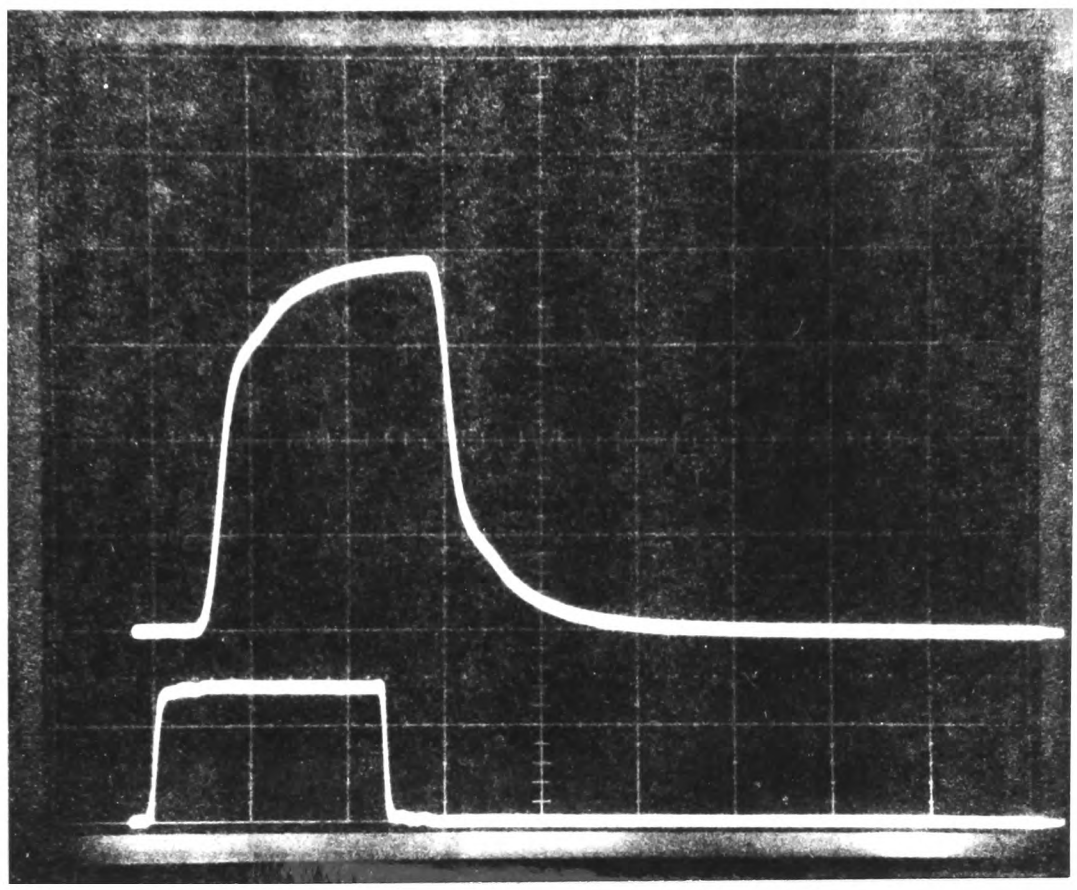
(i) Inspection using an oscilloscope of the square pulse and step function responses (accuracy ∿5%).

(ii) Measurement of frequency response using a sine wave generator (accuracy better than 1%).

A typical measurement of the first type, using a 'scope and a fast square pulse generator, is shown in Fig. IV.2. The photograph shows the prototype preamplifier output (top trace) for a 5 μA x 120 nS input pulse (bottom trace). The amplitude of the output pulse is 385 mV; the simulation predicts 400 mV for the same input pulse. The finite preamplifier risetime of ∿33 nS is observable in both real and simulated outputs. Note, however, the slight distortion of the measured waveform. This is due to parasitic coupling of the input pulse to the first stage. The provision of a suitable generator signal input to the amplifier was made difficult by the current-sensitive nature of the circuit.

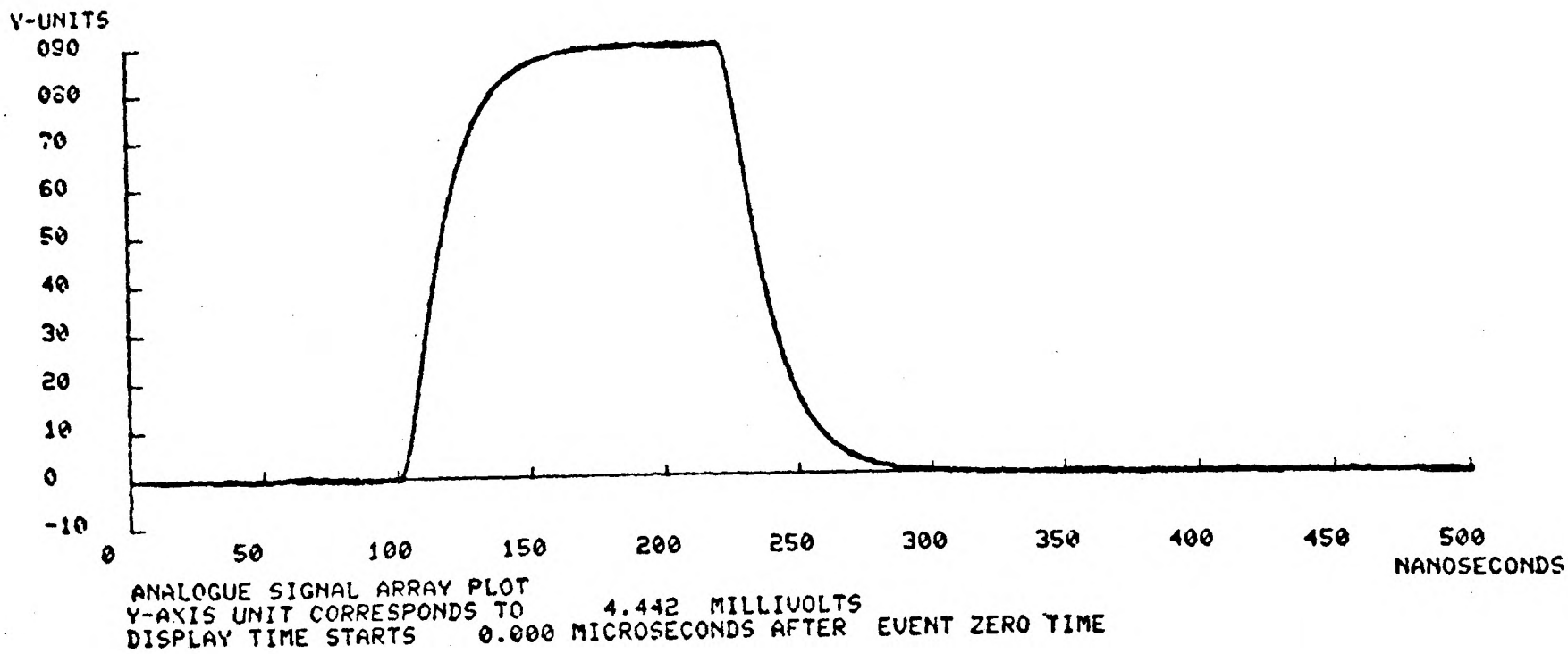
Another example of the use of a semi-quantitative visual comparison of real and simulated waveforms is given in Fig. IV.3. Here is shown a photograph of the response of the prototype shaper (top trace), to a step function input (bottom trace), and the simulated response under identical conditions. Since a critical inspection of the response is required, the 'scope gain was adjusted to allow easy measurement of the waveform using the graticule. As a result, absolute amplitude information is lost in this case.

It can be seen that the response is of a typical high pass type, tending to an asymptotic value determined by R_o of Fig. III.13 (see III.3). The time to fall to 50% of peak is 1.7 μS for the measured response, whereas the simulation predicts a relative amplitude of 47% at this time.



(a) Measured Response.

X: 50nS/div
Y: 100mV/div



(b) Simulated Response

Figure IV.2 Preamplifier Square Pulse Reponse

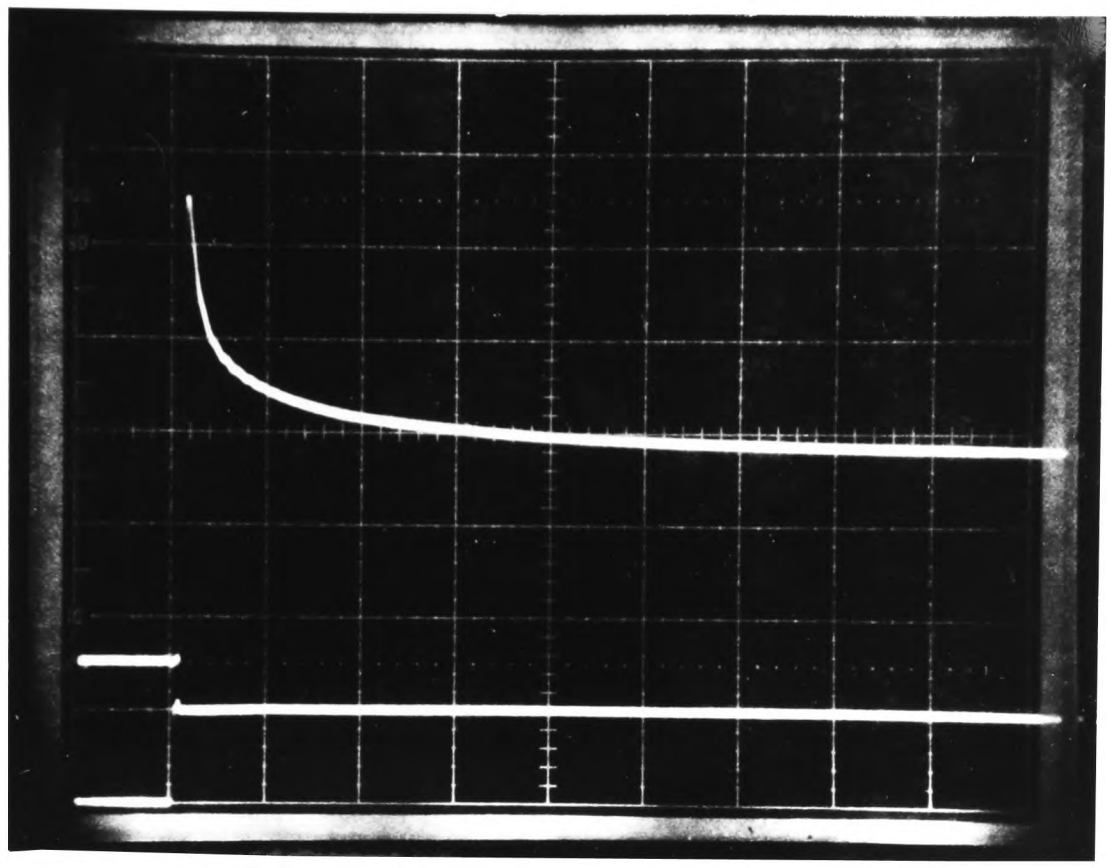
The reason for the difference can be seen in Fig. IV.4. This shows the same situation as Fig. IV.3 but on an expanded time base. The explanation for the discrepancy is that the step input pulse has a finite rise time. This results in a peak output amplitude that is lower than expected, relative to the late portions of the pulse.

Measurement of the frequency domain response - method (ii) - allows an easy yet accurate verification of the characteristics. Typically, a calibrated variable-frequency sine-wave source was employed as input and an ac voltmeter was used to measure the ratio of output to input amplitude.

The measured frequency response curves for the above examples of the prototype preamplifier and shaper are plotted in Figs. IV.5 and IV.6 respectively. On these, the simulated response curves are also shown. The real and computed responses agree over the range 10 KHz to 20 MHz to within ±0.25 dB or ±3% amplitude in both cases. However, the sensitivity of the system performance to effects at the 1% level means that these results, accurate as they are, may not be good enough. If the effects of the deviations can be detected, 'trimming' of the response may be necessary.

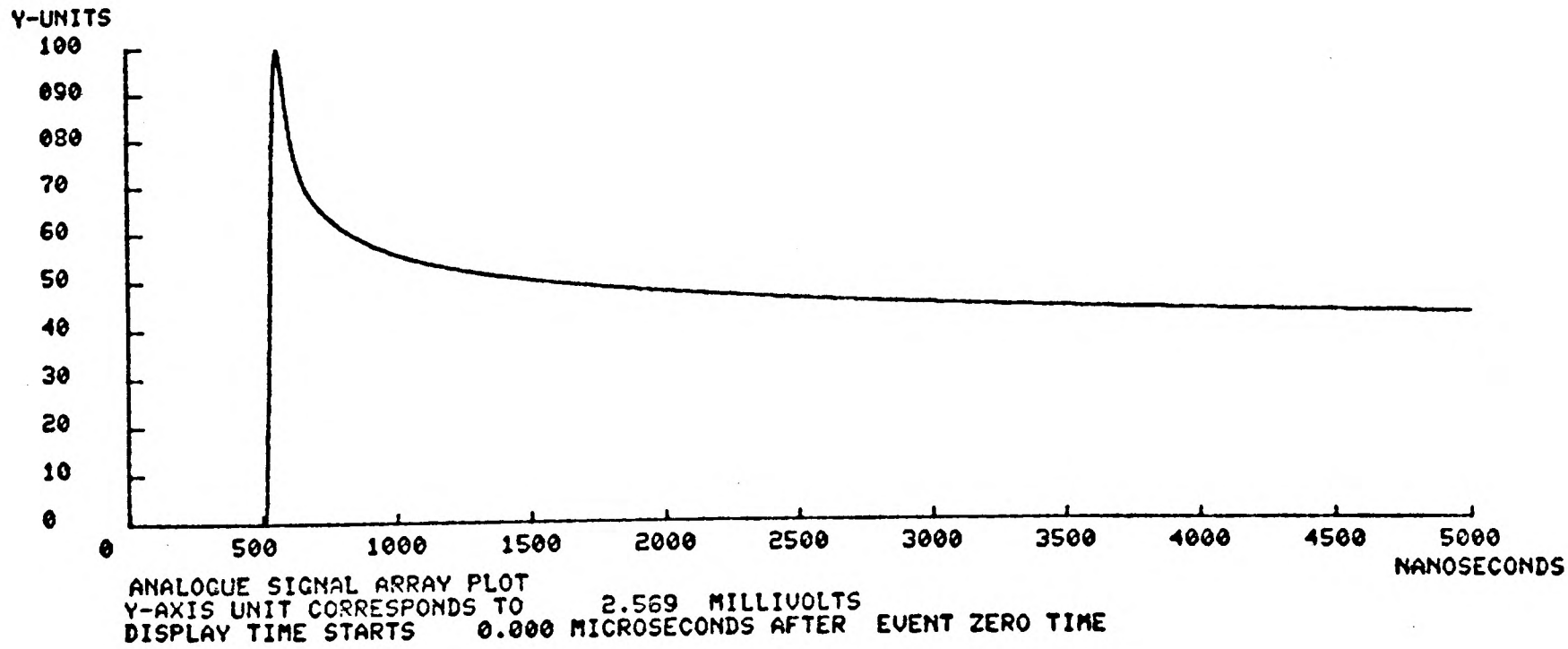
Verification of Noise Response

Accurate predictions are required of the effects on system performance of prevalent signal-to-noise conditions (see IV.5, IV.6). The sources of noise were discussed in II.2. The optimum situation is considered in which the dominant noise is that from the preamplifier front-end. Other noise (r.f. pickup, crosstalk etc.) is assumed to be present only at relatively low intensity. To verify that the



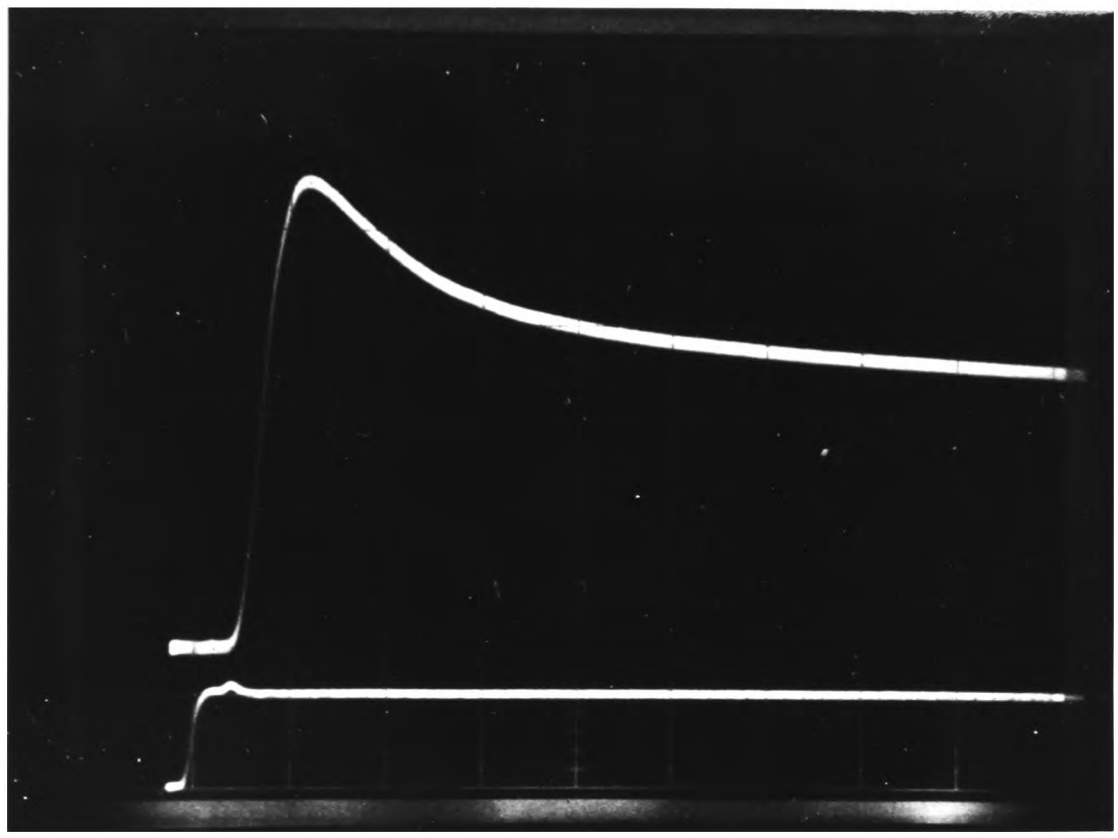
(a) Measured Response.

X: 500nS/div
Y: Uncalibrated

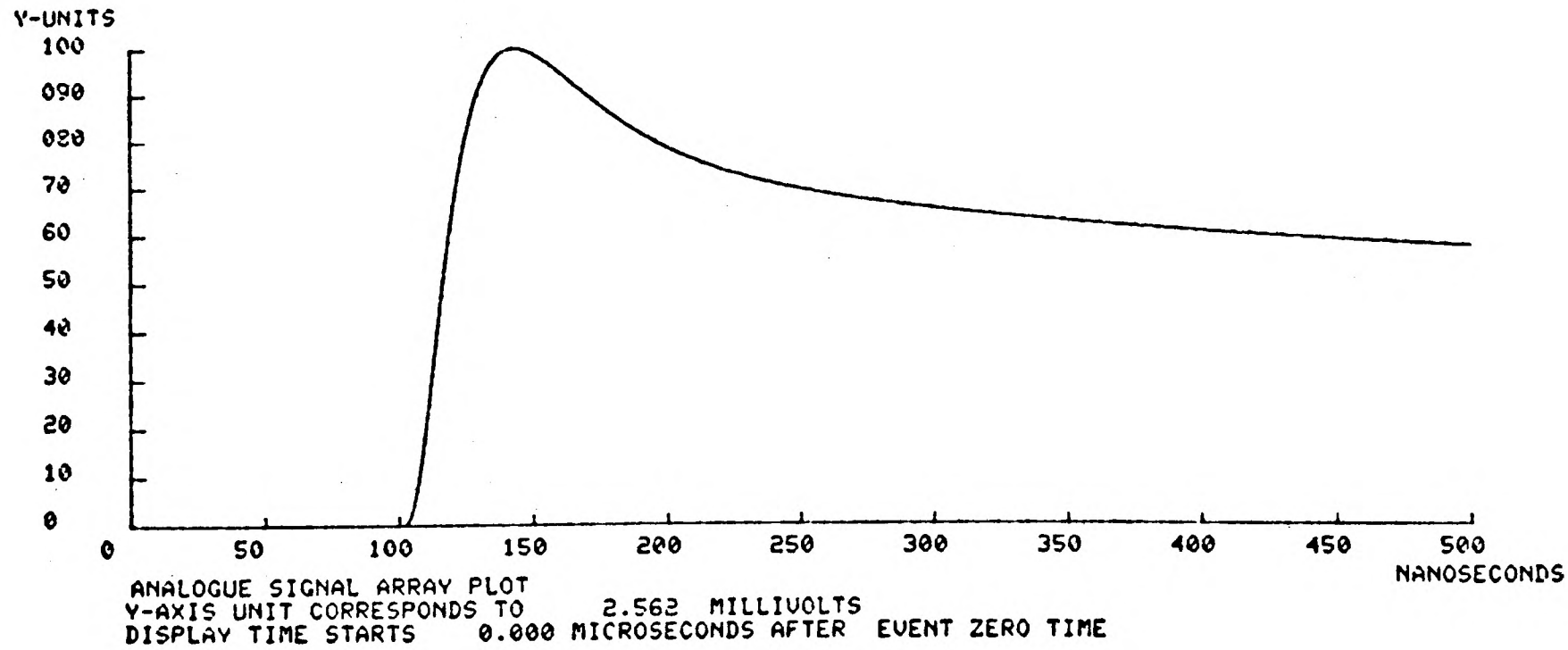


(b) Simulated Response

Figure IV.3 Main Amplifier and Shaper Step Response.

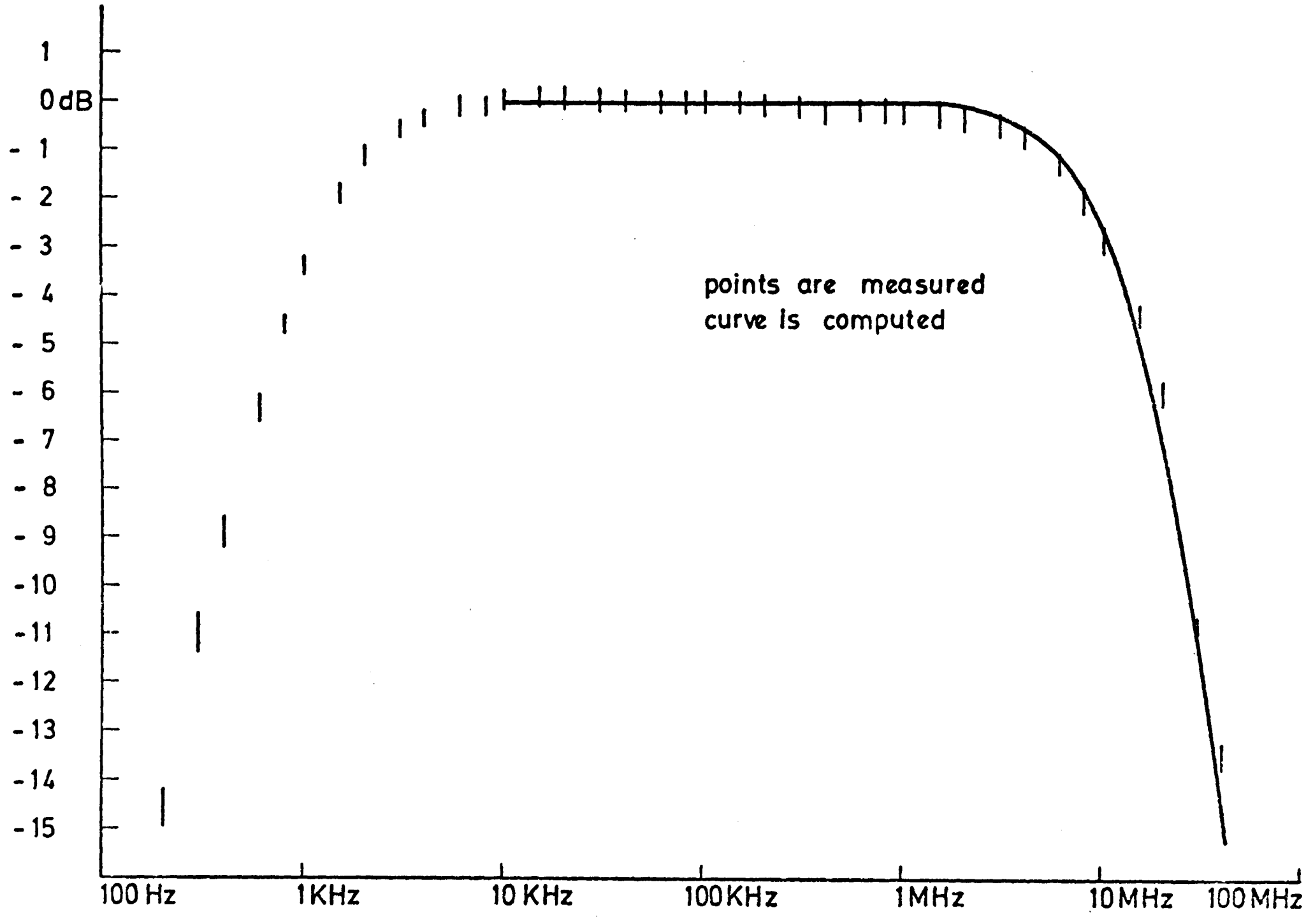


(a) Measured Response. X: 50nS/div
Y: Uncalibrated



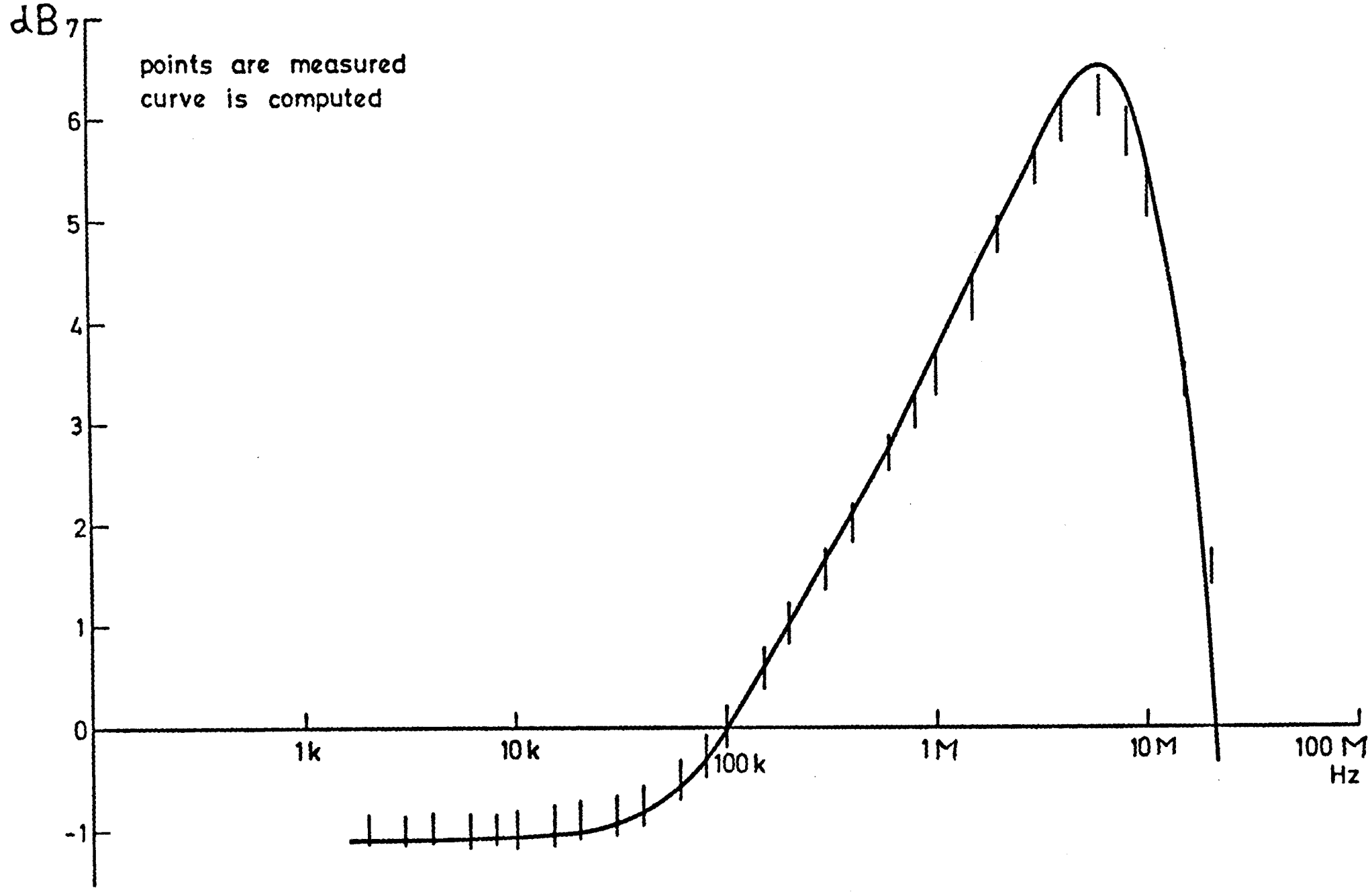
(b) Simulated Response

Figure IV.4 Main Amplifier and Shaper Step Response



Preamplifier frequency response curve.

Figure IV.5



Main amplifier and shaper frequency response curve

Figure IV.6

electronic noise model used in the program is realistic, (see Appendix 4), the results of tests made on the prototype electronics are compared with values obtained from the simulation, in three ways:

(i) RMS noise levels

The measured rms noise levels at different stages of the electronics are compared with those predicted by the simulation. (In this test, and in the two following, the preamplifier was operated with a real chamber capacitance, and under minimum pick-up conditions (see IV.3)). The results of the comparison of noise levels is shown in Table IV.1.

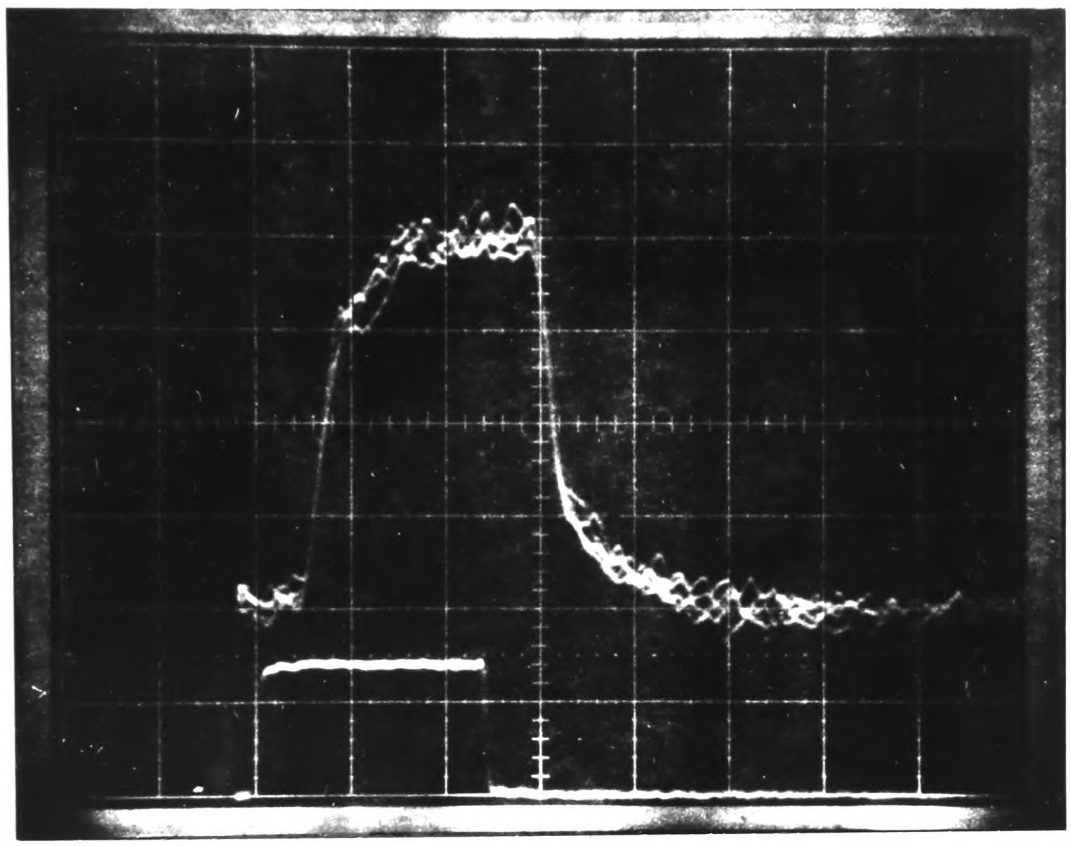
TABLE IV.1 RMS NOISE LEVELS

Measurement Point	Measured Noise RMS mV	Simulated Noise RMS mV
Preamplifier o/p (see text)	(1.25 ± 0.05)	(1.20)
Discriminator i/p	2.1 ± 0.1	2.20
Charging amplifier i/p	1.9 ± 0.1	1.90

The value used in the simulation for the equivalent input noise spectral density was calculated from the measured preamplifier output noise and the preamplifier response. Bearing this in mind, the results are consistent to within the experimental measurement error (∿5%). This indicates that the noise model, in conjunction with the simulation of the system response, is valid to the 5% level.

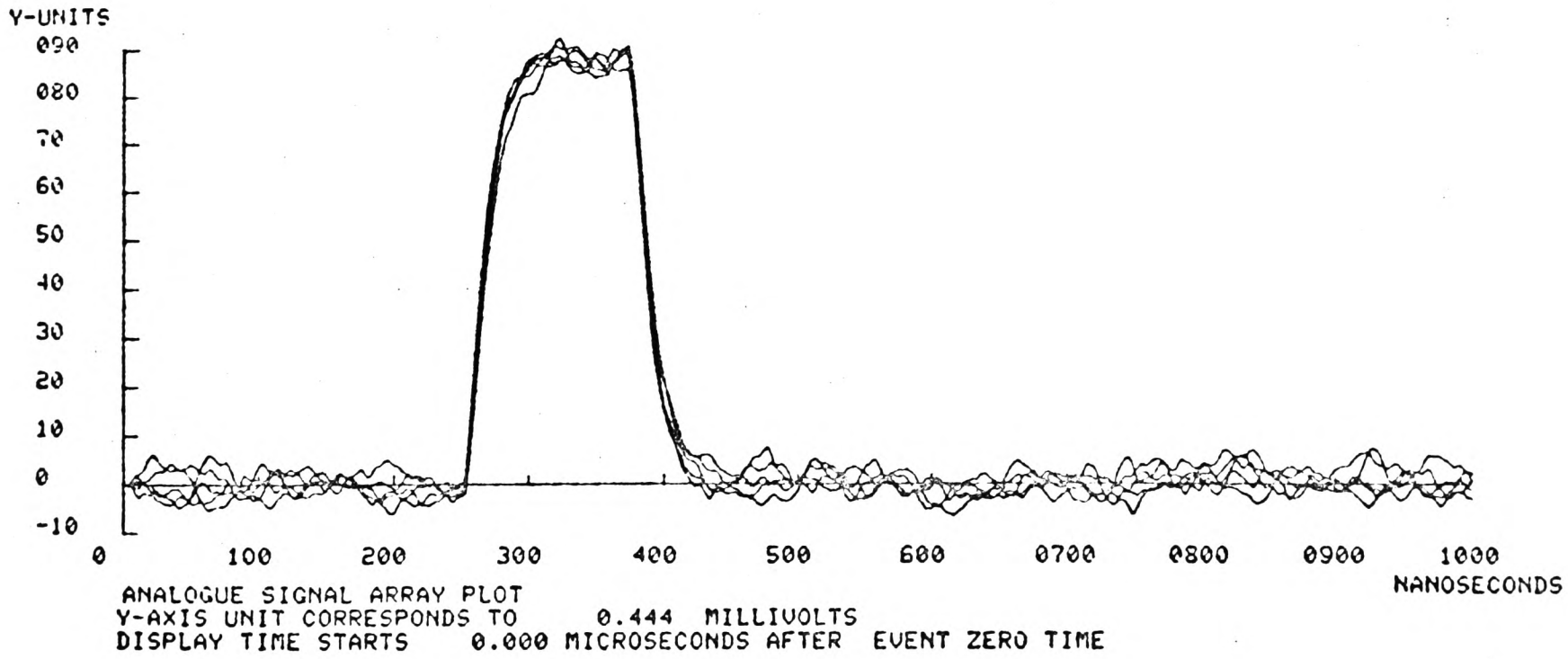
(ii) Visual comparison of noise levels

A qualitative comparison may be made between model and reality by inspection of the waveforms in Fig. IV.7. The 'scope photograph



(a) Measured Response. (5 sweeps)

X: 50nS/div
Y: 10mV/div



(b) Simulated Response (5 sweeps)

Figure IV.7 Preamplifier Small Signal (500nA) Response with Noise.

shows the preamplifier output for five successive input pulses of small amplitude (500 nA). The simulated signals below (for the same conditions) display approximately the same noise amplitude and, more importantly, the same type of noise waveform. This means that the noise spectrum is approximately correct.

(iii) Variation of noise triggering rate with threshold

For the design of optimum SNR, it is necessary to be able to predict the random noise trigger rate for a particular threshold (trigger 'on') level (see III.5, IV.5). Measurements were made of the random trigger rate for various absolute threshold levels; these results are shown in Fig. IV.8. When compared with the simulated results, using a model of an ideal discriminator, large discrepancies were noticed. The disparity was caused by the use of a simplified model for the discriminator. Most discriminators have a finite 'latch time'. This is the time for which a signal must be above threshold before the discriminator fires. For the discriminator used, the latch time was ∿30 nS, (in the case of a signal ∿10% above threshold). When this effect was included in the model, the agreement with experiment became much better, as can be seen in Fig. IV.8. Simulation and measurement now differ by only slightly more than the experimental errors. However, this does not cause concern, since the discriminator treats signals and noise alike.

Verification of Integration Gate Timing

To set up and check the timing of the charge integration gates (see III.4), the electronics was fed with square pulses, and the timing of the integration gates relative to their pulses was observed.

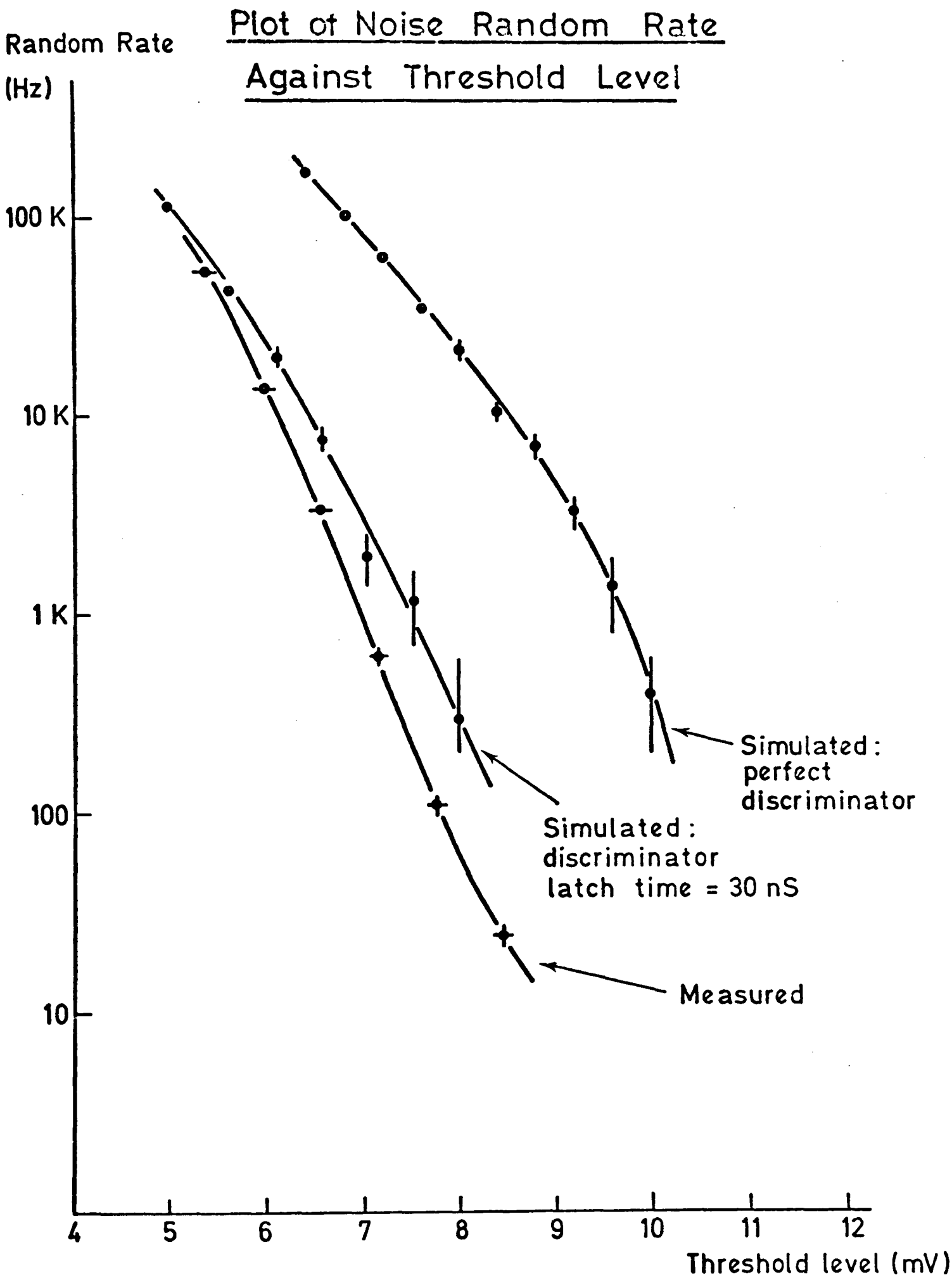
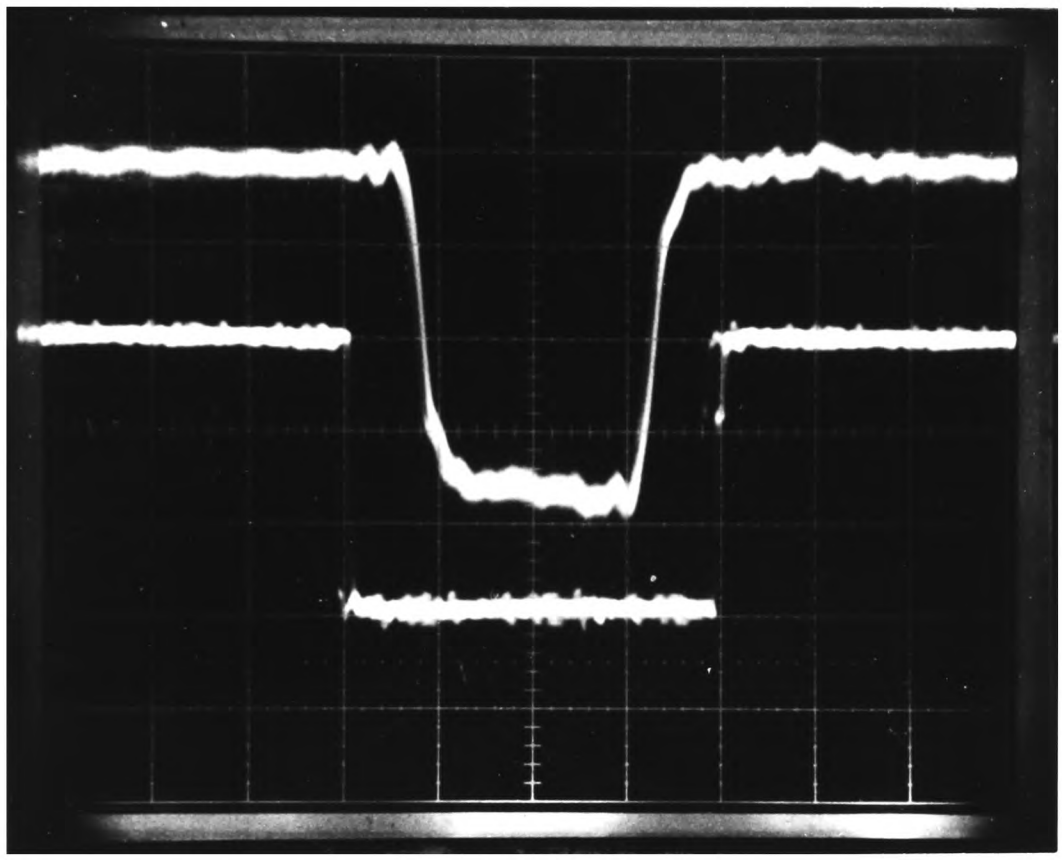
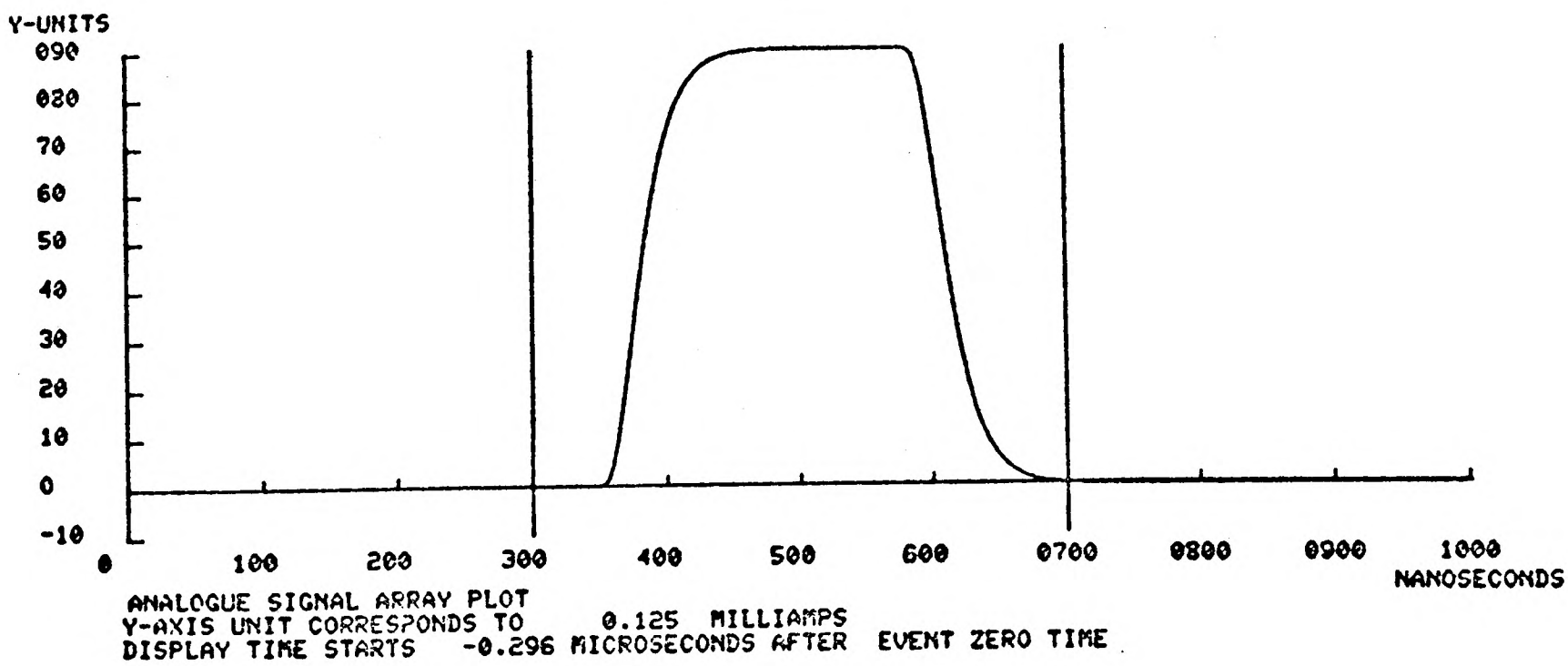

Plot of Noise Random Rate
Against Threshold Level
Random Rate
(Hz)
100 K
10 K
1 K
100
10
Simulated :
perfect
discriminator
Simulated :
discriminator
latch time = 30 nS
Measured
4
5
6
7
8
9
10
11
12
Threshold level (mV)

Figure IV.3



(a) Measured Response. X: 100nS/div
Y: Uncalibrated



(b) Simulated Response

Figure IV.9 Square Pulse Response and Associated Gate Switching Waveform.

This is demonstrated in Fig. IV.9. The photograph shows a typical 'scope display of the analogue pulses and associated integration gates. (Noise on the analogue signal was due to pickup by the 'scope probe.) Below the photo' is a simulation of the same situation. Good agreement is observable: there is approximately 60 nS overlap on both sides of the signal by the gates.

Adjustment of the gate timing involves altering the delay (line) time and the gate extension time, as explained in III.5. The timings shown in Fig. IV.9 were found satisfactory for the tests described in IV.3 and IV.4. However, further work concerning the gate timing is described in IV.5, in relation to optimum performance.

Conclusion

Measurements made on the prototype electronics, and the results of the simulation are consistent to better than 5%. This is a good level of model validity.

IV.3 TESTS WITH X-RAY SOURCES

The tests described in the previous section used, as input, signals available from pulse generators. The characteristics of the signals were markedly different from those due to proportional gas amplification (see II.3). Because of the importance of the signal source in determining the overall system response, it is necessary to check the accuracy of the simulation of gas amplifier signals.

Artificial signals from pulse generators have the attributes of well-defined shape, amplitude and timing. Signals from the gas amplification of ionization have properties dependent on the origin

of the ionization. Consider the ionization signals from the photo-electric conversion near to the wire plane of the photons from a low-energy (∿5 keV) monoenergetic x-ray source. These will have relatively well-defined shape and amplitude (if the ionization has not drifted - diffused - far), but ill-defined timing due to the random nature of the radioactive process. In contrast, the diffuse, drifted, ionization signals from a charged particle track within the ISIS chamber, have ill-defined shape and amplitude, but can have well-defined timing, if external triggering is employed.

In this section and the next, the prototype system performance is compared with simulated results, for signals due to the gas amplification of ionization. This section deals with those results obtained using an x-ray source to produce ionization in a small proportional chamber. This stage in the testing of the prototype is intermediate between the use of well-defined artificial signals and ill-defined particle track signals. The well-defined gas amplifier signals from the x-ray source allowed the collection of much useful quantitative information on the operation of the system, especially the electronics.

Objectives of the Tests with X-Ray Sources

The objectives satisfied by the following tests were:

(i) To check the operation of the specific type of proportional wire chamber geometry described in Chapters I and II, at the working gas gain of $\sim 10^4$. This included making measurements of the required operating voltages, and of the uniformity of response across the chamber.

(ii) To obtain satisfactory overall performance of the analogue and digital electronic systems using, as input, gas amplifier

pulses under realistic SNR conditions. This included making checks on gain, linearity and integrity of the digital system.

(iii) More specifically, to compare the measurements with the predictions of the simulation under the same conditions. This allows checking of those parts of the simulation so far untested, namely the models of ionization dispersion and gas amplification.

The Test Chamber

The geometry of the small proportional chamber used for these tests is shown in Fig. IV.10. The design is of the same type as the ISIS chamber described in Chapters I and II: a wire plane consisting of alternate anode and cathode wires is placed between, and parallel with, two cathode planes. In this particular chamber, the position of the wire plane is asymmetric, the distances to the cathode planes being 2 cm on one side and 4 cm on the other. The wires, of stainless steel, are spaced 3.75 ± 0.01 mm apart, under a tension of a few gms weight. The nominal radii are 12.5μ for the anodes, and 125μ for the cathodes. The use of aluminised mylar film for one of the cathode planes allows soft x-rays to enter the chamber without excessive attenuation. The whole assembly is mounted in a leak-tight fibreglass gas box.

A schematic diagram is shown in Fig. IV.11 of the high voltage connections to the wires and cathode planes. The signal output was taken via 100 pF coupling capacitors from a mid-chamber section consisting of two adjacent anodes and the cathode between them (see II.4). This defined an ionization sample of width 1.5 cm. The other wires were decoupled to ground. Although four separate power supplies

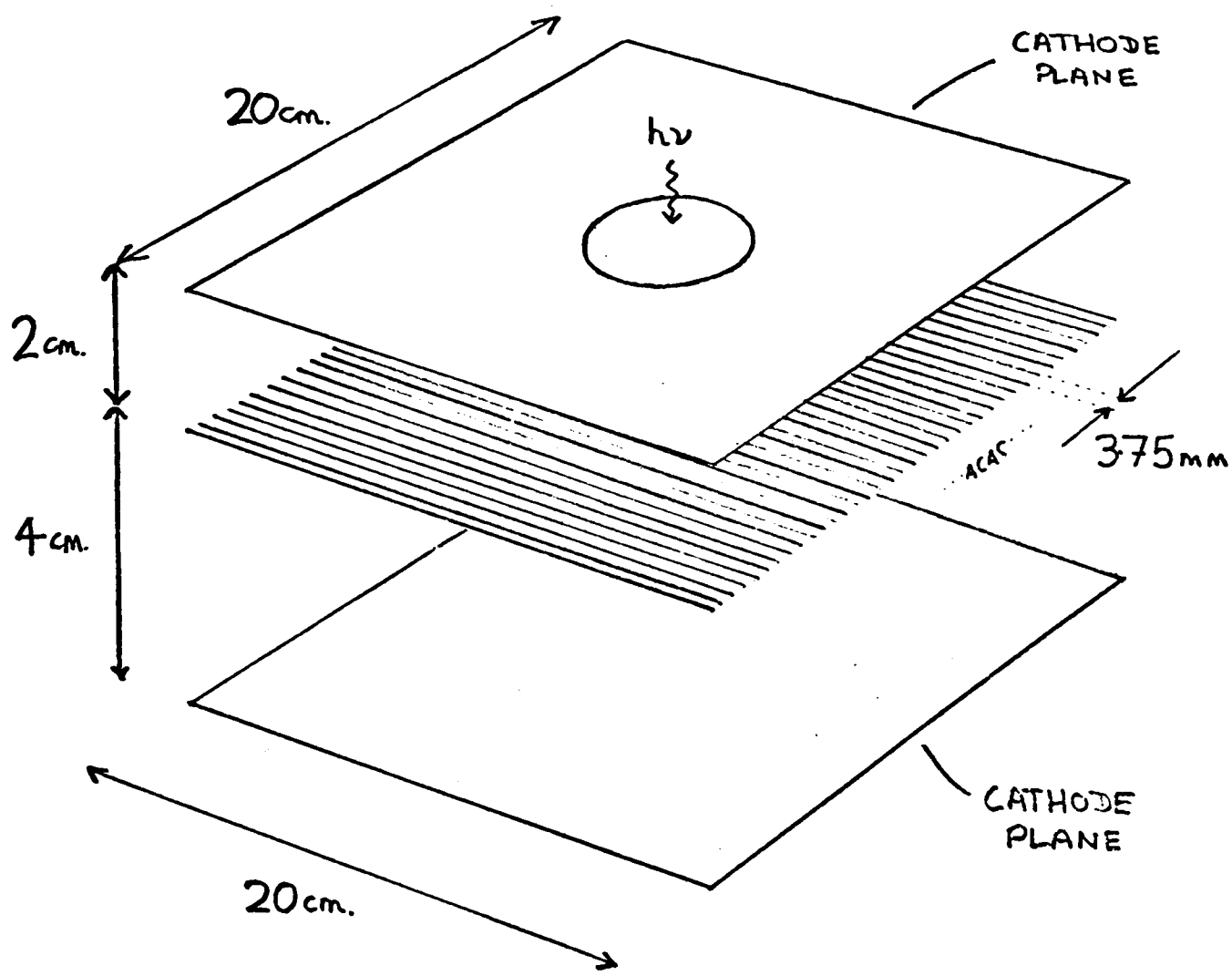
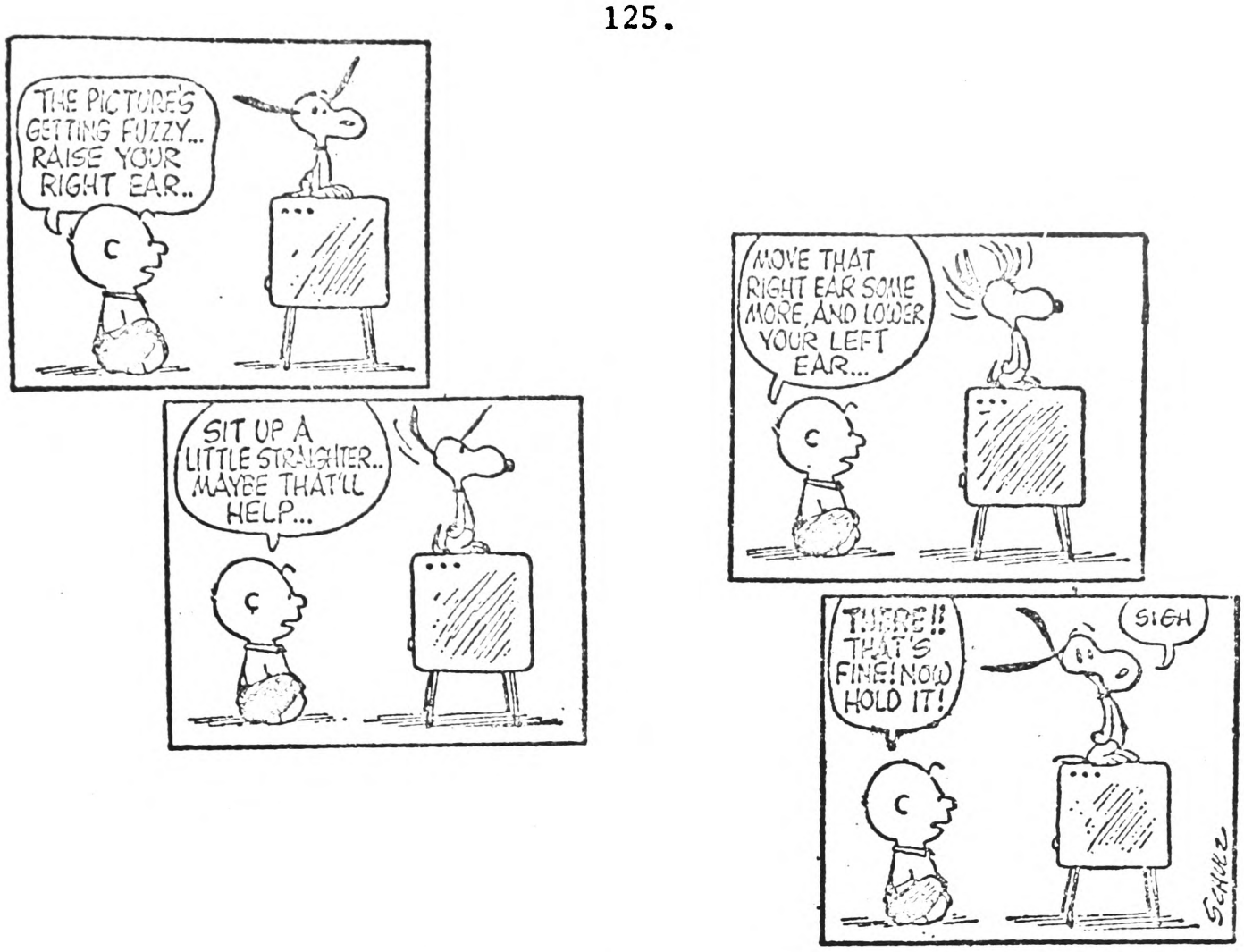


FIGURE IV.10 X-Ray Test Chamber Geometry

were used for versatility, the fields in the chamber are defined by the three voltage differences. Under normal operating conditions, these voltages were adjusted to maintain an equal field on either side of the wire plane (however, see later). Pickup of r.f. by the wires was minimized by precautions involving earthing, screening, and optimum orientation, of the chamber (see top of next page).

The chamber output was fed into the prototype preamplifier and thence to the prototype single channel remote electronics, controlled by a minicomputer, as described in Chapter III.



The chamber was filled with a gas mixture of 80% argon, 20% CO_2, (the proposed filling gas for ISIS - see II.2), at a pressure of about 1" water gauge.

The monoenergetic x-ray source employed for the tests was 2 mCi of Fe^{55}. The photon energy is 5.90 KeV (Mn K_α). This compares with ∿2 KeV for the mean ionization deposited per cm of track for a minimum ionizing particle (see II.1). The use of this source resulted in a conveniently large gas amplifier signal of constant, well-defined, amplitude (see later). The conversion of the photons gave a spatially localized 'blob' of ionization, of cross-section ∿200μ [CJ75]. Because of the small drift distances involved, diffusion of the ionization was minimal. These characteristics allowed investigations to be made of the variation of response across the chamber, at the good resolution of ∿0.5 mm. During most of the tests described later, the source was collimated to illuminate a 1 mm x 10 mm element of the chambers, in a direction normal to the plane of the wires, with the long dimension parallel to the wires. The Fe^{55} signal rate under these conditions was about 1 KHz. (Operation at higher rates of 20-30 KHz

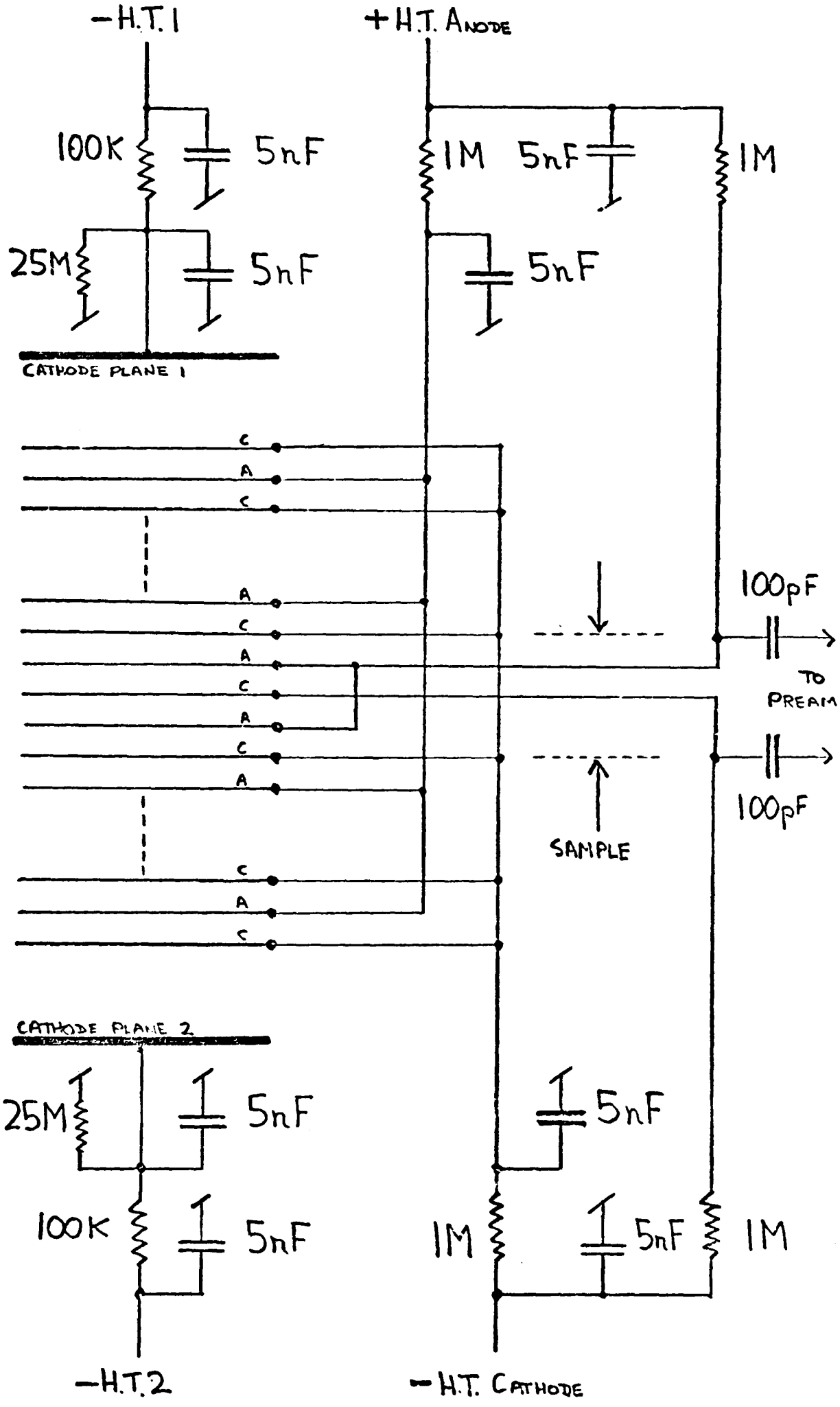


Figure IV.11 Schematic Diagram of Electrical Connections to the X-ray Test Chamber

induced the space charge distortions of gas amplification discussed in II.3.)

The discriminator trigger 'on' level was adjusted to give a random noise rate of a tenth of the signal rate, about 100 Hz (see III.5). This was found to be a satisfactory working point.

Because of the absence of a suitable event trigger (see III.5), artificial event-zero-timing information was supplied by a pulse generator. This resulted in the loss of meaningful time-of-arrival information, but of course did not affect the pulse magnitude data.

The Measurements

The tests performed may be split into two categories:

1. Measurement of a semi-quantitative nature

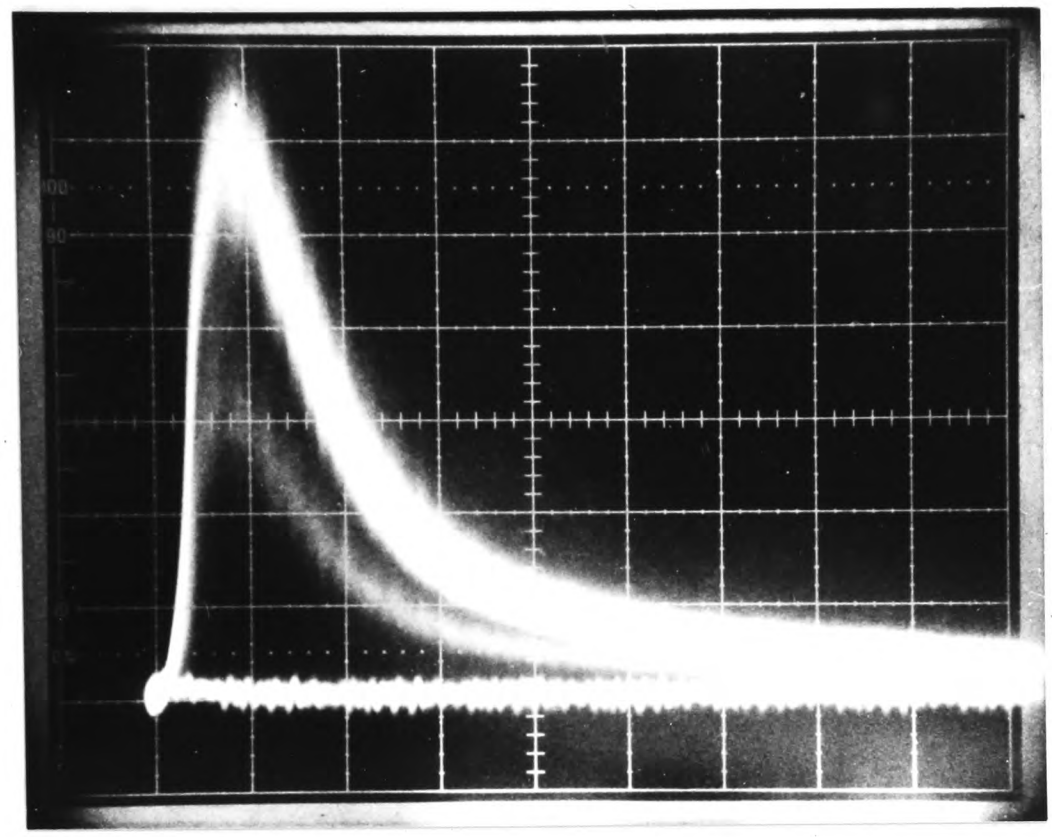
The ionization from the Fe^{55} source photons produces an easily observable and recognizable set of signals. These signals were inspected at various stages of the electronics using an oscilloscope. The waveforms were compared with those predicted by the simulation for a localized ionization of 223 electrons (equivalent to the 5.9 KeV x-ray photon, converting in 80% argon/20% CO_2).

(a) Gas amplifier signals

The chamber signals were examined at the output of the main amplifier, prior to shaping (see III.3). Because of field geometry dispersion of the ionization, the shape of the signal depended on the position of the source (see II.2; diffusion dispersion for the 2 cm drift is small). Two cases are considered:

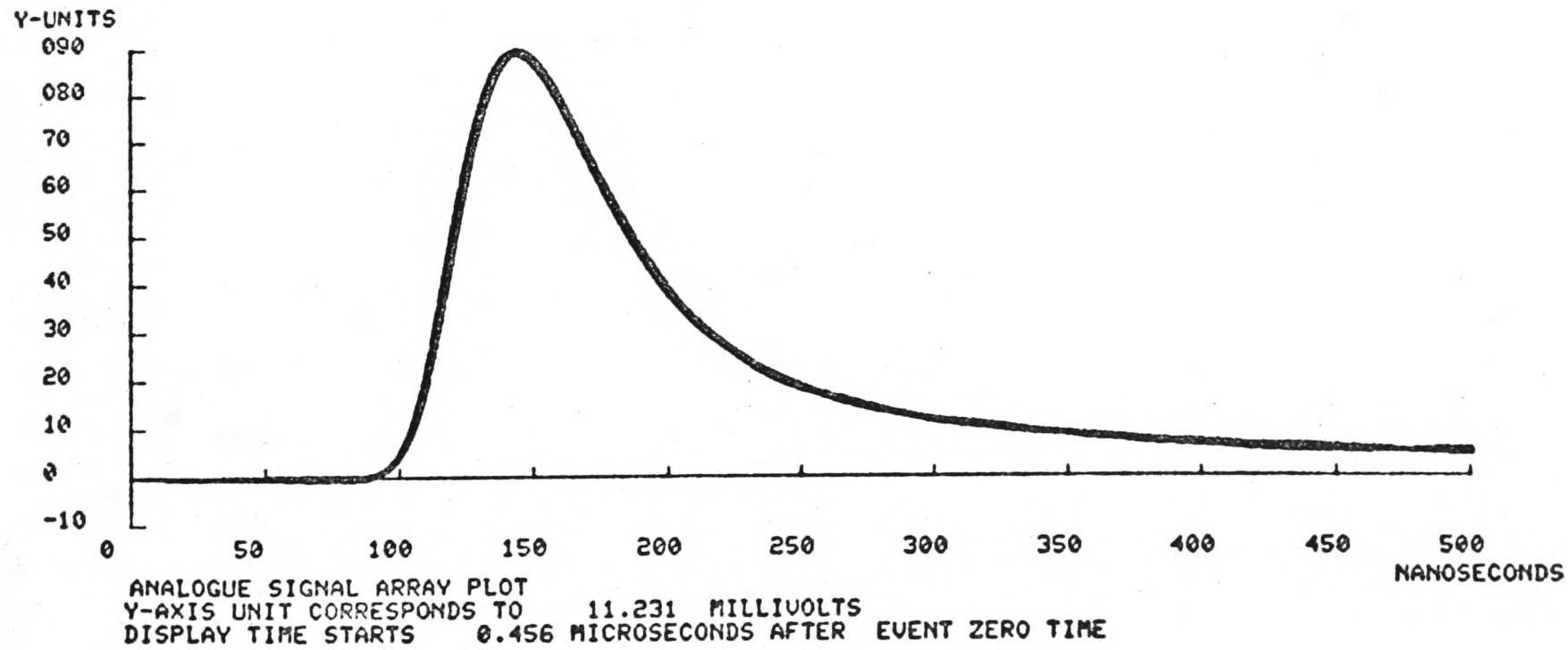
(i) Source over anode

This is the case of minimum dispersion due to field geometry (see Fig. II.3). A photo of the observed signal waveform is shown in Fig. IV.12, together with the simulated wave-



(a) Measured Response.

X: 50nS/div
Y: Uncalibrated



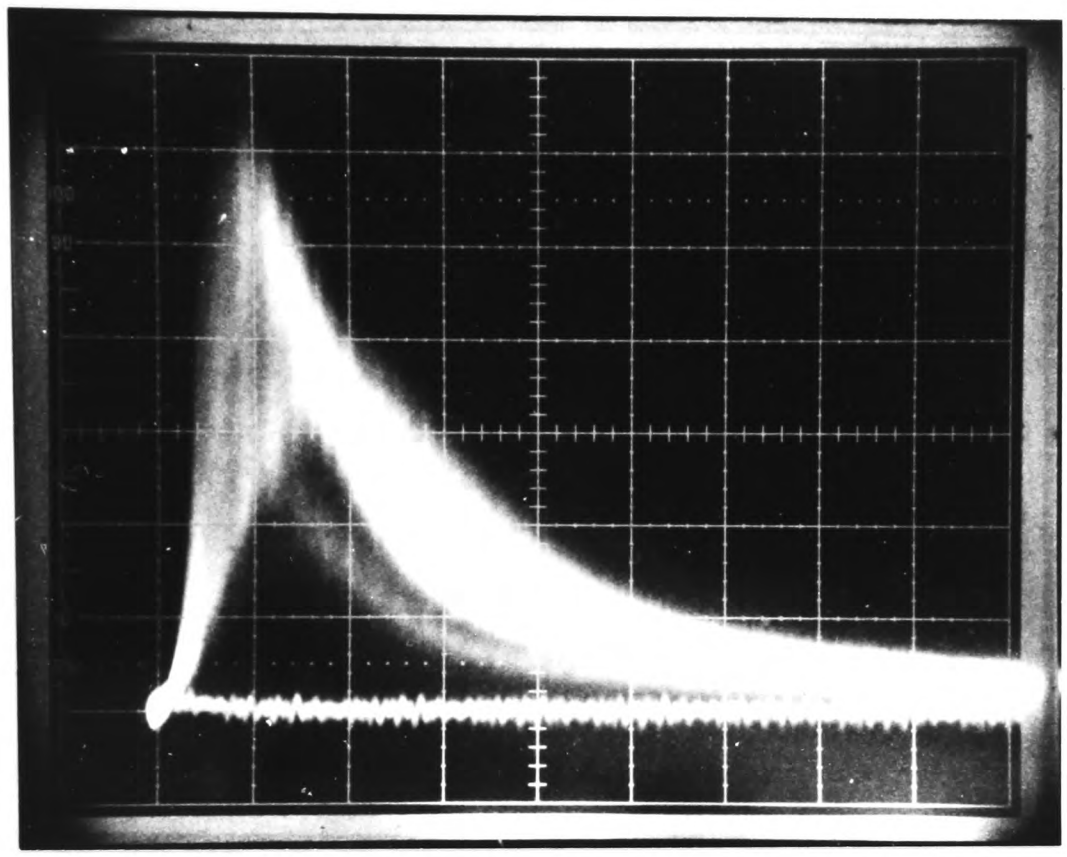
(b) Simulated Response

Figure IV.12 Gas amplification from an Fe^{55} Source over an anode.

form for the same conditions. Qualitatively, the observed and simulated waveforms are very alike. (Note the presence of the 3 KeV argon 'escape' signal in the observed results.) The fixed amount of ionization assumed in the simulation leads to the prediction of a narrower amplitude distribution than observed. In fact, the photon-to-ionization conversion process gives rise to a pulse amplitude distribution of width about 20% (see later). The noisy baseline that can be seen in the 'scope photo was caused by pickup of digital waveforms by the 'scope probe. A more quantitative comparison shows that the 10-90% risetime in both observation and simulation is ∿25 nS, and the 90-10% fall time is ∿150 nS. The measured signal amplitude was 1050 mV, compared with a simulated amplitude of 1000 mV for a gas gain of 10000. The agreement is good.

(ii) Source over cathode

This is the situation of maximum field geometry dispersion (see Fig. II.3). With the x-rays from the source collimated to a width of 1 mm, the effect on the pulse shape is quite noticeable. This can be seen in the photo in Fig. IV.13, and the accompanying simulation of the same case. The spread in arrival times gives rise to wider pulses of lower amplitude. The model of this dispersion is not expected to be highly accurate, because the actual operating conditions differ by ∿5% from those assumed in the calculation of the amount of dispersion. However, the agreement between observed and simulated effects is reasonable: a ∿50 nS time dispersion coupled with a 30% loss of amplitude is apparent in both cases.



(a) Measured Response. X: 50nS/div
Y: Uncalibrated

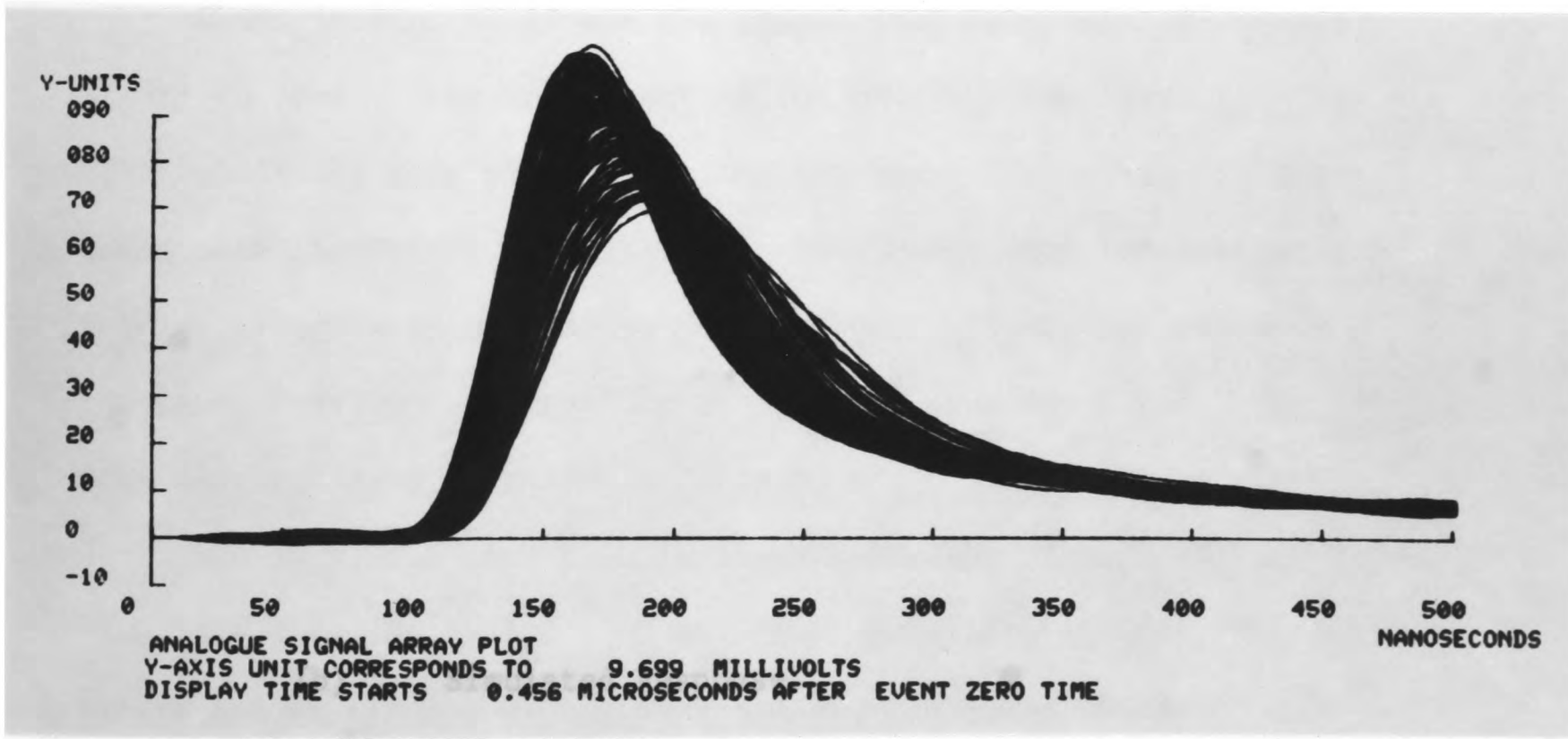


Figure IV.13 Gas Amplifier Signals from an Fe^{55} Source Over a Cathode, Showing Dispersion due to Field Geometry effects.

Measurement of the pulse integral (see later), for the two cases above, showed that there was no loss of ionization due to dispersion, at the level of 2%.

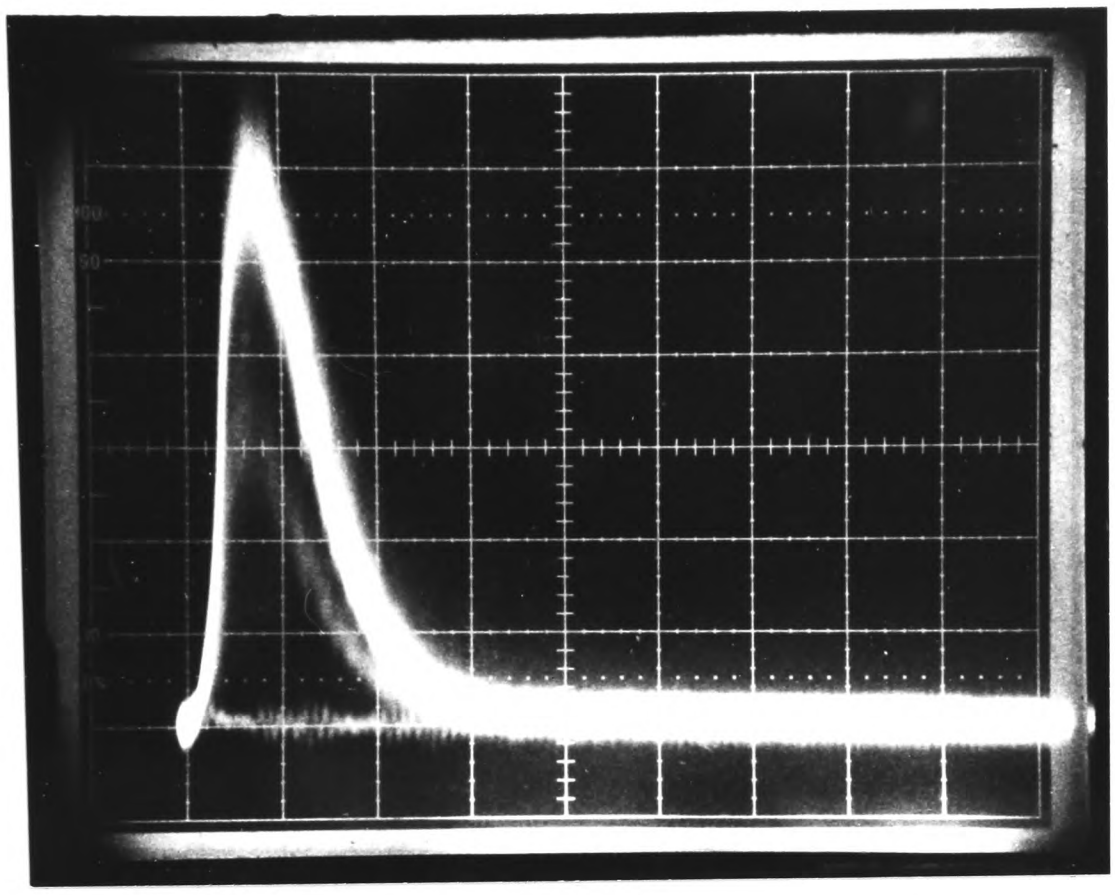
(b) Shaped Signals

To check on the efficiency of the pulse shaping network (see III.3), the Fe^{55} source signals (under the conditions of (a)-(i) above) were inspected at the output of the shaper. A photo of these signals is shown in Fig. IV.14. This may be compared with the accompanying simulation of the same situation. For both examples, recovery to within 2% of baseline occurs in 200 nS. The pulse shaping is thus effective to this level.

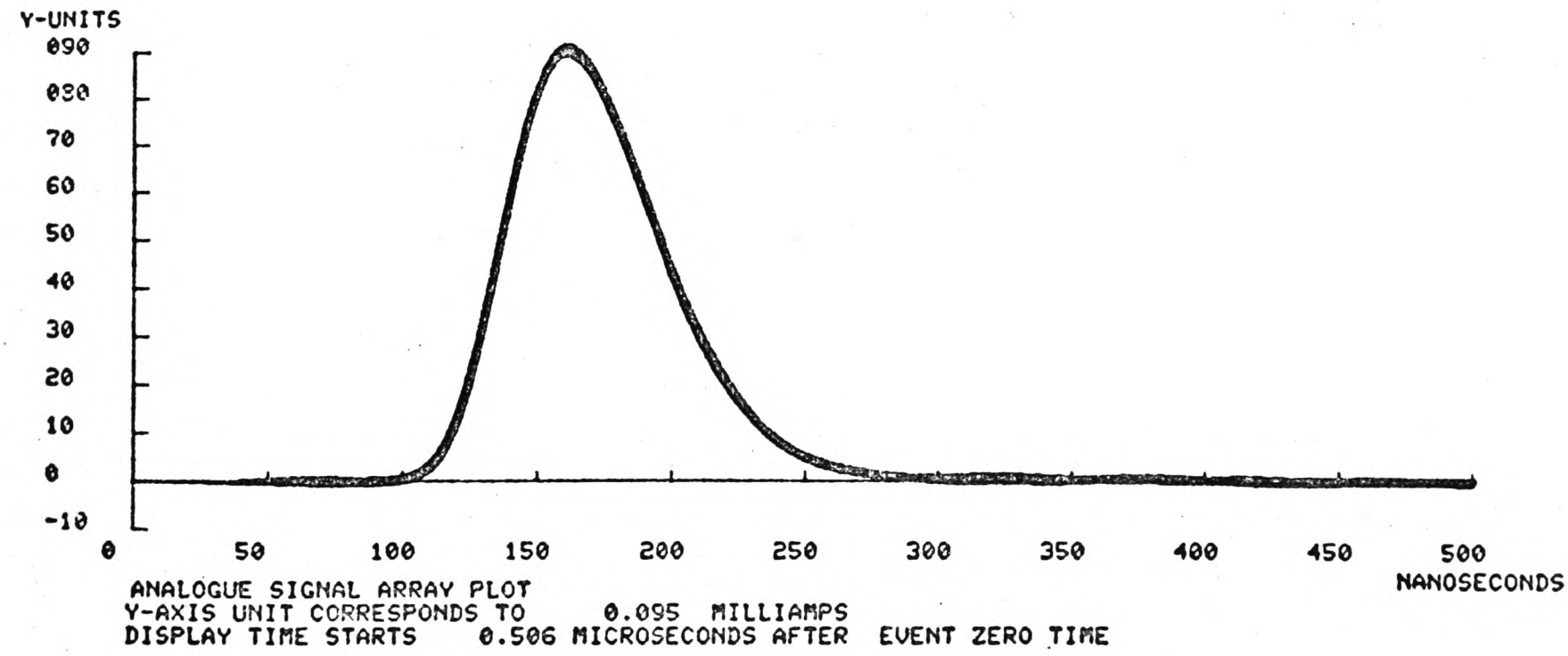
(c) Memory capacitor charging signals and associated integration gates

Shown in Fig. IV.15 are the shaped (and delayed) Fe^{55}-source signal currents, from the output of the charging amplifier (see III.4). (The conditions were the same as for (a)-(i).) These signals are gated onto the memory (integration) capacitors: the integration gate driving waveform is also shown on the photo. It may be seen that the gates overlap the signal by at least 50 nS at each end. The mean measured gate duration is 320 ± 10 nS.

The simulated situation is shown below the photo. The predicted mean gate duration is 300 ± 10 nS. The agreement is good. The pulse shapes and amplitudes of the measured and predicted waveforms are also very similar: the observed amplitude 84 mA, and the predicted is 83 mA with a gas gain of 10000 assumed by the program. In fact this comparison is somewhat irrelevant, since the amplitude information was

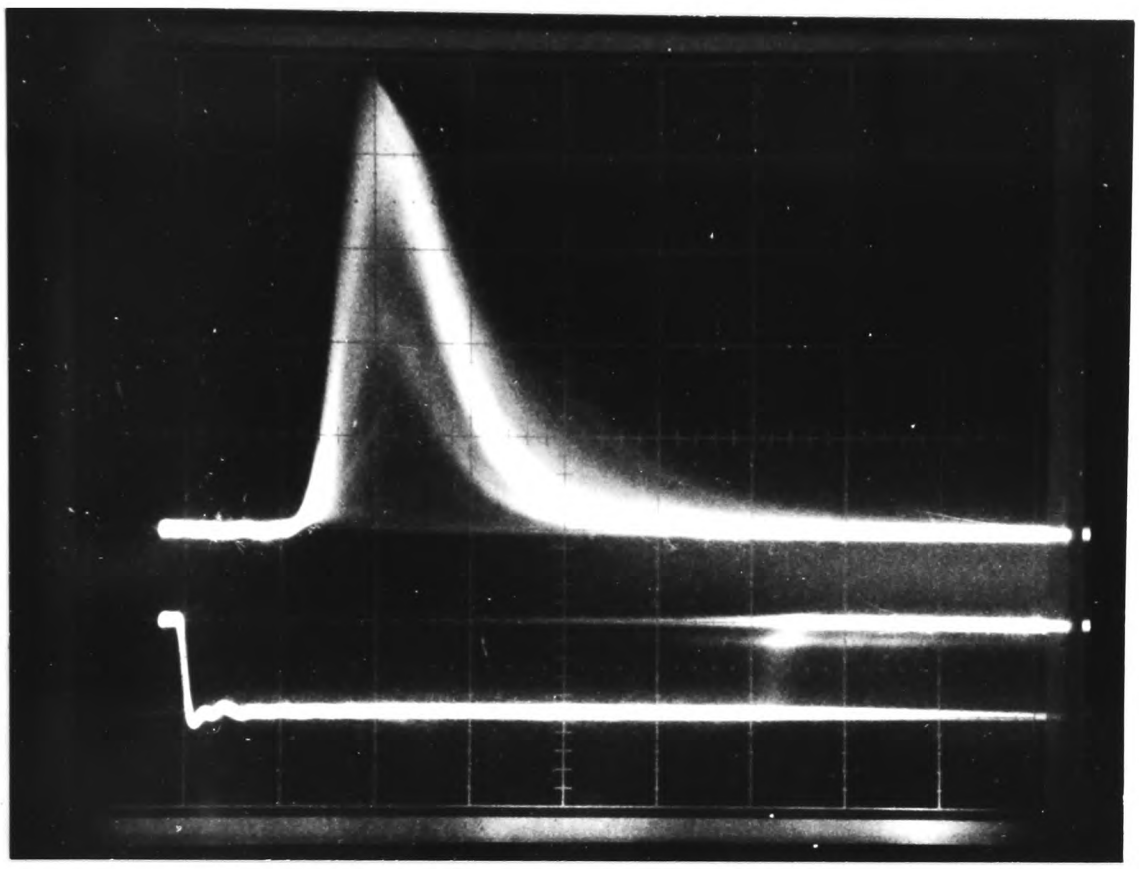


(a) Measured Response. X: 50nS/div
Y: Uncalibrated



(b) Simulated Response

Figure IV.14 Shaped Gas Amplifier Pulses from an Fe^{55} Source

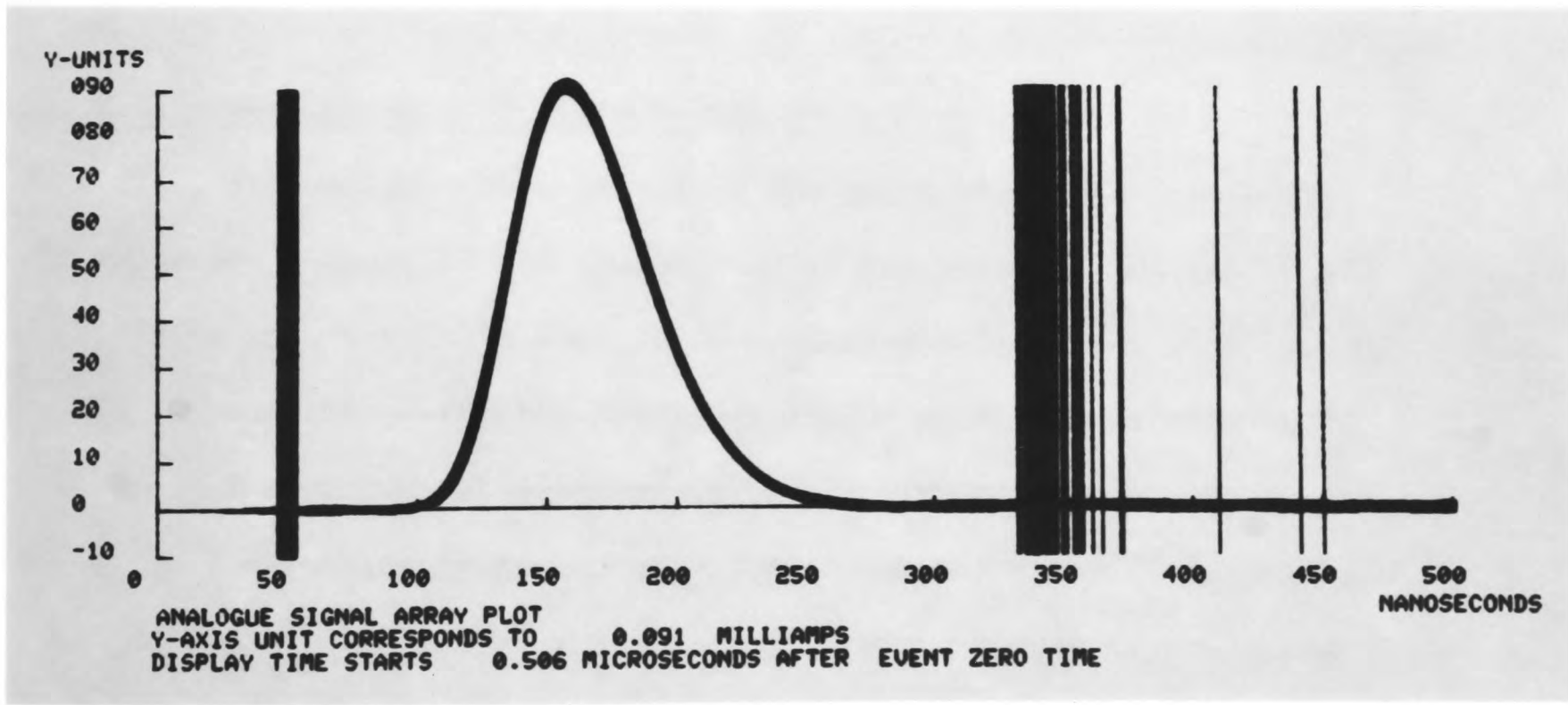


← Capacitor charging current

← Gate switching waveform

(a) Measured Response.

X: 50nS/div
Y: 100mV/div (Top Trace)



(b) Simulated Response

Figure IV.15 Capacitor Charging Current and Associated Gate Waveforms for Fe^{55} Source Gas Amplifier Signals Gas Gain 10^4.

used as input data in the simulation to obtain a value for the gas gain (see later). The above signals gave a mean digitized pulse magnitude of ∿170 (see later). (The maximum digitised pulse magnitude value, from the 8-bit ADC rundown time counter, is $2^8 - 1 = 255$, see III.4.)

These semi-quantitative tests have shown that, in the absence of diffusion dispersion, the simulation of the system is accurate to the 5% level. The predictions of the models of field geometry dispersion, gas amplification, pulse shaping and gated integration have been compared with measurements on a real system. The results are consistent at all stages. In no case is any discrepancy discovered of more than a few percent. This confirmation of the validity of the constituent models increases the trust that may be put in the simulation as a whole.

2. Measurements of Pulse Magnitude Spectra

Systematic errors of >1% in the pulse magnitude data are important because of the sensitivity of the velocity resolution of ISIS to such errors in ionization measurement (see I.2, II.1 [CJ76]). To inspect the systematic behaviour of the prototype to this high level of experimental accuracy ($\lesssim$1%), it is necessary to remove random effects by making large numbers of measurements under identical conditions. The use of a monoenergetic x-ray source to produce a known quantity of ionization facilitates these measurements.

The collection of large amounts of data was effected by the software in the controlling minicomputer, (see III.7). Histograms were built from the 8-bit binary-coded pulse magnitude data, for many hundreds of triggers. The histograms were transferred via paper tape to a larger computer for analysis. The content of typical

histograms ranged from 5000 to 20000 entries. At a trigger rate of ∿300/minute, the run times were 15 to 60 minutes.

An example of an Fe^{55}-source pulse magnitude spectrum is shown in Fig. IV.16(a). The histogram contains data from only one physical memory capacitor, (see III.4), thus isolating any possible inter-capacitor effects. Three peaks may be seen together with the overflow spike at bin #255. The peak centred at bin #170 is associated with the 5.9 KeV Fe^{55} x-rays. The smaller peak around bin #90 is associated with the 3 KeV argon escape energy. The peak at around bin #15 is due to random noise triggers. The FWHM of the main 5.9 KeV peak is 20%. This figure compares favourably with published results using the same x-ray source e.g. [BC71]: 19%.

The position of the 5.9 KeV peak should be compared with that of the peak shown in Fig. IV.16(b). This histogram was obtained by simulation of the treatment of an ionization signal of 223 electrons (≡5.9 KeV photons converting in 80% argon/20% CO_2). The gas gain assumed was 10000, and other conditions were the same as for the experimental cases. The conclusion is that the test chamber was operating at a gas gain of 9800 ± 2000. The large errors are due to uncertainties in the parameters of the gas amplifier model (see III.3 and Appendix 4). The reason for the small width of the simulated peak is because a model of the x-ray photon conversion process was not included.

Fig. IV.16(c) shows a histogram obtained at a reduced gas gain of 2100 ± 400. The three peaks remain well resolved. Observation of the 3 KeV argon escape peak at this gas gain corresponds to a resolution of 0.5 KeV at 10000 gas gain.

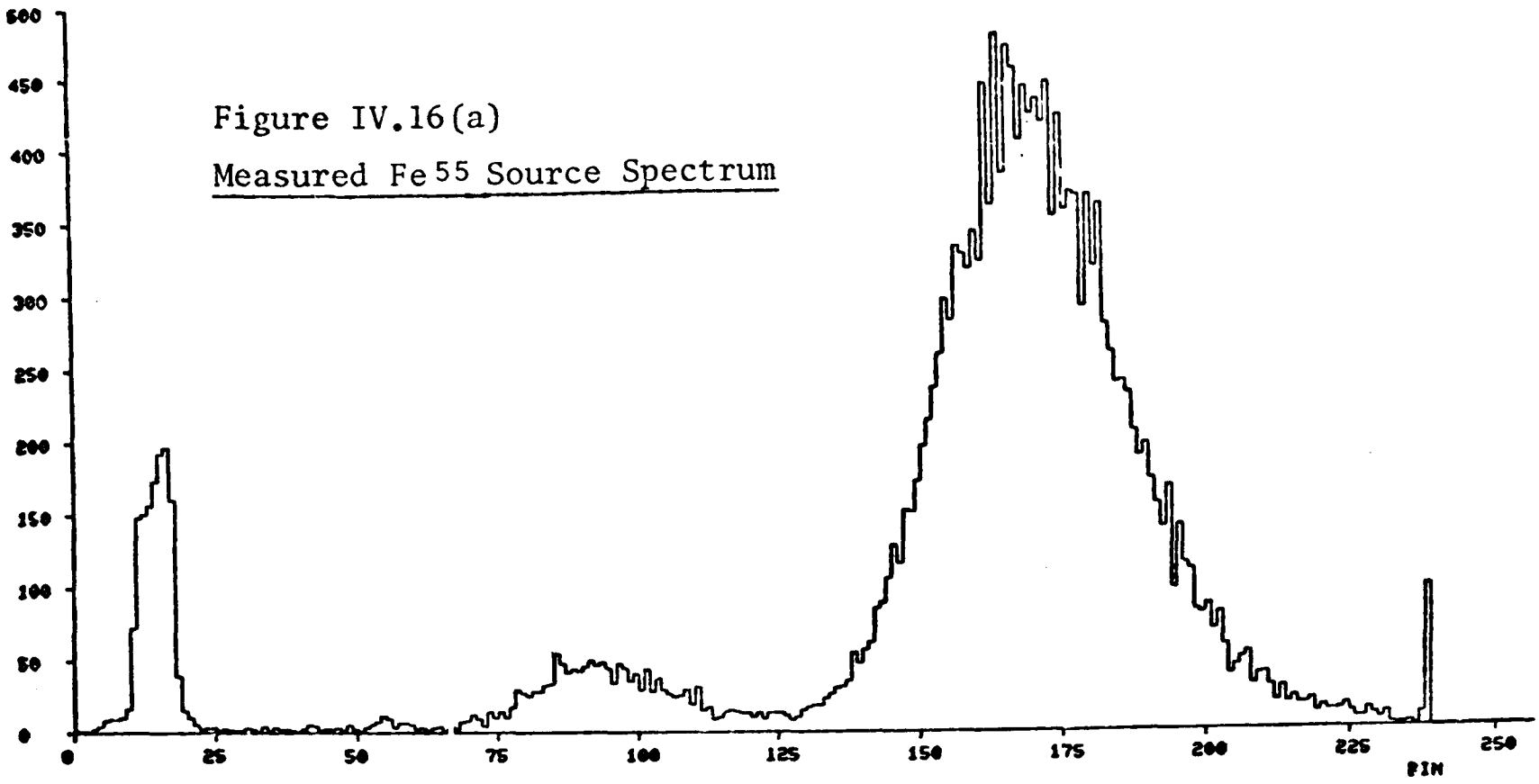


Figure IV.16(a)

Measured Fe^{55} Source Spectrum

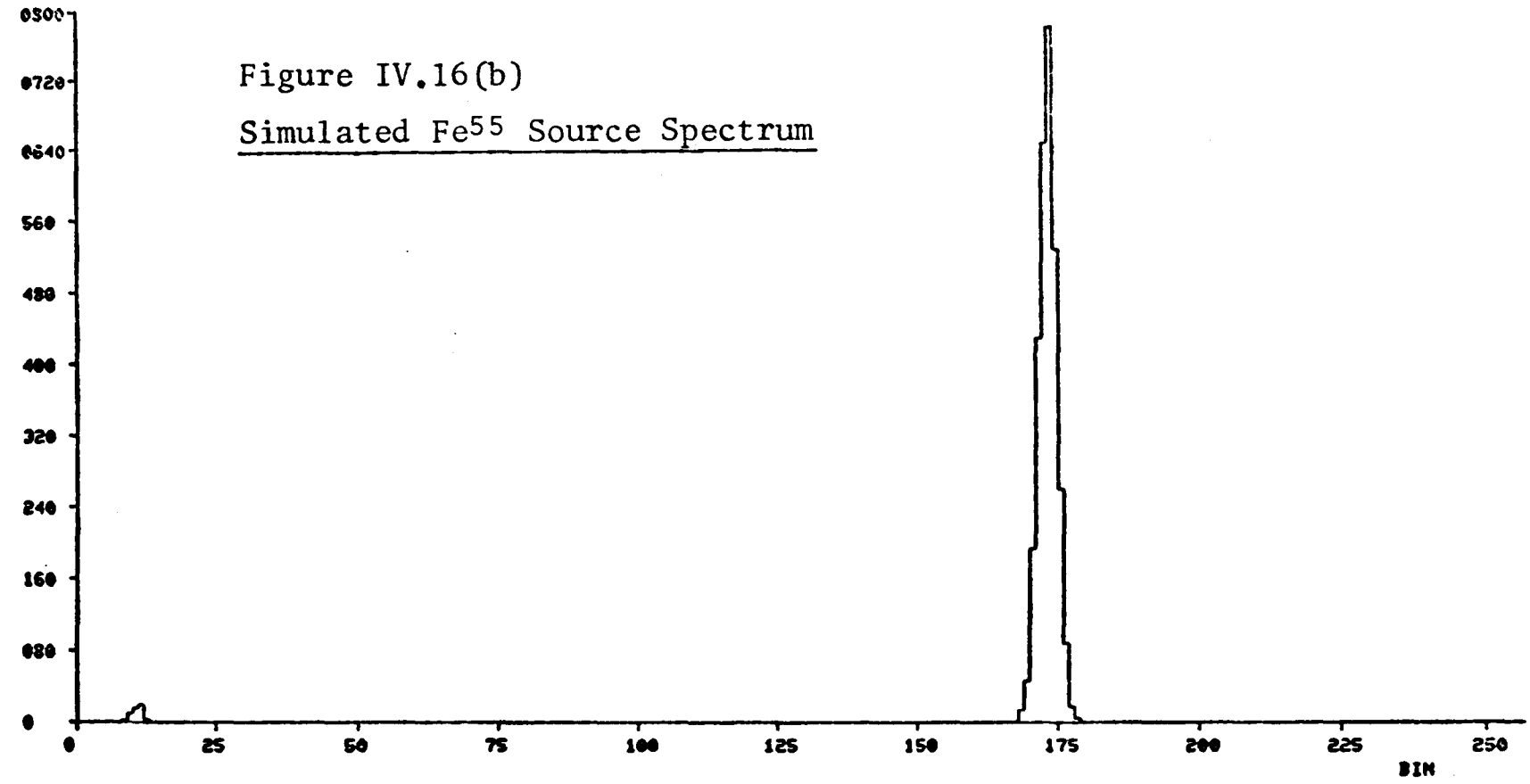


Figure IV.16(b)

Simulated Fe^{55} Source Spectrum

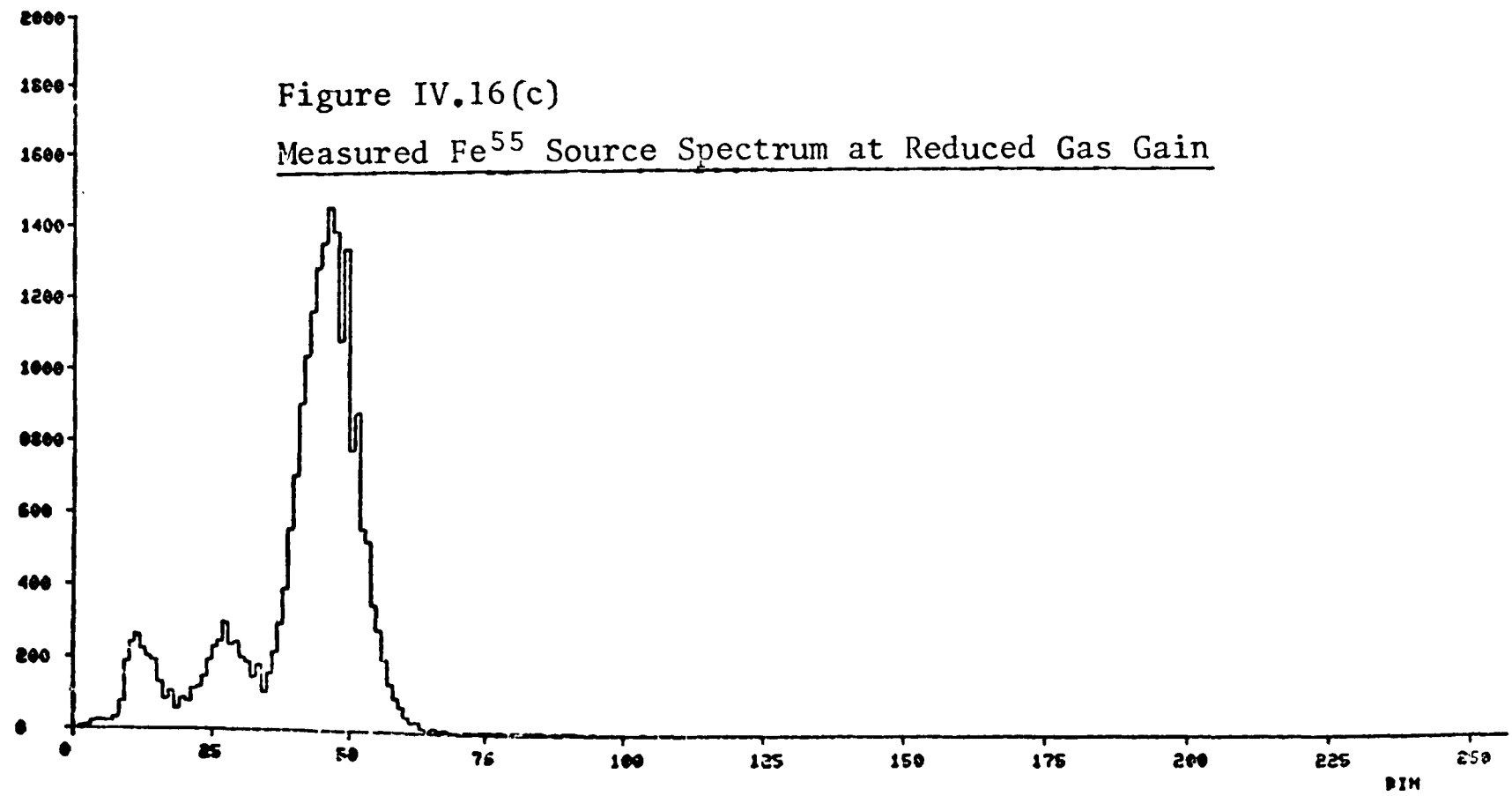


Figure IV.16(c)

Measured Fe^{55} Source Spectrum at Reduced Gas Gain

The results obtained by the collection of pulse magnitude spectra were generally useful. Some of the more accurate measurements on the characteristics of the electronics, described in Chapter III, were done in this way. In addition, important measurements on overall prototype system characteristics were made:

(a) Verification of chamber response

The overall chamber + electronics response was checked for linearity (in respect of variations in the amount of ionization) and uniformity (in respect of variations in sensitivity across the chamber).

(i) Linearity

The position, relative to zero signal, of the centres of the main 5.90 KeV Fe^{55} peak, and the 3.0 KeV argon escape peak, allow an estimation to be made of the linearity of the system. Over the range of energies 0-6 KeV, at a gas gain of 10000, the response of the system to localized ionization is linear to ∿10%. The linearity is expected to be better than that suggested by this figure: the method of obtaining the value was not very accurate. In the final system, calibration measurements will remove the effect of any non-linearity (see I.2).

(ii) Uniformity

Histograms containing a few thousand points each, were obtained for positions of the collimated source, at 1 mm intervals across the width of the 1.5 cm ionization sample. The results show that the chamber ionization sensitivity is uniform to ∿2% across a sample. However, this figure may well be better, since drift occurred in the chamber conditions over the time taken to make the measurements.

(b) Verification of chamber operating voltage characteristics

Measurements were made of the chamber gas gain for several operating voltages. The information was useful for two reasons:

(i) Correct design of the chamber electrostatics requires a reasonably accurate value for the anode wire charge/unit length to be known (see II.2, Appendices 1 and 2). The anode wire charge/unit length was determined from the operating voltages, and the chamber geometry, by the application of the formulae in Appendix 2. For a measured gas gain of 10000, the anode wire charge Q_A is:

$$Q_A(G = 10^4) = 16 \pm 1 \text{ nC/m}$$

The relatively large uncertainty in this value mirrors a lack of accuracy in the value of the anode wire radius. This radius ($\sim$12.5μ) was not measured directly, because of the difficulty of the task; instead, the manufacturer's nominal value was used.

(ii) Determination of the chamber construction tolerances needs a knowledge of the dependence of gas gain on anode wire charge (see II.2, III.4). To make the measurement, all chamber potentials were varied by the same small percentage ($\sim$2%), resulting in the same (percentage) change in electrode charge. Around a gas gain G of 10000, it was found that G varied as:

$$\frac{\Delta G}{G} \approx 13 \frac{\Delta Q_A}{Q_A} \qquad \text{(c.f. II.2)}$$

(c) Observation of an asymmetric response

Normally, the chamber was operated with equal fields on each side of the wire plane. However, the ability to operate the chamber with asymmetric drift fields showed up an interesting phenomenon.

This manifested itself in the appearance, under the asymmetric field conditions, of two output signals of differing integrals, for the same quantity of ionization. Evidence for this is shown in Figs. IV.17 (a) and (b). The voltages at which these histograms were obtained are shown in Table IV.1.

TABLE IV.1

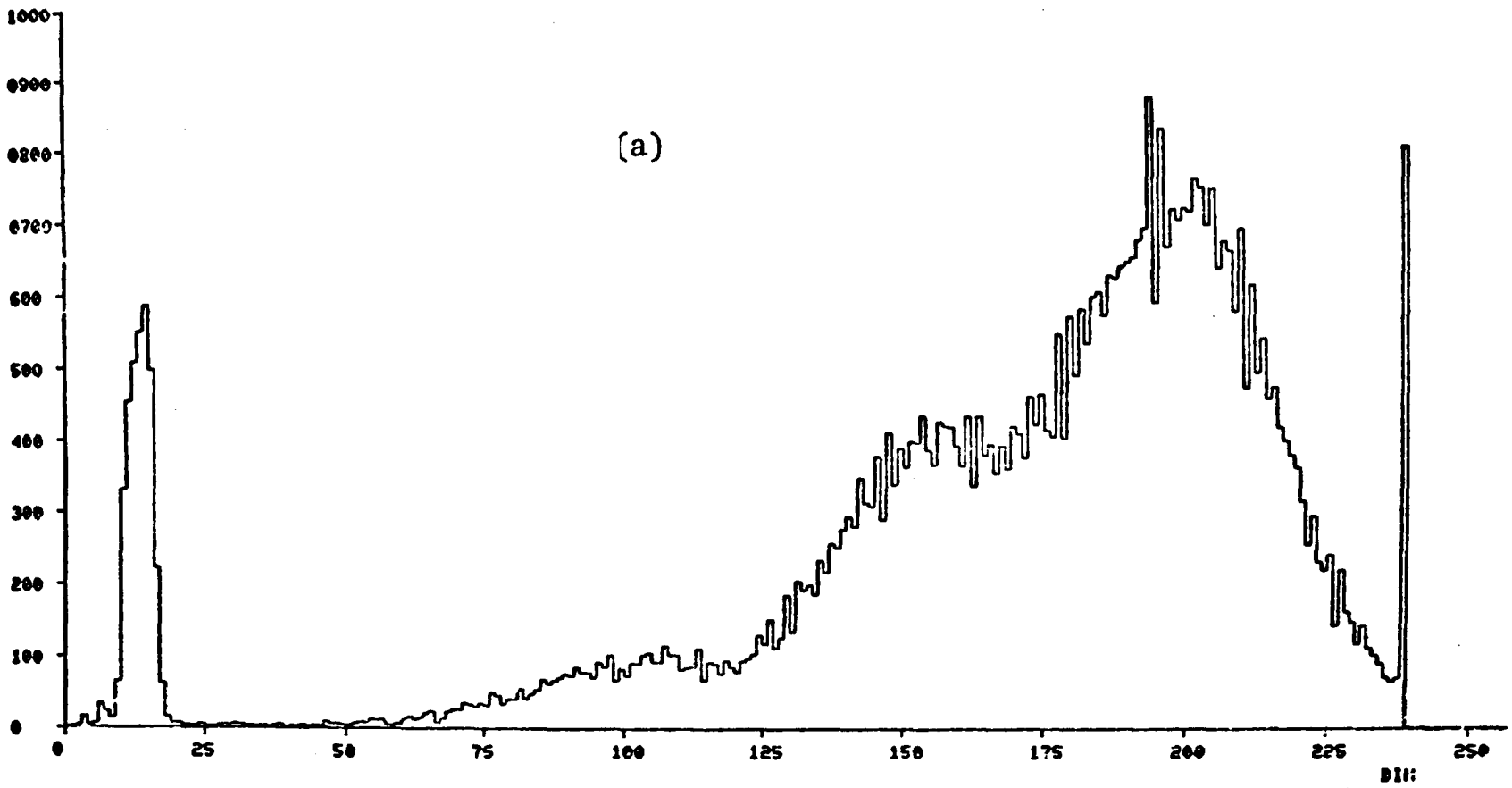
Spectrum Figure No.	Potential Differences		
	Anode Cathode	Anode - 2 cm drift	Anode - 4 cm drift
IV.17(a)	1490	4045	2745
IV.17(b)	1400	3100	5800
IV.16(a)	1400	3800	4300
IV.16(c)	1260	3400	3860

(Also in this table are shown for comparison the operating voltages for the histograms in Figs. IV.16(a) and (c).)

In the case of the results shown in Fig. IV.17(a), the field on one side (2 cm drift) of the wire plane was about 3 times that on the other side (4 cm drift). The reverse situation is shown in Fig. IV.17(b), with the field on the 4 cm drift side being the stronger by a factor of about 1.3. Intermediate situations were also observed.

The source illuminated the chamber from the 2 cm drift side. The Fe^{55} x-rays have a relatively short range of a few millimetres. Thus a greater number of events may be associated with photons converting in the 2 cm drift region than in the 4 cm drift region.

The main feature of the spectra shown in Figs. IV.17(a) and (b) may be seen to consist of two incompletely resolved peaks, of different



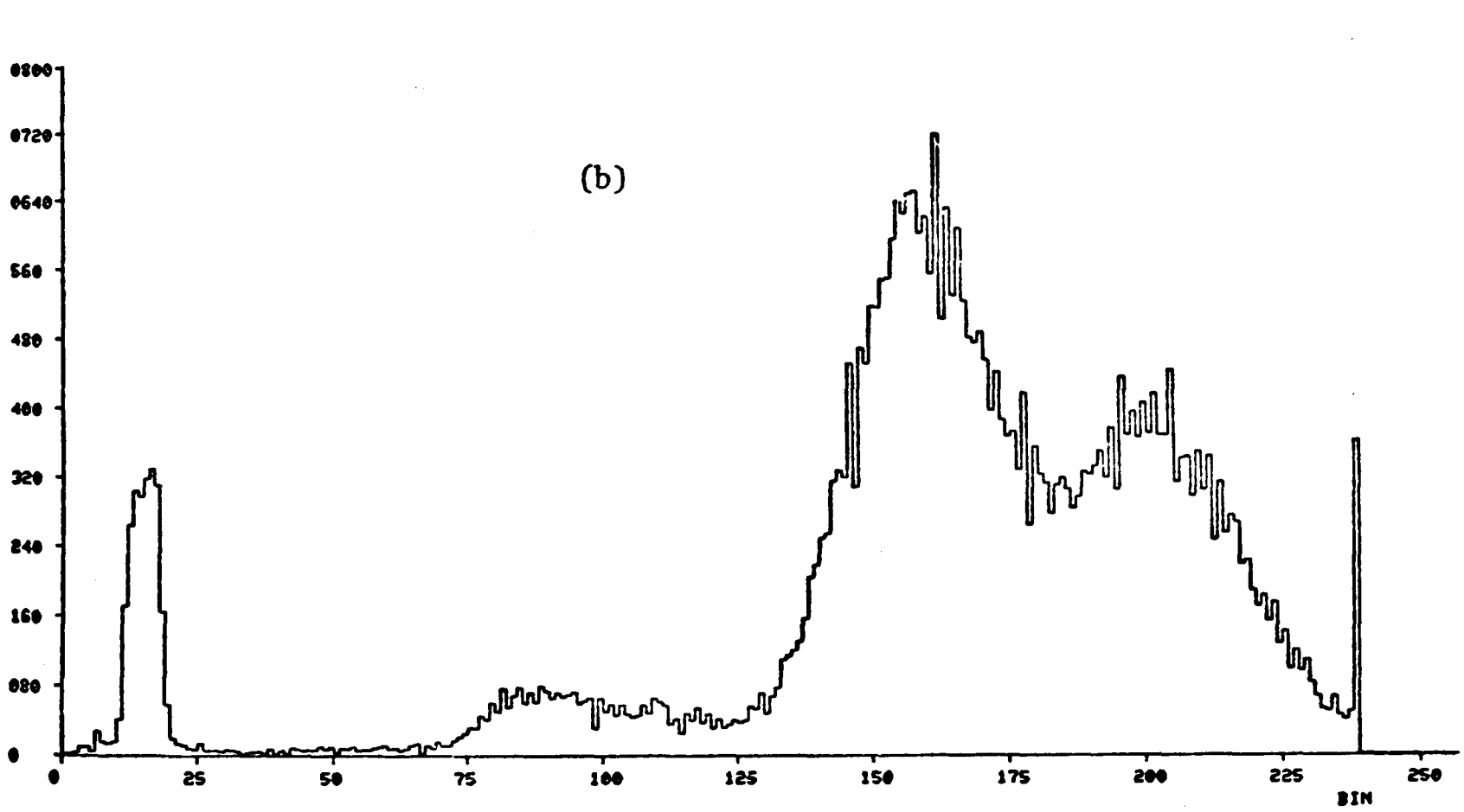


Figure IV.17 The Fe^{55} Spectra Obtained with Asymmetric Fields

heights. The larger peak is assumed to be due to photons converting in the 2 cm drift region. It will be noticed that the position of this larger peak relative to the smaller (4 cm drift region) peak is consistent with the hypothesis that there is a greater gas gain on the higher field side of the wire plane.

Asymmetric drift fields result in a dipole moment on the anode wire. If, as is widely believed (e.g. [WD50], [RP74]), the amplification avalanche of 'hot' electrons spreads evenly around the anode wire, then the presence of a dipole moment on the anode should have no effect. However, if the avalanche is localized to a sector around the wire, then a dipole contribution to the anode wire charge could produce a variation in gain with the azimuthal position of the avalanche. It is believed that the above expeimental results indicate such a situation - the amplification avalanche does not spread evenly around the wire. This may be due to the electron coolant effect of the CO_2 component of the gas (see II.2, II.3).

A similar double peak phenomenon has been observed in a cylindrical proportional counter at a gas gain of 10^5 in 64.4% CH_4/32.4% CO_2/3.2%N_2, (see [CP71], [CP73]). The relative position of the peaks was found to be dependent on operating voltage. However, the authors suggest that the origins of the phenomenon are not electrostatic, but are concerned with space charge (see II.3). It is quite possible that their observations are of a different effect from the asymmetric field phenomenon discussed above.

A more useful conclusion from these measurements is that the field asymmetry must be less than 5% for a tolerable increase in resolution of 1% FWHM. Uniformity of the field at this level is relatively easy to achieve (see [IN26]).

Conclusions

The ability of the simulation to model the gas state processes in ISIS has been demonstrated. When note is taken of the uncertainties in some of the parameters of the model, the predictions of the simulation may be considered to agree well with the result of the tests. This gives rise to much confidence in the model's ability to correctly simulate the gas state, as well as the electronic, processes in ISIS.

The tests were also very useful in terms of operational experience in using the prototype equipment. In addition, no degradation in performance of either chamber or electronics was noticed over the duration of the tests ($\sim$ months). This indicates good long-term stability.

Also, because of the unique electrostatic configuration, an interesting phenomenon has been observed. This leads to the conclusion that gas amplification avalanches may not spread all around the anode wire.

IV.4 TESTS WITH CHARGED PARTICLES

An acid test of the simulation is the correct prediction of the treatment by the system, of drifted charged-particle ionization tracks. A small multi-wire proportional drift chamber, of the same basic design as ISIS, was placed in a high-energy particle beam. Measurements were made of the prototype performance using the gas amplifier signals from this source. These results are compared with the predictions of the simulation.

Unlike the tests made with artificial and x-ray signal sources, these tests were not wholly successful. The performance was poor in several aspects, including:

(i) Low gas gain

(ii) Inefficient triggering

(iii) Excessive multiple triggering

(iv) Distorted pulse magnitude spectra

This degradation in performance was caused by two independent problems:

(i) Gas contamination by CO

(ii) DC Baseline restorer ineffectiveness

These observations are discussed in context later in the section. However it is important to note that all of the problems are now satisfactorily understood - there are no unknown factors. Simple modifications have been made that remove the causes of the poor performance. For instance, a different type of oxygen-removing gas purifier is now in use which cures the problem of gas contamination. The design of the DC Baseline Restorer has been altered; in fact the impressive performance characteristics stated in III.6 refer to the improved version.

Objectives of the Tests with Particles

The objectives were:

(i) To check the principles of the ISIS design of drift chamber, (described in Chapters I and II), insofar as the details had changed since the previous tests. [CJ75], [BJ76] In particular, to gain experience in the operation of the chamber under real conditions, as regards:

(a) The gas system

(b) The effect of ambient electrical noise (r.f. pick up etc. see III.2)

(c) The stability and reliability of the prototype

(ii) To obtain satisfactory performance on signals arising from the gas amplification of drifted ionization tracks, as deposited by charged particles traversing the chamber. More specifically, to compare the measurements with the predictions of the simulation for the same, realistic, SNR conditions. This allows further verification of those critical parts of the simulation, the models of ionization dispersion and gas amplification.

(iii) To investigate the susceptibility of the response to systematic effects. The sources of such effects may include:

(a) The chamber: e.g. gas gain non-linearity (see II.3)

(b) The electronics: e.g. pulse shaping inefficiencies (see III.3)

(c) The data rate: e.g. space charge effects (see III.3), and d.c. baseline shift (see III.6)

Description of the Chamber and Ancillary Electronics

The test chamber used was the original prototype ISIS drift chamber, described in [AW74] and [CJ75]. The construction was modified

from that described in the references, in order to include the main change in design that had occurred: symmetric field operation (see I.2.). The modification involved removing the old wire plane (situated at one end of a ∿100 cm drift region), and replacing it by a wire plane of the new design (see I.2), positioned about 20 cms into the drift region. This is shown in Fig. IV.18. The maximum track drift distance was ∿ 75 cm, in a uniform electric field created by the electrostatic guard structure. The high voltage connections to the guard structure and drift electrodes were changed to obtain a symmetric drift field distribution on either side of the wire plane (whose mean potential remained at zero).

The wire plane, of area 40 cm x 40 cm, consisted of alternate 12.5 μ-radius anode wires, and 125 μ-radius cathode wires, on a 2.5 mm pitch. The wires were of a beryllium-copper alloy; this facilitated the making of electrical contacts by soldering. The connections of the wire plane with the power supplies and the pre-amplifier are shown in the circuit diagram of Fig. IV.19. The wires were grouped together to define ionization samples of width 2 cms, thus splitting the 40 cms of wire plane into 20 samples. Four adjacent anode wires and the three interleaved cathode wires provided the differential signal output from the wire plane to the preamplifier. The common inter-sample cathodes were decoupled to ground. (The configuration for this wire plane differs from the optimum situation considered in II.4, because these tests were performed before completion of the analysis of II.4.) Only one channel-sample was used; the other (unused) outputs were taken to signal ground.

The preamplifier output fed the remote electronics, as described in Chapter III and IV.3. The digitized data available from

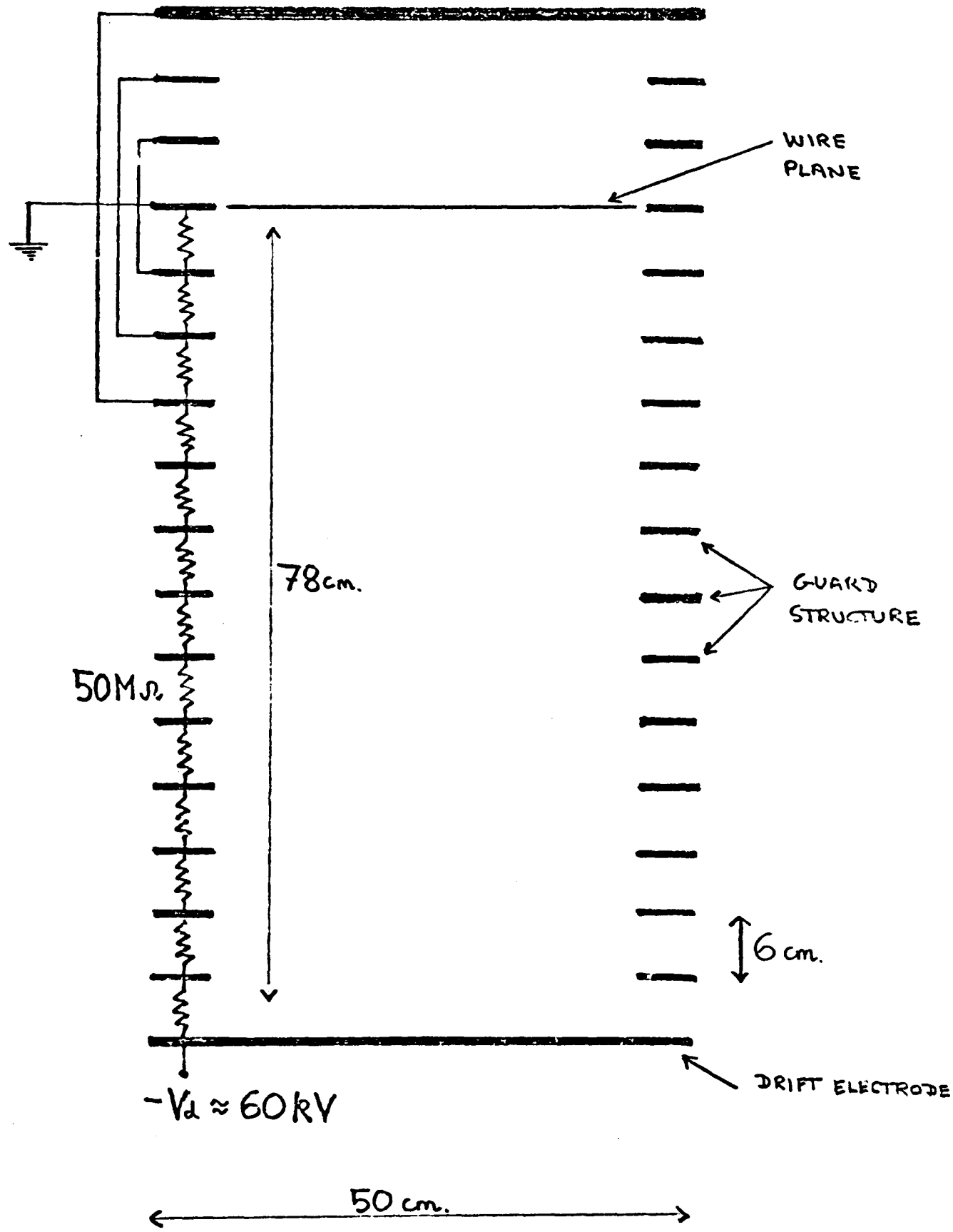


Figure IV.18 Schematic Diagram of the Prototype ISIS Chamber

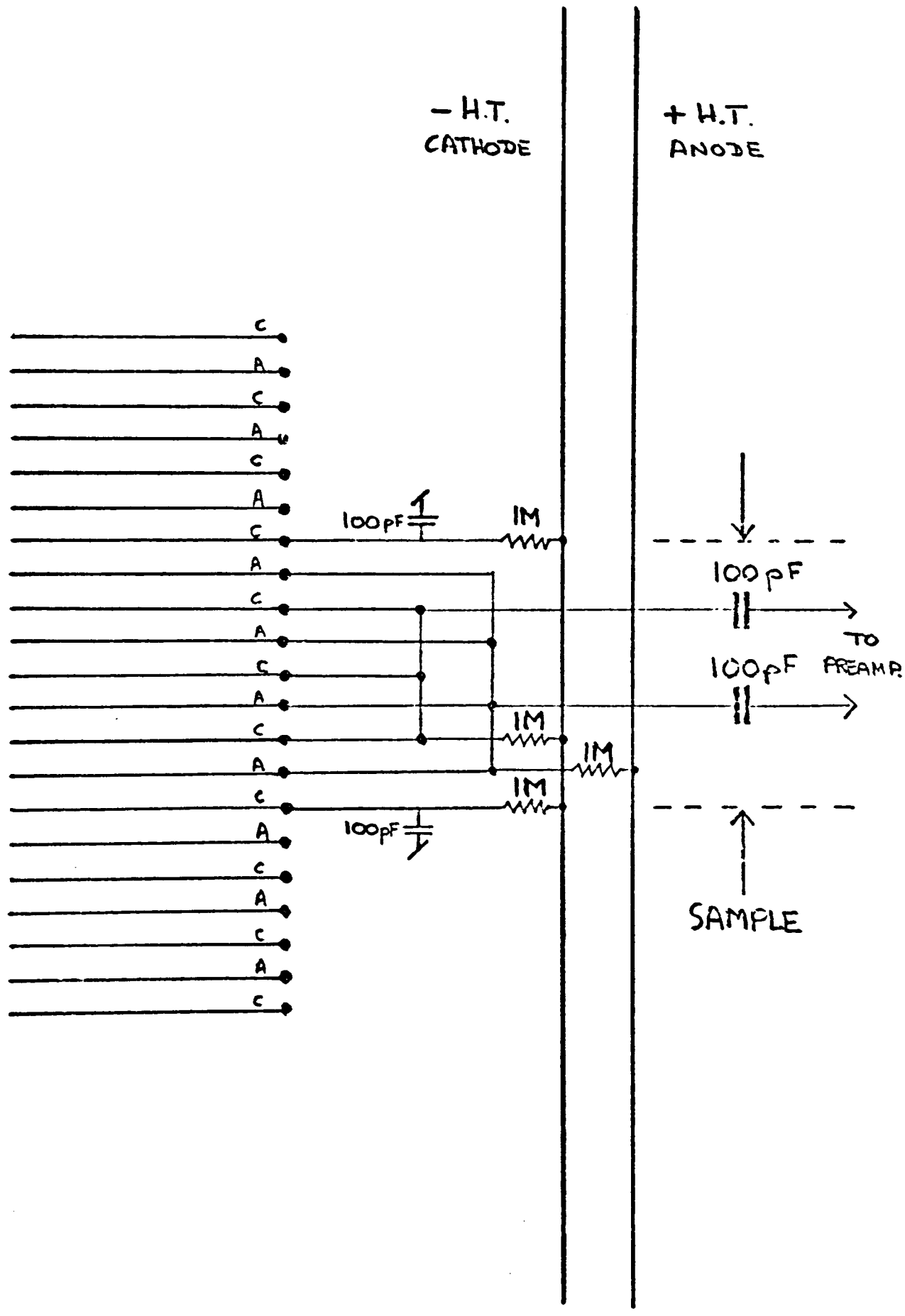


Figure IV.19 Schematic Diagram of the Electrical Connections to the Prototype Wire Plane.

the remote electronics was written onto magnetic tape via the controlling minicomputer, for off-line analysis (see III.7). Also available to access by the computer, using CAMAC, was the output of a scaler, clocked at 50 KHz, and triggered so as to provide a time scale from start of the accelerator beam-spill.

Chamber Operating Voltages

The chamber was operated with drift fields of up to ∿85 kV/m, compared with ∿100 kV/m envisaged in the final device (see II.2). The anode-cathode potential on the wire plane was 1600-1900v depending on drift field and gas amplification. Three sets of operating potentials were used: they are shown in Table IV.2, together with a calculated value for the anode wire charge (see II.3 and Appendix 2).

TABLE IV.2 Test ISIS Chamber Operating Potentials

	Drift Field	Drift Potential	Anode-Cathode Potential	Q_A
	kV/m	kV	V	nC/m
(a)	60.0	-45.0	1901	16.0
(b)	74.1	-55.6	1603	14.4
(c)	82.4	-61.8	1782	16.0

The Chamber Gas Environment

The performance of a drift chamber depends to a great extent on the constituents of the filling gas (see II.2, [CJ75]). Two objectives were borne in mind in the design of the chamber gas supply

system:

(a) to provide an adequate chamber gas environment

(b) to gain experience in the operation of high-purity gas handling equipment.

The chamber filling gas was nominally 80% argon-20% CO_2 see (II.2), at a pressure of about 1" water gauge. This was contained in a double walled gas bag surrounding the electrostatic structure. Including the stainless steel plumbing, the total volume was ∿300L.

The tightest restriction on gas purity is in the amount of oxygen present (oxygen attenuates effective ionization by electron attachment, see [CJ75]). For these tests, an oxygen contamination of less than a few v.p.m. was required for negligible attenuation of drifted ionization. The bottled gas mixture obtained from the manufacturer was good in this respect. Starting with an air-filled chamber, a satisfactory operating point was reached after ∿12 hours purging at a gas flow rate of ∿15 L/min. (approximately one bottle of gas was used).

At this stage the bottled-gas input flow-rate was reduced to 4 L/min. A pump was started which recirculated the gas from the chamber at 15 L/min. through an oxygen-removing purifier, (British Oxygen Co., RPG2 purifier: Ti granules at 700°C). This was capable of removing oxygen to the level of less than 1 v.p.m., in the absence of appreciable leakage of atmospheric oxygen into the chamber.

Chamber conditions were monitored as regards:

(a) <u>gas flow</u> by an automatic gas feed-vent system, and as regards

(b) <u>gas purity</u>, by three instruments.

(i) $[O_2]$: Drovewood DS2000 Zirconia cell oxygen meter, sensitivity <0.1 v.p.m.

(ii) $[CO_2]$: Grubb Parsons IRGA20 infra-red absorption CO_2 meter, sensitivity $\sim$0.2%.

(iii) $[H_2O]$: Shaw gas hygrometer, sensitivity $\sim$10 v.p.m.

The desired operating point for gas purity was:

$[O_2] < 10$ v.p.m.

$[CO_2] = 20 \pm 1\%$

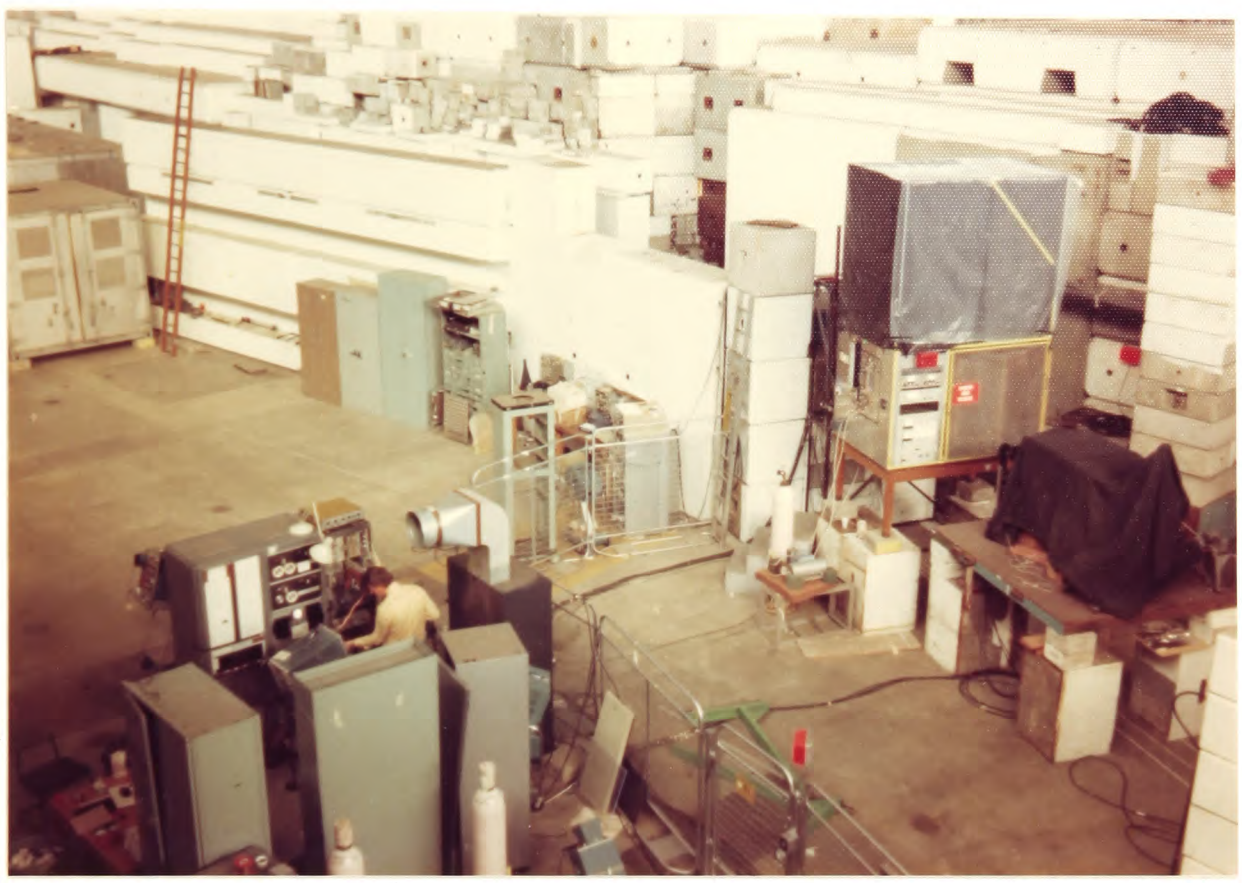
$[H_2O] < 100$ v.p.m.

Organization of Experiments

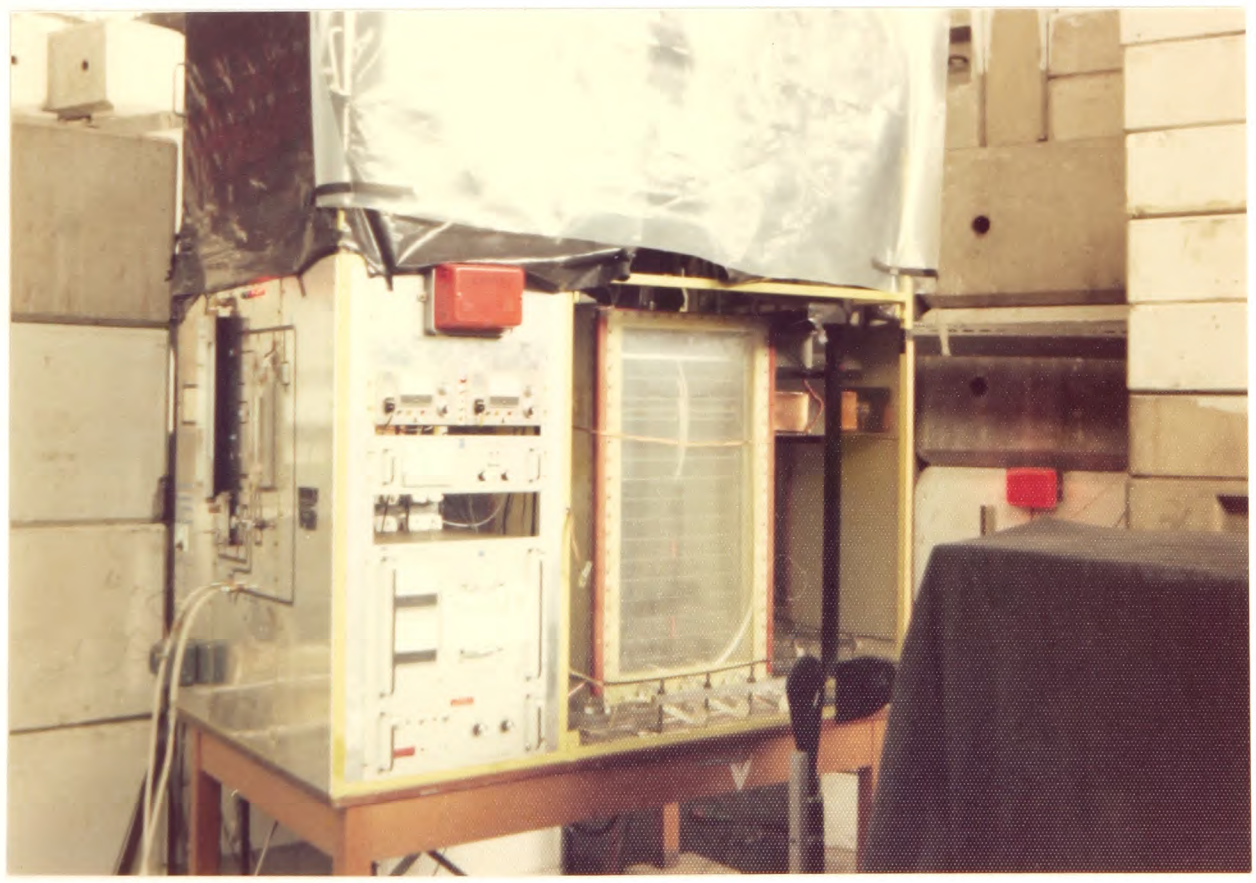
The high energy charged particles, which produced the ionization tracks in the chamber, were obtained from the NIMROD accelerator at the Rutherford Laboratory of the Science Research Council. The chamber was set up in a test beam, as shown in the photographs of Fig. IV.20 (a) and (b). The chamber, in the beam, is on the right side of Fig. IV.20 (a). The direction of the beam was towards the bottom right-hand edge of the photo. The remote electronics and minicomputer may be seen on the left. In the close-up of the chamber, (Fig. IV.20(b)), the electrostatic guard structure may be seen through the mylar chamber windows. The high voltage supplies and gas handling controls are on the left of the chamber. The prototype preamplifier was situated in the small copper box seen at the right hand edge of the chamber.

Particle Beam and Triggering

The particle beam used was a secondary beam of (nominally) pions at a momentum of 2 GeV/c. The beam cross-section in the chamber was about 2 cm x 2 cm, and the nominal rate was $\sim 5 \times 10^4$ over an accelerator beam spill duration of $\sim$600 mS.



(a) Small ISIS Test Chamber in Beam at RHEL



(b) Close-up of Small ISIS Test Chamber

Figure IV.20

The chamber was positioned so that this beam passed through the sensitive volume, parallel to the plane of the wires but perpendicular to the line of the wires, and at the practical maximum drift distance of ∿70 cm.

The event-time-zero trigger for the electronics (see III.4, III.5) was obtained from the coincidence of signals from two scintillation counters. One of the counters was mounted in the beam a few centimetres upstream from the chamber. The scintillator, of dimensions 30 cm x 8 cm x 0.3 cm, was oriented so as to present its thinnest cross-section (∿3mm) to the beam, yet parallel to the wire plane. The output from this counter was taken in coincidence with the output from another, larger (4 cm. sq.), scintillation counter, placed about 3 m upstream. The resulting trigger signal defined the time-zero for ionization tracks drifting from 70 cm, to an accuracy of ∿100 nS in ∿20 μS drift time.

The coincidence rate was typically 4000 to 8000 per beam spill, depending on the setting of the beam collimators.

Typical Signals

Signals from the chamber, associated with the above counter coincidence, were easily observable. In the 'scope photograph of Fig. IV.21, the chamber signals at the output of the pulse shaper (see III.3) are shown, with the derived integration gating waveform. The time base was triggered by the counter coincidence signal. The coincidence signature may be seen as a characteristic spike in the analogue signal, and as a corresponding brightening of the digital gate trace.

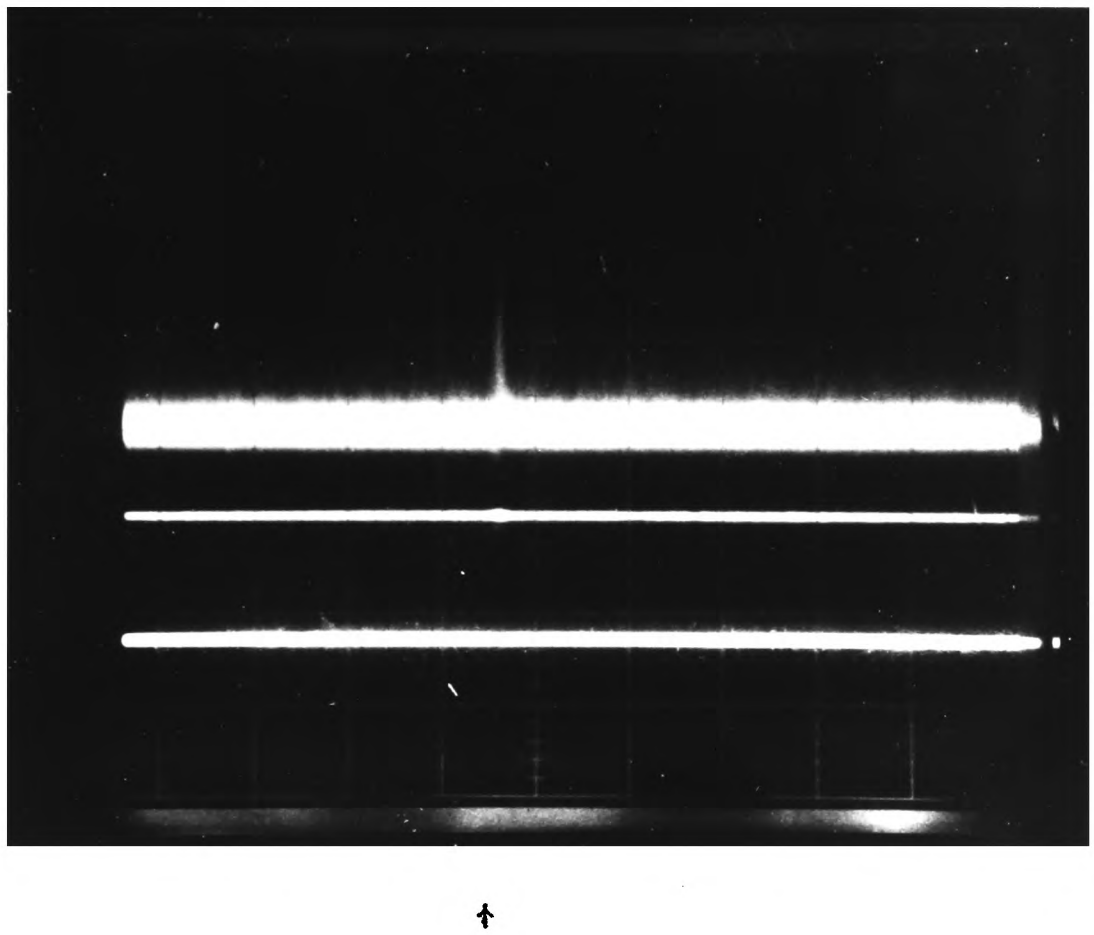


Figure IV.21 Charged Particle Signals and Associated Gate Waveform.

X: 5μS/div

Y: 20mV/div

(Sweep started by counter coincidence)

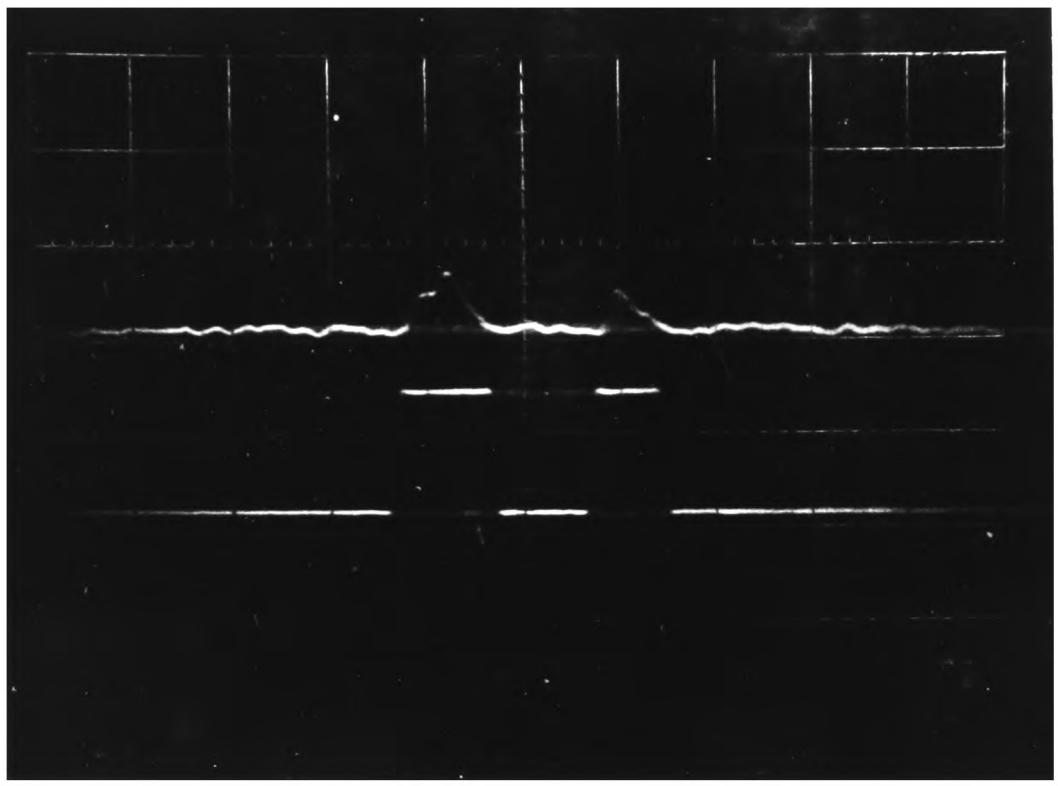
The delay in the signature from the time of coincidence corresponds to the drift time for the tracks. In the case of Fig. IV.21, the drift time was 20.0 ± 0.5 μS, for 70 cm drift in a drift field of 82.4 kV/m. This is equivalent to a drift velocity of 3.5 ± 0.1 cms/μS. (The expected drift velocity at this field is 3.3 cm/μS.)

Having identified the timing of the signals from tracks drifting a known distance (70 cm), it was easy to investigate the detailed profile of these signals on a 'scope, by using a delayed and expanded single-sweep time base. A typical example of the shaped chamber signal, observed under these conditions at the output of the charging amplifier (see III.4) is shown in the photograph of Fig. IV.22(a). The centre of the 'scope trace corresponds to the mean 70 cm drift time.

In the photo, two pulses may be seen, although only one of them should be associated with a 70 cm drift track. Two aspects of these signals are:

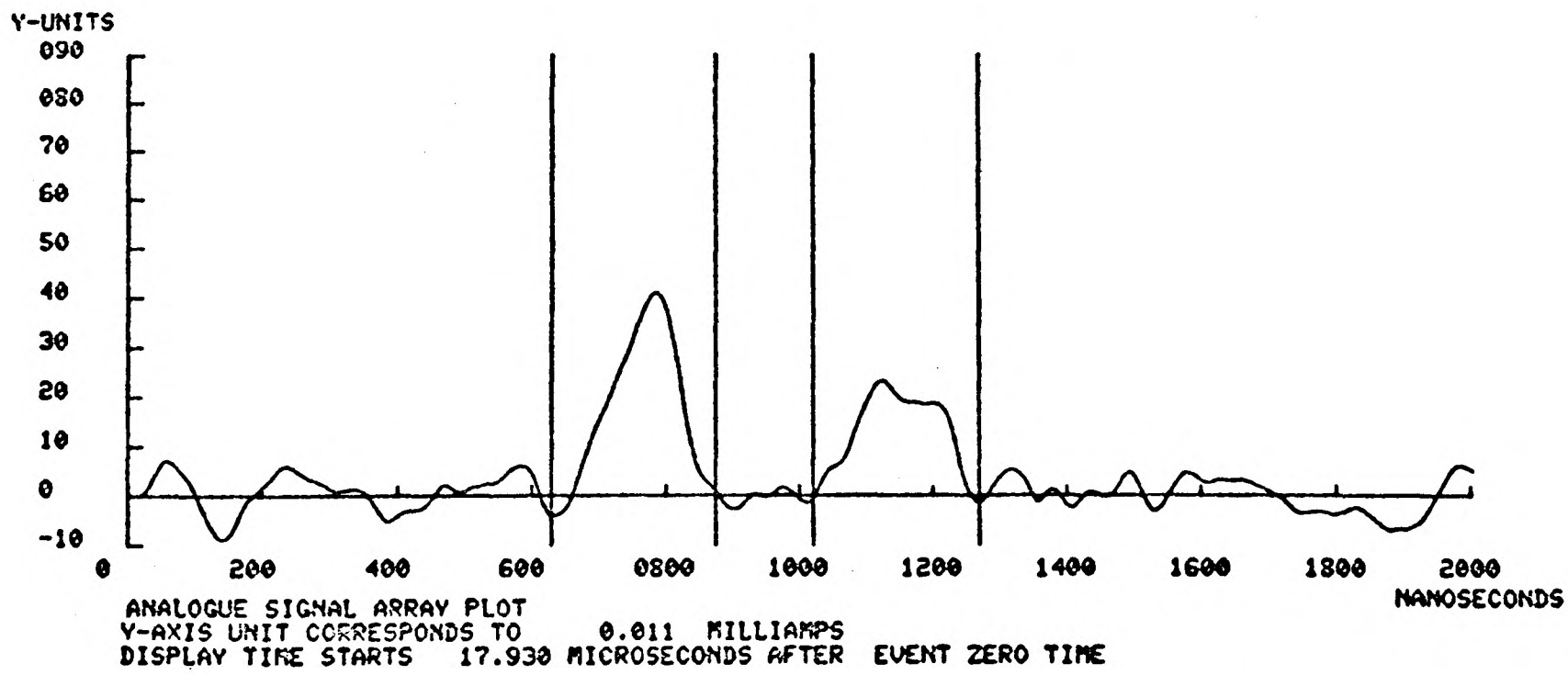
(i) Pulse Amplitude

Although there is a large inherent spread in the size of measured pulses (the Landau distribution, see II.1), the mean measured amplitude of the analogue signals (∿0.5 mA) was much smaller than was expected for the voltage used. This may be seen qualitatively by comparing average observed signals (Fig. IV.22(a)) with simulated ones (Fig. IV.22(b)). The amplitude of the observed signals is ∿0.4 mA; that of the simulated signals is ∿0.35 mA. The conditions of the simulation assumed ionization samples of 150 electrons (≡∿4 KeV ionization loss in the sample, an average value, see II.1) drifting from 70.0 and 71.6 cm, and a gas gain of 1500. The conclusion is that the gas gain was lower than the required value of 10000 by a factor of around 6. This was confirmed by measurements of the trigger



(a) Measured Response X: 200nS/div
Y: 50mV/div

(Sweep delayed to place coincidence signature at centre.)



(b) Simulated response, gas gain 1500.

Figure IV.22 Charged Particle Signals and Associated Gate Waveforms.

efficiency and the pulse magnitude spectra - see later. Any attempt to increase the gas gain by raising the operating voltages failed, because of the onset of electrical breakdown within the chamber. The reason for this behaviour became apparent when it was noticed that the measured CO_2 concentration was not 20%, but ∿5%. Further investigations have shown that the gas purifier, containing Ti granules at 700°C, was not only removing oxygen, but also reducing CO_2 to CO. The chamber gas was not, as expected, 80%A/20% CO_2, but was approximately 80%A/15%CO/5%CO_2. The CO is not as effective as CO_2 in facilitating high, stable gas amplification. (The ultraviolet absorption and metastable state quenching efficiency of CO are not as high as those of CO_2. This results in a reduced plateau for proportional gas amplification, and a lower Geiger threshold (see II.3)). The problem has since been solved by the use of a different type of purifier: Messer-Greisheim's"OXISORB" (silica gel impregnated with chromium trioxide).

(ii) Pulse Timing

The two pulses observable in Fig. IV.22(a), are of width 150-200 nS, and separation ∿300 nS. The associated integration gating waveform is clear, and adequately masks the analogue pulses. The results of the simulation shown in Fig. IV.22(b) are consistent with these measurements: a mean pulse duration of just over 200 nS is predicted.

The widths and separation of the observed pulses may be expressed as distances by multiplying by the drift velocity. The resulting spatial extent of the pulses is ∿0.6 cm, and the (apparent) spatial separation is ∿1.1 cm. These values are typical of ones obtained from other 'scope photographs. The values are also consistent with the results of the simulation - see Fig. IV.22(b) and IV.5, IV.6. The

simulation predicts an equivalent pulse spatial extent of 0.7 cm, for 70 cm drifted signals at the low gas gain (see above). Thus the observations are in qualitative agreement with a predicted two-track spatial resolution of ∿1 cm (see IV.6).

The Noise Level

One of the objectives of these tests was to operate the system under realistic SNR conditions. Measurements of the r.m.s. noise amplitude, and the noise spectrum, showed that the noise level was within 10% of that measured with a dummy chamber capacitance. The noise was relatively free from components at specific frequencies, indicating low pickup and a fairly good r.f. background. (A small amount of pickup was observed however, coincident with the discharge of nearby spark chambers. Because of the low discharge rate, this did not give rise to concern.)

The discriminator trigger-on level was adjusted to give a no-signal noise triggering rate of 20 KHz. This meant that, on average, just over one trigger due to noise would be found in the 64 μS range of the time-of-arrival memory (see III.5 and IV.5). The measured value of the trigger-on level (6.5 mV) under these conditions agrees with that predicted by the simulation (6.0 mV, see IV.2).

In terms of an SNR, the absolute noise level was very near to the expected value, but the measured signal amplitude was lower than desired, by a factor of ∿5. The resulting SNR was thus smaller than anticipated by about 15 dB.

The Measurements

Because of the inherent fluctuations in the size and shape of the signals from ionization tracks (see Chapter II), little information,

beyond that discussed earlier, could be gained from the 'scope traces, (in contrast to what was achieved in IV.3). The discussions in the rest of this section are based on the results of an off-line analysis of histograms containing statistically-significant amounts of data.

Consistent with the philosophy of the tests, the equipment was operated in the same event-driven mode as is intended for the final device, (described in detail in III.4, III.5 and III.7). Briefly, the system remains in a data-acquisition state until the counter-coincidence announces that a particle has crossed the chamber at the 70 cm drift distance. After a fixed internal delay of 40 μS, to allow the drifting ionization to arrive, the data acquisition mode is disabled. This freezes the 'event-picture' held in the remote electronics, of the recent pulse magnitudes and associated times-of-arrival. The digitized values describing the event-picture are subsequently written to the minicomputer and thence to magnetic tape. In the final device a complete event-picture will consist of a raster built up from the output of ∿320 channels (see I.2). In the tests described here, only one channel is used: the output looks like one line of the complete 320-line event-picture.

Several data collection runs were made at different chamber operating voltages. A typical run produced a magnetic tape containing event-by-event data for ∿2000 to ∿10000 events. Each event contained pulse magnitude and time-of-arrival information for an average per event over the run of between 10 and 30 triggers. The time from the start of the beam spill was also recorded for each event. At a data collection rate of ∿10 events/sec., typical run times were of the order of minutes. The total number of triggers for each run was about the same, apprxomately 70000. Some on-line checks were made to ensure data validity (e.g. on-line histogramming, see Fig. III.34(c)).

For the off-line analysis, histograms of specific quantities (e.g. pulse magnitude) were constructed from the event-by event data. It was easy to add further constraints on the data at this stage.

Analysis of the Results

The analysis divides naturally into two sections:

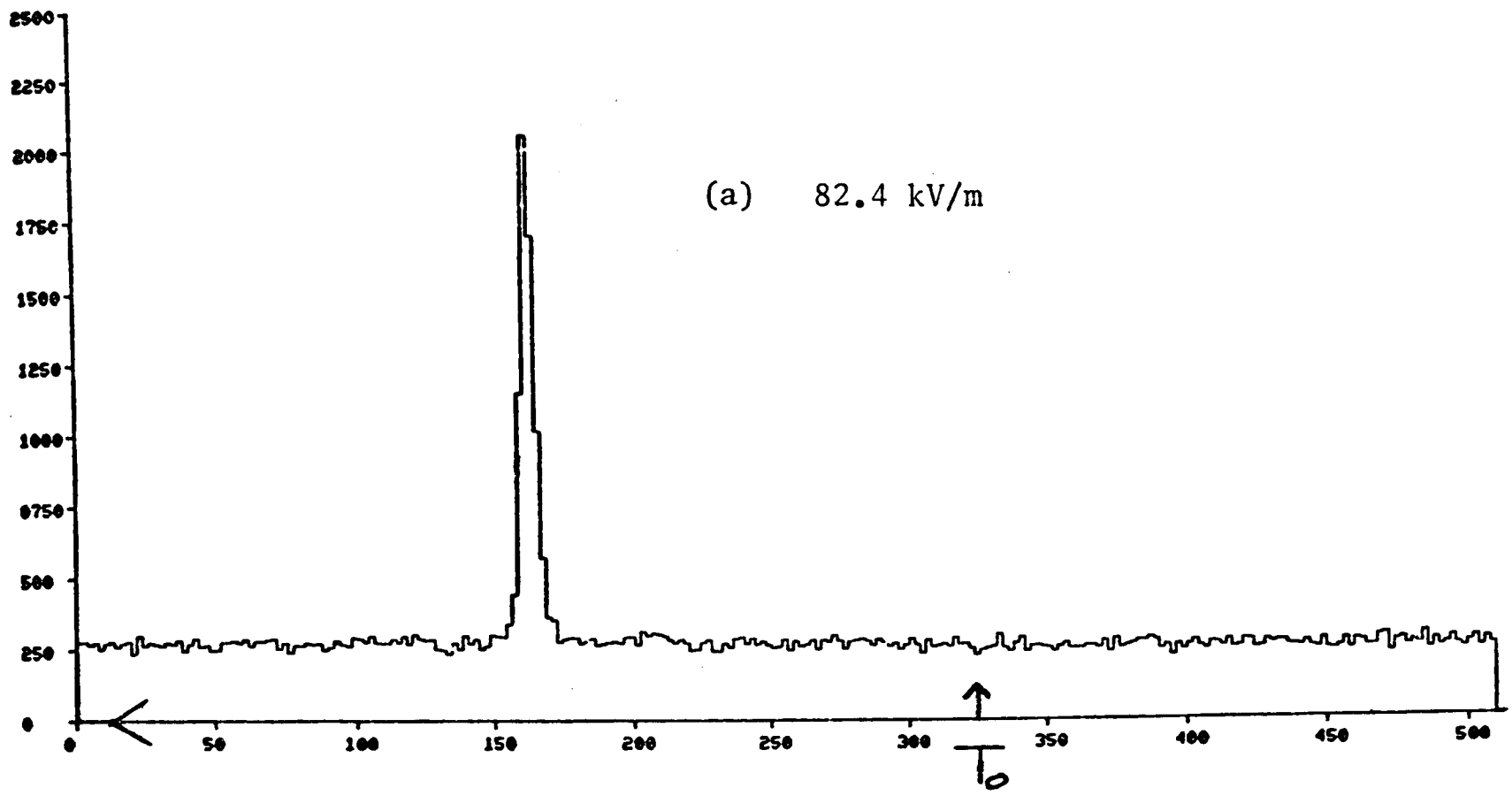
(i) The analysis of the time-of-arrival data.

(ii) The analysis of the pulse magnitude data.

Analysis of the Time-of-Arrival Data

An analysis of the time-of-arrival data yields information about several aspects of performance, including ionization drift velocity and discriminator triggering efficiency.

The necessary event-time-zero knowledge was provided by the counter coincidence. As a result, a signature could be expected in the time-of-arrival data, caused by triggering of the discriminator on the signals from the drifted ionization tracks of the tagged particles. To discover the signature, the time-of-arrival for each trigger in every (selected) event must be subtracted from the internal time-zero (T_o) for the event, also read out from the time-of-arrival memory (see III.5). The resulting time differences bear a fixed relation, over all the events in a run, to the event-time-zero, and may be histogrammed directly to display the coincidence peak. Typical examples of such histograms are shown in Figs. IV.23(a) (82.4 kV/m drift field) and IV.23(b) (74.1 kV/m drift field). The signature is obvious in both cases. The constant 'background' is caused by the randomly-timed signals from the tracks of other particles traversing the chamber.



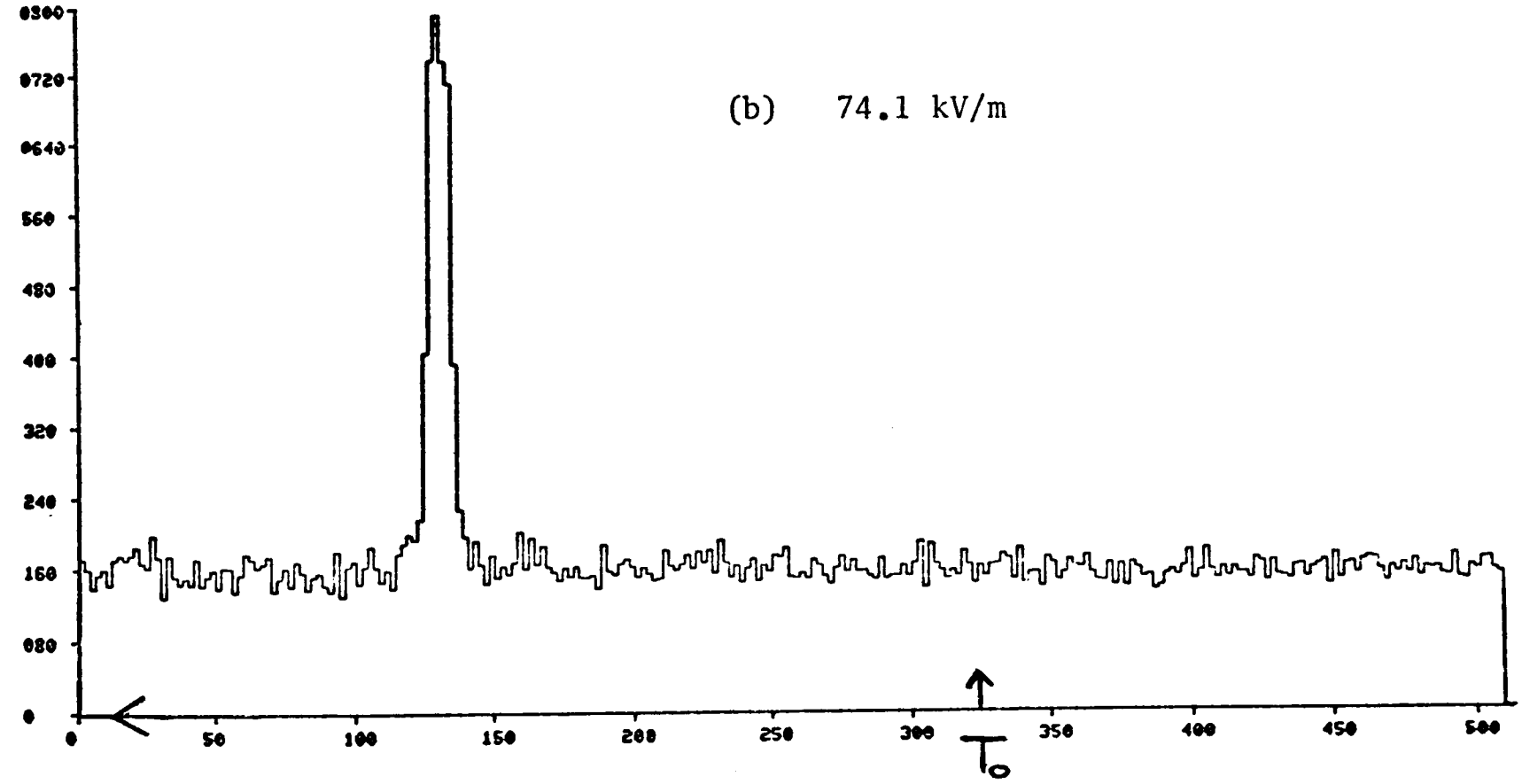


Figure IV.23 Time-of-Arrival (T_o-T) Distributions for two drift fields, showing coincidence peaks.

The units of the horizontal time axes of these two histograms correspond to increments of the time-of-arrival memory address (maximum 511, see III.5). Since this address was decoded from a counter clocked at 8 MHz, each unit of the histogram axis corresponds to 125 nS drift time, or ∿0.44 cm drift distance.

It should be noted that, on these axes, real time increases from right to left. This happens because it was the difference T_o-T that was plotted for each time-of-arrival T. Thus the event-time-zero occurred at a time equivalent to 325 units, on the right of both peaks. Similarly, since the drift time was greater for the lower field case (Fig. IV.23(b)), the peak is to the left of that for the higher field run.

Using these and similarly-constructed histograms, four properties of the time-of-arrival data were inspected:

(i) Trigger Efficiency

A trigger efficiency may be defined as the percentage of events for which a time-of-arrival is found within the coincidence peak in a T_o-T plot, after subtraction of the background. The measurement of each event is initiated by the coincidence, thus an ideal system would have a 100% trigger efficiency. The trigger efficiency as a function of mean trigger rate is given in Table IV.3 for one run.

TABLE IV.3

Mean Trigger Rate (KHz)	Trigger Efficiency (%)
30	87 ± 3
85	80 ± 4
150	67 ± 4
210	62 ± 3

Measured values of trigger efficiency ranged from 90 ± 5% down to 50 ± 10%. These are less than the ideal value. The higher efficiency values ($\tilde{\gtrsim}$90%) were associated with measurements made at low trigger rates ($\lesssim$4 triggers in 64 μS, 63 KHz). The simulation predicts a trigger efficiency of 100% at a gas gain of 10000, and one of 90% at a gas gain of 1000. The predicted value at the lower gain agrees with the measurements made under low rate conditions ($\lesssim$60 KHz). At higher rates ($\tilde{\gtrsim}$20 triggers in 64 μS, 310 KHz) triggering became less efficient. This reduction in efficiency was not consistent with the expected effect of a finite system dead-time. The blame for the loss in efficiency rests with the DC Baseline Restorer (DCBR), which was not operating correctly. The DCBR supplies a reference level to the discriminator, compensating for rate-dependent variations in baseline (see III.6). The DCBR, as used in these tests, was providing incomplete, unstable, baseline restoration, resulting in a loss of discriminator sensitivity at high rates. The effect was reproduced using pulse generators, after the end of the tests. A minor redesign of the DCBR eliminated the tendency, and, as stated in III.6, the DCBR is now capable of baseline restoration, to an accuracy of 1% with pulses of frequency 2 MHz, and mark-space ratio 50%.

(ii) Position Resolution

The quality of the time-of-arrival performance is demonstrated in the T_o-T histogram of Fig. IV.24. This contains only data acquired at low rates ($\lesssim$4 triggers in 64 μS: 63 KHz) and early in the beam spill ($\lesssim$40 mS from the start). Otherwise the conditions were the same as for Fig. IV.23(a).

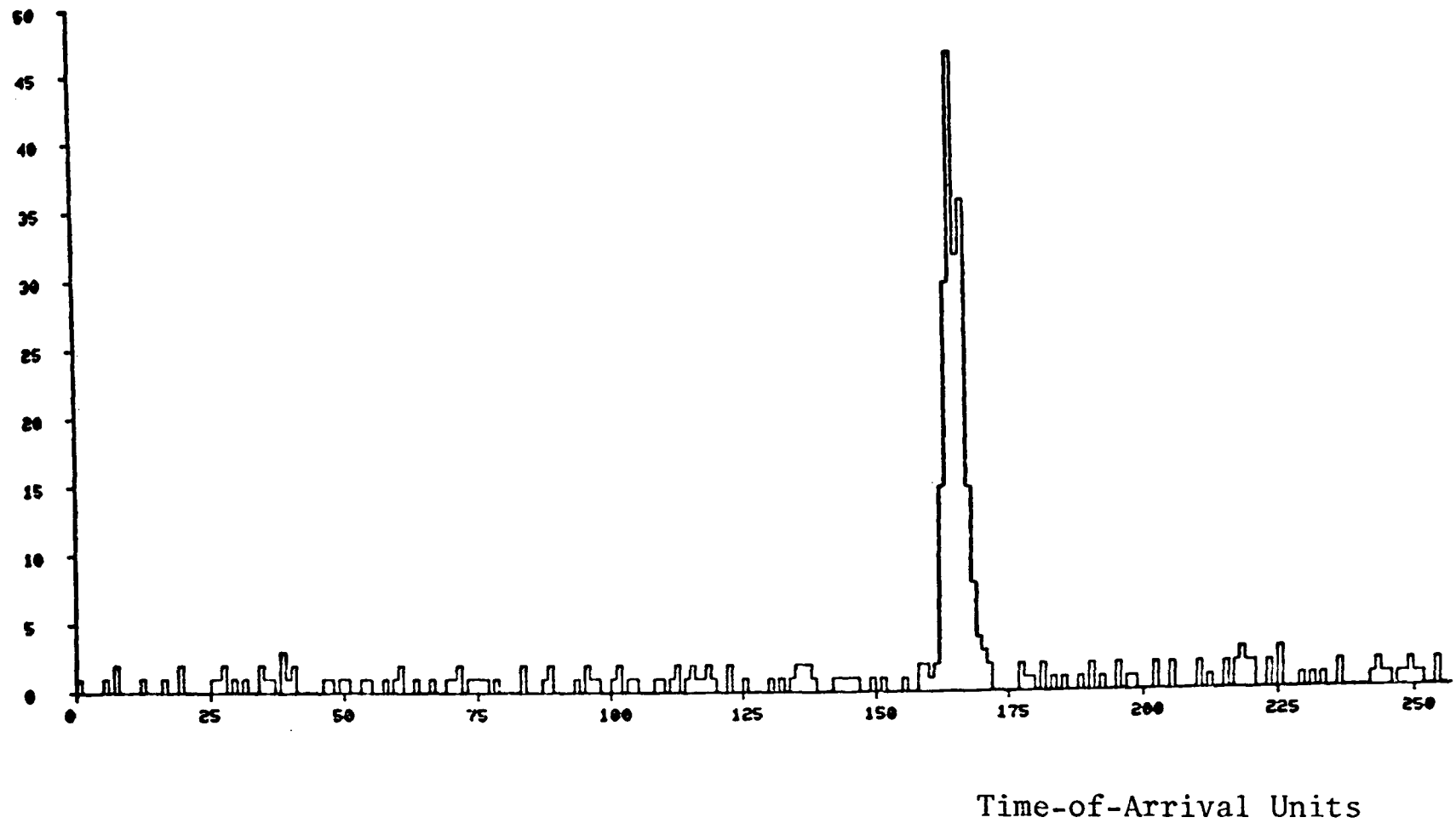


FIGURE IV.24 T_o-T Histogram Obtained at Low Rates, Early in the Beam Spill

The important factor is the width of the coincidence peak: 4 units FWHM. In terms of time, this is 4 x 125 nS = 500 nS FWHM; or in terms of drift distance it is $\tilde{\sim}$1.8 cm. FWHM. This width represents a jitter in the signal timing. There are two main causes of jitter to be considered:

(a) The finite dimensions of the ray-defining scintillator ($\tilde{\sim}$3 mm in the drift direction, see earlier). This problem does not arise in the final device.

(b) The imperfections of the drift field electrostatics in the prototype chamber (estimated to be $\tilde{\sim}$1% or $\tilde{\sim}$7 mm in the drift direction). Much work has gone into the final design of the chamber electrostatics to ensure field uniformity to 0.1%, (see II.2, [IN26]).

Taking these two factors into account the jitter is reduced to the order of ∿200 nS. This is satisfactorily near to the time-of-arrival memory clock period of 125 nS, which represents a minimum

attainable jitter. Thus it can be seen that the system is capable of returning useful position data, accurate for one channel to better than 1 cm. When averaged over the length of a track, these jitter errors, being random in nature, would be further reduced.

(iii) Stability of the Drift Velocity

If the coincidence peaks of Figs. IV.23(a) and (b) are inspected, it will be seen that their widths are 8 and 12 units FWHM respectively. These values are 2-3 times the width of the peak in Fig. IV.24. The reason for the discrepancy lies in the fact that the histograms of Figs. IV.23(a) and (b) contain data from all times during the beam spill, whereas the histogram of Fig. IV.24 contains only data taken in the first 40 mS of beam spill. If the position of the coincidence peak were to shift during the beam spill, then the apparent width of the peak for the whole period would be greater.

Evidence for this is shown in Figs. IV.25(a) and (b). The histogram in Fig. IV.25(a) is part of that in Fig. IV.23. The histogram in Fig. IV.25(b) is from the same run as (a), but contains only data from events occurring between 120 and 160 mS after the start of the beamspill. There is a shift ΔT in the position of the coincidence peak towards later times, of

$$\Delta T = 4.5 \text{ bins}$$
$$= 4.5 \times 125 \text{ nS}$$
$$= 560 \text{ nS}$$

This effect was apparent in every run. In Fig. IV.26 are shown the positions of the coincidence peak against the time into the beam spill ('flat-top') for three drift fields. All results show a shift in the coincidence peak towards longer drift times, as the time from the start of the beam spill increases.

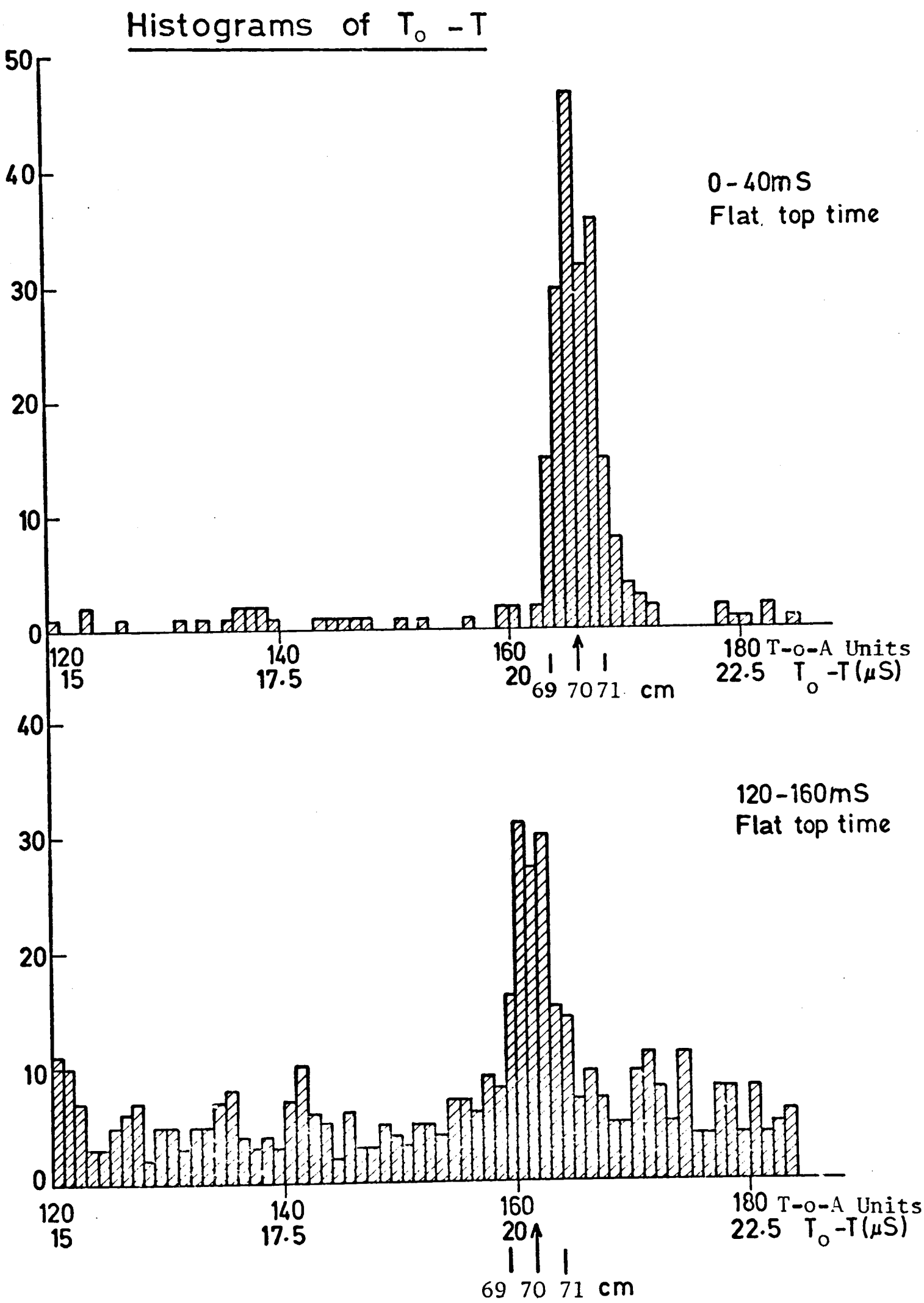
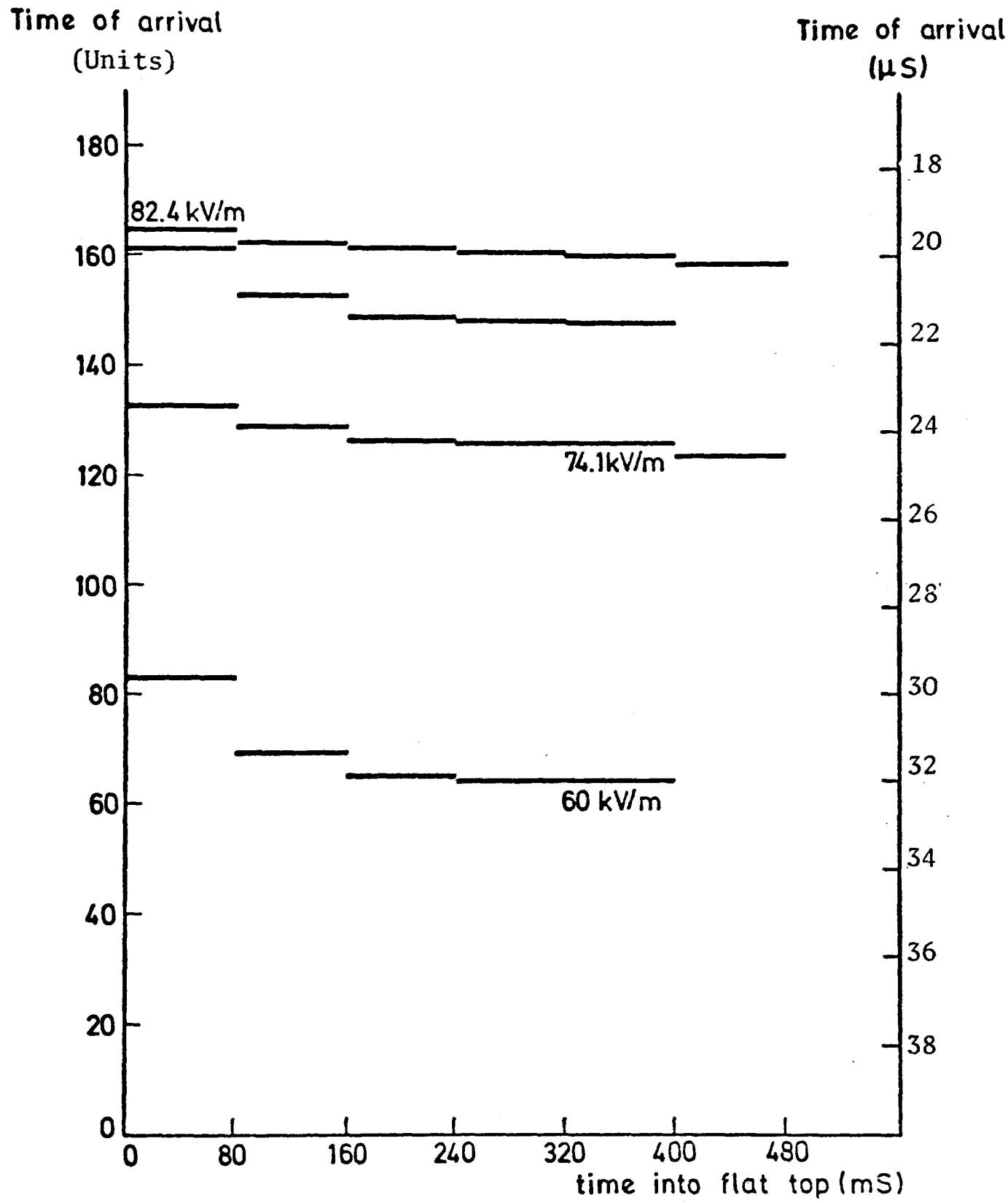


Figure IV.25 T_o-T Histograms Showing Drift Time Shift.



Plot of position of coincidence timing peak against time into flat top.

Figure IV.26

These observations are symptomatic of a space-charge induced effect. The chamber, being initially clear of space charge, fills up with the positive ions generated during gas amplification, in a time of about 40 mS (see II.3). The space charge reduces the effective drift field, and therefore also the drift velocity. The result is a lengthening of the drift time (see [CJ75]).

At lower drift fields, the lifetime of the positive ions is longer. The equilibrium space charge density is thus greater, other conditions being equal, producing a larger shift in drift time over the beam spill. This is observed; in Fig. IV.26 it may be seen that the drift time shift increases at lower fields. The evidence points directly at space charge being the cause of the shift.

Negligible space-charge-induced effects are predicted for the final device [IN20]. It is important to understand where the differences lie between the assumptions made for these predictions, and the conditions for the tests with the prototype chamber. It is possible to calculate an approximate value for the space charge density from the resultant drift time shift. The presence of a small space charge density ρ causes a shift ΔT in the drift time T for tracks drifting a distance S (= 0.70 m):

$$\frac{\Delta T}{T} \approx \rho \frac{(L - S)}{\varepsilon_o E_o} \qquad \text{[CJ75]}$$

where L is the maximum drift distance (of 0.78 m in the prototype) and E_o is the drift field in the absence of space charge. Using this relation, values of ρ were found for two sets of chamber operating voltages: these are given in Table IV.4

The space charge created in the drift regions at a gas gain G is of density:

$$\rho = \emptyset G.e\bar{N}_e \cdot \frac{\tau(1-\alpha)t_r}{2} \qquad \text{(see II.3)}$$

in which $\emptyset$ = mean particle flux per unit effective frontal area of chamber per second

G = gas gain

e = electronic charge

$\bar{N}_e$ = ($\tilde{}10^4$/m) mean number of ionization electrons per unit length of non-inclined track.

$\frac{\tau(1-\alpha)t_r}{2}$ = a chamber-specific parameter consisting of:

τ = positive ion lifetime, equal to the positive ion drift time for the chamber length

α = space charge drain parameter

t_r = effective gas amplifier duty cycle, due to gas gain switching.

It is in the chamber-specific parameter that differences between the prototype and the final device are to be found.

With a positive ion mobility of 1.5×10^{-4} $m^2/v/s$, (see II.3), the positive ion lifetime τ is

$$\tau = \frac{6.6 \times 10^3 \, L}{E_o} \quad \text{seconds}$$

Thus τ = 82 mS at 60 kV/m
62 mS at 82.4 kV/m } for the prototype

133 mS at 100 kV/m for the final device.

The space charge drain parameter α depends on the wire charges and their spacing, (see II.4):

$(1-\alpha) \equiv 0.5$ for the prototype

$\equiv 0.8$ for the final device

The main difference between the two devices is in the value of the gas amplifier duty cycle. Gas gain switching (see Appendix 2) was not used in these tests, but will be used in the final device:

$t_r = 1$ for the prototype

$= 0.06$ for the final device (2 mS every 33 mS, see Appendix 2).

The resulting values of the chamber-specific parameter are:-

$$\frac{\tau(1-\alpha)t_r}{2} = \begin{cases} 21 \text{ mS at } 6.0 \text{ kV/m} \\ 15 \text{ mS at } 82.4 \text{ kV/m} \end{cases} \text{ prototype}$$

3.2 mS at 100 kV/m final device

Thus the mean space charge density in the final device will be a factor of ∿6 smaller than that in the prototype for the same ØG.

The values of ØG for the prototype chamber, calculated from the space charge density, are given in Table IV.4. The two results are approximately equal, at about $1.5 \times 10^{10}/m^2/sec$.

An estimate of the gas gain can be made, since a rough value for the flux is known. The mean trigger rate at which the drift time shift occurred, was ∿20 ± 10 triggers per event. Allowing for a triggering efficiency of ∿75%, this corresponds to a beam rate of ∿400 KHz. The effective chamber cross-section, as determined by the width of the beam and the drift distance, was ∿2 cm x ∿75 cm $\tilde{\sim}$ 0.02 m^2. The flux was therefore of the order of:

$$\phi \tilde{\sim} 10^7/m^2/sec$$

The gas gain is then (see Table IV.4)

$$G \tilde{\sim} 1500^{+3000}_{-1000}$$

The beam rate and the effective cross-section were not known accurately - these results may be in error by as much as an order of magnitude. However, this gas gain value is about equal to those obtained by other means, e.g. pulse magnitude measurement, see later.

It is also important to note the main difference between the environment of the prototype and that of the final device. In the

TABLE IV.4 CALCULATION OF GAS GAIN FROM EFFECT OF SPACE CHARGE

Drift Field (kV/m)	T (μS)	ΔT (μS)	$\Delta T/_T$	ρ (c/m^s)	$\emptyset G$ ($/m^2/s$)	G for $\emptyset = 10^7/m^2/s$
60.0	29	2.5	8.5×10^{-2}	5.6×10^{-7}	1.6×10^{10}	1500^{+3000}_{-1000}
82.4	20	0.6	3×10^{-2}	3.0×10^{-7}	1.3×10^{10}	

prototype, the mean effective flux was:

$$\phi_{prototype} \tilde{\sim} 10^7/m^2/sec$$

In the final device, the maximum mean effective flux will be:

$$\phi_{final} \tilde{\sim} 5 \times 10^4/m^2/sec \qquad [IN26],[EHSP]$$

These are over two orders of magnitude different. The results are thus consistent with the prediction of negligible space-charge-induced effects in the final device.

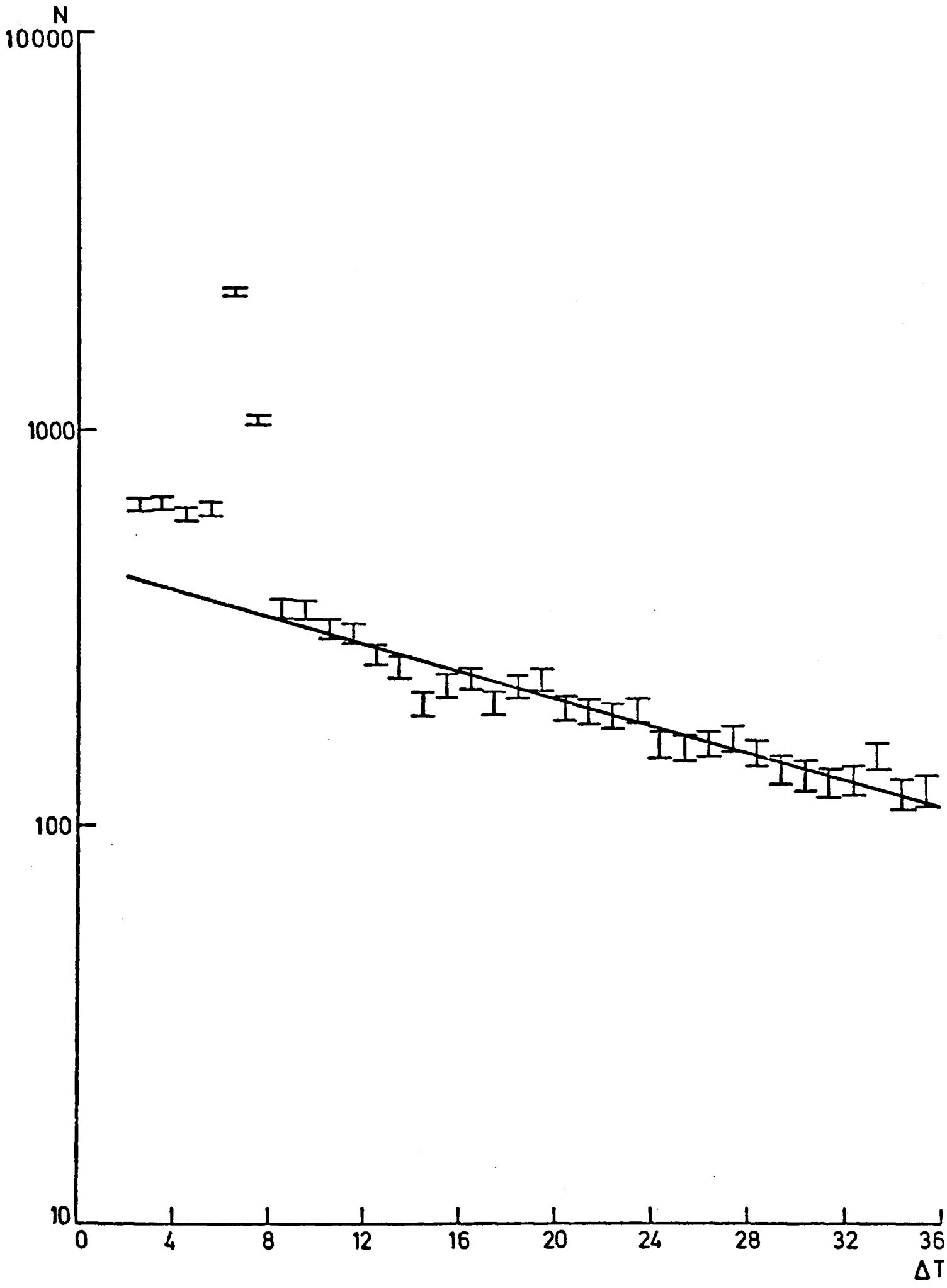
(iv) Distribution of Inter-Trigger Timings

The particles are assumed to have crossed the chamber at random times. There should not be any correlation between the individual measured trigger times. To test this assertion, the total number N of events was found, for which a trigger had occurred a certain time ΔT after the previous one. Plots of log N against ΔT were produced for events having a mean trigger rate within a certain narrow range. On a plot of this form, uncorrelated trigger times lie along a straight line, the slope of which is determined by the mean trigger rate. A typical plot is shown in Fig. IV.27, for a range of mean trigger rates of 25-30 KHz. (The units of ΔT are, as usual, time-of-arrival memory address increments, see III.5.)

It may be seen that, for $\Delta T > 8$, the trigger times display the characteristics of being uncorrelated. However, at smaller ΔT, there are deviations from the expected behaviour, which were caused by:

(a) Excessive Multiple Triggering

Some of the triggers for which $\Delta T = 3,4, 5$ or 6, were generated by double or multiple firing of the discriminator on one signal. This proportion amounts to about 5% of the total number of triggers; the



Plot of No. of events against $\Delta T = T_i - T_{(i-1)}$

Figure IV.27

expected value is 1-2% (see IV.6). The effect was probably due in part to the noisy nature of the signals, which would have been accentuated by the low gas gain. However, most of the multiple triggers will have been carried by the DCBR instability, as explained below.

(b) Excessive Retriggering

The large numbers of events for which $\Delta T = 7$ or 8 were caused by a malfunction within the DCBR. On long, large signals, a time-out causes the gate generator to retrigger every 1 μS, (see III.5). This time interval may be identified with the $\Delta T = 7$ and 8 events, since the time-of-arrival memory clock period was 125 nS. The long, large signals were not real; they have been traced to a temporary instability of the DCBR, which supplies a DC reference to the discriminator. The effect was reproduced afterwards, using pulse generators. This fault has been rectified, as explained earlier.

Analysis of the Pulse Magnitude Data

The preliminary analysis of the single-channel pulse magnitude data involved building histograms of the pulse magnitude component from each (selected) trigger in a run. The observed distribution of pulse magnitudes should mirror the Landau distribution of ionization loss (see II.1). However, the combination of low non-linear gas amplification and incomplete baseline restoration (see earlier) produced pulse magnitude data of poor quality.

A typical histogram is shown in Fig. IV.28(a), of the pulse magnitudes from every trigger in a run. The gas gain, and thus the measured pulse magnitude are highly sensitive to the presence of positive ion space charge (see II.3). The existence of space charge during these tests has been demonstrated by the effect on drift

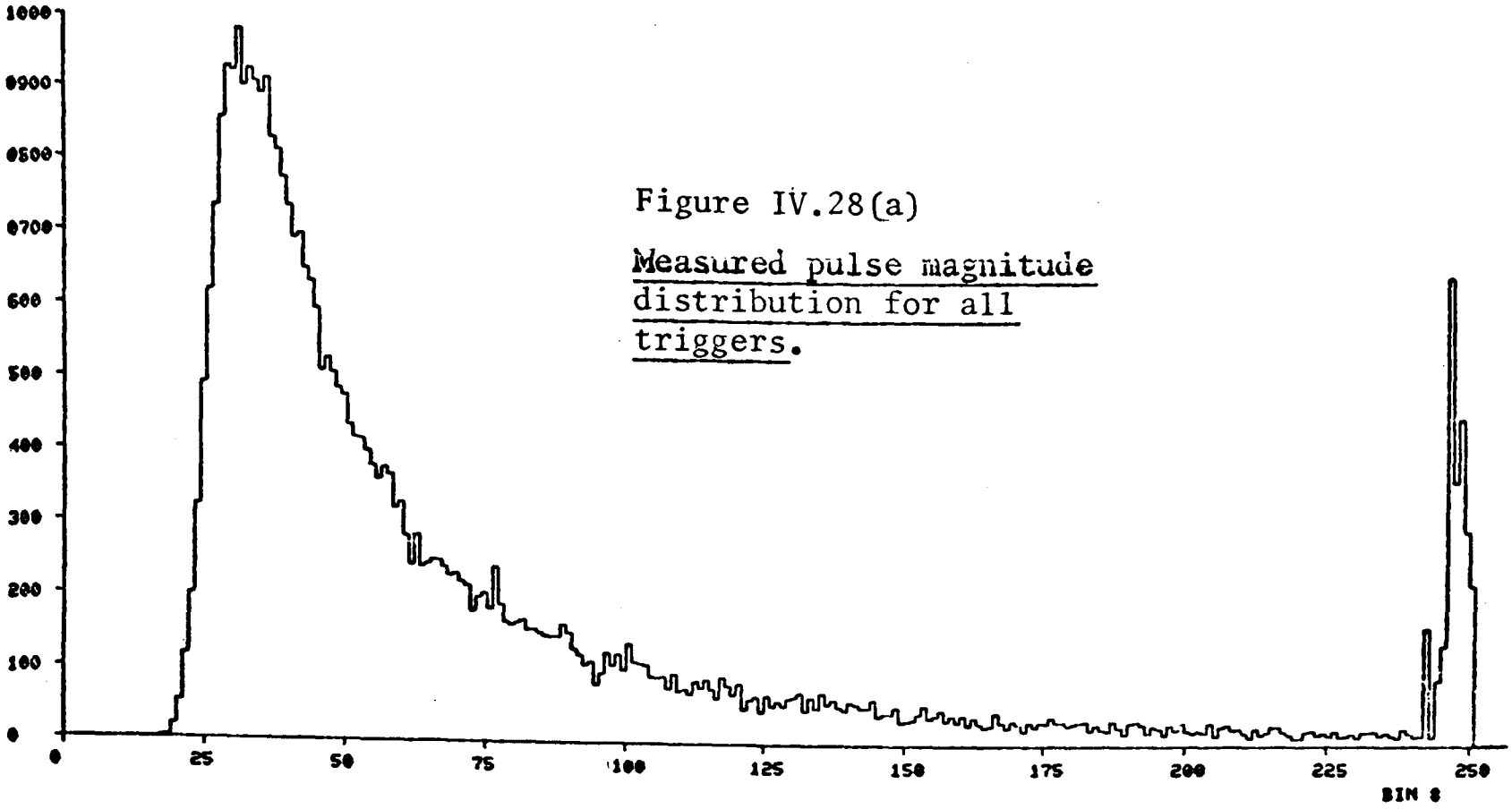


Figure IV.28(a)

Measured pulse magnitude distribution for all triggers.

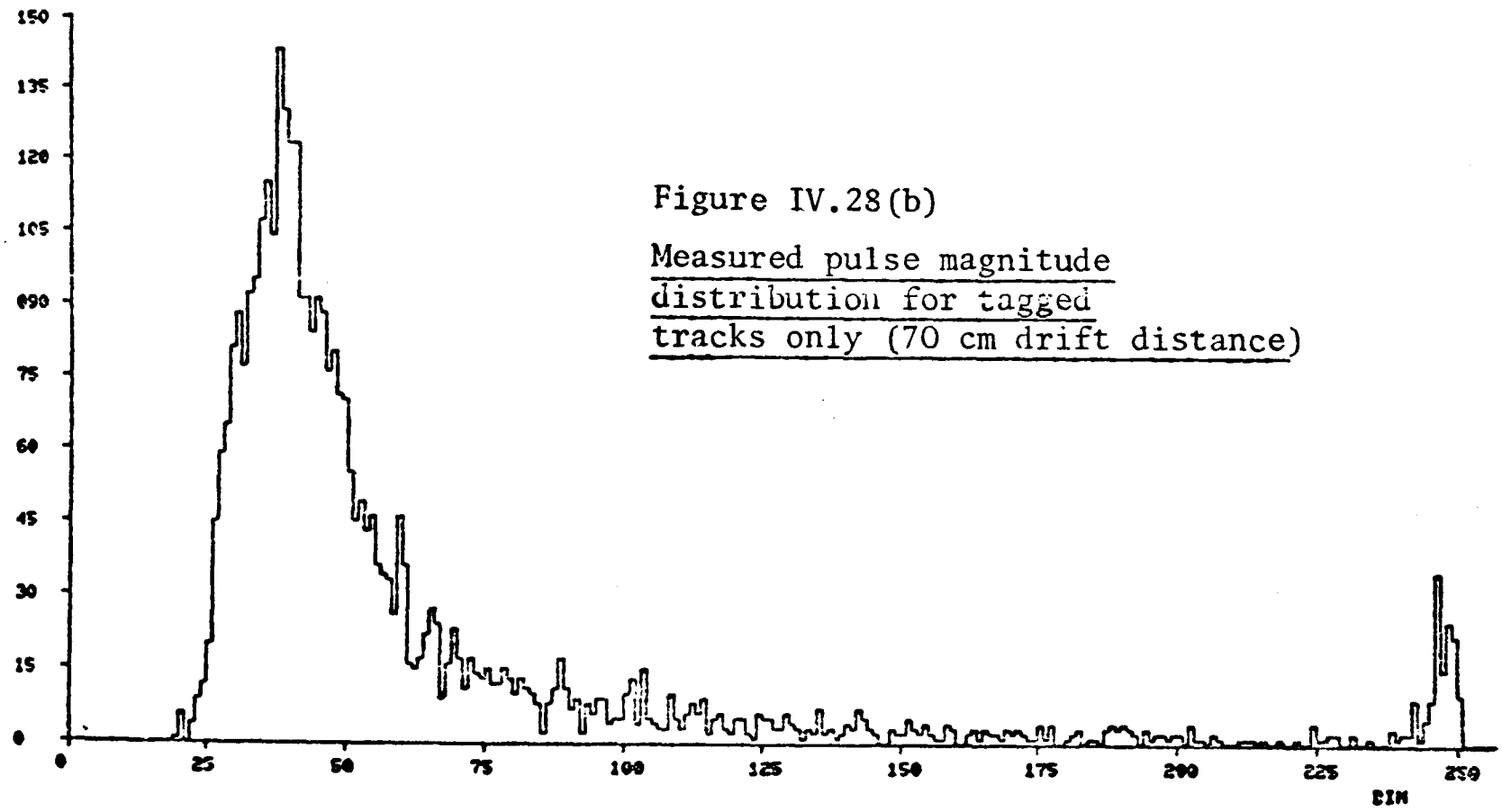


Figure IV.28(b)

Measured pulse magnitude distribution for tagged tracks only (70 cm drift distance)

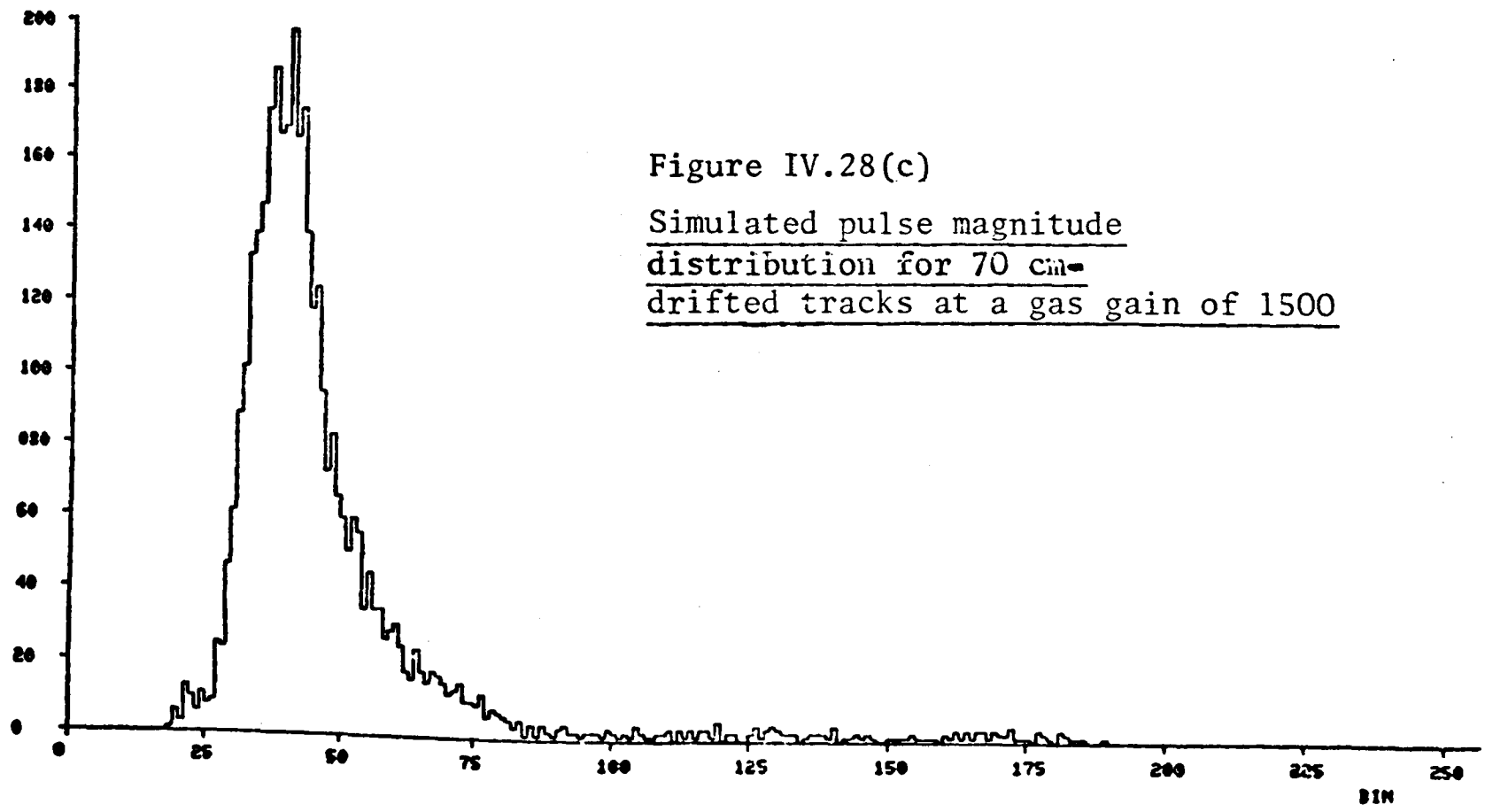


Figure IV.28(c)

Simulated pulse magnitude distribution for 70 cm-drifted tracks at a gas gain of 1500

velocity (see earlier). To reduce, as far as possible, resultant changes in the gas gain, this and subsequent histograms contain only data acquired during the first 40 mS of beam spill. Histograms of pulse magnitude data from later in the beam spill do indeed show a reduced gain.

To compensate for the slight variation (∿3%) in pedestal between analogue memory capacitors, a subtractive correction was made to each pulse magnitude. The value of the correction depended on the pre-measured pedestal for the memory capacitor on which the pulse magnitude was stored (see III.4). As a result it was possible to combine the data originating at different analogue memory capacitors. On the histograms in Fig. IV.28, pulse magnitude zero occurs at bin #20.

The histogram of Fig. IV.28(a) bears a poor resemblance to the Landau distribution of Fig. II.1. This is because Fig. IV.28(a) shows the measured ionization distribution for <u>all</u> signals causing a trigger, independent of particle velocity, drift distance or, particularly, track orientation (which effectively amplifies the ionization loss by $1/\cos\theta$).

It is more meaningful to select data from only those triggers associated with the coincidence. The resulting subset of pulse magnitudes may be confidently identified with the 70-cm-drifted ionization samples from the well-defined tracks of the tagged particles. The histogram shown in Fig. IV.28(b) is made up of data selected in this way from that of Fig. IV.28(a). The new histogram contains only 10% of the old, and is itself contaminated with about 10% of random background triggers.

The histogram of Fig. IV.28(b) should be compared with that of Fig. IV.28(c), which was obtained by simulation at the low gas gain of 1500. (This particular value was derived by demanding that the peak

of the simulated histogram (c) occurred at the same bin number (#38) as that of the measured histogram (b)). Comparing (a), (b) and (c), the similarity in shape of the ionization distribution is stronger between (b) and (c) than between (a) and (c). For example, in (a) the high energy side of the peak falls off less quickly than in (b) and (c). This reflects the importance of using only that data associated with a well-defined particle track trajectory. However, (b) and (c) are by no means identical in shape. The reasons were that:

(i) the gas amplification was not proportional, because of the contamination of the gas by large amounts of CO,

(ii) the baseline restoration was inefficient, causing a rate-dependent reduction in pulse magnitude, (see III.6).

Both these problems have since been solved (see earlier.

Further analysis of the pulse magnitude data was felt to be unjustified, because the gas amplification and DCBR had produced an unacceptable degradation of the results. The detailed investigation of small systematic effects was not attempted.

The conclusion from this simple analysis of the pulse magnitude data is that the effective gas gain used was 1500 ± 50%.

Conclusion

The quality of the data collected during these tests was poor. The reasons were:-

(i) Bad gas

(ii) Bad dc baseline restoration.

Both these problems have since been cured. It should be noted that previous tests have given good results [CJ75], [BJ76], and that the problems arose as the result of independent modifications intended

to improve performance and efficiency.

As regards verification of the predictions of simulation, the results are disappointing. However, there is no reason to doubt the validity of the simulation: no inconsistencies were discovered.

On the positive side, a large amount of useful operational experience was gained during the tests.

IV.5 DERIVATION OF OPTIMUM SYSTEM DESIGN

As stated in IV.1, the objectives of the investigation described in this Chapter are basically twofold:-

(i) to obtain an optimum design for the signal processing system in ISIS, and

(ii) to predict the resulting performance characteristics.

The former of these is discussed in this section, and the latter in IV.6.

It has been demonstrated, in the first part of the Chapter, that it is possible to simulate, to a reasonable degree of accuracy, the processes involved in the detection and measurement of the signals from a drift chamber of the ISIS design. The confidence established in the validity of the simulation, allows trust to be placed in the predictions, of situations for which there is not, as yet, much experimental verification.

In both this section and the next, the results of the simulation are used extensively in providing the data necessary for the analysis. There is, however, a proviso on the use of the data, that the

simulated situations should not deviate too far from those for which the simulation has been checked.

The derivation of the optimum design is a three-stage process:

(i) the definition of a few basic performance criteria

(ii) the definition of an operating window, as constrained by these criteria

(iii) the choice of the best operating point within the window.

The optimum design is defined with reference to three inter-dependent performance criteria:

1. Quality of Ionization Data

As outlined in I.2 and II.1, particle velocity is derived from the measured distribution of ionization along the track of the particle. The velocity value is obtained from the pulse magnitude data for the track by an algorithm which weights the lower values of pulse magnitude (below about 5 KeV, see [CJ76]). As a result, the effect of any systematic errors in the measurement of smaller quantities of ionization is accentuated. Since the velocity value is vulnerable to systematic effects at the level of 1% [AW76], the measurement of small quantities of ionization must be accurate.

In order to define a quantitative criterion for small signal performance, the expected distribution of signals must be inspected. The required information is given by the Landau ionization-loss distribution (see II.1, and Fig. II.1). A suitable performance target is: the ability to measure the ionization in 95% of all signals to a mean accuracy of 1% or better. Taking the worst case of a minimum-ionizing particle ($^{P}/M_{o}C \tilde{\gtrsim} 4$), this is equivalent to being able to measure all signals resulting from an ionization loss in the

1.6 cm sample of 1.3 KeV or greater (50 ionization electrons in 80% A/20% CO_2) with an average accuracy of 1%. A 100% triggering efficiency for such signals is implied.

The main systematic error, in the measurement of small amounts of ionization, is under-estimation of the amount of ionization in the sample. This can arise for instance, if part of the pulse is outside the duration of the integration gate (see III.4, and later). This situation may occur when the SNR is small because of the finite trigger-on level. The lowest SNR's are encountered when the ionization has drifted from the maximum distance of 2 m, because the diffusion dispersion is greatest. The first performance criterion may thus be stated:

> Criterion 1: For track ionization samples containing 50 electrons or more, drifting from the maximum distance of 2m, measurements of the amount of ionization must be, on average, accurate to 1% or better.

2. Quality of Position Information

Ionization tracks may arrive at the wire plane at arbitrary times. The ability to process correctly, signals occurring within a short time (∿100 nS) of each other, depends on the effective dead time of the electronics. As a consequence of the electronic design, the effective dead time is equal to the integration gate duration (see III.4, III.5). Because of finite SNR, the gate duration is the sum of two components:

(i) The Signal-Dependent Discriminator Output

The minimum signal duration is determined by the dispersion of the ionization as it drifts (see II.2) convoluted with the gas amplifier response. However, to increase the SNR, non-gated linear

(RC) integration of the signal occurs within the electronics. This also results in an increase of the signal duration. If excessive, linear integration will lengthen the signal duration so much as to harm the ability to accept close signals. There is thus a compromise to be made, between an acceptable close-track performance, and a reasonable SNR.

(ii) A Fixed Signal-Independent Gate Extension Time

In order to measure accurately the pulse integral for the weakest signals, it is necessary in generating the integration gates, to extend the duration of the discriminator output pulses. (This is explained fully in III.5.) The minimum gate extension time is fixed at the value required to satisfy Criterion 1. However, for larger, sharper pulses, a smaller extension would be sufficient, for a satisfactory integration performance. The fixed extension may thus represent an unnecessary addition to the system dead time for these signals. Tracks which have drifted only a small distance ($\lesssim$20 cm) will give rise to these sharp, well-defined signals. Therefore the fixed extension will cause an unnecessary loss of close-track performance for such tracks. This is especially important because the density of tracks near to the wire plane is expected to be high [EHSP]. To give good resolution of the closest tracks under all SNR conditions, the value of the fixed signal-independent gate extension time should be as small as allowed by Criterion 1.

To this extent, then, a compromise exists between the possible systematic errors of ionization measurement, and the tolerable two-track performance.

Criterion 2: For best resolution of closely-timed signals:

(a) the signals should be linearly integrated as little as possible, subject to obtaining an acceptable SNR,

(b) the fixed gate extension time should be as small as is consistent with satisfying Criterion 1 at the ambient SNR.

3. The Tolerable Effect of Noise-Induced Triggering

Signals whose amplitudes are greater than the trigger-on level are detected by the discriminator. The presence of noise in addition to signal causes spurious noise-induced triggering. In order to detect smaller signals, the trigger-on level must be reduced. However, if this alone is done, the noise triggering rate increases. For a given noise triggering rate, the size of the smallest detectable signals is determined by the noise level.

The third performance criterion answers the question, "What is a tolerable noise triggering rate?"

Two factors are relevant in this discussion:

(i) The ratio of mean noise-induced triggering rate $\bar{R}_n$ to mean signal-induced triggering rate $\bar{R}_s$

If no other method existed of determining which triggers were due to noise, and which to signal, then it would be necessary to operate with a very low relative noise triggering rate to ensure data integrity, say $\bar{R}_n \lesssim \bar{R}_s/1000$. This is the traditional compromise between probability of detection and false-alarm rate. However it is possible to distinguish noise triggers and signal triggers. Signal-

induced triggering occurs when a charged particle traverses the chamber. The data output from all ∿320 channels may be viewed as an 'event-picture' (see I.2, IV.4). Signal triggers are identified as those which form tracks in the event-picture. Noise triggers occur randomly throughout the event-picture, and may therefore be discarded. With this additional knowledge, thenoise-induced triggering rate may be raised without harming data integrity. If this is achieved by loweringthe trigger-on level, smaller signals will be detected. A tolerable mean noise triggering rate R_n may be as high as $R_n \tilde{\sim} R_s/10$. For a mean signal rate of 400 KHz (25 tracks within the ISIS chamber, see I.2), this indicates that a noise rate of ∿40 KHz would be tolerable.

(iii) The finite data capacity of the electronics

The pulse magnitude and time-of-arrival data for each trigger are stored temporarily in the electronics, before being transferred to more permanent storage e.g. magnetic tape (see I.2). The temporary storage in the electronics has a finite data capacity. The valueless data from noise-induced triggering will use up some of this space.

The tighter constraint on temporary storage size is set by the number of capacitors (32) in the analogue charge memory (see III.4). At any one time, this memory can contain the pulse magnitude data for a maximum of 30 signals. Clearly, most of this limited storage space must be used for signal data. A suitable criterion for the noise triggering rate is that there should not be, on average, more than 1 noise trigger in the 50 μS 2 m-drift time: $\bar{R}_n$ = 20 KHz. At this noise rate, only 3% of the available pulse magnitude storage will be taken up by noise data. In terms of a typical event-picture, there will be an average of one noise trigger per channel, or ∿320 in total.

(The effect of noise on the pulse magnitude measurement itself is small. The noise is integrated over the duration of the signal integration gate (see IV.4). Thus the effective bandwidth here (of the order of 1 MHz), is much lower than that at the discriminator input (∿10 MHz). The result of this integration is that the estimated noise width of the system is 0.15 KeV (simulated), which is negligible compared to the ∿2 KeV FWHM of a Landau distribution (see II.1).)

Criterion 3: The mean no-signal noise-induced triggering rate should be 20 KHz.

In summary, the criteria require decisions to be taken on values for the following interdependent parameters:

(i) gas amplification factor G

(ii) amount of linear (RC) integration in the electronic stages

(iii) discriminator trigger-on level

(iv) integration gate extension time.

These are arranged in order of increasing mutual dependence, given the initial condition of a fixed equivalent input noise level. For instance, the gate extension time depends on the SNR (as determined by the gas gain G, the input noise level and the amount of linear integration) and on the trigger-on level. The trigger-on level itself only depends for a given noise trigger rate on the (fixed) noise level and the amount of integration. Thus the order of dependence is also the order in which decisions should be made on values for these parameters.

The Gas Amplification Factor G

To obtain the best performance from any system, it is necessary to operate at the highest SNR compatible with such considerations as linearity and systematic effects. ISIS is no different; to obtain the highest SNR, the (noise-free) gas amplification must be at its highest permissible value. The upper limit to G is determined by space-charge induced non-linearity and systematic gain-shift effects (see II.3 and IV.4). The maximum value is estimated to be

$$G_{max} = 10000$$

With differential operation (see III.2), the equivalent gas gain is

$$G_{eq.max} = 15000$$

These values were assumed in obtaining the following simulation results.

The Linear Integration Within the Electronics

The response of the electronics does not extend to infinite frequencies: the bandwidth is limited. In the time domain, this results in, and is equivalent to, a linear integration of the signals, including any noise. The amount of linear integration introduced by an electronic process may be parametrized by the resultant 10-90% risetime of the output for a step function input. For a single-pole integrating RC time constant this rise time is of value 2.20 RC.

All electronic stages have an integrating effect to a greater or lesser extent. In the ISIS electronics, there are three main contributions to signal integration:

(i) the risetime of the preamplifier input stage: τ_{input}, (see III.2)

(ii) the risetime of the cables taking the signals from the preamplifier to the remote electronics: τ_{cable}, (see III.2)

(iii) the risetime of the analogue delay line: τ_{delay}, (see III.4, III.5).

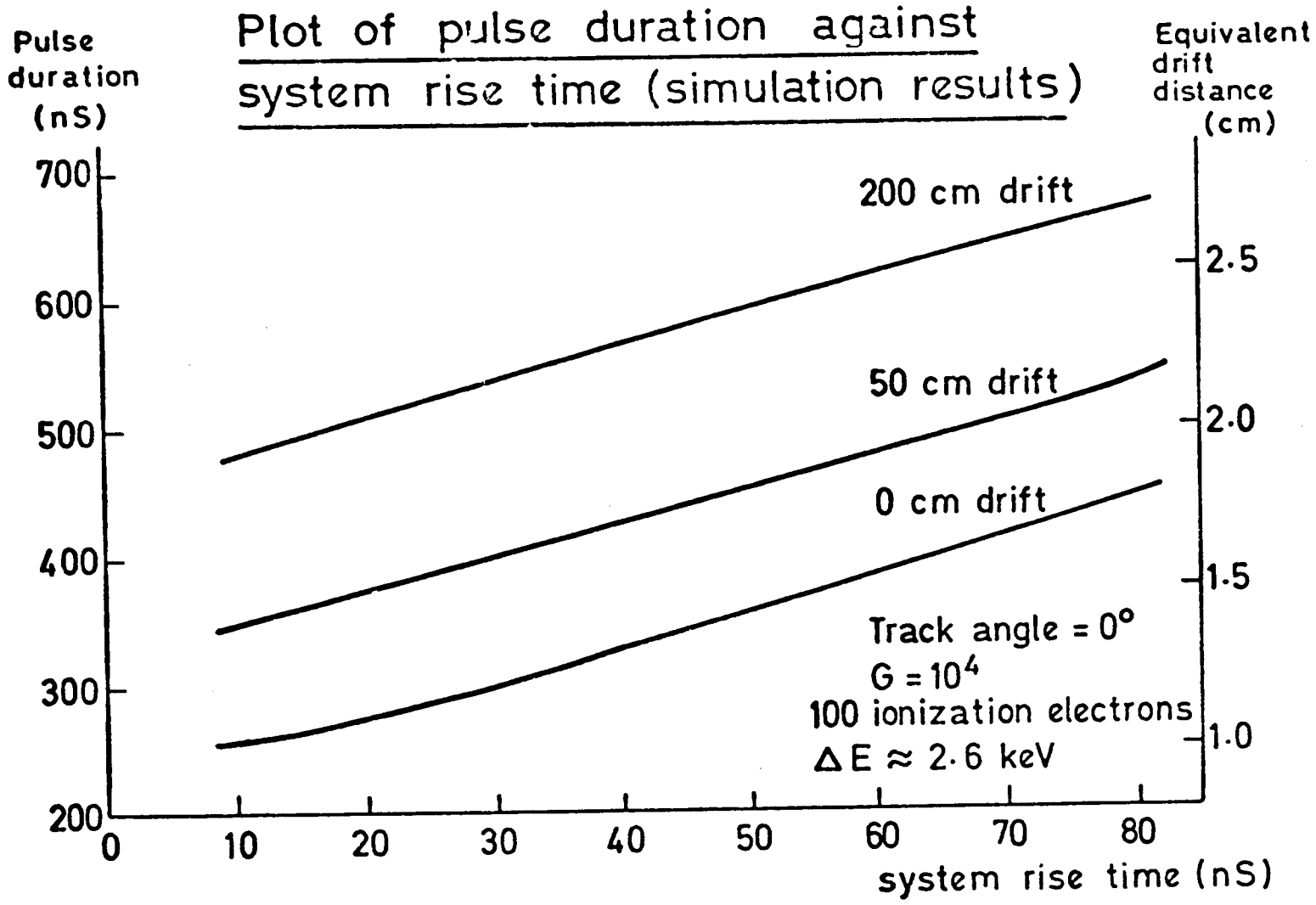
For these three components, a fast risetime (~10's nS) is a critical practical characteristic; in all other stages, fast risetimes of this order are relatively easily achieved (see Chapter III).

There is nothing to be gained by making one of the three risetimes any faster than the others. A "system" risetime is defined as:- (this being the common risetime value)

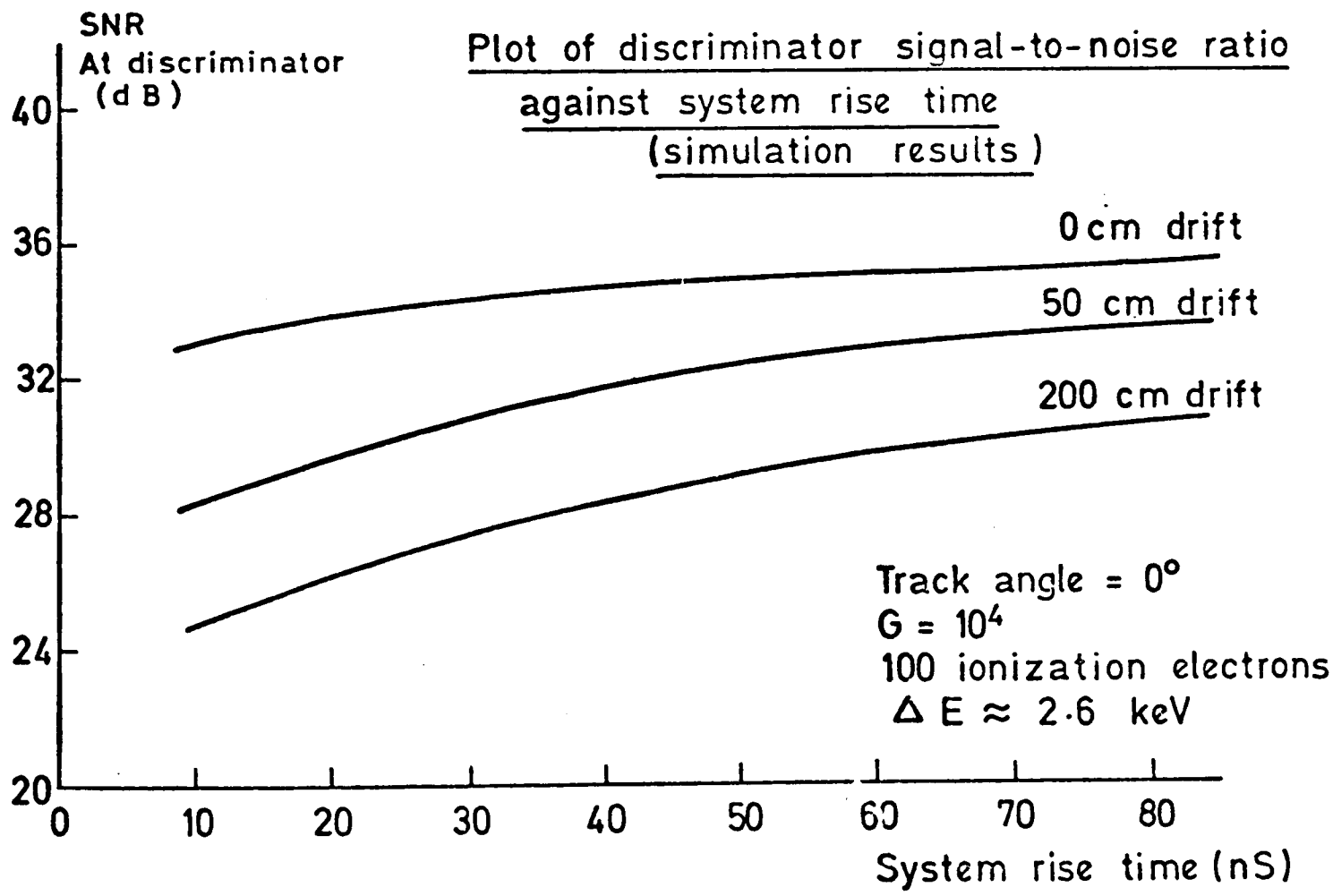
$$\tau_{system} = \tau_{input} = \tau_{cable} = \tau_{delay}$$

As stated above, the system risetime affects the duration of the signals and also the SNR. Using the simulation, both these aspects were investigated. For the purposes of simulation, the three main risetime contributions were each approximated to an equivalent single-pole RC integrator of the appropriate time constant. The approximation is good for the input risetime τ_{input}. However, both τ_{cable} and τ_{delay} are strictly only equivalent RC risetimes, since both elements are, by nature, distributed. All other stages were each assumed to have a nominal integrating effect, equivalent to a single-pole RC integrator of 10 nS risetime.

The results of the simulation are shown in Fig. IV.29(a) and (b). The mean duration of the signal is plotted against system risetime in Fig. IV.29(a), for three drift distances. The SNR, at the discriminator input, is similarly shown in Fig. IV.29(b). For both these graphs, a mean ionization track sample of 100 electrons (2.6 KeV) was assumed, with a track angle of 0°, and gas gain 10000. As expected, the gate



(a)



(b)

Figure IV.29

duration is longest for the 2m-drifted signals, and the SNR is largest for the zero-drifted signals.

It may be seen that the signal duration for zero-drifted signals increases from 250 nS (≡1.0 cm drift distance) at 10 nS system rise time, to 450 nS (≡1.8 cm) at 80 nS system rise time. Over the same range of rise time, the SNR for 200 cm-drifted signals increases from 25 dB to nearly 31 dB. Beacuse of the importance of good close-track performance at small drift distance, an operating value for the system rise time of 30 nS was chosen. This gives a tolerable mean signal duration of 300 nS (≡1.2 cm) for zero drifted signals, and a useful SNR for 2m-drifted tracks of 27 dB. The resulting 3 dB system bandwidth is about 8 MHz.

$\tau_{system} = 30$ nS

The Discriminator Trigger-On Level

Once the system bandwidth has been defined, the value of the discriminator trigger-on level, relative to the r.m.s. noise level at the discriminator input, is determined only by the desired rate of random triggers (see earlier). In Fig. IV.30, the simulated no-signal random triggering rate is plotted against the trigger-on level (threshold level). A latch time of zero was assumed (see IV.2). The noise bandwidth was limited by the system rise time of 30 nS (see above). The simulated input white noise spectral density was equal to the measured equivalent input noise spectral density of 115 nA/$\sqrt{\text{GHz}}$ (see III.2 and Appendix 4). As stated in Criterion 3, the required noise triggering rate is 20 KHz. The trigger-on level appropriate to this rate is 8.0 mV.

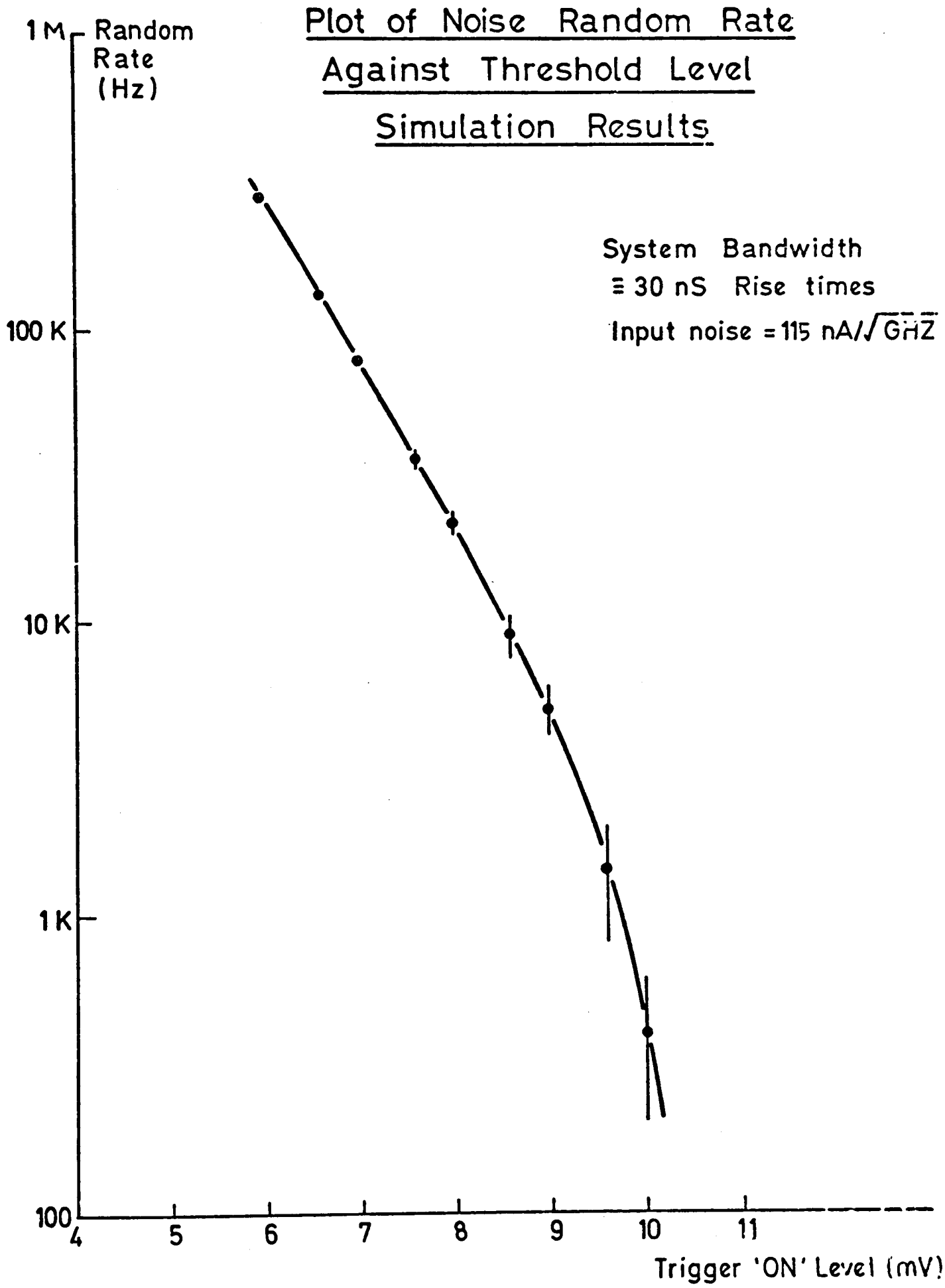

Plot of Noise Random Rate
Against Threshold Level
Simulation Results
1 M
Random
Rate
(Hz)
100 K
10 K
1 K
100
System Bandwidth
≡ 30 nS Rise times
Input noise = 115 nA/√GHZ
4
5
6
7
8
9
10
11
Trigger 'ON' Level (mV)

Figure IV.30

Translated to an equivalent input trigger level, the discriminator will fire on a signal produced by the arrival at an anode of 4 ionization electrons (within ∿30 nS of each other) at a gas gain of 10000. Fig. IV.31 shows this 4-electron signal together with the trigger-on level, and typical sections of noise waveform, as produced by the simulation.

An equivalent noise charge (ENC) is defined as the charge that, instantaneously deposited at the input, produces a signal at the output of the same amplitude as the r.m.s. noise level, [NP74]. Assuming a noiseless equivalent gas gain of 15000, the ENC for ionization is:

$$ENC_i = 1.0 \text{ ionization electrons.}$$

No direct comparison with other work is available here, since this calculation, unlike others, takes into account both the gas amplifier response and pulse shaping. However, an optimum ENC, at the preamplifier input, for a system of comparable bandwidth is

$$ENC_p = 1000 \text{ r.m.s. electrons} \qquad [RV74]$$

Naively dividing this by an equivalent gas gain of 15000 gives an ENC for ionization of:

$$ENC_i = 0.07 \text{ ionization electrons.}$$

However, the effect of the gas amplifier response and pulse shaping will be to increase this value.

Similarly, an equivalent trigger charge (ETC) may be defined as the charge that, instantaneously deposited at the input, will cause the discriminator to fire. For a noiseless equivalent gas gain of 15000, the ETC for ionization is

$$ETC = 3.7 \text{ ionization electrons,}$$

with a noise triggering rate of 20 KHz.

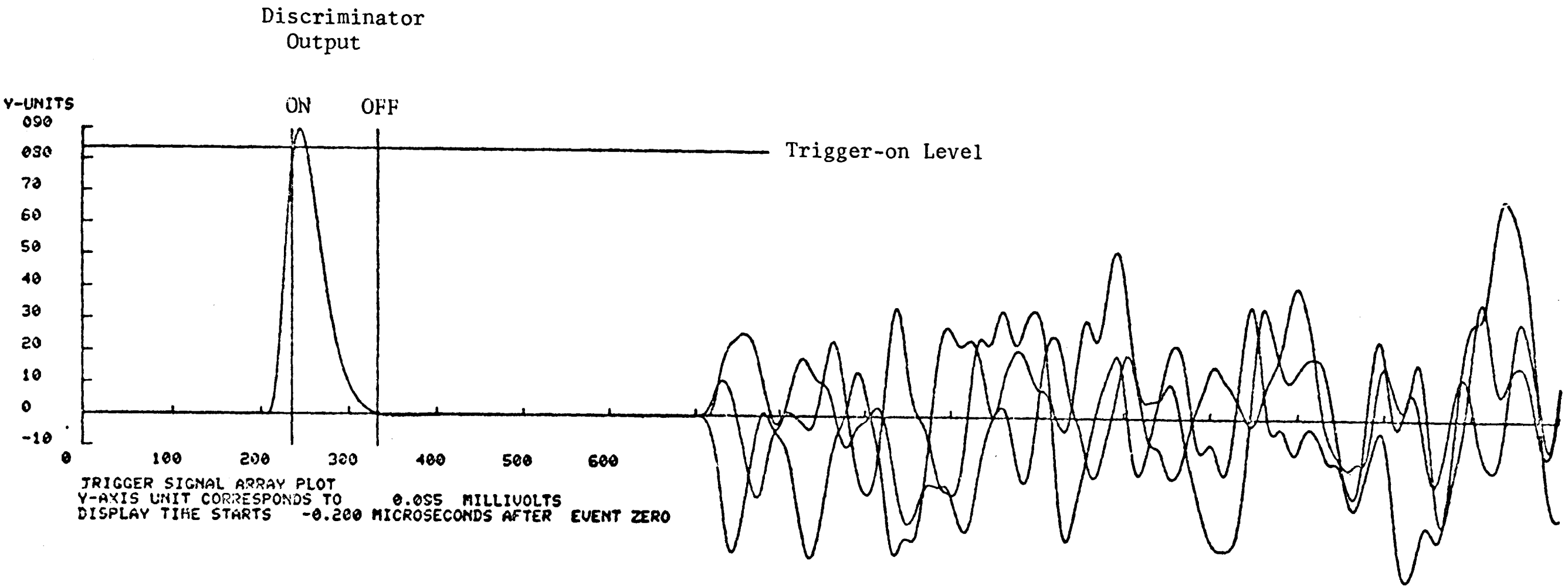


Figure IV.31 A 4-electron signal, and sections of noise wa eform, as generated within the simulation, seen at the discriminator input.

Integration Gate Extension Time

As shown above, the electronics will not trigger on single ionization electrons. The trigger level is too high; the ETC is 3.7 ionization electrons. Thus, on the arrival at the discriminator of the signal from a dispersed sample of (typically) 100 ionization electrons (≡2.6 KeV), triggering may not occur for an appreciable time (∿100 nS) after the true start of the signal. As explained in III.5, the duration t_d of the discriminator output pulse under these conditions is less than the true duration t_s of the signal. In order to measure accurately the magnitude of the signal, the integration gate duration t_g must equal the true signal duration. Since the integration gate is generated from the discriminator output pulse, an additional gate extension time t_e must be added to the duration of the discriminator output pulse:

$$t_g = t_e + t_d = t_s$$

In general, the discriminator output duration t_d is a function of SNR. The necessary value of t_e required for a given SNR is simply:

$$t_e = t_s - t_d$$

Associated with the gate extension time is an equal analogue signal delay, prior to integration, of value d_s. This is to allow the leading part of the signal, missed by the discriminator, to be captured by the integration gate (see III.5). In summary, to determine t_e and d_s both t_s and t_d are required.

The true duration t_s of a signal, for the purposes of efficient integration, is defined to be the integration gate duration above which no increase of more than 1% is observed in the value of the measured analogue signal integral. In other words, t_s is the minimum

integration gate duration for which the signal amplitude is negligible outside the gate. In determining the operating point, a measure of the quality of signal integration is required. The 'percentage charge lost' under given conditions is defined as: the percentage by which the mean analogue charge on the integration capacitor falls short of the total signal charge obtained with an arbitrarily long integration gate duration ($\gtrsim \bar{t}_s$).

Assuming an integration gate extension time of zero, the percentage charge lost must tend to zero at large SNR, since the mean discriminator output duration $\bar{t}_d$, and hence the mean integration gate duration $\bar{t}_g$, will tend to the true mean signal duration $\bar{t}_s$:

$$\lim_{SNR \to \infty} (\bar{t}_d) = \lim_{SNR \to \infty} (\bar{t}_g) = \bar{t}_s$$

This behaviour is shown in Fig. IV.32. On this diagram, simulation results for percentage charge lost and integration gate duration are plotted against an effective input SNR. The gate extension was zero:

$$\bar{t}_d = \bar{t}_g \lesssim \bar{t}_s$$

The SNR was parametrized usefully as the ratio of equivalent gas gain G_e to equivalent input noise spectral density I_n. Results over a range of SNR were obtained by scanning G_e from 5000 to 150000, while keeping I_n at the constant measured value of 115 nA/$\sqrt{\text{GHz}}$. It was therefore not necessary to vary the discriminator trigger-on level: the mean noise triggering rate remained at 20 KHz. The input ionization was, as defined in Criterion 1, a 50-electron sample ($\equiv$1.3 KeV), deposited at the maximum distance of 2m from the wire plane in drift fields of 50 kV/m and 100 kV/m (see II.2). Each point plotted in Fig. IV.32 represents the mean value taken over 300 repetitions of signal simulation for the particular conditions.

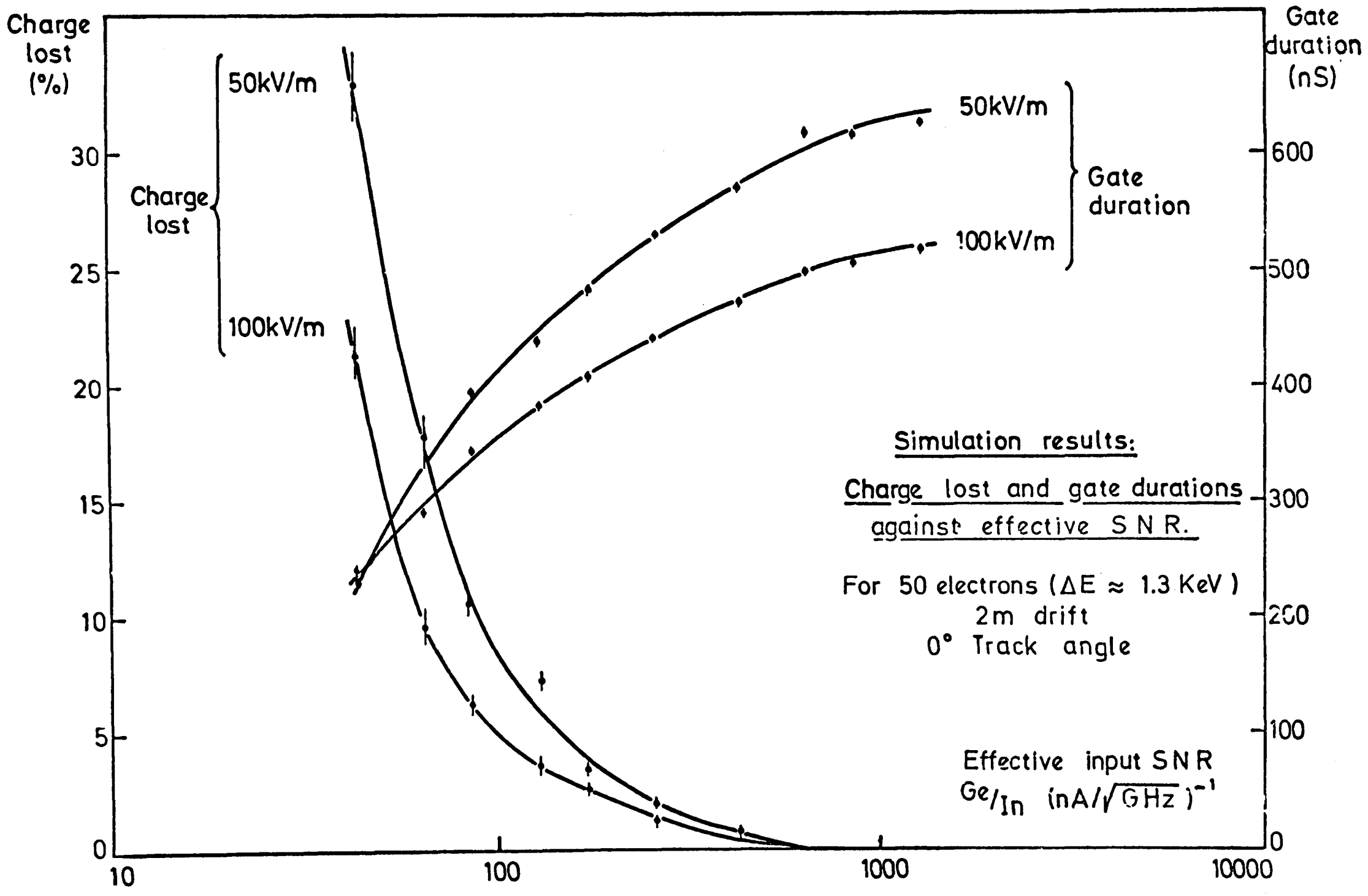

Charge lost (%)
Gate duration (nS)
50kV/m
100kV/m
Charge lost
50kV/m
100kV/m
Gate duration
30
25
20
15
10
5
0
600
500
400
300
200
100
0
10
100
1000
10000
Simulation results:
Charge lost and gate durations against effective S N R.
For 50 electrons (ΔE ≈ 1.3 KeV)
2m drift
0° Track angle
Effective input S N R
Ge/In $(nA/\sqrt{GHz})^{-1}$

Figure IV.32

From Fig, IV.32, it may be seen that a zero charge loss is predicted at and above an effective input SNR of 600 $(nA/\sqrt{GHz})^{-1}$, independent of drift field. The integration gate durations at this SNR, corresponding to true signal durations, were

$$t_g = 610 \pm 10 \text{ nS} \quad \text{at} \quad 50 \text{ kV/m}$$
$$= 500 \pm 10 \text{ nS} \quad \text{at} \quad 100 \text{ kV/m}$$
$$= t_s$$

The mean duration of the signal at the lower drift field is ∿20% larger than that at the higher field, because the diffusion dispersion is greater (see II.2). At smaller SNR's, the integration gate duration drops, resulting in an appreciable loss of signal charge.

Noting the equality between t_d and t_g for the data in Fig. IV.32, the required gate extension time $t_e = t_s - t_d$ may be easily determined. In Fig. IV.33, t_e is plotted against the effective input SNR for both drift field values. The proposed operating point is shown on the diagram:

$G_e = 15000$ (see earlier)

$I_n = 115 \text{ nA}/\sqrt{GHz}$ (see III.2)

At the resultant effective SNR of 130 $(nA/\sqrt{GHz})^{-1}$, the gate extensions required to satisfy Criterion 1 are:

$t_e = 175 \pm 10$ nS at 50 kV/m (≡ 7 mm drift distance)
$= 120 \pm 10$ nS at 100 kV/m (≡ 4 mm drift distance)

The optimum signal delay time in the analogue signal path to the integration gates was determined by trial-and-error, using initial values equal to the gate extension times. It was found that the delay times required were about 40 nS less than the corresponding gate extensions:

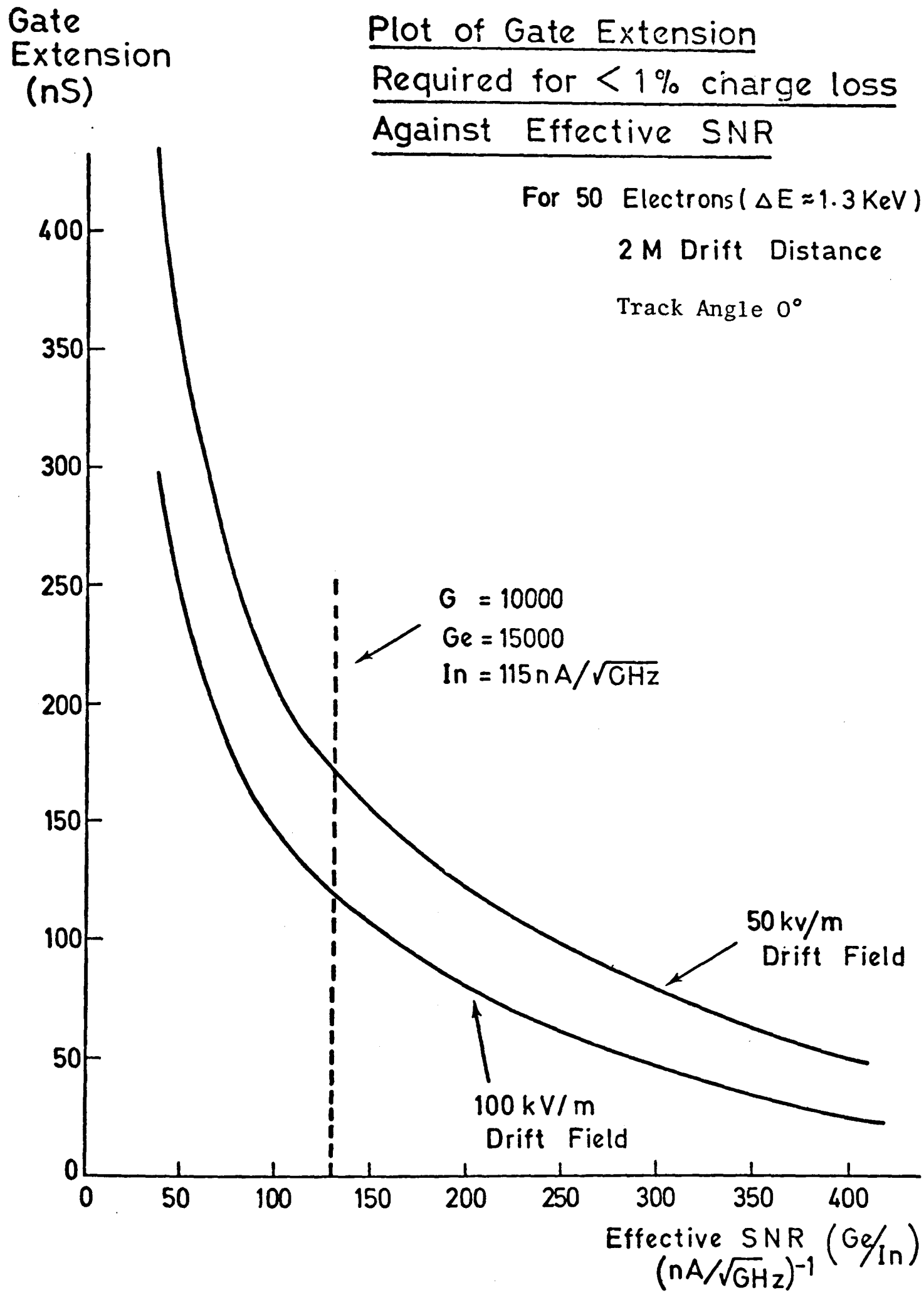

Gate Extension (nS)
Plot of Gate Extension
Required for < 1% charge loss
Against Effective SNR
For 50 Electrons (ΔE ≈ 1.3 KeV)
2 M Drift Distance
Track Angle 0°
G = 10000
Ge = 15000
In = 115 nA/√GHz
50 kv/m
Drift Field
100 kV/m
Drift Field
0
50
100
150
200
250
300
350
400
Effective SNR (Ge/In)
(nA/√GHz)-1

Figure IV.33

$$d_s = 130 \pm 10 \text{ nS} \quad \text{at} \quad 50 \text{ kV/m}$$
$$80 \pm 10 \text{ nS} \quad \text{at} \quad 100 \text{ kV/m}$$

The reasons for the differences are that:

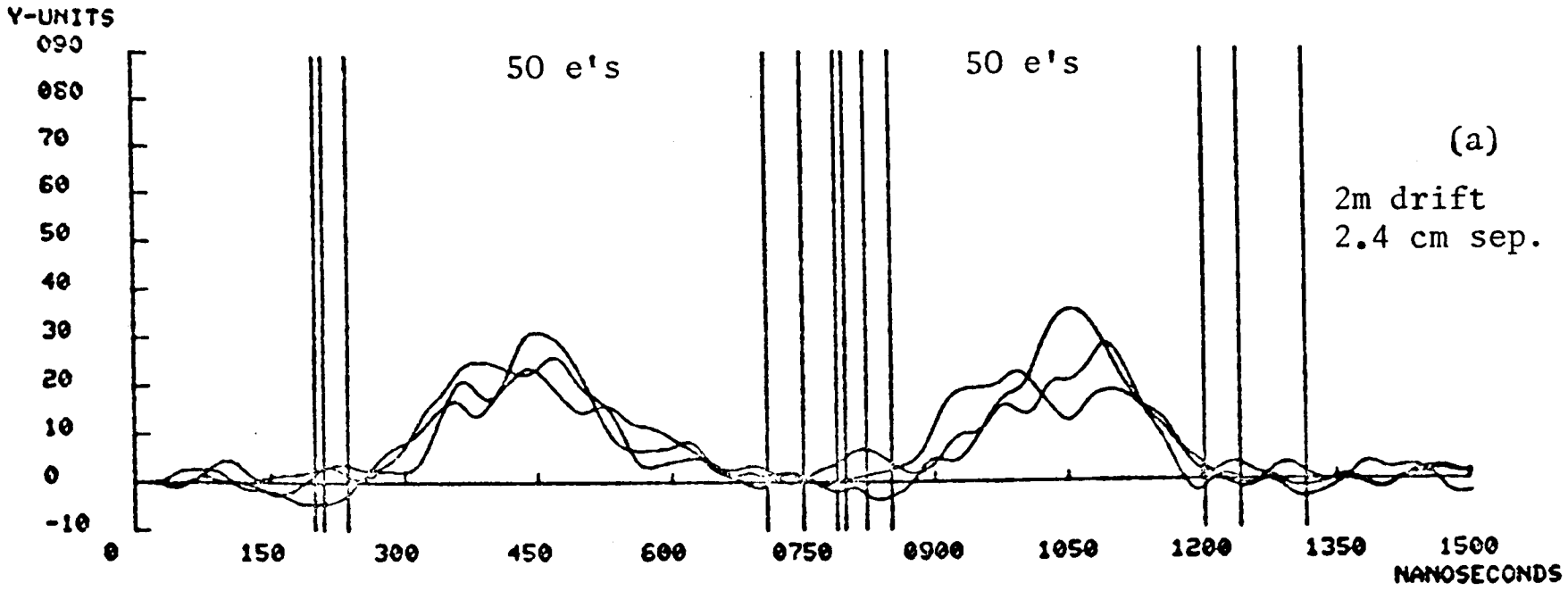
(a) The rise time of the delay line itself causes an appreciable lengthening of the signal (∿30 nS). Since the delay occurs after discrimination, the discriminator does not see the effect of this rise time.

(b) The trigger-off level is set to zero. Thus a noise-induced reset of the discriminator will cause a bias towards an early trigger-off point.

The operating window extends to an effective input SNR of about 30 $(nA/\sqrt{GHz})^{-1}$. Below this value, a 100% trigger efficiency is no longer maintained for Criterion 1 signals. There is thus a safety margin of a factor of ∿4 in the operating SNR. However, the price paid at reduced SNR is that a longer gate extension is required, resulting in worse close-track performance at small drift distances - see Criterion 2.

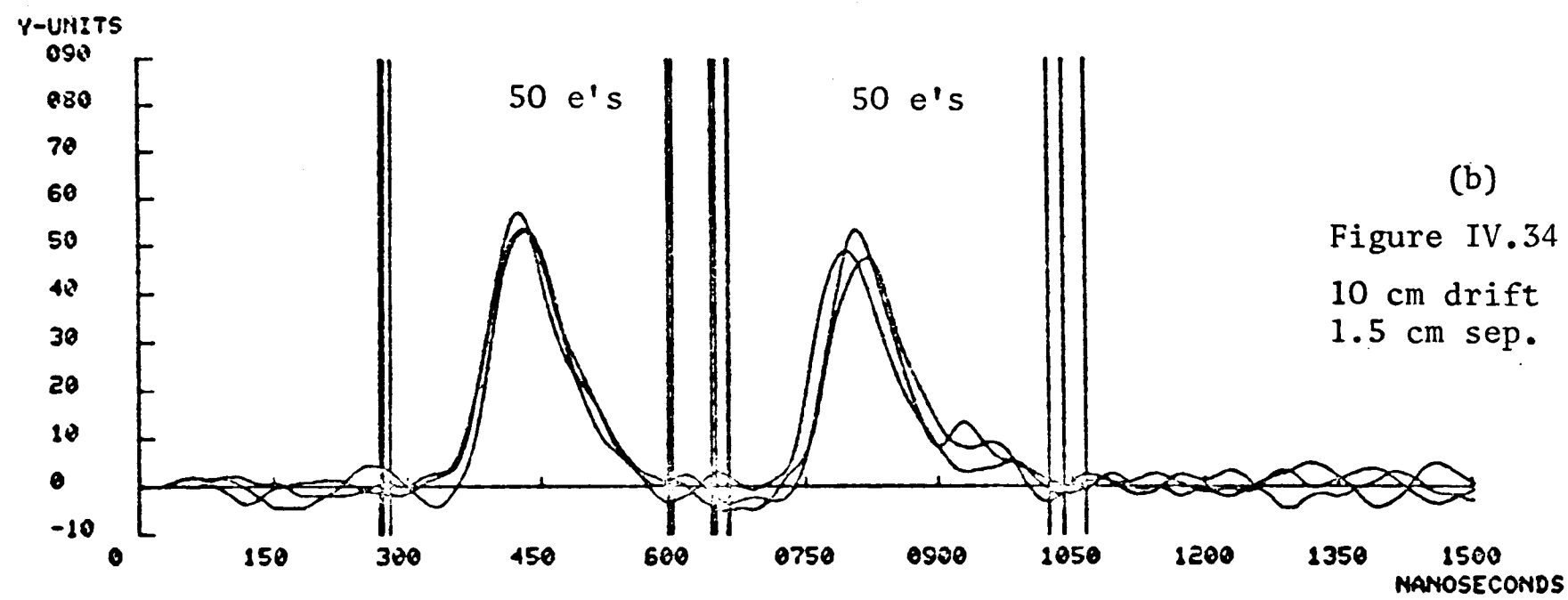
Typical Signals

The simulated integration capacitor charging waveforms and integration gate timings for several typical signals are shown in Fig. IV.34 (a)-(d). The conditions are given in Table IV.5. The drift field was 100 kV/m and the track angle was zero. The values of the integration gate extension and analogue delay times were those derived above for 100 kV/m.



(a)

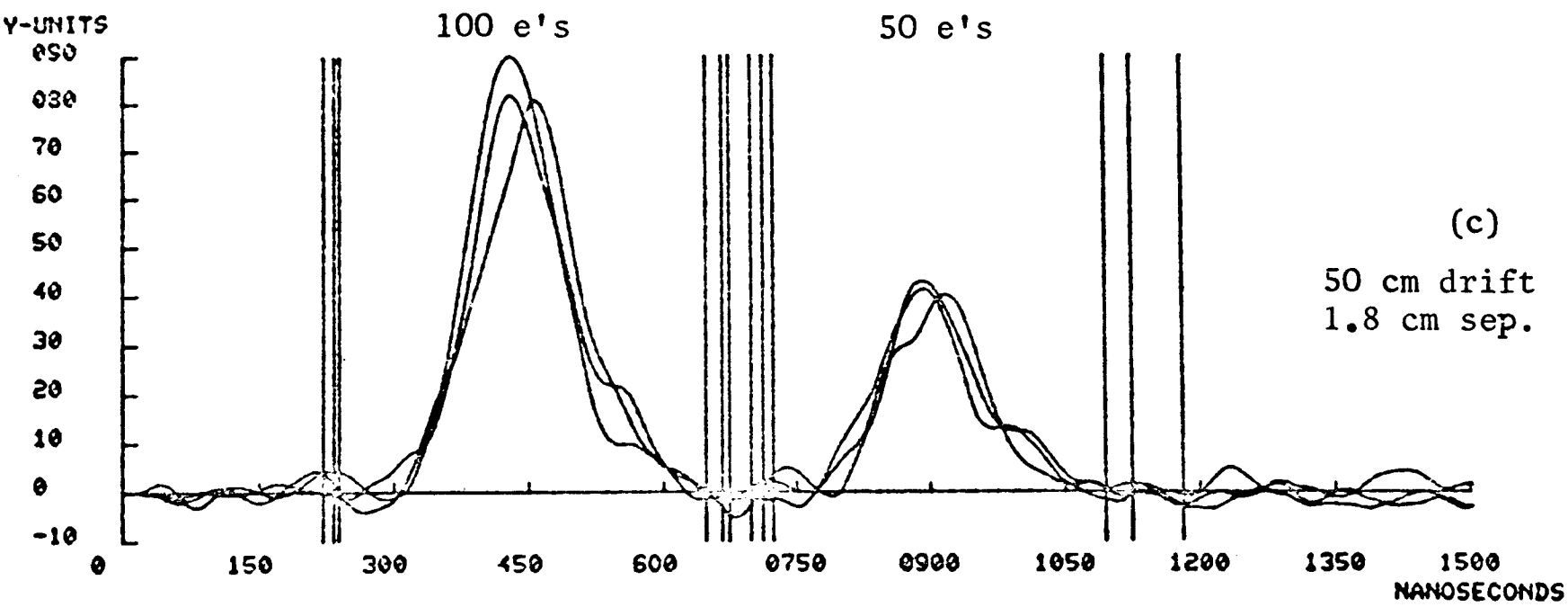
2m drift
2.4 cm sep.



(b)

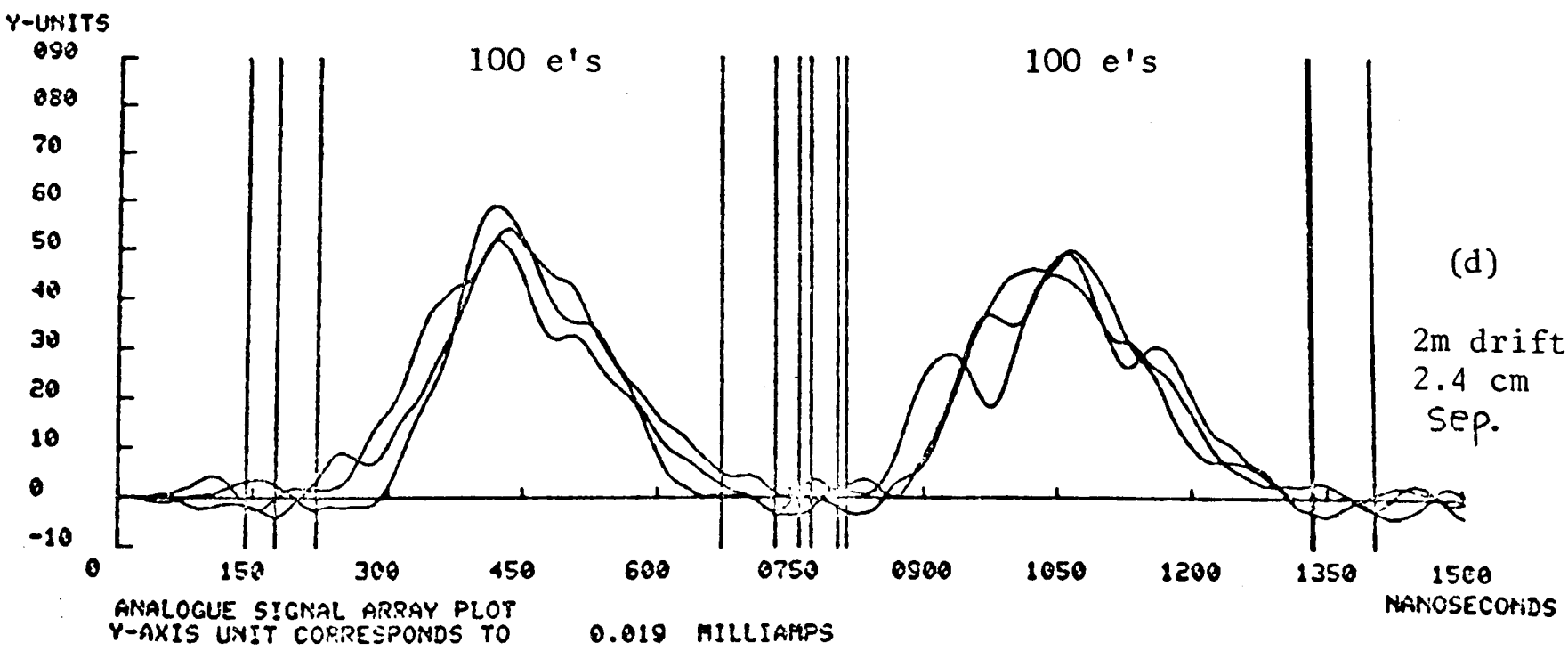
Figure IV.34

10 cm drift
1.5 cm sep.



(c)

50 cm drift
1.8 cm sep.



(d)

2m drift
2.4 cm
sep.

TABLE IV.5

Figure	Track 1		Track 2	
Fig. IV.34	No. of ionization electrons	Drift distance (cm)	No. of ionization electrons	Drift distance (cm)
(a)	50	197.6	50	200
(b)	50	10	50	11.5
(c)	100	50	50	51.8
(d)	100	197.6	100	200

The scales for all four figures are the same, enabling easy comparison of the different cases. There are several observations to be made:

(i) SNR

Fig. IV.34(a) shows the profiles of three signals under the conditions defined in Criterion 1 (50 electrons, 2 m drift). The signals are noisy. However, there is no difficulty in detecting them; the equivalent trigger-on level occurs at about 8 y-units (for all four plots). Fig. Iv.34(b) shows signals resulting from the same amount of ionization, but after a short drift of ∿10 cm. The signal amplitude, and hence the SNR, are much higher, by a factor of ∿2. Figs. IV.34(c) and (b) also show signals of larger SNR. Fig. IV.34(c) is the more typical case, of signals with differing amplitudes. Fig. IV.34(d) shows, like (a), signals after a 2m drift, but with twice the magnitude (100 electrons).

(ii) Integration gate timings

For all of the pulses shown in Fig. IV.34, the integration gates adequately mask the signals. The gate durations vary between ∿500 nS in Fig. IV.34(a) to ∿300 nS in (b). This demonstrates the advantages of a signal-derived gate over a fixed duration gate in reducing system dead time (see earlier, and IV.5). Note however the effect of the (fixed) gate extension time. In Fig. IV.34(b) and (c) especially, the gate opens unnecessarily about 50 nS before the arrival of the signal. This results in an increase in system dead time (see Criterion 2).

(iii) Two track performance

The signal profiles shown in Fig. IV.34 are also a useful graphical representation of the two track performance. The time scale is converted to one of drift distance by multiplying by the drift velocity of 4 cm/μS (see II.2). This allows estimates to be made on the minimum track separation for correct operation:

Drift Distance	Separation	
10 cm	1.3 cm	(b)
50 cm	1.8 cm	(c)
200 cm	2.1 cm	(a, d)

These values are approximate. The two track performance is investigated in greater detail in IV.6.

Conclusion

Performance criteria have been defined to give a minimum level of performance in respect of:

(i) quality of ionization information

(ii) quality of position information

(iii) the tolerable effect of noise

The existence of an operating window has been demonstrated. The optimum operating point within the window has been determined by the choice of appropriate values for the following system parameters:

(i) Gas gain factor

(ii) Linear integration time constant

(iii) Discriminator trigger-on level

(iv) Integration gate extension time

(v) Analogue signal delay time.

A discussion on the accuracy of the results is deferred until the next section.

IV.6 THE PREDICTED PERFORMANCE OF ISIS

In the previous Section, an optimum design for ISIS was derived, with respect to three basic performance criteria. In this Section, predictions are made using the simulation about the performance of the design beyond that demanded by the criteria. Three critical aspects are discussed in detail:

(i) the performance in ionization measurement, in particular for small signals,

(ii) the performance for close tracks,

(iv) the triggering characteristics.

These are investigated over a large range of the expected signals.

Finally, there is a brief discussion of the errors in, and the possible causes of deviation from, the predicted performance, and the remedies available if the performance is harmed.

Performance in Ionization Measurement

A single-track charge collection efficiency (CCE) may be defined, as a measure of the quality of an ionization measurement. In the same way as the 'percentage charge lost' (IV.5), the CCE describes what proportion of a signal is represented by the charge on the analogue memory capacitor. The ideal CCE value is 100%.

The CCE is calculated by expressing the predicted charge on the memory capacitor as a percentage of that obtained for the same sample of ionization, but under perfect SNR conditions. As stated in Criterion 1 of IV.5, the CCE must be better than 99% for all signals from an ionization of 50 electrons (≡1.3 KeV) or greater.

The single-track performance will be poorest when the SNR is least. This occurs when the ionization has drifted the maximum distance of 2m, since the ionization dispersion is then greatest. In Fig. IV.35, simulation results for the CCE are plotted against the amount of ionization in the sample, for such 2m-drifted tracks. The drift field assumed was 100 kV/m; the appropriate gate extension and delay times, as derived in IV.5, were used. The points plotted are average values taken over 300 repetitions of the simulation; the bars represent true errors. Results for two track angles, 0° and 18°, are given. Also shown on the diagram above the axis is the Landau distribution for a minimum ionizing particle (theoretical curve, see II.1 and [BJ76]). This facilitates an assessment of the effects of any inefficiency.

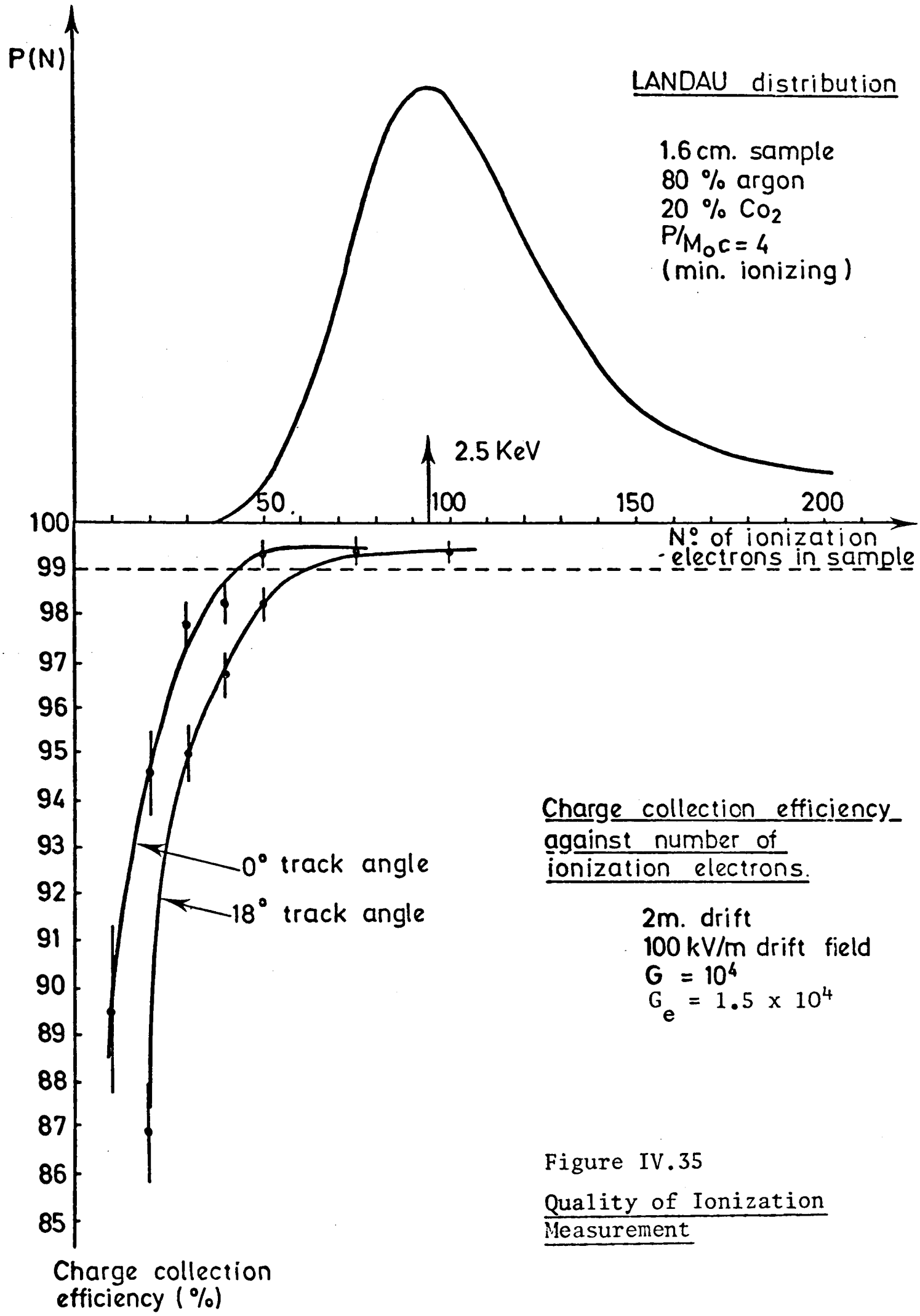
It may be seen that, at 0° track angle, the CCE is greater than 99% for all samples containing more than ∿45 ionization electrons. The Landau distribution drops to zero probability below about 40 electrons; at this point the predicted CCE is still above 98%. This level of performance is satisfactory.

For 18° track angle, the CCE falls below 99% for signals of less than 60 electrons. At this point where the Landau probability falls to zero, the CCE is still above 96%. This, too, is adequate performance.

At shorter drift distances, the ionization measurement accuracy improves, since the SNR increases.

The Performance for Close Tracks

Another very important device characteristic is the resolution for track position within the chamber. The question is asked, "What is the minimum separation between tracks, for the resultant signals to be correctly treated by the electronics?" A parameter describing this



Charge collection efficiency against number of ionization electrons.

2m. drift
100 kV/m drift field
$G = 10^4$
$G_e = 1.5 \times 10^4$

Figure IV.35

Quality of Ionization Measurement

is the two-track resolution (TTR), defined to be the minimum drift distance between two tracks to ensure a CCE of at least 99% for each track (Criterion 1, IV.5). For useful results from ISIS, the TTR should not be more than about 1 cm at small drift distances, where close beam tracks are expected. However, a larger value of about 2 cm is acceptable at large drift distances, where the density of tracks is less (see I.2, [EHSP]).

As explained in the last section, the ability to accept close tracks is controlled by the system dead time, equal to the integration gate duration. Thus an estimate of the TTR may be obtained directly from the mean integration gate duration, converted to a distance by multiplying by the drift velocity of 4 cm/μS. Figure IV.36 shows the resulting TTR, as a function of drift distance, for two sizes of signal; 50 and 200 ionization electrons (≡1.3 and 5.2 KeV). The drift field was 100 kV/m, and a zero track angle was assumed.

The TTR is not independent of signal size: the TTR at zero drift is 1.4 cm for 50 electron signals, and 1.6 cm for 200 electron signals. At 2m drift, these values increase to 1.9 cm and 2.4 cm respectively.

As the track angle increases from 0° to the maximum of 18°, the TTR deteriorates because of the additional dispersion (see II.2). The value of the increase in TTR at 18° track angle is 0.4 cm, independent of drift distance. The TTR will also increase at lower drift fields, in accordance with the results of II.2

The variation of the TTR with signal size arises because of the use of a finite trigger-on level. The trigger-on level, expressed as a fraction of the signal amplitude, is inversely proportional to signal amplitude. Thus, for large signals, the discriminator sees a greater percentage of each signal: the gate durations will in general be longer.

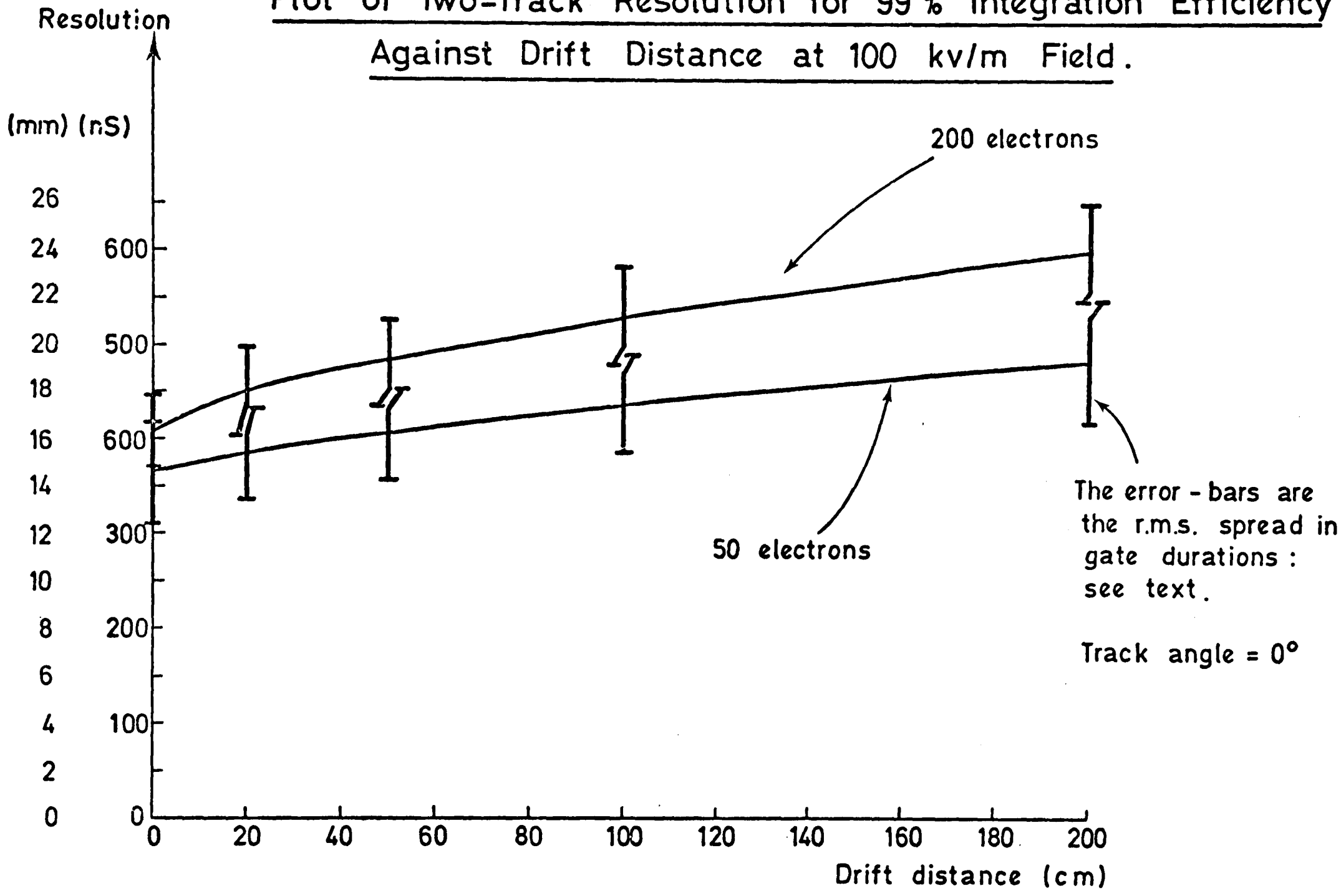

Plot of Two-Track Resolution for 99 % Integration Efficiency
Against Drift Distance at 100 kv/m Field.
Resolution
(mm) (nS)
26
24 600
22
20 500
18
16 600
14
12 300
10
8 200
6
4 100
2
0 0
200 electrons
50 electrons
The error - bars are the r.m.s. spread in gate durations : see text.
Track angle = 0°
0 20 40 60 80 100 120 140 160 180 200
Drift distance (cm)

Figure IV.36

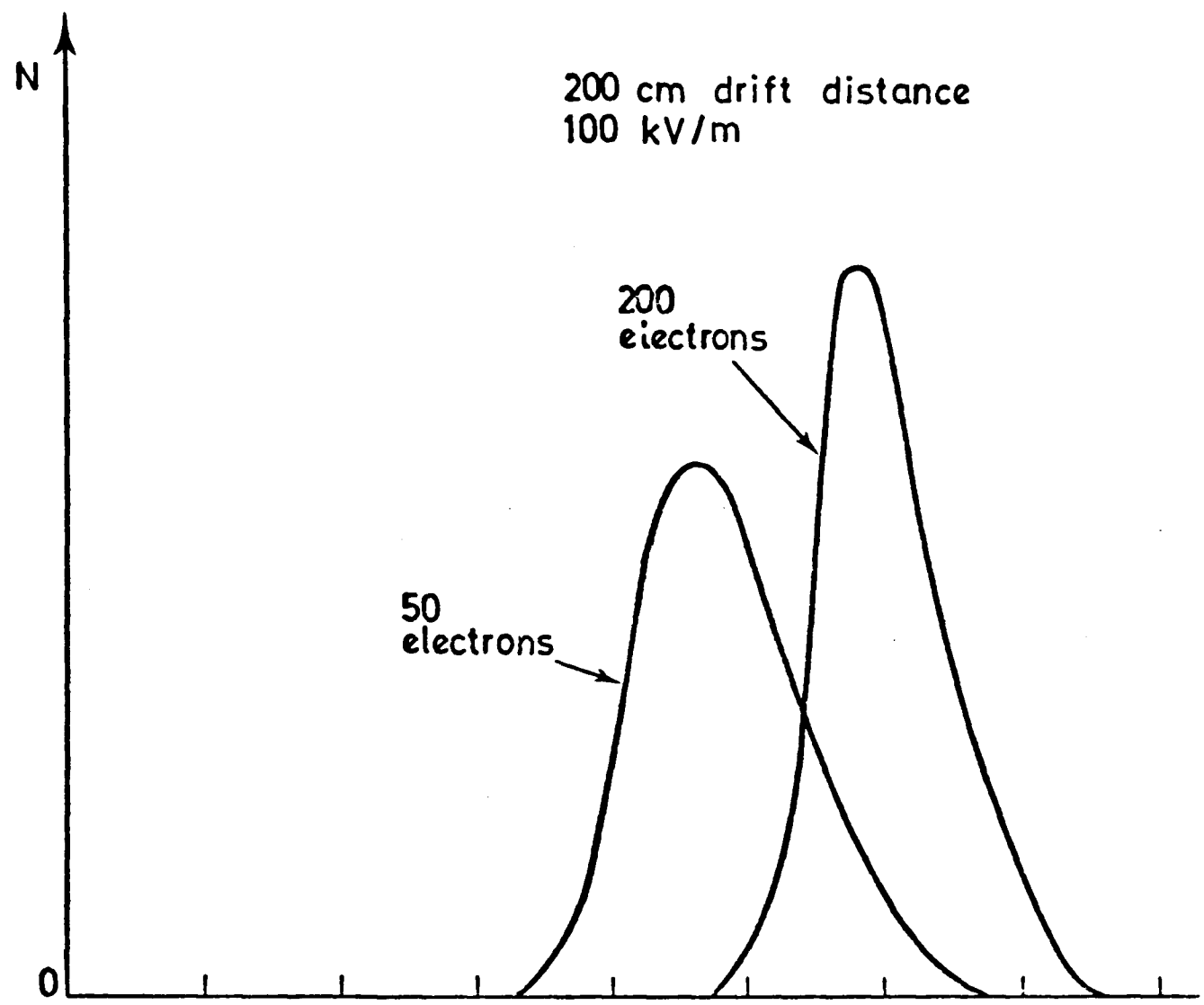


FIGURE IV.37 Simulated Gate Duration Distribution

The effect of noise is to produce a broad distribution of gate durations. The error bars on Fig. IV.36 represent the r.m.s. width of the gate duration distribution. Figure IV.37 shows the simulated distributions for the 2m-drifted results of Fig. IV.36. The 200 electron signals give rise to a narrower gate duration distribution (r.m.s. width = 50 nS), than do the 50 electron signals (r.m.s. width = 65 nS). This is because the 200 electron signals have a smaller shot noise component than do the 50 electron signals.

To investigate further the two-track performance, the CCE's and triggering characteristics have been determined, as a function of track separation, for two interesting two-track situations:

(i) Equal Signals

To parametrize the two-track resolution for triggering alone, the 'percentage unresolved' (PUR) is defined to be percentage of times for which the discriminator does not reset and retrigger in between two signals. The PUR is thus a measure of the percentage of the data that cannot be used in determining the ionization loss for the tracks. In Fig. IV.38, the predicted CCE's for each of the tracks and the predicted PUR are plotted as a function of track separation, for equal track ionization samples of 100 electrons (≡2.6 KeV). Two sets of results are shown, for zero-drifted, and for 2m-drifted, tracks. The track angle was zero, and the drift field was 100 kV/m.

As a generalization of Criterion 1, IV.5, an acceptable pulse integration performance is one for which the CCE is within the range 100 ± 1%. It may be seen in Fig. IV.38, that the integration performance starts to deteriorate at a track separation of less than 1.3 cm for zero-drifted tracks, and at one of less than 2.1 cm (for the nearer track) in the 2m-drifted case. At these separations, the PUR is 20% for zero drift distance, and 30% for 2m drift distance. (Loss of 25% of the data causes a worsening of the ionization resolution by 0.6% to 5.3% [AW76]). A zero PUR (no data lost) is obtained at a separation of 1.8 cm for zero drifted tracks, and 2.4 cm for 2m-drifted tracks. The conclusion is that the TTR for these equal signals is 1.3 cm for a zero drift, and is 2.1 cm for a 2m drift distance.

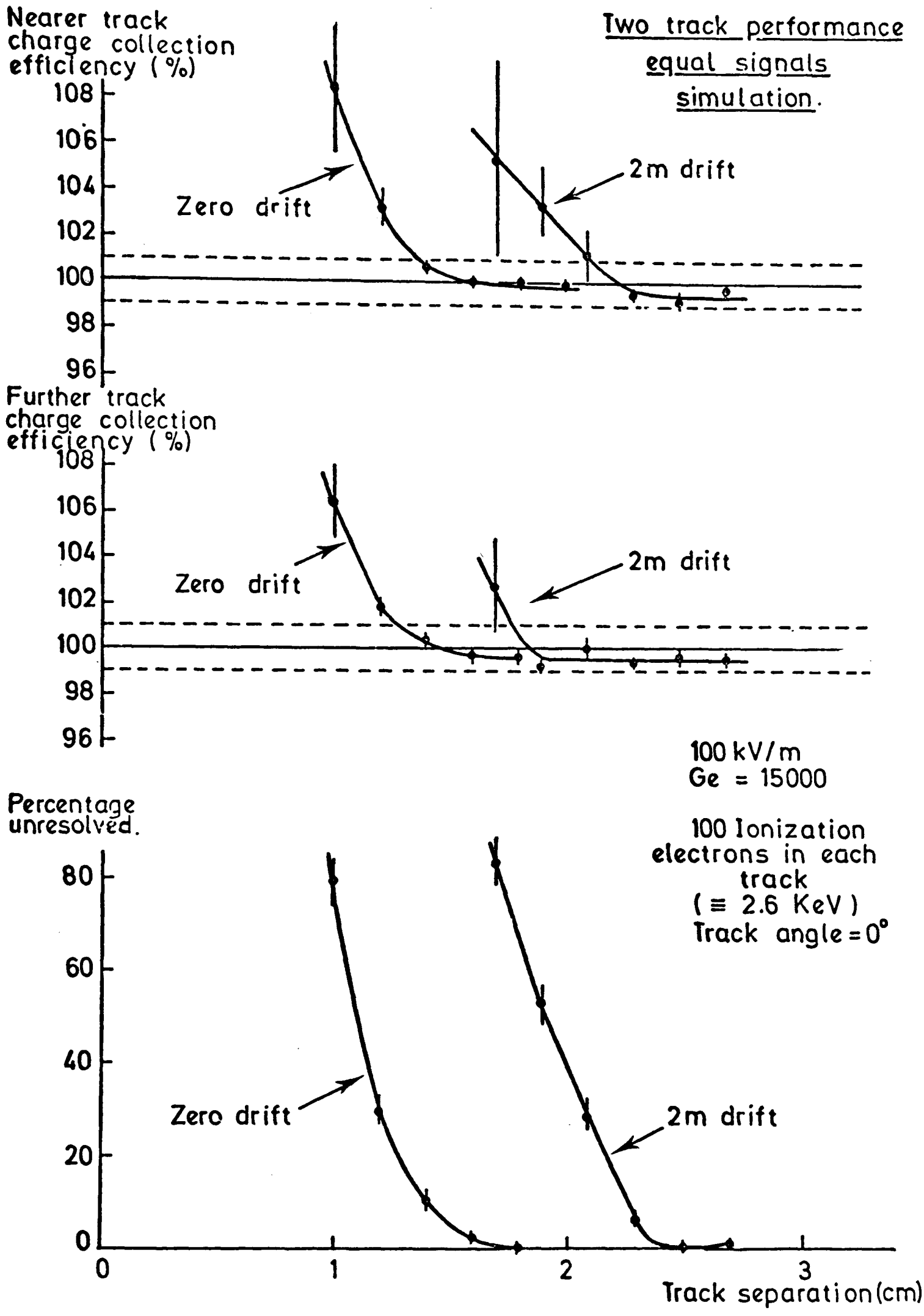

Nearer track charge collection efficiency (%)
108
106
104
102
100
98
96
Zero drift
2m drift
Two track performance
equal signals
simulation.
Further track charge collection efficiency (%)
108
106
104
102
100
98
96
Zero drift
2m drift
Percentage unresolved.
80
60
40
20
0
0
1
2
3
Track separation (cm)
Zero drift
2m drift
100 kV/m
Ge = 15000
100 Ionization electrons in each track
(≡ 2.6 KeV)
Track angle = 0°

Figure IV.38

(ii) Large Signal - Small Signal

The effect of a large signal on the measurement of a subsequent smaller one was also investigated. The CCE's and the PUR were found, by simulation, for the situation of a 200-electron signal (≡5.2 KeV), followed closely by a 50-electron signal (≡1.3 KeV). The other conditions were the same as for the equal signal case. The results are shown in Fig. IV.39.

At zero drift, the CCE for the nearer track - the larger signal - rises above 101% at a track separation of 1.3 cm. The CCE for the second track - the smaller signal - drops below 99% at 2.2 cm separation, to a minimum of 98% at 1.8 cm, before rising past 101% at 1.3 cm separation. The reduction in CCE for the second track between 1.5 cm and 2.2 cm separation is caused by a biassing of the signal by the slight negative 'overshoot' of the earlier, larger, signal (see III.3). The effect is not great and may be neglected: there will not be any appreciable change in the measured ionization distribution of the second track under the normal conditions of crossing tracks. The PUR at zero drift distance with 1.3 cm separation is 30%.

For a 2m drift distance, the CCE for the nearer track remains within 100 ± 1% down to a separation of 1.8 cm. The CCE for the further track shows the same behaviour as that for zero drift distance: the CCE drops below 99% at 2.9 cm separation, to a minimum of 98% at 2.2 cm, and then rises past 101% at 1.9 cm. The PUR at 1.9 cm separation is 55%; over half of the track-pairs will be unresolved.

Thus the TTR for these unequal signals is also 1.3 cm for a zero drift, but is 1.9 cm for a 2m drift distance compared with 2.1 cm for equal signals. The apparent improvement in the 2m-drift TTR for the unequal signal case occurs because of biassed selection of the sharper signals by the discriminator. The larger PUR value indicates that

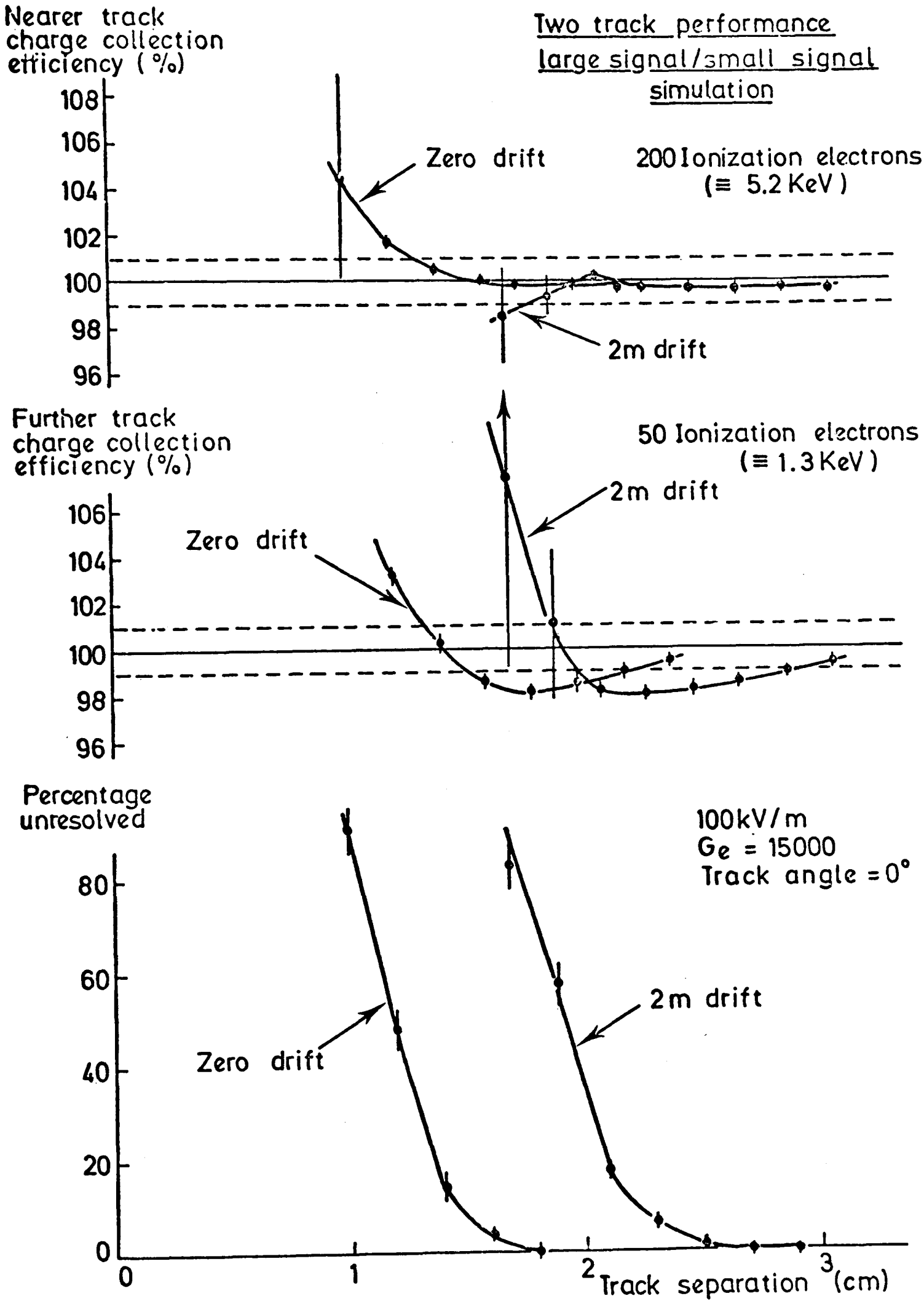

Nearer track
charge collection
efficiency (%)
Two track performance
large signal/small signal
simulation
108
106
104
102
100
98
96
Zero drift
200 Ionization electrons
(≡ 5.2 KeV)
2m drift
Further track
charge collection
efficiency (%)
50 Ionization electrons
(≡ 1.3 KeV)
2m drift
Zero drift
106
104
102
100
98
96
Percentage
unresolved
100kV/m
Ge = 15000
Track angle = 0°
80
60
40
20
0
Zero drift
2m drift
0
1
2
3
Track separation (cm)

Figure IV.39

this lower TTR value was gained at a cost: the broadest signals are not resolved as being a pair.

These results are summarized in Table IV.6. The TTR at zero drift is ∿1.3 cm, and at 2m drift is ∿2 cm. The TTR is independent of signal size, to a good approximation. At track separations equal to the TTR, about 30% of the track-pairs will not be resolved.

TABLE IV.6 Two Track Resolution

Drift Distance m	Signal Magnitudes (Nos. of Ionization Electrons)	Two-Track Resolution (cms)	Percentage of Track-Sample Pairs Unresolved at These Separations
0	100 + 100	1.3	20%
0	200 + 50	1.3	30%
2	100 + 100	2.1	30%
2	200 + 50	1.9	55%

The Triggering Characteristics

(i) The Triggering Efficiency

The predicted trigger efficiency for a particular set of conditions is the percentage of simulated signals for which a discriminator firing occurs at some time during the expected duration of the pulse. The trigger efficiency must be 100% for the signals defined in Criterion 1 of IV.5 (50 ionization electrons, 2m drift distance). In fact the triggering efficiency is predicted to be better than this: a 100.0% trigger efficiency is maintained for signals from as few as 25 ionization electrons (≡650 eV) after a 2m drift. An efficiency of 99.3%is expected for 20-electron signals, dropping to

63% for 10-electron signals, at the 2m drift distance. After taking into account the Landau ionization probability distribution, the predicted trigger efficiency for the signals from a minimum ionizing particle track is 100.0%, even for a 2m drift distance. This performance is good.

(ii) Multiple Triggering Rate

Because of the noisy nature of the signals, it is possible that, during the duration of a pulse, the signal amplitude could fall to zero. This is particularly likely near the leading and trailing edges of small dispersed signals.

If the signal amplitude falls below the trigger-off level, the discriminator will reset. If, later in the pulse, the amplitude rises above the trigger-on level again, the discriminator will re-trigger. Thus two triggers, or more, may be registered for the one signal. This is undesirable, since it will not be possible to obtain accurate ionization data from such signals. The sequential integration capacitor selection will mean that the signal will be gated onto successive capacitors. To parametrize this effect, a multiple triggering rate Rm is defined as that percentage of signals for which more than one trigger is predicted as occurring within the duration of the signal.

Because of the high CCE required on small signals, (see Criterion 1, IV.5), the multiple triggering rate Rm must be low, not more than about 1%. The simulation shows that this level of performance is achieved. For signals from 50 ionization electrons or more, Rm is predicted to be less than 1% in all cases. The value of Rm increases to a maximum of about 5% on signals of small amplitude e.g. for 30 electron, 2m drift distance, 18° track angle, Rm = 5%.

Reviewing these results in the light of the desired quality of ionization information (see earlier and IV.5), there is no problem from inefficient or multiple triggering.

Model Validity, Parameter Precision and the Resulting Practical Considerations

It would be unreasonable to suppose that the models used within the simulation are correct in all aspects. Various simplifying assumptions have been made. In addition, there is uncertainty associated with the values used for the parameters of the simulation. The possible consequences of these assumptions and inaccuracies are discussed below, together with any resulting practical considerations.

(a) Formation of the Ionization Track (II.1)

The model in the simulation assumes that the ionization is uniformly distributed along the line of the track. In reality, this is not true. On average, a relativistic charged particle makes ∿30 ionizing collisions within a 1.6 cm sample. The amount of ionization produced in each collision may vary widely. Thus a non-uniform ionization distribution along the track may be expected, varying at the ∿1mm level. The resulting noise contributions will, however, be attenuated by the 'smoothing' effects of ionization dispersion (diffusion etc.) and by the linear signal integration within the electronics.

The spatial extent of the ionization produced is of the order of a few hundred microns, so in this respect the assumption in the simulation of a line ionization track is good. There is however a certain small probability (∿a few %) of long-range δ-ray production [LJ59]. Such an occurrence will result in a much larger ionization signal than is important in the consideration of the SNR conditions.

(b) Dispersion of the Ionization (II.2)

(i) Diffusion

The electron temperature is not known accurately: there is an error of ±30% on the value of 0.28 eV used in the simulation. This results in an uncertainty of ±15% in the width of the pulse at the 1% level. Thus a similar percentage error may be assumed for derived parameters, e.g. the two-track resolution, integration gate extension time etc.

(ii) Field geometry dispersion

As explained in II.2, a worst-case model is used in the simulation. The field geometry dispersion is very probably smaller than predicted. This will result in an increased SNR, and, more importantly, a decreased pulse width at the 1% level. The two-track resolution will be improved.

(c) Gas Amplification (II.3)

In the model of the gas amplifier, there are two assumptions which should be discussed:

(i) Field independent positive ion mobility

A field-dependent positive ion mobility would result in a different ion pulse response to the $^{1}/t + t_o$ response assumed in the model. The effect would occur at small times $t \tilde{\sim} t_o$, when the field experienced by the ions is largest. Although the total signal charge (α gas gain) would remain the same, the resulting pulse shape would be altered. If this effect is observed, a slight redesign of the shaping elements of the electronics will cure the problem. (See Appendix 1.)

(ii) Average gas gain

A mean value of the gas gain is assumed in the simulation, resulting in an impulse response which is the same for every primary electron (see II.3). The gas amplification process is noisy; the

gas gain in fact varies about the mean from pulse-to-pulse. However, this variation is small (a few %) compared with the width of the Landau ionization loss distribution (∿100%) [RP74].

The operational value of the gas gain will be determined by the ambient background particle flux (see II.3). If the flux is greater then anticipated, a lower gas gain may be necessary to eliminate space-charge induced effects. This would result in a lower SNR, and a worse two-track resolution at small drift distances (see IV.5). The SNR may be increased by connecting further anodes in parallel, thus increasing the sample size. A marginal increase in the 'effective gas gain' also occurs (see III.2). This procedure reduces the two-track resolution, because of the increased track-angle dispersion, and is viewed only as a contingency measure. If, on the other hand, the actual flux is lower than anticipated, the gas gain may be increased, although not by more than a factor of ∿2, because of the onset of gas amplifier non-linearity. A better performance would be achieved as the result of a higher SNR.

(d) Noise and Triggering (III.2, III.5)

Further improvements in preamplifier design may reduce the noise level in the system. The resulting increase in SNR would be helpful.

The model of the discriminator used in predicting system performance possessed a zero latchtime. Tests have shown that this is not in practice true (see IV.2) However, a non-zero latch time allows a lower trigger-on level to be used, because short, sharp noise pulses are effectively suppressed. This results in a better pulse detection capability, a lower integration gate extension time, and thus an improved two-track resolution at small drift distances.

(e) Pulse Shaping (III.3)

An optimum pulse shaper design was derived using idealized models for the gas amplifier and electronic responses. As stated in III.3, the shaping network may require 'trimming' to regain a good pulse shape characteristic for real signals. Although the duration of the signals is important, the shaped pulses also have to be inspected for the presence of a 'tail' at the 1% level. The pulse shape performance for real signals was not investigated to quite this accuracy during the tests described earlier in this chapter. This aspect of performance remains to be checked accurately. However, the success of the prototype shaper, as measured, leads to the conclusion that no major alterations to the shaping network will be needed. In addition, once an optimum network design is obtained for one channel, an identical design may be used for all channels.

(f) Integration Gate Timing (III.4, III.5)

The uncertainties in the magnitudes of the dispersive processes may lead to errors in the prediction of the integration gate extension time and the associated analogue signal delay. Although values for these parameters have been determined using the simulation, the operational values may be different.

If measurements are made of the variation of the mean ionization loss (for the 2m-drifted tracks from particles of a particular P/m_oc) with gate extension time, then it should be seen that the mean ionization loss remains at a constant maximum value above a certain minimum gate extension time. It is this value of the gate extension time which should be used throughout the system: the value for one channel may be used for all channels.

Conclusion

The simulation has shown that the performance of the ISIS device justifies its construction.

(i) The quality of the ionization measurement is predicted to be sufficient to provide useful data on particle velocity, in particular for the separation of $K/\pi/p$.

(ii) The two-track resolution of the device is predicted to vary between:

1.3 cm ± 0.3 cm for tracks deposited near to the wire plane

and

2.0 cm ± 0.4 cm for tracks from the maximum drift distance of 2m.

(iii) The triggering characteristics are predicted to be satisfactory in the aspects of triggering efficiency (100%) and multiple triggering (∿1%).

CHAPTER V

CONCLUSION

A detailed technical design for ISIS has been derived involving:-

(a) An evaluation of several important chamber parameters, e.g. wire spacing, ionization dispersion etc.

(b) A low noise input configuration.

(c) An optimised pulse shaping stage.

(d) A pulse-width sensitive discriminator.

(e) A novel multiplexed integrating analogue memory.

The problems arising from the high data rate have been solved by:

(i) The use of parallel processing (inherent in the design).

(ii) The use of fast temporary analogue and digital memory.

(iii) The use of a fast DC baseline restorer.

The slow process of analogue-digital conversion is delayed until there is time available for the readout of the data.

Prototype electronics has been constructed and successfully tested.

The signal-to-noise conditions in ISIS have been examined using a computer simulation. This has enabled the performance of the device to be investigated in depth. The validity of the simulation has been checked experimentally with the prototype equipment, using both artificial and real (particle-derived) signals. An optimum point within an adequate operating window has been determined. A spatial resolution of between 1.3 cm and 2 cm is predicted, depending on the trajectory of the particle through the chamber. The resolution for ionization is good enough to ensure the identification of kaons, pions and protons at the 90% level in the momentum range 3-100 GeV/c depending on the particles involved.

APPENDIX 1

THE FORM OF THE GAS AMPLIFIER OUTPUT PULSE

The multi-electrode nature of the wire-plane electrostatics requires an extended derivation of the form of the gas amplifier output pulse from that given in, for example, [WD50]. For the purposes of the calculation, the case is considered in which only one primary electron arrives in the vicinity of the anode wire. An avalanche occurs: a large number ($>10^3$) of positive ions are created. The measured signal arises from the variation of the induced charge on the electrodes as the positive ions move away from the anode. (The motion of the secondary electrons adds only a small amount (<10%) to the signal, because the electrons have only relatively low potential to fall through before reaching the anode [WD50]. This contribution is ignored, but can only increase the signal amplitude.)

The generalized configuration for a multi-electrode proportional counter is shown in Fig. A1.1 in terms of an equivalent circuit. A single anode may be surrounded by several other electrodes, assumed to be cathodes. The circuit impedances for the i^{th} cathode are shown. In the ISIS device one anode wire has, as its nearest neighbours, two cathode wires (see III.2).

The signal is measured as a current by a low impedance amplifier connected between anode and cathodes. The amplifier is isolated by coupling capacitors from the high impedance polarizing potential. Relating this to the equivalent circuit of Fig. A1.1,

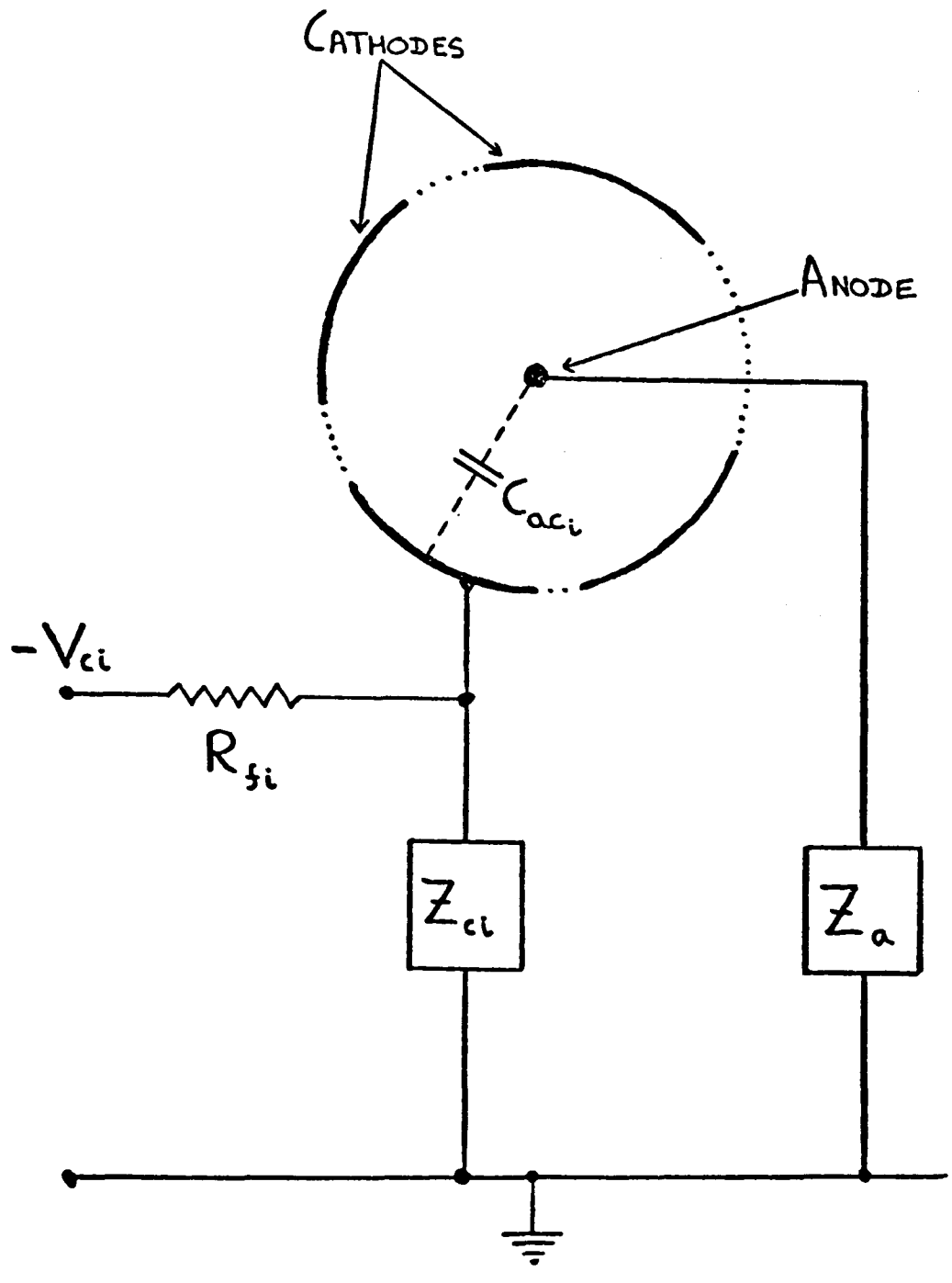


FIGURE A1.1 The Equivalent Circuit of a Multi-electrode Proportional Counter.

the impedance Z_a is low resistance of ∿100Ω. The impedance Z_{ci} is capacitative, ∿500 pF, being made up of two 1000 pF coupling capacitors in series. The h.t. feed resistance R_{fi} is 200 KΩ, or two 100 KΩ resistors in series. The anode-cathode capacitance C_{aci} is 17 pF per cathode. Further details on these values are given in III.2.

In terms of time constants, the anode (signal) circuit time constant is small (a few nS) compared with the signal duration of ∿200 nS. The h.t. feed time constant is long (∿100 μS) compared with the signal duration. The following analysis assumes these conditions: a short time constant for signal currents, a long time constant for the h.t. feed voltage.

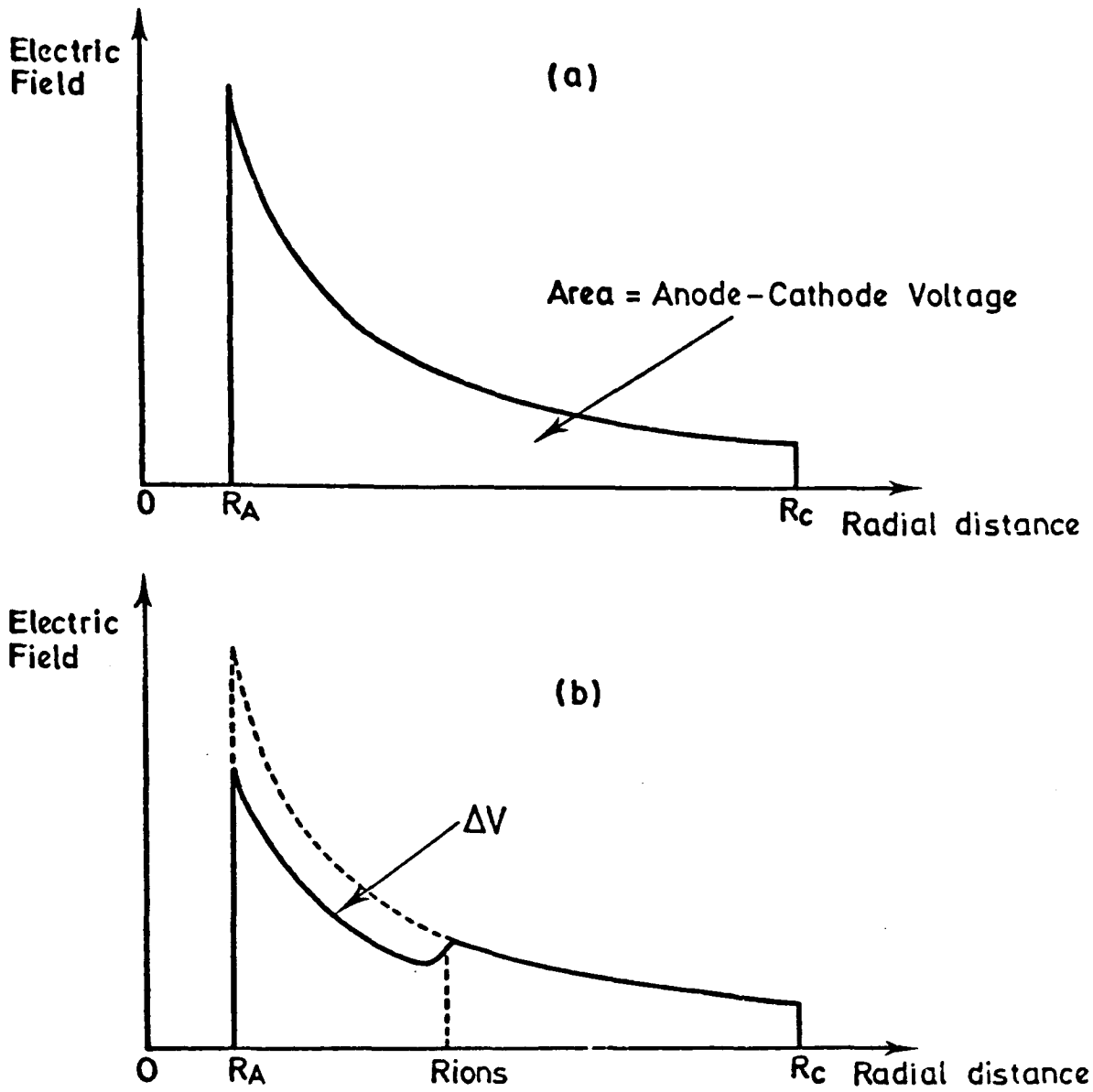


FIGURE A1.2 Schematic Diagram of Fields Around an Anode During the Amplification Process.

Consider the electric field in a long counter of cylindrical geometry (Fig. A1.2(a)). A time t after the avalanche, the positive ions form a cylinder around the anode, resulting in the electric field distribution shown in Fig. A1.2(b). This cylinder is localized to a short length of the wire (a few mms). (By a Fourier argument, an assumption that the cylinder is long does not affect the result [LJPC].) There is a change in voltage across the counter of ΔV

$$\Delta V = \frac{Q_I}{C_{AI}}$$

where Q_I is the charge in the positive ion cylinder

C_{AI} is the capacitance of the anode to the positive ion cylinder

If G is the gas gain

$$Q_I = eG.$$

The change in voltage across the counter is not restored by the ht supply during the duration of the signal because of the long ht feed time constant. A signal charge flow occurs in the external circuit, through the preamplifier input impedance Z_a, of

$$Q_S = \Delta V C_{AC}$$

where C_{AC} is the counter anode-cathode capacitance. In the case of the multi-electrode configuration, C_{AC} is the sum of all anode-cathode capacitances:

$$C_{AC} = \sum_{i=1}^{n} C_{aci}$$

The total capacitance is used because the change in potential is seen by all cathodes.

The time evolution of the signal charge is given by:

$$Q_S(t) = Q_I \frac{C_{AC}}{C_{AI}}(t)$$

In terms of a signal current $I_S(t)$,

$$I_S(t) = \frac{\partial}{\partial t} Q_S(t) = -Q_I \frac{C_{AC}}{C_{AI}^2(t)} \frac{\partial C_{AI}}{\partial t}(t)$$

The development of the signal may be divided into two consecutive stages:

1. While the positive ions are travelling radially away from the anode,
2. When the positive ions disperse to more relatively incoherently to the different cathodes.

The first situation is the one which produces the useful signal current. The second stage gives rise to a small background, almost dc, current at long times ($\sim\mu S$) after the avalanche (see later).

In the calculation of the useful signal current generated in the first stage, a simple capacitance formula may be used for C_{AI}, since the geometry is cylindrical. For unit length of counter:

$$C_{AI} = \frac{2\pi\varepsilon_o}{\ln(R_I/R_A)} \qquad \text{[BB65]}$$

where R_I is the radius of the ion cylinder

R_A is the radius of the anode wire.

Thus

$$\frac{\partial C_{AI}}{\partial t} = \frac{-2\pi\varepsilon_o}{[\ln(R_I/R_A)]^2} \cdot \frac{1}{R_I} \cdot \frac{\partial R_I}{\partial t}(t)$$

The radial velocity $\frac{\partial R_I}{\partial t}(t)$ of the positive ions is obtained from their mobility μ_+ and the electric field $E(R_I)$. A field independent mobility is assumed.

$$\frac{\partial R_I}{\partial t} = \mu_+ E(R_I) = \frac{\mu_+ Q_A}{2\pi\varepsilon_o R_I}$$

where Q_A is the anode charge per unit length. The radial position of the ions after a time t is found by integration:

$$2\pi\varepsilon_o \int_{R_A}^{R_I} R_I dR_I = \mu_+ Q_A \int_o^t dt$$

Or

$$R_I^2 = R_A^2 + \frac{\mu_+ Q_A}{\pi\varepsilon_o} t$$

Therefore the signal current is:

$$I_S(t) = Q_I \, C_{AC} \frac{\mu_+ Q_A}{(2\pi\varepsilon_o R_I)^2}$$

Substituting for R_I:

$$I_S(t) = \frac{Q_I C_{AC}}{4\pi\varepsilon_o} \left[\frac{1}{t + \frac{\pi\varepsilon_o R_A^2}{\mu_+ Q_A}} \right]$$

This is of the form:

$$I_S(t) = \frac{Q_o}{t + t_o}$$

where $$Q_o = \frac{Q_I C_{AC}}{4\pi\varepsilon_o}$$

and $$t_o = \frac{\pi\varepsilon_o R_A^2}{\mu_+ Q_A}$$

These results are consistent with those given in [WD50] and [MS69].

Typically,

$$\left.\begin{aligned} G &= 10^4 \\ R_A &= 12.5 \pm 0.7\mu \\ Q_A &= 16 \pm 4 \text{ nC/m} \end{aligned}\right\} \qquad \text{II.3}$$

$$\mu_+ = (1.5 \pm 0.5) \times 10^{-4} \text{ m}^2/\text{v/S [EA65]}$$

for A^+ ions

The capacitance C_{AC} can be found from the results of Appendix 2.

Since: $$C_{AC} = \frac{dQ_A}{dV_A}$$

therefore: $$C_{AC} = \frac{\partial Q_A}{\partial V_{AC}} + \frac{\partial Q_A}{\partial V_{AD}}$$

where V_A is the anode potential

V_{AC} is the anode-cathode wire potential difference

V_{AD} is the anode-drift electrode potential difference

From Appendix 2,

$$Q_A = 6.7 \times 10^{-12} V_{AC} + 2.5\ 10^{-14} V_{AD}$$

This gives:

$$C_{AC} = 7 \pm 1 \text{ pF/m}$$

Substituting the above values,

$$Q_o = 10 \pm 2 \times 10^{-17} \text{ C}$$

$$t_o = 1.8^{+1.2}_{-0.8} \text{ nS}$$

Thus, when an ionization electron reaches the anode, the signal current at the instant of avalanche formation, is:-

$$I_s(0) = \sim 55 \text{ nA}$$

The second stage of signal development is reached when the electric field around the anode departs from radial. This occurs at a distance of about $s/5$ from the anode, where s is the wire spacing, of 4 mm. This is at a time of about

$$t_R \doteq \frac{(s/5)}{R_A} t_o$$

or about 7μS with t_o = 1.8 nS. At this point, the signal current has fallen to about $1/4000$ of its initial value. Thus the motion of the positive ions as they continue on their way to the cathodes may be ignored. This slowly varying component of the signal will be removed by the DC Baseline Restorer (see III.6).

The assumption of a field-independent mobility μ_+ has the effect of making the pulse sharper than it really is at short times $t \lesssim 30$ nS. This is because μ_+ is smaller at the high fields experienced close to the anode than it is at low fields [EA65]. At the surface of the wire, μ_+ is 30% of the low field value, increasing to 60% at a distance of three wire radii from the wire (reached about 20 nS after the avalanche [LF57].) This effect is ignored in the simulation, but is unlikely to effect the results since it occurs at times short compared with the system rise time (see IV.5, IV.6, Appendix 4).

APPENDIX 2

WIRE PLANE OPERATING VOLTAGES AND GAS GAIN SWITCHING

Given a particular chamber electrostatic geometry, it is possible to calculate the anode, cathode and drift electrode potentials from the desired values of the drift field and anode wire charge per unit length. The relations between electrode potentials and charges have been derived semi-analytically for the ISIS geometry [LJPC]. For the anode-cathode potential V_{AC}:

$$V_{AC} = \frac{Q_A}{2\pi\varepsilon_o}\left[\ln\left(\frac{2s}{\pi R_A}\right) + \propto \ln\left(\frac{2s}{\pi R_C}\right)\right]$$

For the anode-drift electrode potential V_{AD}:

$$V_{AD} = \frac{Q_A}{2\pi\varepsilon_o}\left[\ln\left(\frac{s}{R_A}\right) + \frac{\pi H}{2s} - 1.137 - \alpha\left(\frac{H}{2s} - 0.607\right)\right]$$

where

$$\alpha = -\frac{Q_C}{Q_A} \qquad \text{(see II.4)}$$

Q_A, R_A, Q_C, R_C = charge per unit length and radii of the anode and cathode wires respectively.

H = the maximum drift distance

s = the anode cathode wire spacing

At the proposed operating point,

H = 2m (see I.2)

s = 4mm (see II.4)

R_A = 12.5μ (see II.3)

R_C = 125μ (see II.3)

The above relations reduce to:

$$V_{AC}\ (\text{volts}) = 95.7\ (1 + 0.567\alpha)\ Q_A\ (^{nC}/m)$$

$$V_{AD}\ (\text{kV}) = 14.2\ (1 - \alpha)\ Q_A\ (^{nC}/m)$$

Thus for a drift field of 100 kV/m, and an anode wire charge of 16 nC/m, (typical values, see below),

$$V_{AC} = 1640\text{v}$$

$$V_{AD} = 200\ \text{kV}$$

The Charge on the Anode Wires

The charge on the anode wires for a particular gas gain is best determined experimentally. A knowledge of the operating conditions for measured gas gains on chambers of known geometry allows the calculation to be performed.

For 12.5μ-radius wires, in 80% A/20% CO_2, it has been found that a gas gain of $\sim 10^4$ is obtained at an anode wire charge of 16 ± 2 nC/m (IV.3, [CJ75], [BJ76]). Noting the high dependence of gas gain on charge, a safe operating window for the anode wire charge is 12-20 nC/m. This is an ample range for all contingencies.

Gas Gain Switching

To alleviate the undesirable effects of the positive ion space charge (see II.3), the gas amplifier may be switched off during the time that signals are not required from the chamber [IN26]. This entails lessening the potential difference between anode and cathode wires. The mean space charge density within the chamber is reduced by a factor equal to the effective on-off duty cycle, assuming a constant particle flux. The duty cycle is determined by certain constraints involving the other parts of the experimental apparatus.

In the presently proposed system [EHSP], the gas amplifier duty cycle is fixed by the bubble chamber duty cycle. The bubble chamber is sensitive for ∿1 mS every ∿33 mS. Allowing for stabilization of the gas gain, the gas amplifier is effectively 'on' for ∿2 mS every ∿33 mS. Thus the duty cycle is ∿0.06.

With the gas gain 'on', the anode wire charge is ∿16 $^{nC}/_{m}$. From an inspection of the dependence of gas gain on operating voltage, the anode charge must be reduced to ∿3 nC/m, to switch the gain off. The drift field must remain constant; the switching is performed at constant $(Q_A + Q_C)$. As a result, the rest of the electrostatics does not see the transition.

The table A.1 contains the values of the anode-cathode voltages V_{AC} needed for various anode wire charges and for two drift fields. The final operating voltages will be decided upon in the light of the ambient chamber conditions and the value of the required gas gain.

TABLE A.1

ANODE-CATHODE OPERATING VOLTAGES

Wire Spacing = 4 mm

Q_A nC/m	Drift Field = 50 kV/m		Drift Field = 100 kV/m	
	α	V_{AC} (volts)	α	V_{AC} (volts)
3.0 (off)	-1.34	+69	-3.73	-320
12.0 (on)	+0.41	+1410	-0.18	+1030
16.0 (on)	+0.56	+2020	+0.12	+1640
20.0 (on)	+0.64	+2603	+0.29	+2220

APPENDIX 3

ELECTROMECHANICAL STABILITY OF THE WIRE PLANE

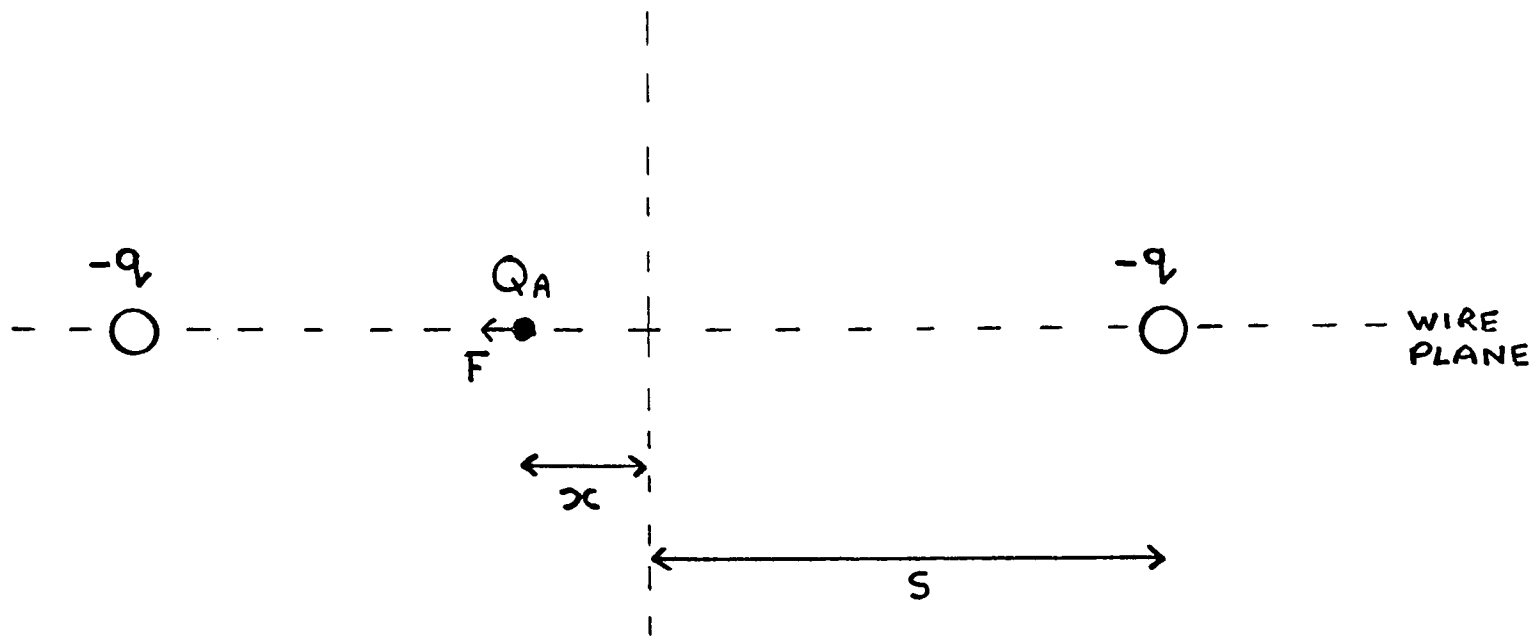
In this Appendix, the stability of the wires against displacement by the electrostatic forces in the chamber is investigated. The movement of one 12.5μ-radius anode wire is considered. The cathode wires, being ten times thicker and under a correspondingly greater tension, are assumed to be rigid.

Compared with the inter-wire spacing of 4 mm, the drift electrodes are at a great distance (2m) from the wire plane. Any variation in electrostatic energy due to a change in the anode-drift electrode capacitance as a result of anode movement, is ignored.

Electromechanically, the wire plane must be unconditionally stable at all times: with the gas amplification in the 'on' state, in the 'off' state, and during the transition between the two. As explained in Appendix 2, the gas gain is switched by changing the potentials on the wires. In the 'on' state, the anode has a charge Q_A of ∿16 nC/m. Turning the gain off entails reducing this to about 3 nC/m. The switching is performed at constant $(Q_A + Q_C)$: the drift field does not change.

Depending on the relative signs of Q_A and Q_C, the anode wires are either attracted to or repelled by the cathodes. In the case of attraction, the tendency is for the anodes to move in the plane of the wires. In the case of repulsion, the anodes tend to move out of the plane of the wires.

In-Plane Distortion

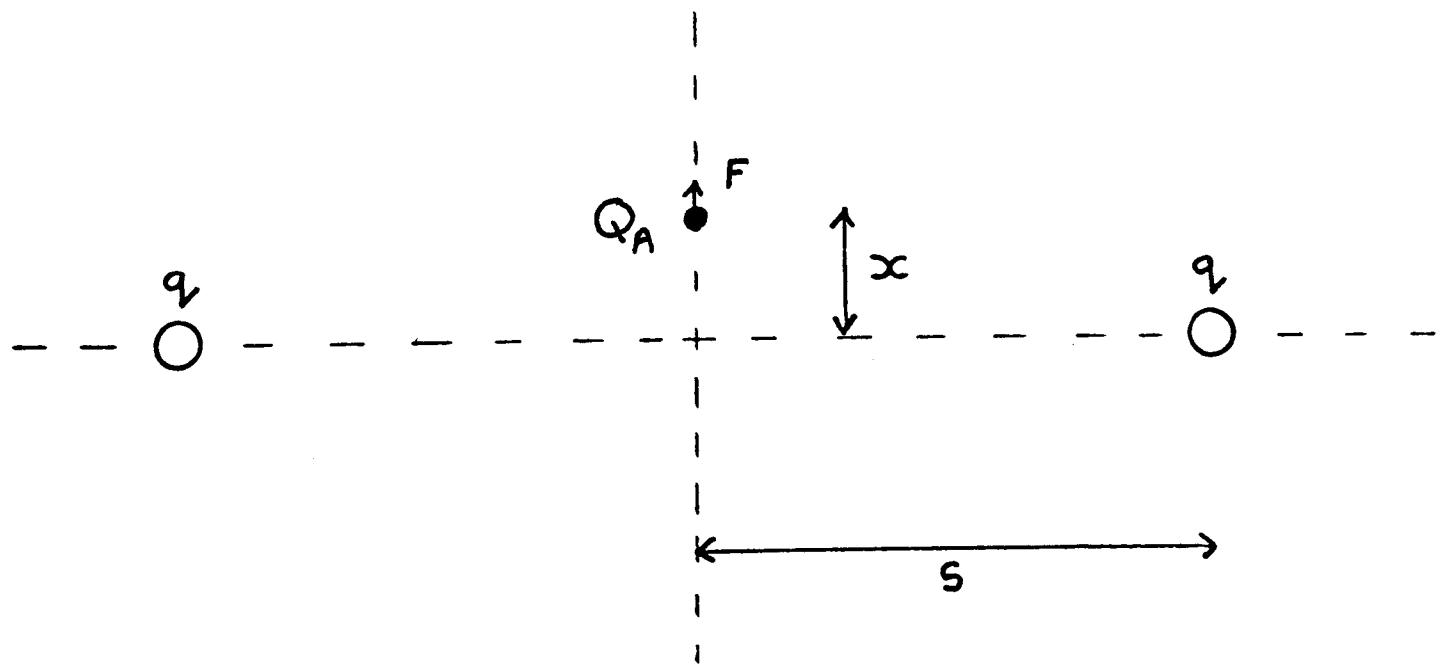


The force on a length dl of the anode wire is:

$$Fdl = \frac{Q_A dl}{2\pi\varepsilon_o} .q. \left(\frac{1}{s-x} - \frac{1}{s+x} \right)$$

where x is the displacement from the undistorted position.

Out-of-Plane Distortion



The force on a length dl of anode wire is:

$$Fdl = \frac{Q_A dl}{2\pi\varepsilon_o} \quad \frac{2q}{s} \quad \frac{x}{s} \qquad (x << s)$$

For the condition x << s, these two forces are algebraically identicaly, although of opposite sign:

$$|Fdl| = \frac{Q_A dl}{\pi\varepsilon_o} \frac{x}{s^2} q$$

The effect of other wires in the plane may be included by summation:

$$Fdl = \frac{Q_A dl}{\pi\varepsilon_o} .x \sum_{i=1}^{\infty} \frac{Q_C}{s^2(2i-1)^2} + \frac{Q_A}{s^2(2i)^2}$$

Evaluating the sum:

$$Fdl = \frac{Q_A dl}{\pi\varepsilon_o} \frac{x}{s^2} (1.23Q_C + 0.41Q_A)$$

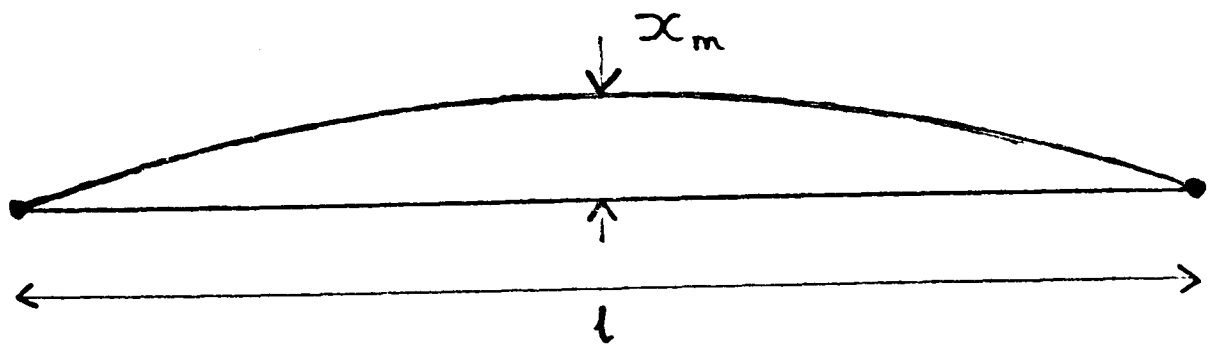
Integrating now to find the electrostatic energy of the whole wire:

$$E_{es} = \int_o^l \int_o^x Fdx\ dl$$

$$E_{es} = \frac{Q_A l \bar{x}^2}{2\pi\varepsilon_o s^2} (1.23Q_C + 0.41Q_A)$$

where $\bar{x}^2$ is the mean value of x^2 of the whole wire. In terms of a maximum displacement x_m from the undistorted position, as shown below

$$\bar{x}^2 = \frac{8}{15} x_m^2$$



Therefore:

$$E_{es} = \frac{4x_m^2 \; 1 \; Q_A \; (1.23Q_C + 0.41Q_A)}{15\pi\varepsilon_o s^2}$$

This energy is balanced by the mechanical potential energy from the extension of the wire:

$$E_m = \frac{8Tx_m^2}{31}$$

where T is the tension in the wire. The system is electro-mechanically stable if:

$$\frac{8T}{31} > \frac{4 \; 1 \; Q_A \; (1.23Q_{AC} + 0.41Q_A)}{15\pi\varepsilon_o s^2}$$

Defining a minimum tension T_m:

$$T_m = \frac{1^2 \; Q_A(1.23Q_C + 0.41Q_A)}{10\pi\varepsilon_o s^2}$$

This value agrees with the result given in [RP74].

If the wire plane is strung with the anode wires at an unchanged tension T_o, then the anode wire fundamental vibrational frequency, when charged, will be:-

$$f = \frac{1}{21}\sqrt{\frac{T_o - T_m}{m}}$$

where m is the mass/unit length. For stainless steel wire, density 7.8×10^3 kg/m^3, radius 12.5μ, and length 2.5m, then:

$$f(\text{Hz}) = 10.0 \sqrt{T_o(\text{gms wt.}) - T_m(\text{gms wt.})}$$

The breaking tension on this wire is about 70 gms. wt. (measured). Operation of a wire plane with a static anode wire tension of T_o = 50 gms wt. is feasible.

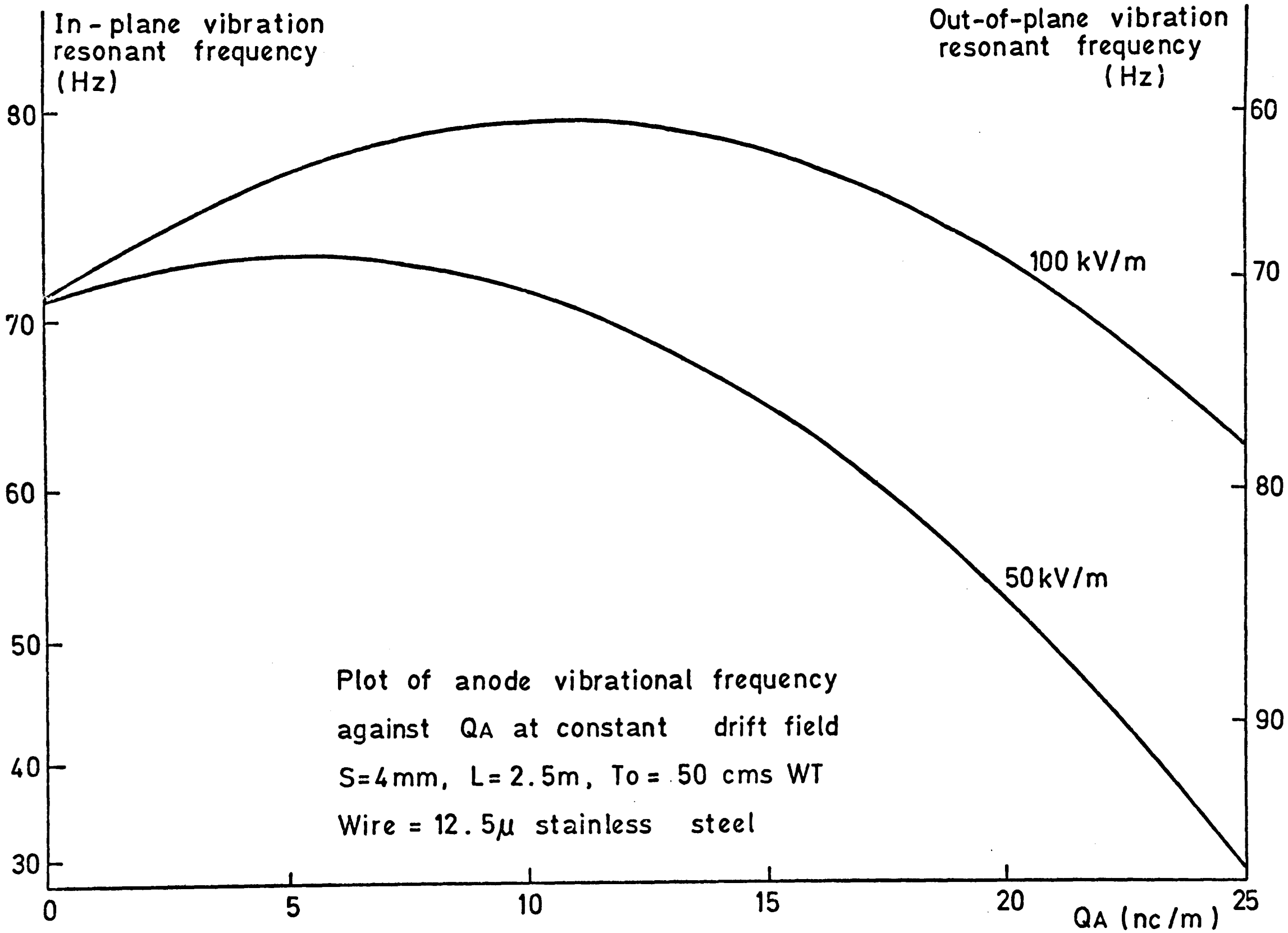
Putting in the numerical values:

$$T_m(\text{gms. wt.}) = \frac{2.29}{s^2} . Q_A(1.23Q_C + 0.41Q_A)$$

where s is in millimetres, and Q_A and Q_C are in nC/m.

The stability situation may be studied by evaluating the fundamental vibrational frequency of the wires. The graph of Fig. A3.1 shows the variation of the in-plane and out-of-plane resonant frequencies as Q_A is changed at constant drift field $(Q_A + Q_C)$. The wire spacing assumed was 4 mms.

The conclusion is that, as the gas gain is switched, $(Q_A = 20 \rightarrow 3$ nC/m), the resonant frequencies remain above 40 Hz. As stated in II.3, this is an acceptable lower limit on the resonant frequency.



Plot of anode vibrational frequency against Q_A at constant drift field
S=4mm, L=2.5m, To=50 cms WT
Wire = 12.5μ stainless steel

APPENDIX 4

SIMSYS: THE ISIS SIMULATION PROGRAM

SIMSYS is a structured modular computer program. It provides facilities for the simulation, in the time domain, of the behaviour of complex signal generation and signal processing systems in the presence of noise. SIMSYS contains a specific set of routines designed to model the various components of the ISIS device. With these routines, SIMSYS can simulate the treatment of the signal from one ionization sample (one channel) in ISIS, together with the associated noise. An overview of the simulation is given in IV.1.

Control over the program and its parameters is exercised interactively via an on-line terminal. The design of SIMSYS allows two basic modes of operation:

(1) User-Driven

The parameters of the simulation may be varied interactively. The user can observe the effects of these variations in the form of, for instance, the changes in a displayed signal profile.

(2) Free-Running

For accurate prediction of system behaviour under noisy conditions, the program allows the repeated execution of a particular simulation using the same parameter values each time. The program calculates the mean and rms spread of predicted results over the run, from data provided by the constituent models. For example, the mean and rms spread of the triggering times are available from the data supplied by the model of the discriminator.

General Features of the Simulation Program

The time profile of a simulated signal is held in the program as an array containing the values of the signal amplitude at 0.5 nS intervals. The maximum duration of signal that may be accommodated is 4 μS.

The models making up the simulated process are present in the program as subroutines which, when called, operate on the elements of the signal array in a manner appropriate to the modelled function. Standard routines are also included which do not alter the signal array, but instead provide a useful facility:

e.g. Displaying the signal profile on graphics devices that are attached to the computer

Calculating the rms, maximum and minimum values of the signal array

Printing the program parameter list, etc.

In addition, special function routines are available to generate specific frequently-used signals:

e.g. Step function generator

Sine wave generator

The sequence in which the routines are called must be provided by the user. However, this results in great flexibility.

The program was written in FORTRAN, and is about 4500 statements long. The storage requirement is about 250 K bytes. The CPU usage for one execution of the simulation is about 4 seconds, on a DEC KI-10 processor. Thus a 300-repetition run takes about 20 minutes CPU time.

The Features Specific to ISIS

The constituent models of the ISIS simulation are each discussed briefly below. The relationship between the models is shown in Fig. IV.1. The parametrization of the models should be easily understood if reference is made to the appropriate earlier

sections. The optimum values of the parameters are given: the derivation of these is explained in IV.5.

1. The model of ionization deposition (see II.1)

The number of ionization electrons per sample, for up to two tracks, may be chosen in one of two ways:

(i) A fixed value, provided by the user, of up to 1000 electrons may be employed.

(ii) A random value of the ionization loss may be found by a Monte Carlo method from the theoretical Landau distribution of a minimum ionizing particle [BJ76]. The number of ionization electrons is calculated by dividing this ionization loss by the mean ionization loss per ion pair of the gas.

Input data

(i)	Number of tracks		(<2)
(ii)	Sample width		1.6 cm
(iii)	Track angle		0-18°
(iv)	No. of ionization electrons		
	Track 1	Variable	(Optional)
	Track 2	Variable	(Optional)
(v)	Integrated Landau probability distribution look-up table		-
(vi)	Mean ionization loss per ion pair (for 80% A/20% CO_2)		26.4 eV

Output

Number of ionization electrons per track sample.

2. The model of ionization dispersion (see II.2)

Every ionization electron has ascribed to it an arrival time at the anode, dependent on the drift distance and the dispersive processes. The drift distance is converted to a drift time by dividing it by the drift velocity, and then adding the event time zero. The drift velocity is calculated as the product of the electron mobility and the drift field. The effects of the three types of dispersive processes are included as small corrections to the drift time. The model can handle the drifting of either one or two tracks simultaneously.

(a) Diffusion

The dispersion of the ionization due to diffusion is Gaussian in nature. The rms width depends on the electron temperature, the drift field and the drift distance. A Monte Carlo method is used to obtain a random drift time correction, with a Gaussian weighting of the appropriate width.

(b) Field Geometry Dispersion

For each ionization electron, a random position along the length of the sample is chosen. The additional delay in the time-of-arrival of the electron due to the field geometry effect, is found from a look-up table of delay against position in the sample.

(c) Track Angle Dispersion

The random position of the electron within the sample is also used in the calculation of the correction in time-of-arrival due to non-zero track angle.

Input data:

(i) Drift distance

Track 1	0-2m
Track 2	0-2m

(ii)	Event time zero	
	Track 1	Any
	Track 2	Any
(iii)	Electron mobility	400 $m^2/KV/s$
(iv)	Drift field	100 kV/m
(v)	Electron temperature	0.28 eV
(vi)	Integrated Gaussian probability look-up table	-
(vii)	Field geometry delay versus position-in-sample look-up table	-
(viii)	Track angle	0-18°
(ix)	Sample width	1.6 cm

Output:

(i) RMS width of track due to diffusion

(ii) Time-of-arrival for each electron

(iii) Drift velocity

(iv) Nominal drift time (undispersed)

3. The model of gas amplification II.3

The single-electron gas amplifier response, as the signal profile $I(t) = \frac{G_e Q'}{t + t_o}$, is added to the signal array at displaced times corresponding to the arrival times of the ionization electrons at the anode. (The superimposition of single-electron signals to produce a mutli-electron signal has been shown to be valid [FH75]).

Input Data:

(i)	Equivalent gas gain G_e (This is made up of the product of the real gas gain G = 10000, and the effective signal boost factor of 1.5 due to the differential input operation, see III.2)	15000

(ii)	Gas amplifier output current	Q'	5.5 pA/unit gas gain
(iii)	Gas amplifier time constant	t_o	1.8 nS

4. The model of electronic noise (see III.2)

A simulated electronic noise component is added to the signal array, before any bandwidth-limiting processing is performed i.e. before the signal array is passed to one of the models of the electronic stages.

The noise contribution consists of random, positive and negative, Gaussian-weighted values that are added to each element of the signal array. The rms width of the Gaussian weighting is determined by the required input noise spectral density.

The properties of this noise model have been investigated, and it has been shown that the noise generated in 'white' up to frequencies of ∿300 MHz.

Input data:

Equivalent input current spectral density	115 nA/$\sqrt{\text{GHz}}$	(measured)
Integrated Gaussian distribution look-up table		

5. The models of electronic amplification (see III.2)

Electronic amplification occurs over two stages: the pre-amplifier and the main amplifier. Each stage is modelled to have, in sequence:

(i) a single RC integration time constant, defined as a 10-90% rise time, representing the amplifier input bandwidth limitation.

(ii) a single RC differentiation time constant, representing the ac coupling between stages,

(iii) a single RC integration time constant, also defined as a 10-90% risetime, representing the amplifier output bandwidth limitation.

Because of the exponential nature of the above responses, only one scan through the input signal array was required to calculate the output signal array. The coding for the routine is given in Fig. A4.1.

Input data:

(a) Preamplifier

Input risetime	30 nS
Input coupling time constant	100 μS
Output risetime	10 nS
Gain: transresistance	160 mV/μA

(b) Main amplifier

Input risetime (cable risetime)	30 nS
Input coupling time constant	100 μS
Output risetime	10 nS
Gain	5.63

6. The model of signal shaping (see III.3)

The signal array at the output of the shaper is derived from that at the input, by summing the appropriate proportions of three differently-differentiated input signals, with the unchanged input signal. A single RC integration and a gain factor are also applied.

Input data:

RC differentiated components:

Time constant 1	190 nS	31.0%
Time constant 2	1100 nS	21.0%

```
      SUBROUTINE RCCRRC (RT1,CTC,RT2,TC1,TC2,GAIN)

C*******SIMULATES AN AMPLIFIER WITH TWO RC INTEGRATING TIME
C*******CONSTANTS OF RISE TIMES  'RT1' AND 'RT2', AND
C*******(RETURNED) RC TIME CONSTANTS 'TC1' AND 'TC2',
C*******SEPARATED BY A COUPLING TIME CONSTANT 'CTC',
C*******WITH DC GAIN 'GAIN',

      COMMON/SIGN/ SIGNL(0/8000),ISAE,ARRMAX,ARRMIN,PUNIT(2)
      COMMON/PRGT/ TINC,TSTARS,TSTART,TLEAD

C     INITIALIZE
      ARRMAX = 0.0
      ARRMIN = 0.0
      DELS1 = 0.0
      DELS2 = 0.0
      DELS3 = 0.0
      PREVS1 = 0.0
      PREVS2 = 0.0
      PREVS3 = 0.0
      SIGD1 = 0.0
      SIGD2 = 0.0
      SIGD3 = 0.0

C     CONVERT RISE TIMES INTO RC TIME CONSTANTS
      TC1 = RT1/2.20
      TC2 = RT2/2.20
      ECTC = EXP (-TINC/CTC)
      IF (TC1.EQ.0.0) GO TO 10
      ETC1 = EXP (-TINC/TC1)
      GO TO 15
10    ETC1 = 0.0
15    IF (TC2.EQ.0.0) GO TO 20
      ETC2 = EXP (-TINC/TC2)
      GO TO 25
20    ETC2 = 0.0

C     LOOP OVER SIGNAL ARRAY TO CALCULATE NEW SIGNAL
25    DO 1000 I = 0,ISAE
C     FIRST RC INTEGRATION
      ASIG = SIGNL(I)
      DELS1 = ASIG - PREVS1
      PREVS1 = ASIG
      SIGD1 = SIGD1 + DELS1
      BSIG = ASIG - SIGD1
C     TRAP TO STOP FLOATING UNDERFLOW MESSAGES
      IF (ABS(SIGD1).GT.1.0E-36) SIGD1 = SIGD1 * ETC1
C     RC DIFFERENTIATION
      DELS2 = BSIG - PREVS2
      PREVS2 = BSIG
      SIGD2 = SIGD2 + DELS2
      CSIG = SIGD2
C     TRAP TO STOP FLOATING UNDERFLOW MESSAGES
      IF (ABS(SIGD2).GT.1.0E-36) SIGD2 = SIGD2 * ECTC
C     SECOND RC INTEGRATION
      DELS3 = CSIG - PREVS3
      PREVS3 = CSIG
      SIGD3 = SIGD3 + DELS3
      DSIG = (CSIG - SIGD3) * GAIN
C     TRAP TO STOP FLOATING UNDERFLOW MESSAGES
      IF (ABS(SIGD3).GT.1.0E-36) SIGD3 = SIGD3 * ETC2
      SIGNL(I) = DSIG
C     MAX AND MIN OF NEW ARRAY
      IF (ARRMAX.LT.DSIG) ARRMAX = DSIG
      IF (ARRMIN.GT.DSIG) ARRMIN = DSIG
1000  CONTINUE

      RETURN
```

FIGURE A4.1

Time constant 3 30 nS	100.0%
Unchanged component	65.0%
Shaper amplifier risetime	10 nS
Shaper amplifier gain	0.203

7. The model of the discriminator (see III.5)

A single RC integration is applied to the signal array. The array is then scanned to determine the profile of the digital discriminator output, by comparing the signal amplitude with the trigger-on and trigger-off levels.

Input data:

Discriminator input risetime	10 nS
Trigger-on level	8.0 mV
Trigger-off level	0.0 mV

Output:

Trigger-on time Trigger-off time Trigger duration	for each trigger

8. The model gated integration (see III.4)

The signal delay and integration gate extension times are added. Two RC integration time constants are applied, the first to simulate the delay line risetime, and the second to simulate the charging amplifier risetime. The voltage-to-current conversion is performed. The charge on the memory capacitor is found as a result of gated integration of the signal current.

Input data:

Analogue signal delay	80 nS
Integration gate extension time	120 nS

Delay line risetime	30 nS
Charging amplifier risetime	10 nS
Charging amplifier transconductance	0.020 mA/mV

Output:

Gate Durations	for each trigger
Memory capacitor charge	

9. The model of charge digitization

The digital value of the charge on the analogue memory capacitor is found by dividing the charge by a digitization sensitivity. A pedestal count is added.

Input data:

Pedestal value	10
Maximum digitized value	255 (8 bits)
Charge required for maximum digitized value	697 pc

Output:

Digitized charge for each trigger

Histogram of the digitized charges

Conclusion

SIMSYS has proved very useful in the design of the ISIS device. The simulation of:

(i) the microscopic processes involved in signal generation, and

(ii) the electronic treatment of the signals in ISIS,

has provided much valuable information about the performance of the whole system. The cost of implementing a suitable simulation was a fraction of the cost of constructing ISIS. In the author's opinion, the use of a simulation may prove effective for systems possessing:-

(i) A poor signal-to-noise ratio

(ii) A high interdependency among the parameters of the system.

(iii) An accurate definition of the physical processes involved in signal generation.

(iv) A relatively low number of carriers (∿100's) involved in these processes.

(v) A well-defined statistical description of the noise contributions.

REFERENCES

[AM74] Aderholz, M., et al, Nucl. Instr. & Meth., 118, 419 (1974).

[AM75] Aderholz, M., et al, Nucl. Inst. & Meth., 123, 237 (1975).

[AW72] Allison, W.W.M., Rutherford Laboratory Memorandum, RHEL/M/H21, p84, (1972).

[AW74] Allison, et al, Nucl. Instr. & Meth., 119, 499 (1974).

[AW76] Allison, W.W.M., et al, Nucl. Instr. & Meth., 133, 325 (1976).

[BA75] Brandt, A., et al, Nucl. Instr. & Meth., 126, 519 (1975).

[BB65] (Bleaney, B.)[2] 'Electricity and Magnetism', O.U.P., (1965).

[BC71] Bugenis, G.K., et al, Nucl. Instr. & Meth., 93, 525 (1971).

[BJ76] Bunch, J.N., D.Phil. Thesis, Oxford University (1976).

[BL62] Brillouin, L., 'Science and Information Theory', Academic Press (1962).

[BM72] Bertolaccini, M. and Bussolati, C., Nucl. Instr. & Meth. 100, 349 (1972).

[BM74] Buckingham, M.J. and Faulkner, E.A., Radio and Electronic Eng., 44, 125 (1974).

[BR74] Bouclier, R. et al, Nucl. Instr. & Meth. 115, 235 (1974).

[BS59] Brown, S. 'Basic Data of Plasma Physics', Wiley (1959).

[BW73] Bambynek, W., Nucl. Instr. & Meth., 112, 103 (1973).

[CA70] Charpak, G., et al, Nucl. Instr. & Meth., 80, 13 (1970).

[CG70] Charpak, G., Ann. Rev. Nucl. Sci., 20, 195 (1970).

[CJ75] Cobb, J.H., D.Phil Thesis, Oxford University (1975).

[CJ76] Cobb, J.H., et al, Nucl. Instr. & Meth., 133, 315 (1976).

[CJPC] Cobb, J.H., Personal Communication.

[CP71] Campion, P.J. and Kingham, M.W., X^{th} Int. Conf. on Phenomena in Ionized Gases, pub. D. Parsons & Sons (1971), p88.

[CP73] Campion, P.J., Nucl. Instr. & Meth., 112, 75 (1973).

[DW58] Davenport, W.B. and Root, W.L., 'Theory of Random Signals and Noise', McGraw-Hill (1958).

[EA65] von Engel, A., 'Ionized Gases', Chapter 7, O.U.P., (1965).

[EHSP] CERN Publication 'European Hybrid Spectrometer'. Proposed by Allison, W.W.M., et al, CERN/SPSC/76-43. See also [RLP1].

[FE75] Faulkner, E.A., Journ. Phys. E., 8, 533 (1975).

[FH75] Fischer H.G., et al, Proc. Int. Meeting on Proportional and Drift Chambers at Dubna, p152 (1975).

[GA53] Gillespie, A.B. 'Signal, Noise and Resolution in Nuclear Counter Amplifiers', Pergamon (1953).

[GF72] Goulding, F.S., Nucl. Instr. & Meth. 100, 493 (1972).

[GR73] Gabriel, R., Nucl. Instr. & Meth. 112, 539 (1973).

[HD68] Hoescher, D.F. 'Analogue-Digital and Digital-Analogue Conversion Techniques', Wiley (1968).

[HG49] Hanna, G.C., et al, Phys. Rev. 75, 985 (1949).

[HL70] Herbst, L.J., 'Electronics for Nuclear Particle Analysis' O.U.P. (1970).

[HR69] Hendricks, R.W., Rev. Sci. Instr. 40, 1216 (1969).

[IN2] Oxford University Nuclear Physics (No. 2)
[IN17] Laboratory; ISIS Project Group (No. 17)
[IN23] Internal Reports (No. 23)
[IN26] (No. 26)

[IRE60] I.R.E. Subcommittee on Noise, Proc. I.R.E. 48, 69 (1960).

[JD73] Jeanne, D. et al, Nucl. Instr. & Meth., 111, 287 (1973).

[JJ75] Jackson, J., 'Classical Electrodynamics' Chapter 13, Wiley (1975).

[LJ59] Lloyd, J.L. et al, Proc. Phys. Soc., 73, 277 (1959).

[LJPC] Lloyd, J.L., Personal Communication.

[LL44] Landau, L., J. Phys. USSR, 8, 201 (1944).

[LM57] Livingston, M.S. and Bethe, H.A., Rev. Mod. Phys., 9, 245 (1957).

[MC73] Motchenbaker, M.C. and Fitchin, F.C., 'Low Noise Electronic Design', Wiley, (1973).

[ME71] Magrab, E.B. and Blomquist, D.S., 'The Measurement of Time-Varying Phenomena', Wiley (1971).

[MJ74] Millard, J.K., et al, I.E.E.E. Trans. Nuc. Sci., NS-19 388 (1972).

[MS69] Mitra, S., SLAC-Report, SLAC-108, (1969).

[NDPC] Nygren, D., Personal Communication;
LBL-PEP Proposal PEP-4, (1976).

[NP74] Nicholson, P.W., 'Nuclear Electronics', Wiley (1974).

[OA74] Ogata, A., Nucl. Instr. & Meth. 115, 313 (1974).

[PA72] Pratt, A.R., Proc. NATO Adv. Study Institute on Signal Processing, p375, Academic Press (1972).

[PJ76] Planinic, J., Nucl. Instr. & Meth., 136, 165 (1976).

[PV74] Palladino, V. and Sadoulet, B., LBL Preprint, LBL-3013.

[RB52] Rossi, B., 'High Energy Particles', Prentice Hall, (1952).

[RF62] Robinson, F.N.H., 'Noise in Electrical Circuits', O.U.P. (1962).

[RLP1] Rutherford Laboratory Proposal No. 167, 'Proposal to Study Multihadron Events Involving Identified Particles in High Energy Interactions at the SPS'.

[RL61] Robinson, L.B., Rev. Sci. Instr. 32, 1057 (1961).

[RP74] Rice-Evans, P., 'Spark, Streamer, Proportional and Drift Chambers', Chapter 7, Richelieu (1974).

[RV67] Radeka, V., Rev. Sci. Instr. 38, 1397 (1967).

[RV68] Rudeka, V., I.E.E.E. Trans. Nucl. Sci., NS-15, 455 (1968).

[RV72] Radeka, V., Nucl. Instr. & Meth., 99, 525 (1972).

[RV74] Radeka, V., I.E.E.E. Trans. Nucl. Sci. NS-21, 51 (1974).

[SB75] Sadoulet, B., I.E.E.E. Trans. Nucl. Sci., NS-22, 892 (1975).

[SC75] Sequin, C.H. and Tompsett, M., 'Charge Transfer Devices'. Supplement 8 to Adv. Electronics and Electron Physics. (1975).

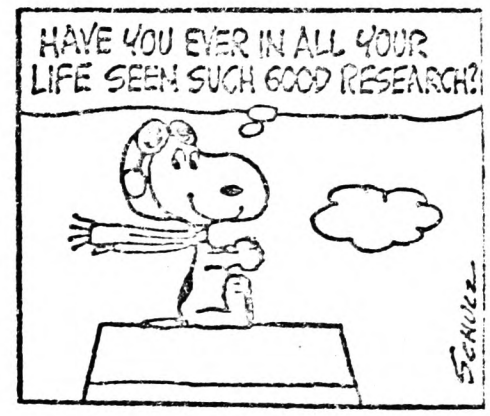
[SW68] Smythe, W.R., 'Static and Dynamic Electricity', McGraw-Hill (1968).

[WD50] Wilkinson, D.H., 'Ionization Chambers and Counters' C.U.P. (1950).

[WG76] Westphal, G.P., Nucl. Instr. & Meth., 136, 271 (1976).

[WH50] Wilkinson, D.H., Proc. Phil. Soc., 46, 508 (1950).

[ZA70] van der Ziel, A., Proc. I.E.E.E., 58, 8 (1970).


HAVE YOU EVER IN ALL YOUR LIFE SEEN SUCH GOOD RESEARCH?
SCHULZ